Univerzita Palackého v Olomouci

Přírodovědecká fakulta

Ubiquitin system in human pathologies

Habilitační práce

RNDr. Michal Šimíček, Ph.D.

Obor: Molekulární a buněčná biologie

Ostrava 2021

Prohlašuji, že předloženou práci jsem vypracoval samostatně s využitím informačních zdrojů, které jsou citovány.

V Ostravě dne 22.2.2021   RNDr. Michal Šimíček, Ph.D.

Acknowledgement

Thesis summary

The presented Habilitation Thesis is composed as a brief commentary to the major achievements of the applicant research after completing the doctoral studies. Significant part of the discussed results was already published in the top peer reviewed journals. The Thesis also contains a number of yet unpublished data obtained during the applicant´s postdoctoral work in the Laboratory of Molecular Biology, Medical Research Council in Cambridge, UK. Additionally, several yet unpublished results gathered at the current group leader position are included. All author´s publications directly related to the presented Thesis are attached in the appendix.

Table of content

Introduction

Central dogma of molecular biology defines protein as a molecule made according to sequence presented in nucleic acid chains. Upon ribosome driven translation newly formed polypeptides adopt an appropriate structural fold spontaneously or with a help of other protein factors. In eukaryotic cells, a vast majority of newly formed polypeptides requires not only proper folding but also further processing or adjustments to function properly.

The essential mechanism used by cells to diversify protein functions and dynamically coordinate their signalling network is based on covalent protein post-translational modifications. There is a large diversity of modifications that a nascent peptide can acquire upon its synthesis. Most of the post-translational modifications comprise the addition of small chemical groups or organic rings and chains to the protein surface. Methylation, acetylation, hydroxylation, phosphorylation, ADP-ribosylation, lipidation, glycosylation and many others belong to these types of modifiers and were characterised in the initial stages of protein research.

In the early 1980s, a group of scientists including Aaron Ciechanover, Avram Hershko and Irwin Rose discovered a novel mechanism of protein degradation based on a heat-stable polypeptide that they named ATP-dependent proteolytic factor 1. It was later shown to be identical to ubiquitin, a protein named for its ubiquitous expression. Several homologous ubiquitin-like proteins were then found both in eukaryotic and even prokaryotic cells. Following studies have uncovered complex molecular machinery responsible for reversible attachment of ubiquitin to other proteins.

A deeper exploration of ubiquitin implicated its importance not only in protein degradation but also in an enormous variety of other cellular processes ranging from transcription, translation, protein folding to vesicular trafficking, cell cycle, signal transduction and many more. Therefore, it is not surprising that defects in the ubiquitin system were linked to numerous developmental disorders and human diseases. The tremendous clinical success of selective compounds interfering with the ubiquitination machinery positions the ubiquitin system at the forefront of targeted drug discovery.

1. Ubiquitin system

Almost every protein in eukaryotic cell is post-translationally modified during its life span. After phosphorylation, a covalent attachment of small protein ubiquitin appears to be the most common protein modification. During ubiquitination the 8.5-kDa protein ubiquitin is covalently linked via its carboxyl group of the C-terminal glycine G76 to the ε-amino group of surface exposed lysine side chain or the very N-terminal amino group of a target proteins. In rare cases, also other reactive amino acids such as cysteine, threonine or serine might serve as a site of ubiquitin attachment (McClellan et al., 2019).

Ubiquitin is highly conserved among all eukaryotes with about 96% of amino acid sequence identity between human and yeasts. Human ubiquitin is encoded by four genes, which are expressed in form of two precursors: polyubiquitin - a protein consisting of four or more copies of the head to tail linked ubiquitin molecules encoded by *UBB* and *UBC* genes; and the fusion of ubiquitin and small or large essential ribosomal polypeptides encoded by *RPS27A* and *UBA56* genes, respectively (Kimura & Tanaka, 2010). These precursors are further cleaved to single ubiquitin units by multiple ubiquitin-specific proteolytic enzymes known as deubiquitinases.

Ubiquitination is reversible, highly versatile and many different forms of this posttranslational modification exist. In a process of monoubiquitination a single ubiquitin molecule is covalently linked to a protein. Multi-monoubiquitination occurs when several lysines of the target protein are tagged with single ubiquitin units. Moreover, ubiquitin itself can be further modified with another ubiquitin resulting in the formation of several topologically different polyubiquitin chains (Deol et al., 2019; Komander & Rape, 2012).

The presence of ubiquitin remodels the molecular surface and has a significant impact on the properties and functions of substrate proteins. Historically, ubiquitination was associated mainly with proteasome mediated degradation. In the past decade, however, it became clear that covalent attachment of ubiquitin might alter protein subcellular localization, enzymatic activity or protein-protein interactions (Chen & Sun, 2009; Kleiger & Mayor, 2014).

In addition to ubiquitin, several ubiquitin-like (Ubl) proteins including SUMO, NEDD8, ISG15, FAT10 and UFM1 were found. Most of these Ubl proteins are used to modify proteins in a similar manner as ubiquitin (Cappadocia & Lima, 2018). However, in contrast to ubiquitin, their functions are usually restricted to certain cellular processes.

1.1 Ubiquitination cascade

Conjugation of ubiquitin to a target protein is regulated by a sophisticated three-step enzyme cascade which requires collaborative action of the E1 ubiquitin-activating enzymes, the E2 ubiquitin-conjugating enzymes and the E3 ubiquitin ligases (Fig 1) (Pickart, 2001). The ubiquitination process is initiated by the E1 enzyme that hydrolyses ATP and adenylates ubiquitin C-terminal glycine. Modified ubiquitin is then attached to the active site cysteine of E1, forming ubiquitin-thioester and free AMP. In the second step, ubiquitin loaded on E1 is transferred to the catalytic cysteine of the E2 enzyme in an ATP-dependent reaction. The E3 ligases and also certain E2 enzymes catalyse the final step of the ubiquitination cascade, when isopeptide bond between lysine of the substrate protein and the C-terminal glycine of ubiquitin is formed (Deshaies & Joazeiro, 2009).
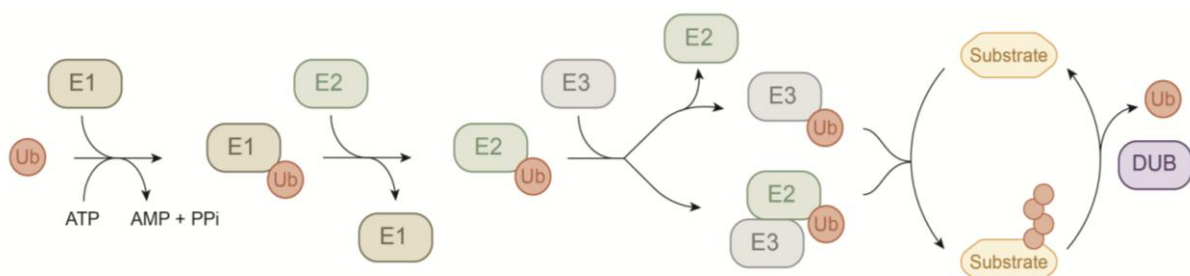

Figure 1: Schematic representation of the ubiquitination cascade

There are currently two recognized human E1 enzymes that catalyze the first stage of ubiquitin cascade: UBA1 and UBA6. To ensure specificity of the transfer only ubiquitin charged E1 can bind its cognate E2s with significant affinity (Groettrup et al., 2008; Schulman & Wade Harper, 2009). Humans possess 38 different E2 enzymes characterized by their highly conserved structure comprising the ubiquitin-conjugating catalytic domain with the active site cysteine and selective N-terminal binding motifs, where the respective E3 enzymes bind. The E2 enzymes are able to govern both initial conjugation of ubiquitin to substrate protein and also independent ubiquitin chain elongation, when longer polyubiquitin chains are formed (Wickliffe et al., 2011; Wijk & Timmers, 2010). The type of ubiquitination is in most cases defined by combined activities of the E2 and E3 enzymes (David et al., 2011). Because a single E2 enzyme can bind multiple E3 ligases and vice versa, the entire system is very robust and versatile. It is estimated that the human genome encodes for more than 600 different E3 enzymes (W. Li et al., 2008). The exact number of all human E3 enzymes is not known as many proteins containing domains with a potential E3 ligase activity were not yet functionally characterized.

The eukaryotic E3 enzymes can be divided on a basis of their structure and mechanism of action into two major classes: the Homologous to the E6-AP Carboxyl Terminus (HECT) domain and the Really Interesting New Gene (RING) together with the closely related U-box

domain E3 ligases (Buetow & Huang, 2016). HECT domain of the E3 enzymes contains catalytic cysteine that receives ubiquitin from E2. The HECT E3 ligase subsequently catalyzes ubiquitin conjugation to a specific lysine residue of an associated target protein. In contrast to the HECT E3 enzymes, the RING E3 ligases do not form a thioester bond with ubiquitin but rather promote the transfer of ubiquitin from E2 on the substrate protein (Zheng & Shabek, 2017). Therefore, the RING E3 ligases act as specific allosteric adaptors rather than real enzymes.

The RING E3s can be further separated into three families: simple RING E3 ligases, RING-in-between-RING (RBR) ligases and cullin-RING E3 ligases (CRLs). Mechanistically, the RBRs E3 enzymes represent RING/HECT hybrids. In RBR enzymes, the first RING domain functions as an adaptor by recruiting ubiquitin-charged E2 enzyme. The E2-bound ubiquitin is further transferred to the catalytic cysteine of the second RING-like domain in RBR ligase that finally mediates ubiquitin conjugation to the substrate (Deshaies & Joazeiro, 2009). CRLs are modular protein complexes containing scaffolding protein cullin, which brings in proximity a selective substrate recognition unit, the RING E3 and the ubiquitin-charged E2 enzymes. To be fully functional CLRs have to be modified with a ubiquitin-like (Ubl) protein NEDD8 (Schwechheimer, 2018). The cooperative action of all proteins in CRLs complexes is critical for the specificity and efficiency of many ubiquitination reactions.

1.2 Deubiquitination

The reversiblity of ubiquitination is accomplished by hydrolytic enzymes known as deubiquitinases (DUBs). The human genome encodes about 100 DUBs which oppose the function of E3 ligases. They can be subdivided into six families: ubiquitin-specific proteases (USPs), ovarian tumor proteases (OTUs), ubiquitin C-terminal hydrolyzes (UCHs), Josephin and MINDY family, and JAB1/MPN/MOV34 metalloenzymes (JAMMs). The USP, OTU, UCH, Josephins and MINDY are cysteine proteases, whereas members of the JAMM family coordinate zinc ion in their active site and function as metalloproteases (Abdul Rehman et al., 2016; Komander et al., 2009; Morrow et al., 2018).

DUBs regulate several crucial steps in ubiquitin processing. First, they are required for the generation of monoubiquitin by cleaving its precursors or free ubiquitin chains. To keep constant levels of free ubiquitin, DUBs can also rescue ubiquitin molecules that were accidently bound via their C terminal carboxyl to small cellular nucleophiles such as glutathione or polyamines (Reyes-Turcu et al., 2009). Second, DUBs can remove ubiquitin from modified proteins reversing their fate (Lee et al., 2011). Third, sequential action of DUBs and E3 enzymes may edit the topology of polyubiquitin chains that stay attached to proteins (Winborn et al., 2008). Many E3 ligases are known to form a complex with DUB enzymes (L. Li et al., 2015). Whether there is a common mechanism important for ubiquitin

processing in the E3-DUB complexes remains unclear. It is tempting to speculate that the E3-DUB pairs are involved in a selective editing of ubiquitin chains during their synthesis.

1.3 Ubiquitin chains

In the polyubiquitin chain several ubiquitin molecules are linked together via the C-terminal glycine (G76) of distal ubiquitin and one of the seven lysine residues (K6, K11, K27, K29, K33, K48, K63) exposed on the surface of proximal ubiquitin. Moreover, ubiquitin N-terminal methionine (M1) can serve as a site for the attachment of another ubiquitin, thus giving a rise to a special type of so called linear ubiquitin chains (Ikeda & Dikic, 2008; Komander & Rape, 2012). Altogether, eight types of polyubiquitin chains can be formed. The abundance of each ubiquitin polymer differs between cell types. Quantitative biochemical and mass spectrometry analysis revealed K48 and K63 as the most predominant linkages (Swatek et al., 2019). Recent studies including our work (see below in section 1.5) determined different topologies, unique biochemical properties and biological functions of each ubiquitin chain type (Boughton et al., 2020; Michel et al., 2015, 2017; Ohtake et al., 2018).

Ubiquitin polymers, where all ubiquitin molecules are connected with the same type of linkage, are known as homotypic chains. Heterotypic ubiquitin chains containing more than one linkage type within the same chain are also found in the cell. Ubiquitin polymers can be even branched when multiple ubiquitin moieties are anchored to distinct lysine residues in a single ubiquitin (Fig 2). On top of that, other Ubl proteins, such as SUMO and NEDD8 can be integrated into ubiquitin chains generating mixed heterologous chains (Swatek & Komander, 2016). The abundance and biological significance of these highly complex ubiquitin polymers are poorly characterized mainly due to the lack of appropriate experimental approaches. As novel techniques are being developed, the enigma of ubiquitin code is being gradually resolved.
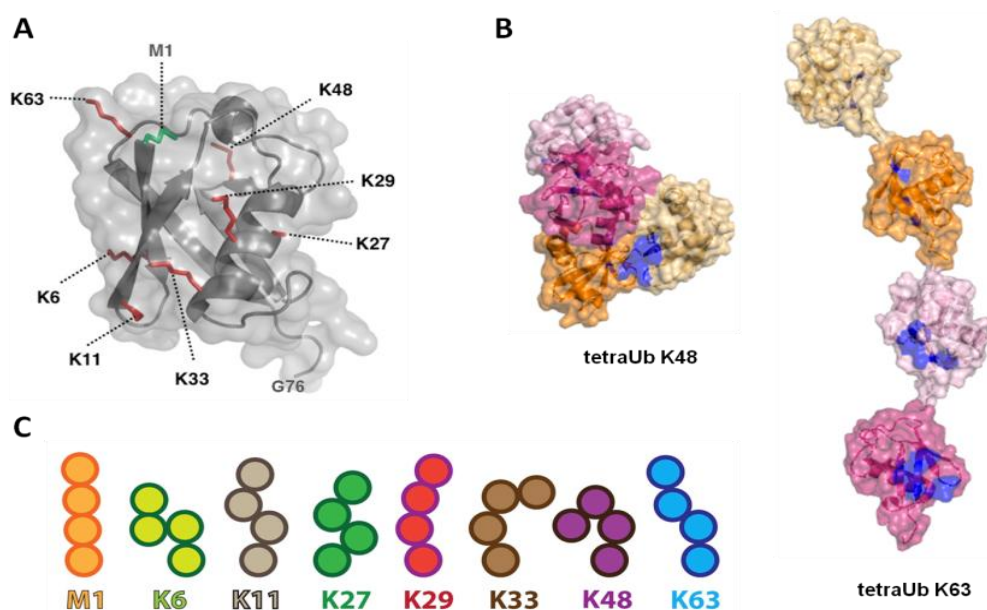
Figure 2: Ubiquitin and ubiquitin chains structure *A) Ubiquitin structure (PDB: 1UBQ), in read are the surface exposed lysines, in green is the N-terminal Met1 residue. B) Structures of tetra-ubiquitin K48 (PDB: 1TBE) and tetra-ubiquitin K63 (PDB: 3HM3), in blue are the Ile44 patches. C) Schematic topology of homotypic ubiquitin chains.*

The type of linkage in the ubiquitin chain is determined either by the E2 enzyme or E3 ligase. The RING E3 ligases are usually responsible for the selection of substrate lysine on non-ubiquitin protein targets. In these cases, chains extension and the linkage type in polyubiquitin are determined by associated E2 enzyme. In contrast, the HECT E3 ligases synthetize ubiquitin chains of defined topology themselves and in some cases they are even able to change linkage specificity despite using the same E2 enzyme (Ye & Rape, 2009).

To selectively regulate particular ubiquitin modifications, DUBs can display binding and hydrolytic specificity for both modified protein and/or a particular type of ubiquitin chain. In addition to conserved catalytic domains, accessory modules, motifs and posttranslational modifications of DUBs can drive their substrate specificity and enzymatic activity (Mevissen et al., 2013; Swatek et al., 2019). Moreover, we and others have shown that the deubiquitinating enzyme OTUB1 can inhibit the ubiquitination of target proteins in a catalytically independent manner (see below in section 2.3).

1.4 Post-translational modification of ubiquitin

As ubiquitin is not only a protein modifier but also protein itself, it can be subject to additional post-translational modifications including phosphorylation. Large-scale proteomic studies revealed that ubiquitin can be phosphorylated on most of its serine, threonine and tyrosine residues. The predominant phosphorylation site in human ubiquitin is at S65 (Swaney et al., 2015). Under basal conditions, only a very small fraction (1%) of ubiquitin is phosphorylated (Yau & Rape, 2016). The importance of ubiquitin S65 modification became apparent in the recent studies of neurodegenerative disorders, particularly Parkinson´s disease (Okatsu et al., 2015; Shiba-Fukushima et al., 2014, 2017).

Several genetic and biochemical studies have associated PINK1 kinase with Parkinson´s disease (Narendra et al., 2010; Valente et al., 2004). In healthy cells, mitochondria associated PINK1 is proteolytically cleaved resulting in the release of its kinase domain to the cytosol. Upon indelible damage of mitochondria, cleavage of PINK1 is prevented and the active kinase accumulates on the outer membrane of the damaged organelle (Matsuda et al., 2010). There it phosphorylates ubiquitin S65, increasing the amount of phospho-ubiquitin up to 20% of mitochondria associated ubiquitin (Ordureau et al., 2014). Phosphorylation of ubiquitin significantly affects not only its fold and also interactions with E2/E3 enzymes, DUBs or ubiquitin-binding domains (Wauer, Swatek, et al., 2015).

Additional PINK1 substrate is the counterpart serine residue in the Ubl domain of the RBR family E3 ligase Parkin that is often mutated in patients with Parkinson´s disease (Kane et al., 2014). The E3 ligase Parkin is a perfect example of phospho-ubiquitin meditated signalling, which is induced by the activity of PINK1 that decorates proteins on the surface of damaged mitochondria with phospho-ubiquitin to mark them for clearance by autophagy. This creates novel interaction interface that recruits and activates Parkin, which in turn ubiquitinates many surrounding proteins. The newly formed ubiquitin chains are further phosphorylated by PINK1, thus forming new binding sites to attract more Parkin molecules resulting in amplification of the signal. Finally, a large number of phospho-ubiquitin chains on mitochondria surface provide unique binding platform for selective autophagy adaptors, which ultimately deliver damaged mitochondria to autophagosome for degradation (Heo et al., 2015; Lazarou et al., 2015).

Our study revealed that ubiquitin phosphorylation is a double-edged sword. We solved the crystal structure of partially active E3 ligase Parkin, where the phospho-ubiquitin is bound to its allosteric site (Fig 3). This interaction induces dramatic structural reorganization of the entire Parkin molecule and it is important for induction of Parkin catalytic activity (Wauer, Simicek, et al., 2015).
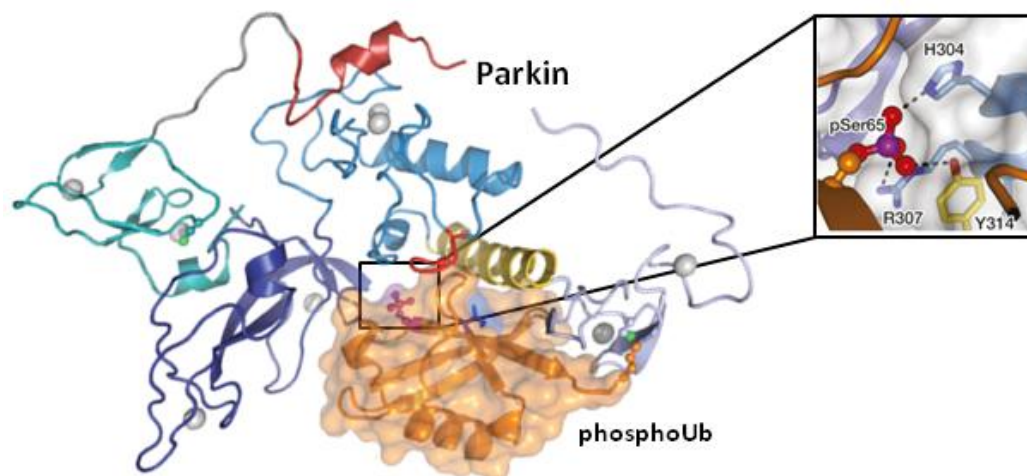
Figure 3: Structure of a Parkin bound to phospho-ubiquitin *with the close-up view of Parkin and phospho-S65 in ubiquitin. Adapted from Wauer T., Simicek M. et al. Nature 2015.*

To validate our structural model, we tested phospho-ubiquitin-binding mutants of Parkin in the cellular system. The immunofluorescence experiments revealed that Parkin relocalisation to damaged mitochondria and ubiquitination of outer mitochondrial proteins is critically dependent on its ability to bind phospho-ubiquitin (Fig 4). On the other hand, we and others have shown that Parkin uses phospho-ubiquitin less efficiently than unmodified ubiquitin and cannot form polyubiquitin chains composed exclusively of phospho-ubiquitin (Wauer, Swatek, et al., 2015).

Figure 4: Parkin localization on mitochondria. *A) Localisation of wild type (WT) and phospho-ubiquitin binding mutant (A320R) of Parkin on damaged mitochondria. Scale bars 10 μm. B) Parkin-dependent ubiquitination of mitochondria outer membrane protein Tom20. Adapted from Wauer T., Simicek M. et al. Nature 2015.*
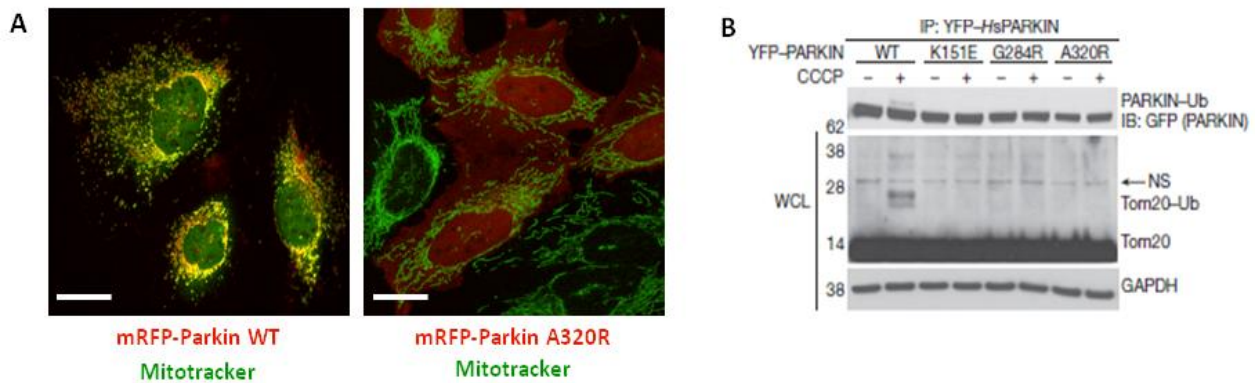
In addition to phosphorylation, ubiquitin can be posttranslationally modified with acetyl residues on K6 and K48. These modifications inhibit a build-up of K6, K11, K48 or K63-linked polyubiquitin chains (Ohtake et al., 2015). However, only 0.03% of ubiquitin molecules were found to be acetylated in resting cells and the responsible acetylation enzyme is not known (Swatek & Komander, 2016). Therefore the biological significance of these modifications remains elusive. It is likely that as in the case of PINK1 mediated phosphorylation also acetylation of ubiquitin is restricted to the specialised biological processes.

1.5 Ubiquitin binding domains

Ubiquitin conjugated to protein substrates is recognized by a wide array of proteins containing highly defined ubiquitin-binding domains (UBD). In humans, there are over 200 different proteins containing UBDs involving approximately 20 different protein families. Most of UBDs and smaller ubiquitin binding motifs recognize single mono-ubiquitin. Certain UBDs can also selectively bind to specific linkages in ubiquitin polymers. Based on their structure, UBDs can be broadly characterized as α-helix based that contain ubiquitin interacting motif, zinc-finger based, pleckstrin homology-like or ubiquitin conjugating-like domains (Husnjak & Dikic, 2012).

Except for the flexible C-terminal tail, the ubiquitin structure is relatively rigid with mainly polar residues on its surface. Majority of the known UBDs bind to the unique hydrophobic patch centered on isoleucine 44 (I44) on the ubiquitin surface. Several other ubiquitin interacting interfaces were found comprising aminoacid residues I36, F4 and D58 (Penengo et al., 2006; Sloper-Mould et al., 2001). This creates a possibility that a single ubiquitin might continually recruit several UBDs.

For a long while due to the lack of proper biochemical tools most of the characterized UBDs were either unselective or bound to K48 or K63-linked ubiquitin polymers. In our study we have described for the first time enzyme-based biochemical approach to generate *in vitro* ubiquitin chains containing K29 and K33 linkage types and determined their 3D structures (Michel et al., 2015). Moreover, by studying DUB called TRABID we found a novel UBD specifically recognizing these polyubiquitin chains. TRABID contains three N-terminal Npl4-like zinc finger domains (NZF1-3), where NZF1 acts as a unique K29/K33 UBD. Deletion or mutations in NZF1 abrogated ubiquitin binding and cellular localization of TRABID, whereas the equivalent mutations in NZF2 or NZF3 did not lead to significant changes (Fig 5) proving TRABID NZF1 as an interesting tool to study the atypical K29/K33-lined ubiquitin chains in living cells.
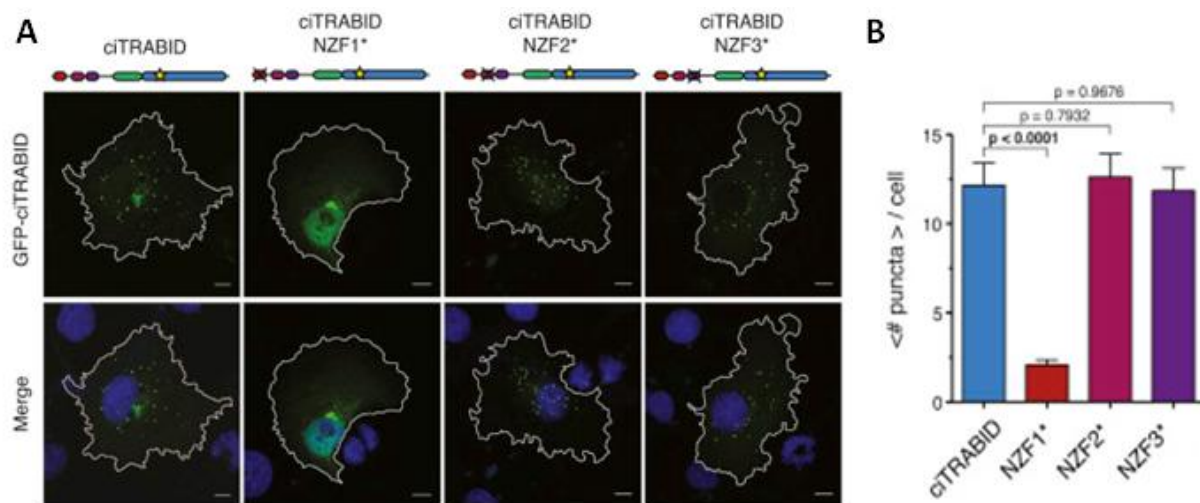

Figure 5: Localization of TRABID mutants. *A) Localization of catalytically inactive full-length GFP-TRABID (ciTRABID). Mutations in the ubiquitin binding interface of NZF1 (NZF1*) lead to a significant decrease in the number of TRABID-positive dots, whereas the equivalent mutations in NZF2 (NZF2*) or NZF3 (NZF3*) do not change positioning and number of puncta. Scale bars, 10 μm. B) Statistical analysis of experiments in A. Adapted from Michel M. et al. Mol Cell 2015.*

In general, the affinity of most UBDs for ubiquitin is relatively low, ranging in micromolar range. However, the presence of multiple UBDs or ubiquitin interacting motifs in a single protein greatly increases the avidity of protein-ubiquitin complex. Further, the combinatorial use of UBDs and other protein-protein interaction domains and surrounding sequence motifs might contribute to the stabilization of larger protein complexes. Many UBDs containing proteins are often themselves monoubiquitinated in a mechanism referred to as coupled monoubiquitination, which prevents UBDs *in trans* binding to the ubiquitinated cargo (Woelk et al., 2006).

1.6 Ubiquitination as a marker for protein degradation in proteasome

Historically, the main function of ubiquitin was attributed to its involvement in protein turnover mediated by the ubiquitin-proteasome pathway. Later studies, including our work associated ubiquitin modifications with autophagy, a proteasome independent degradatory route (Pohl & Dikic, 2019; Simicek et al., 2013).

Proteasome is a large protein assembly with a barrel-shaped structure comprising a central proteolytic core made of four ring structures, flanked by two cylinders containing ubiquitin receptors that allow entry of ubiquitinated proteins (Bard et al., 2018). The polyubiquitin chains are recognised by the proteasome ubiquitin receptors with the highest affinity for K48-linked ubiquitin polymers. *In vitro,* all homotypic ubiquitin chains might be efficiently processed by proteasome. In cells, however, particularly K63-linked polyubiquitin and branched heterotypic chains are not efficiently processed by proteasome (Kravtsova-Ivantsiv & Ciechanover, 2012) and have exclusively non-proteolytic functions (Chen & Sun, 2009; Wong et al., 2008).

In addition to ubiquitin receptors integral to proteasome, eukaryotic cells express several soluble ubiquitin binders including RAD23A that shuttle polyubiquitinated proteins to proteasome (Dantuma et al., 2009). Even though K48-linked polyubiquitin is most efficient marker for proteasome degradation, structural and biophysical experiments revealed that RAD23A is not able to distinguish between homotypic K48 or K63-linked chains and branched ubiquitin trimers containing these linkages (Nakasone et al., 2013). To shed more light on this interesting phenomenon, we studied K63-linkage specific deubiquitinase OTUD1 found in the previous proteomic study in complex with RAD23A. Our biochemical analysis confirmed the interaction and mapped the binding epitope to the catalytic domain of OTUD1 and Ubl domain of RAD23A. To understand detailed molecular features of this complex, we have crystallized both proteins and solved the crystal structure (Fig 6). Close inspection of the interaction interface indicates that RAD23A Ubl uses a conserved I49 patch (homologous to ubiquitin I44) to bind OTUD1 outside of its catalytic core.
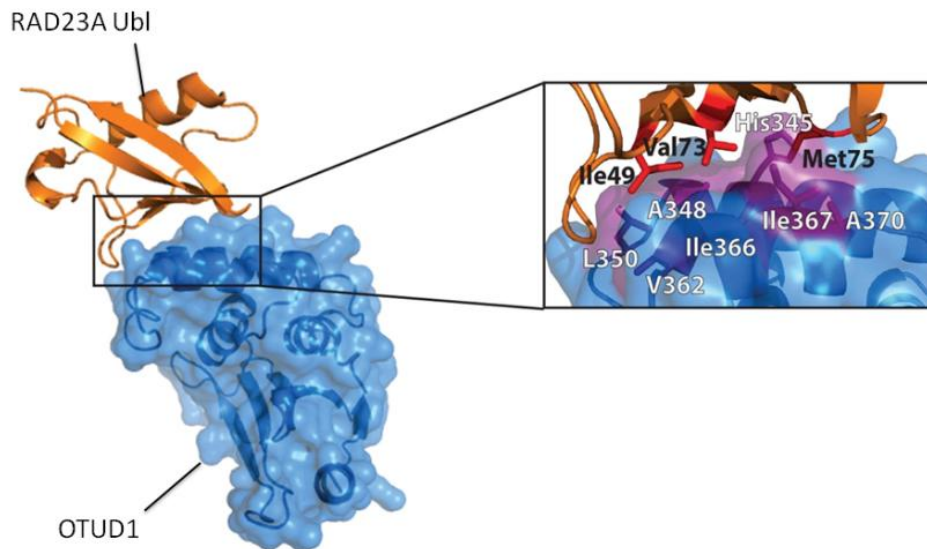
Fig 6: Crystal structure of OTUD1 in complex with RAD23A. *A) Structure of OTUD1 catalytic domain bound to RAD23A Ubl domain. B) Close-up view of the interaction interface highlighting aminoacids mediating the interaction. Simicek M. et al. unpublished*

As the crystal structure may lead to artifacts, especially in the case of dynamic protein complexes, we applied NMR analysis to examine the interaction characteristics in the solution. As shown in Fig 7, the obtained resonance data further supported our structural model derived from the crystallographic experiments.
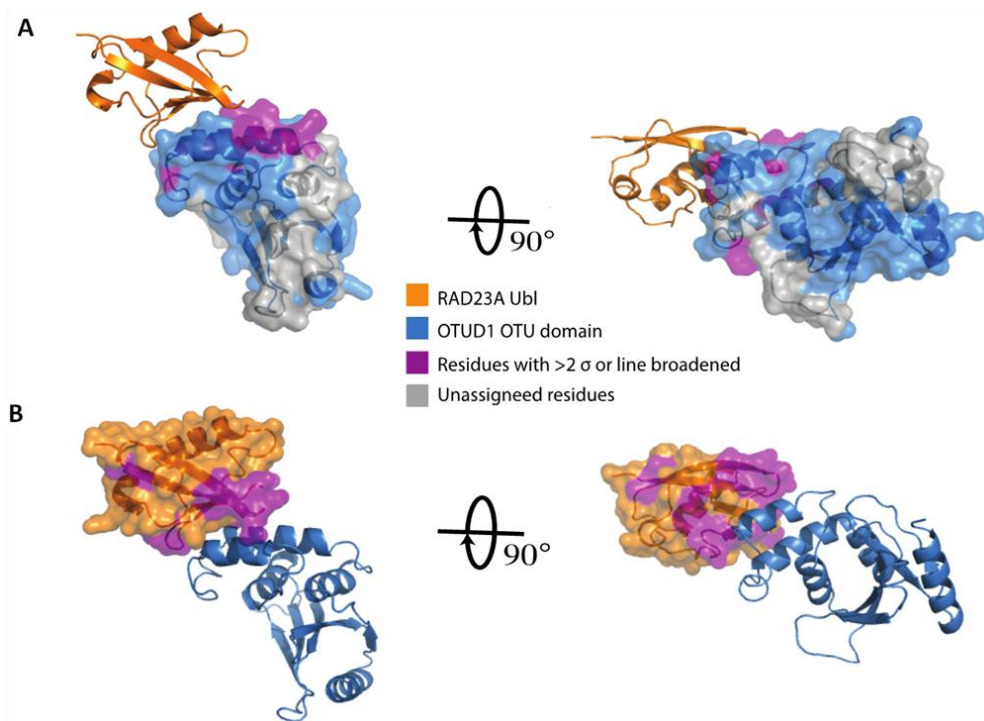

Fig 7: Solution structure of OTUD1 in complex with RAD23A. *A) NMR structure of OTUD1 catalytic domain with superposed RAD23A Ubl. B) NMR structure of RAD23A with superposed OTUD1 catalytic domain. Simicek M. et al. unpublished*

Both structural models suggested that binding of RAD23A does not sterically hinder ubiquitin interaction with OTUD1 catalytic core. To test whether OTUD1 bound to RAD23A can still associate and cleave K63-linked polyubiquitin, we performed several biophysical experiments including surface plasmon resonance (SPR) and *in vitro* deubiquitinase assay (Fig 8). To avoid destruction of di-ubiquitins on the SPR chip, we used catalytically inactive OTUD1 C320A
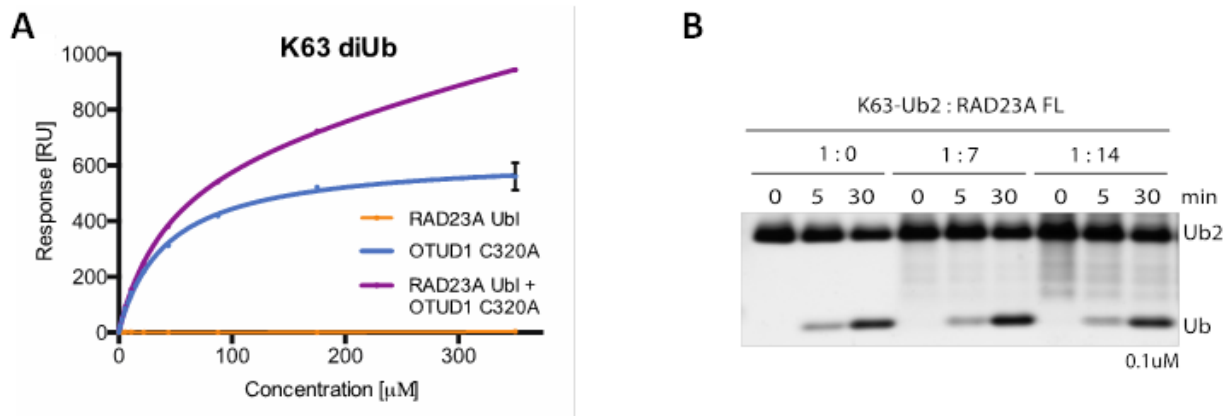
Fig 8: Biophysical and enzymatic analysis of OTUD1-RAD23A complex *A) SPR analysis of OTUD1 and RAD23A Ubl binding kinetic. B) In vitro deubiquitination assay. OTUD1 was used in a single concentration (0.1 µM). Simicek M. et al. unpublished*

In addition to the Ubl domain, RAD23A also possess two UBA domains that can bind longer ubiquitin chains. To expose our model to a more complex cellular environment, we used RAD23A as bait to purify ubiquitinated proteins from cell lysate. The extracted complexes were further treated with wild type (WT) or RAD23A binding mutant (A348R) OTUD1. This experiment revealed that RAD23A-bound OTUD1 retains its selectivity for K63-linked polyubiquitin on endogenous proteins (Fig 9).
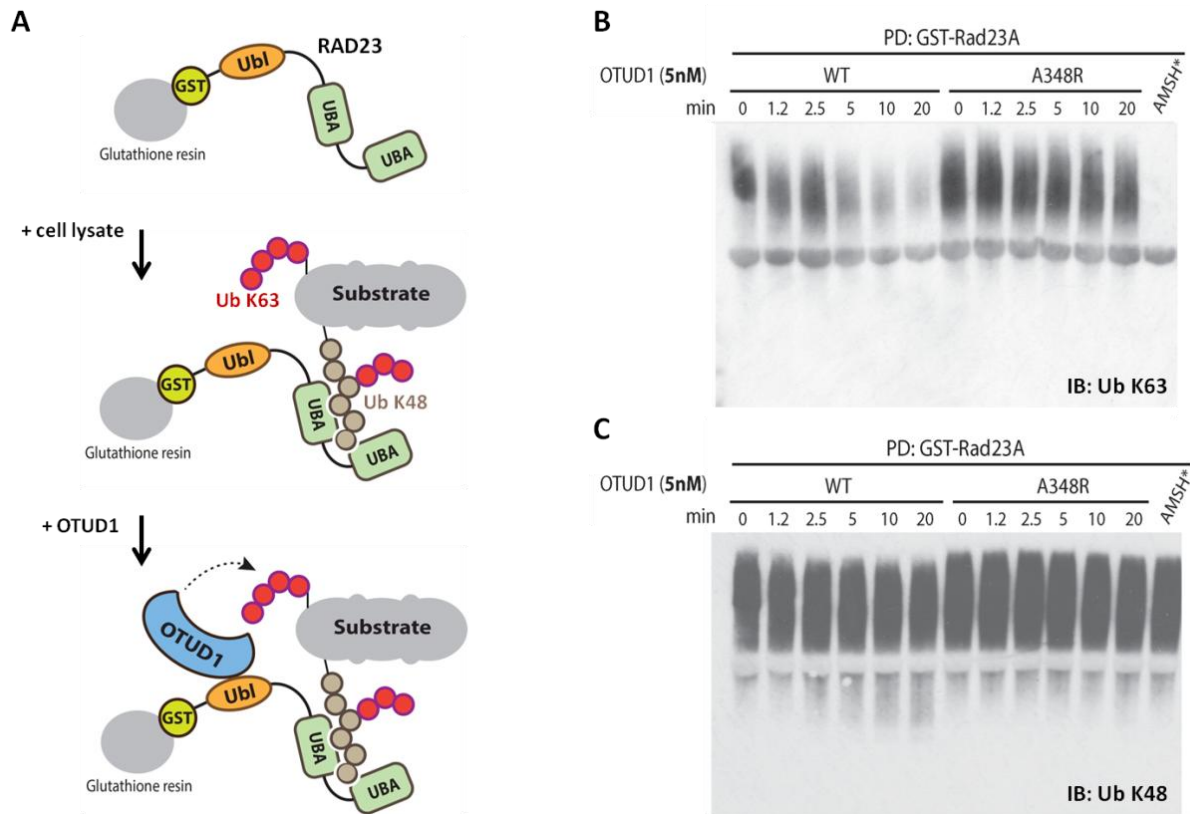
Fig 9: Biochemical analysis of OTUD1-RAD23A complex. *A) Schematic of the experimental setup. B-C) Western blot analysis of the RAD23A pull downs treated with OTUD1. K63-specific deubiquitinase AMSH was used as a control. Simicek M. et al. unpublished*

Collectively, our structural, biophysical and biochemical data suggest on a novel model, where K63-specific deubiquitinase OTUD1 regulates RAD23A-dependent protein degradation in proteasome by editing complex polyubiquitin modifications such as K63-linked polyubiquitin, heterologous or mixed ubiquitin chains, which would otherwise inhibit proteasome processing as summarized in Fig 10. Even though our knowledge of the ubiquitin code is quickly expanding, further cell-based studies are required to elucidate the precise role of complex ubiquitin modifications in proteasome degradation.
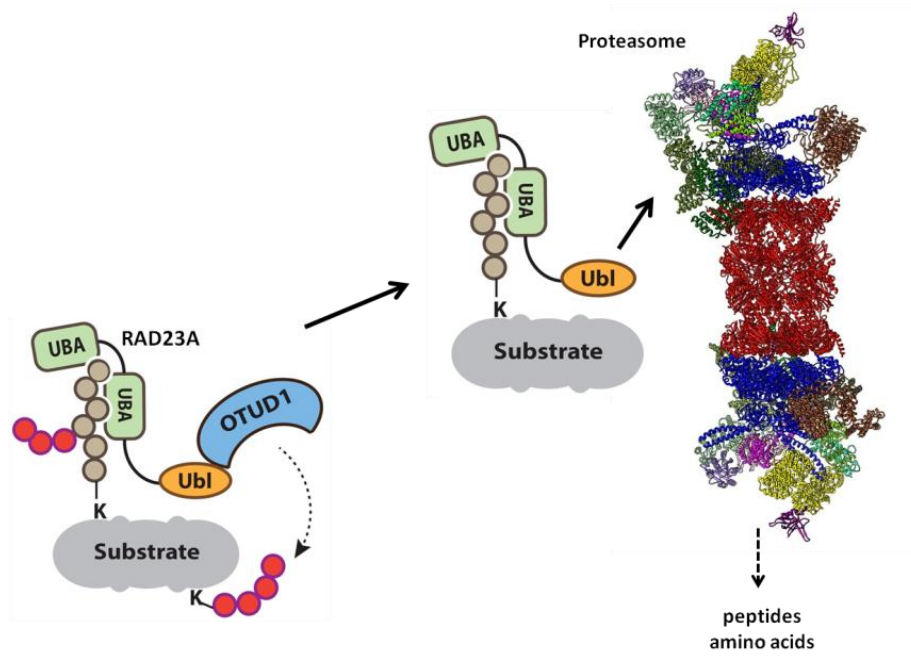
Fig 10: A working model of OTUD1-RAD23A complex function. *RAD23A-bound OTUD1 might selectively edit polyubiuitinated proteins associated with RAD23A UBA to promote fast destination and processing of target proteins in proteasome. Simicek M. et al. Unpublished.*

2. Non-degradative ubiquitination in (non)-oncogenic signaling

Ubiquitin does not serve only as a tag driving protein degradation. It is also an important mediator of additional cellular processes including protein trafficking, cell cycle regulation, apoptosis, DNA repair, protein quality control, transcription, translation, signal transduction and many others (Kliza & Husnjak, 2020). In this section, several examples of non-degradative ubiquitination in cell pathophysiology are described in more detail.

One of the best studied roles of non-degradative ubiquitination in cancer and immune disorders is the activation of the transcription factor NF-κB (Skaug et al., 2009). Signals from many receptors such as TNFR1, IL-1R1 or TLR4 converge at the stage of the inhibitor of IκB kinase (IKK) complex (Zinngrebe et al., 2014). In addition to ubiquitin-mediated proteasome degradation of IκB, ubiquitination has been implicated in the dynamic spatiotemporal regulation of the IKK complex. Numerous upstream molecules in NF-κB pathway are modified with K11, K63 or linear M1-linked ubiquitin chains, which allow transient formation of large signaling assemblies. At least two DUBs, A20 and CYLD, were found to negatively regulate signaling routes leading to NF-κB activation (Emmerich et al., 2013; Lork et al., 2017) .

Sequential recruitment and action of different E3 ubiqutin ligases and DUBs play an intimate role in the control of protein assemblies involved in DNA damage response (DDR) that is often deregulated in many cancers. For example, the formation of double stranded brakes in DNA leads to phosphorylation of histone 2AX (yielding γH2AX) and associated checkpoint protein MDC1 by ATM kinase (Eliezer et al., 2014). Phosphorylated MDC1 triggers attraction of the E3 ligase RNF8. Ubiquitination products generated by RNF8 are recognized by UBDs of another RING domain E3 ligase, RNF168 (Bartocci & Denchi, 2013; Kongsema et al., 2016). The primary outcome of RNF8/RNF168-mediated ubiquitination during early steps of DDR is recruitment and retention of DNA repair and signaling factors including BRCA1 on chromatin sites surrounding DNA lesions (Rosen, 2013). BRCA1 constitutes also E3 ligase activity and together with BARD1 assembles K6-linked ubiquitin chains on itself or other DDR proteins (Wu-Baer et al., 2003).

At later stages of DDR, site-specific ubiquitination of DNA sliding clamp PCNA determines how the cell will replicate regions of damaged DNA. Monoubiquitinated PCNA is recognized by low fidelity DNA polymerases that trigger error prone DNA synthesis while PCNA modified with K63-linked ubiquitin chains initiate error free replication by mechanisms that are not yet fully understood (Takahashi et al., 2020; Zhao & Ulrich, 2010).

Modification of integral membrane proteins with ubiquitin generally acts as a sorting signal for delivery to specific cellular destinations. In yeasts, ubiquitination mediates Golgi-to-endosome transport and determines whether a protein will be delivered to the plasma

membrane or endosome. In mammalian cells, ubiquitination is often sufficient but not required for internalization of membrane receptors by endocytosis (MacGurn et al., 2012). Therefore, it is not surprising that many endocytic proteins contain UBDs. For example, proteins from the Epsin family interact with ubiquitin attached to membrane proteins via tandem UIM motifs and connect ubiquitinated substrates with clathrin and AP-2 adaptors (Piper et al., 2014). Internalized receptors are further separated in endosomes and either recycled back to the plasma membrane or following ubiquitin-dependent sorting are destined to and degraded in lysosomes (Haglund & Dikic, 2012).

In addition to the regulation of multimeric protein assemblies, ubiquitination might also determine the specific subcellular localization of modified protein. As an example, the RING family E3 ligase TRAF6 mediates polyubiquitinatination of Akt kinase with K63-linked ubiquitin chains (W. L. Yang et al., 2009). This modification is required for the membrane localization and full activity of this proto-oncogene. On the other hand, attachment of K48-linked ubiquitin chains by TTC3 ligase promotes Akt degradation in proteasome (Suizu et al., 2009).

The number of cellular events driven by non-degradative forms of ubiquitination is overwhelming and our knowledge about this type of posttranslational modification is steadily increasing. The above mentioned examples represent only a very small snapshot of cellular processes driven by ubiquitin-dependent mechanisms. Particularly in cancer research and immunology, the understanding of the ubiquitin regulatory pathway is of high importance as many E3 ligases and DUBs constitute potential drug targets (Deng et al., 2020; J. Liu et al., 2021).

The following sections are focused on oncoproteins from the Ras family and our findings connecting Ras signaling with ubiquitin machinery.

2.1 Ras GTPases

The ability of every cell to perceive and correctly respond to signals from its intra- and extracellular environment is mediated by a complex system of the dynamic network of signaling pathways. In order to maintain the system flexible cells express many proteins, whose activity can be rapidly switched on and off in response to upstream signals. Small GTP-binding proteins referred to as monomeric GTPases mastered this activation twist. This large protein family is determined by the presence of conserved globular GTP-binding domains. All GTPases share the same mechanism of activation mediated by presence of guanidine nucleotides in their nucleotide-binding pocket. In the active, GTP-bound state, large conformational changes create unique surface epitopes with a high affinity for downstream targets. Induction of GTP hydrolysis then returns GTPase to the low affinity mode (Biou & Cherfils, 2004).

Most the GTPases involved in signal transduction fall within the Ras superfamily that is evolutionary very conserved with orthologs found in *Drosophila, C. elegans, S. cerevisiae, Dictyostelium* and plants. Gene duplication has resulted in a large expansion of this protein family in all vertebrate genomes. Over 150 members of the Ras superfamily can be subdivided into five groups: Ras, Rho, Rab, Ran and Arf (Colicelli, 2004). Proteins from the Ras family regulate cell proliferation, differentiation, morphology, and apoptosis (Karnoub & Weinberg, 2008). Members of the Rho family are involved in signaling networks that regulate actin reorganization, cell polarity, cell cycle progression, and gene expression (Jaffe & Hall, 2005; Sit & Manser, 2011). The largest branch of Ras-related GTPases constitutes Rab proteins that participate in vesicular cargo delivery and protein trafficking between different organelles via endocytotic and secretory pathways (Stenmark, 2009). In humans, the Ras subfamily constitute 36 members that are involved in diverse range of cellular functions including gene expression, proliferation, differentiation, cell and tissue polarity, autophagy and innate immune response (Wennerberg et al., 2005).

Ras-related GTPases have a relatively small size (183 to 340 amino acids) without any conspicuous functional motifs extended from the compact, globular, ~20kDa GTPase domain (G domain). A typical fold of Ras GTPases consists of five α-helices around a central six β-sheets that are connected with ten loops. Crucial parts of every G domain are G1-G5-boxes, highly conserved nucleotide binding elements common to all Ras family members. Amino acids present in these motifs are required for coordinating magnesium ion, guanosine nucleotides and the actual GTP hydrolysis. Mutations occurring in these regions usually affect GTPase activity (Khan & Ménétrey, 2013; Pertz, 2010; Wong et al., 2008). Substitution of Ras G12 with any other amino acid prevents access of water molecule needed for the GTP hydrolysis and leads to hyperactivation of Ras. Therefore, Ras G12V or similar mutations are often found in many human tumors (Hobbs et al., 2016). The surrounding sequences are usually specific to a particular protein and contribute to the functional specificity of each GTPase.

Most of the Ras subfamily members localize predominantly to the plasma membrane or associate with intracellular vesicles. Membrane localization is determined mainly by prenylation of the C-terminal CAAX motif (C = Cys, A = aliphatic, X = C-terminal amino acid), in which the cysteine residue is modified by isoprenoid farnesyl or geranyl soon after protein synthesis (Gotoh et al., 2001; Hancock, 2003). Processing continues on the cytosolic leaflet of the endoplasmic reticulum where RceI enzyme proteolytically removes the AAX motif (Boyartchuk et al., 1997). For permanent association with membrane Ras proteins require an additional targeting signal. In KRas4B, the second signal is comprised of a polybasic lysine-rich sequence located upstream of the C-terminal Cys. Positively charged lysine residues then facilitate association with negatively charged plasma membrane phospholipids

(Quatela et al., 2008). In contrast to KRas, farnesylated HRas and NRas are further modified in Golgi with palmitoyl group (Apolloni et al., 2000; Laude & Prior, 2008). A similar relationship appears between Rap1 (prenylation + polybasic region) and Rap2 (prenylation + palmitoylation) (Canobbio et al., 2008), while other Ras-related GTPases RalA and RalB undergo exclusively geranylgeranylation (Falsetti et al., 2007). These modifications are essential for facilitating membrane association and subcellular localization and are also critical for the correct biological activity of particular GTPase.

2.2 Mechanisms of Ras activation

All Ras GTPases cycle between inactive, GDP-bound, and active, GTP-bound states. Transition between these states is followed by significant conformational changes localized primarily to the switch I and switch II regions. GTP-binding induces reorganization of these flexible loops creating the effector binding site. The rate-limiting step in the Ras activation is the exchange of GDP for GTP. If not catalyzed, this process is very slow (3.4×10^{-4} sec for HRas) even in presence of a high GTP:GDP (10:1) ratio in the cytosol. Therefore, the main pool of Ras GTPases is kept inactive in the quiescent cells (Buday & Downward, 2008).

To promote fast activation of Ras GTPases, a set of enzymes called GTP exchange factors (GEF) stabilizes GTPases in their transition ,open' state allowing dissociation of GDP that is replaced with more abundant GTP, thus promoting activation of GTPases. The intrinsic GTPase activity of Ras proteins is relatively low ($\sim 4.2 \times 10^{-4}$ sec), which would tend to prolong signal transduction (Shutes & Der, 2005, 2006). To terminate Ras activity, GTPase activating proteins (GAP) greatly enhance GTP hydrolysis leading to deactivation of GTPases. The molecular mechanism of GAP mediated GTP-hydrolysis is based on conserved arginine residue (Arg finger) that is present in all known GAP proteins. The Arg finger stabilizes the negative charges of β and γ phosphate in GTP developing the transition state and positioning the conserved glutamine in the GTPase switch II (Q61 in Ras) to activate water molecule for in-line nucleophilic attack of the γ phosphate of GTP, eventually establishing a bona fide enzymatic active site (Bos et al., 2007; Cherfils & Zeghouf, 2013). Therefore, it is not surprising that the second most common Ras mutation occurs in position Q61 (Prior et al., 2012).

The third type of GTPase regulators are guanosine nucleotide dissociation inhibitors (GDIs) that bound to inactive, GDP-loaded GTPases and block the release of GDP and its exchange for GTP. Further, GDI proteins inhibit membrane localization of certain GTPases by protecting their lipid modifications. Moreover, all Ras family GTPases may be regulated by multiple GEF and GAP proteins enabling dynamic regulation and involvement in different signaling pathways (Cherfils & Zeghouf, 2013). The GTPase cycle and accompanying regulatory factors are summarized in Fig 11.
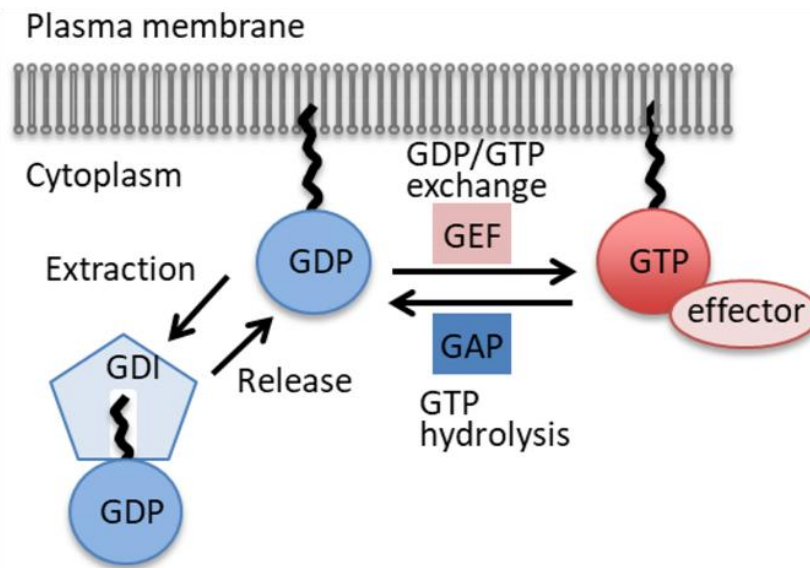
Fig 11: Schematic of the GTPase cycle in Ras-like GTPases. *GEF and GAP enhance the rate of guanidine nucleotide exchange and hydrolysis, respectively. GDIs act as inhibitory molecules for inactive GDP-bound GTPases and can modulate their release from plasma membrane. Adapted from: Toma-Fukai & Shimizu, 2019*

2.3 Non-degradative ubiquitination of Ras

Beyond oncogenic mutations, overexpression of GEFs and loss of GAPs also contribute to tumorigenic properties of Ras (Vigil et al., 2010). Further, post-translational modifications including phosphorylation (Bivona et al., 2006), lipidation (Hancock, 2003), and acetylation (M. H. Yang et al., 2013), were described to modulate Ras activity. Polybiquitination mediated by the E3 ligases β-TrCP1, NEDD4 and LZTR1 triggers degradation of Ras in the proteasome (Shukla et al., 2014; Steklov et al., 2018; Zeng et al., 2014). Previous studies described non-degradative forms of mono- and diubiquitination of several Ras family members (Jura et al., 2006; Sasaki et al., 2011; Xu et al., 2010). Our work revealed a novel mechanism of non-degradative ubiquitination of Ras-related GTPase RalB in the regulation of autophagy and anti-viral response (Simicek et al., 2013).

Oncogenic Ras is expressed as three major isoforms (HRas, NRas and KRas), which all were found to be modified with mono- or diubiquitin without significant effect on their stability (Baker et al., 2013). Attachment of single ubiquitin to specific lysines on the Ras surface seems to be critical for the Ras driven pathways. For example, the E3 ligase RABEX5 ubiquitinates NRas and HRas that subsequently relocalize from the plasma membrane to intracellular vesicles, leading to inactivation of canonical Ras signalling (Xu et al., 2010). On the other hand, ubiquination of HRas on K117 enhances its intrinsic nucleotide exchange and promotes GTP loading (Baker et al., 2013). Similarly, ubiquitin conjugated to KRas K147 impairs the NF1-mediated GTP hydrolysis and thus increases Ras activity (Sasaki et al., 2011).

In our study (Baietti and Simicek et al., 2016), we aimed to identify the enzyme responsible for removing ubiquitin from Ras and potentially attenuating Ras signaling. Initially, we performed a selective protein-protein interaction assay with a large panel of human DUBs. Between other hits, we found OTUB1 as potential Ras interactor. OTUB1 is a unique DUB that can inhibit protein ubiquitination both via classical hydrolytic reaction and also non-catalytically by preventing the E2-mediated ubiquitin conjugation (Pasupala et al., 2018). The later mechanism is based on the extended OTUB1 N-terminus that binds and sterically interferes with the transition of ubiquitin from the E2 catalytic cysteine to target proteins (Wiener et al., 2012).

Our biochemical analysis revealed that OTUB1 can remove mono- and diubiquitin moieties from NRas in a catalytically independent manner. As deletion of OTUB1 N-terminal residues 1-30 prevented a negative effect on NRas ubiquitination, we concluded that the previously described E2-binding mechanism is responsible for the inhibitory effect of OTUB1 on NRas mono- and diubiquitination (Fig 12).
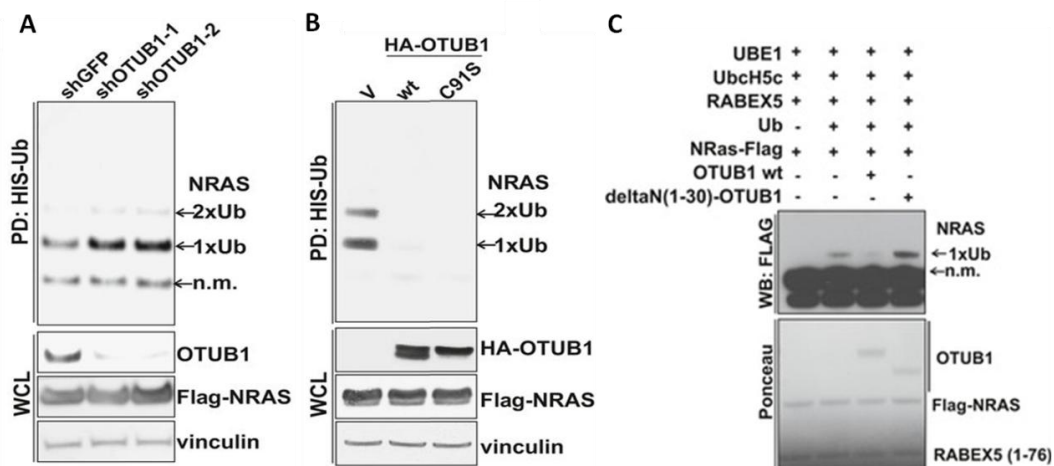
Fig 12: OTUB1 regulates NRas ubiquitination in a catalytically independent manner. *A) Pull down of ubiquitinated NRas from cells with OTUB1 knock down. B) Pull down of ubiquitinated NRas from cells overexpressing OTUB1 wild type (WT) and catalytic mutant (C91S). C) In vitro ubiquitination assay of NRas with E1 (UBE1), E2 (UbcH5c), E3 (RABEX5) enzymes in presence of WT or N-terminally truncated OTUB1. Adapted from Baietti FM. and Simicek M. et al. EMBO Mol Med. 2016.*

The OTUB1-mediated inhibition of NRas ubiquitination resulted in relocalization of the GTPase to the plasma membrane, where most of the NRas specific GEFs are found. Therefore, we hypothesized that OTUB1 not only prevents NRas ubiquitination but also indirectly promotes its activity. As expected, the pool of GTP-loaded NRas and also activation of the downstream MAPK pathway was significantly potentiated in OTUB1 overexpressing cells (Fig 13).
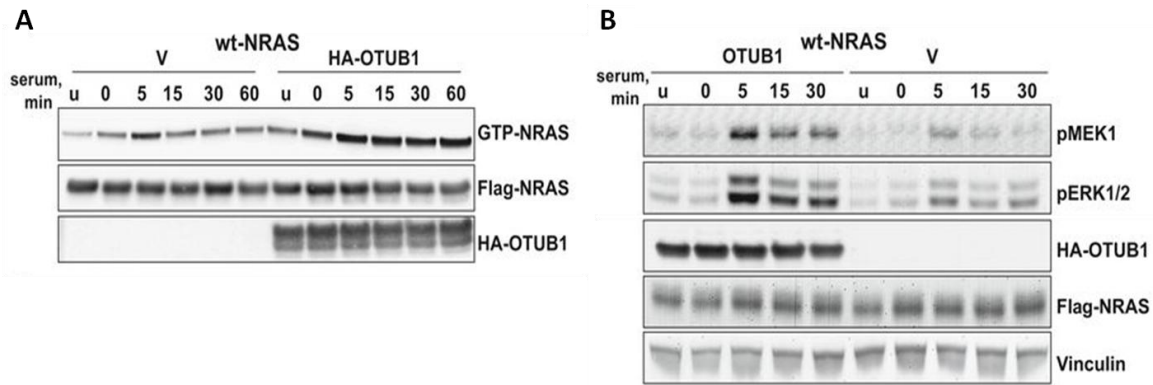
Fig 13: OTUB1 potentiates NRAS signaling. *A) Isolation of GTP-bound wild type (WT) NRas upon serum stimulation from cells with and without overexpression of OTUB1. B) Analysis of phosphorylation pattern of the MAPK components upon serum stimulation in cells with and without overxpression of OTUB1. Adapted from Baietti FM. and Simicek M. et al. EMBO Mol Med. 2016.*

Further mass spectrometry analysis revealed K128 as the predominant ubiquitination site in NRas. To gain deeper mechanistic insight on the regulation of NRas activity by non-degrative forms of ubiquitination, we developed a method for *in vitro* site specific ubiquitination of NRas. The method is based on the replacement of the isopeptide bond between the C-terminal ubiquitin glycine and substrate lysine with cysteine-based disulfide bond. The strategy for non-enzymatic, site-specific ubiquitination of NRas is shown in Fig 14.

Fig 14: *Schematic of the in vitro site-specific ubiquitination of NRas.* *Simicek M. et al. unpublished.*

This novel approach allowed us to study the interaction properties of NRas conjugated to monoubiquitin exclusively at K128. We successfully applied this system to pull down Ras regulatory proteins. Results of the biochemical experiments were in line with the biological phenotype, when ubiquitinated NRas was able to interact with the GEF protein SOS1. At the same time, binding to RAS GAP p120 was l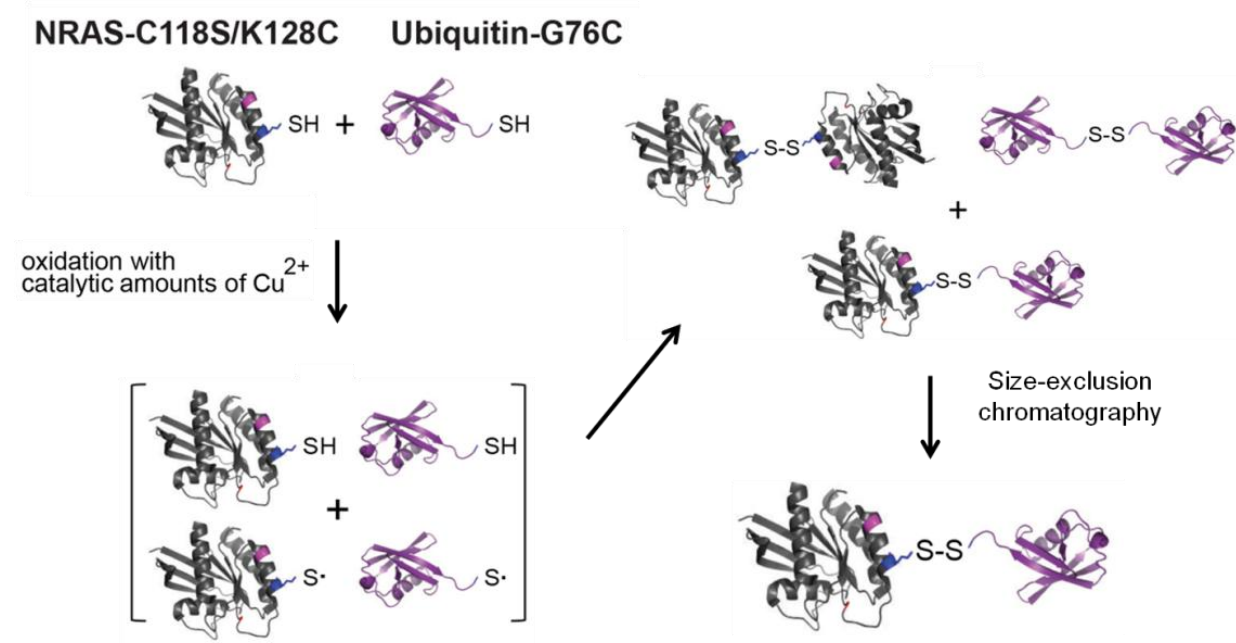argely abolished by ubiquitin on NRas K128. Additionally, we performed structural prediction that further supported the experimental data. In this model, ubiquitin fused to NRas K128 allowed association with SOS1, while the same modification would create steric hindrance in NRas GAP complex (Fig 15).
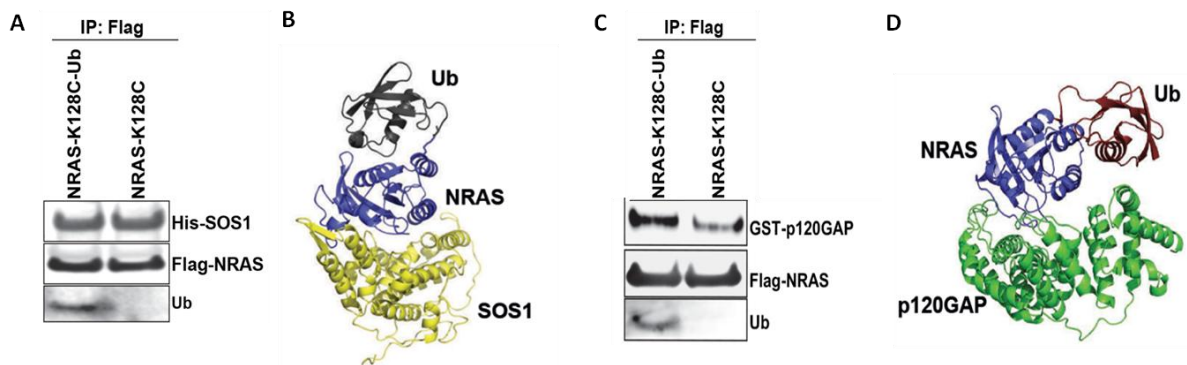
Fig 15: Interaction of K128-ubiquitinated NRas with GEF and GAP proteins. *A) Pull down of NRas and NRas-K128-Ub with SOS1. B) Structural prediction model of NRas-K128-Ub in complex with SOS1. C) Pull down of NRas and NRas-K128-Ub with p120GAP. D) Structural prediction model of NRas-K128-Ub in complex with p120GAP. Simicek M. et al. unpublished.*

Our results suggested that elevated OTUB1 expression might alter Ras activity independently of the classical Ras oncogenic mutations. Analysis of The Cancer Genome Atlas (TCGA) revealed a gain of the 11q13.1 locus (Huang et al., 2002), where the *OTUB1* gene resides. This genomic aberration is commonly found in both human lung adenocarcinomas and lung squamous cell carcinomas. Therefore, we quantified the expression of OTUB1 mRNA in series of human lung cancer samples and found OTUB1 upregulated in a majority of adenocarcinomas and squamous cell carcinomas compared to normal tissue samples. Interestingly, patient samples analysis further showed that OTUB1 overexpression was mutually exclusive with KRas mutation state (Fig 16).
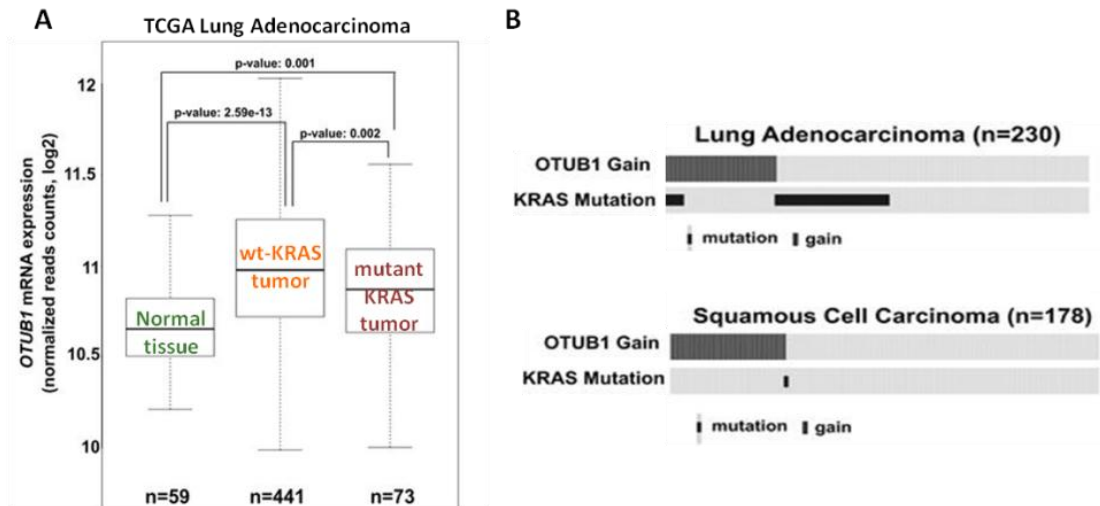
Fig 16: OTUB1 is overexpressed in KRas WT lung tumors. *A) OTUB1 mRNA levels in normal lung tissue and lung tumors bearing WT or mutant KRas. B) Gain of OTUB1 locus and KRas mutations in lung cancers. Adapted from Baietti FM. and Simicek M. et al. EMBO Mol Med. 2016.*

To experimentally test the possibility that OTUB1 promotes KRas tumorigenic potential, we ectopically overexpressed OTUB1 in lung cancer cell lines possessing wild type (WT) or mutant KRas. Consistent with our hypothesis, OTUB1 promoted growth only of tumor cells with WT but not mutant KRas both in cell culture models and in mouse subcutaneous xenografts (Fig 17).
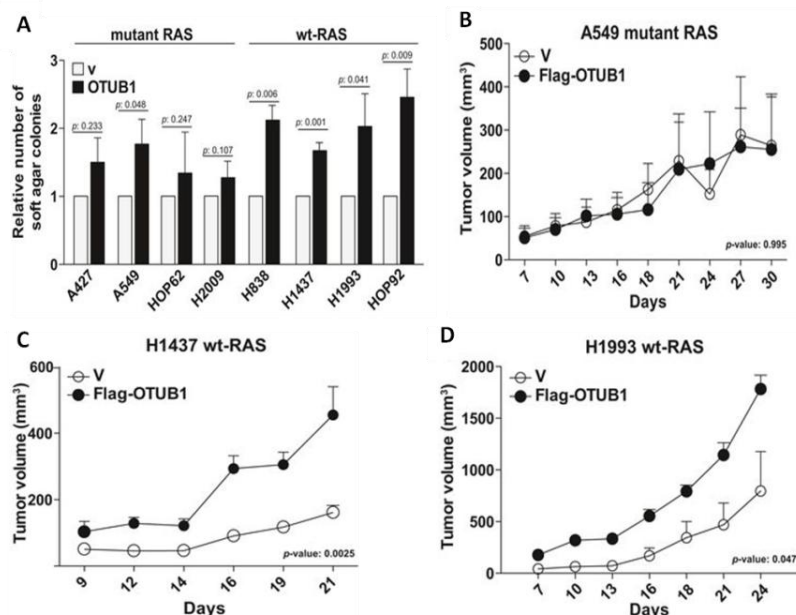
Fig 17: OTUB1 promotes tumorigenic effect of WT KRas in lung tumors. *A) Quantification of soft agar assay using WT and mutant KRas cell lines. B,C,D) Xenograft tumor growth of cancer cells overexpresing control vector (V) or OTUB1. Adapted from Baietti FM. and Simicek M. et al. EMBO Mol Med. 2016.*

In summary, our study pointed to OTUB1 as an important regulator of Ras activity by mediating Ras ubiquitination status. Altered ubiquitination affected Ras activity, localization and protein-protein interactions but not degradation. Most importantly, our data suggest that dysregulation of Ras ubiquitination represents an alternative mechanism to activate WT Ras and drive its tumorigenic properties in human lung cancer.

Our following research identified Ras as a specific substrate of the E3 ligase LZTR1, which ubiquitinates Ras on K170. Similarly as in OTUB1 suppressed cells, overexpression of LZTR1 inhibited Ras plasma membrane localisation (Fig 18). This suggested that LZTR1 could act as a tumor suppressor. Indeed, mutations or haploinsufficiency of the *LZTR1* gene were associated with Noonan syndrome and schwannomatosis (Piotrowski et al., 2014). In our model system, LZTR1 deletion or disease-associated mutation affected the activation of Ras both in cell culture and *in vivo*. In summary, our study for the first time provided a mechanistic explanation for the partial loss and mutation in *LZTR1* gene in human disease (Steklov et al., 2018).

Fig 18: Structural superposition of monoubiquitin at K170 of HRas (A) and NRas (B). *The prediction supports the model, where conjugation of ubiquitin in a near proximity to the flexible C-terminus abrogates Ras association with plasma membrane. Adapted from Steklov M. at el. Science. 2018.*

3. Targeting ubiquitin-proteasome pathway in human cancer

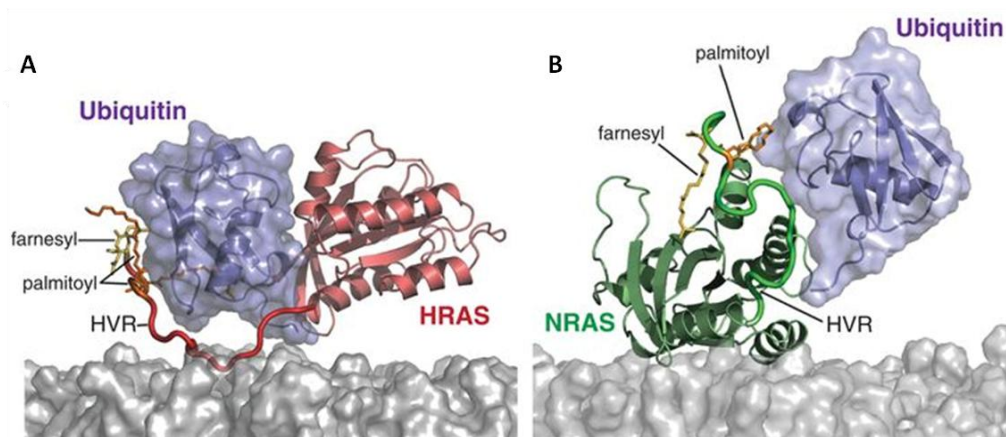Increased proteosynthesis is required to sustain the needs of highly proliferating malignant tissue and is a hallmark of every cancer (Hanahan & Weinberg, 2011). The increased load of newly formed polypeptides creates enormous pressure on protein quality control mechanisms. To maintain cellular homeostasis, tumor cells tend to acquire very efficient and selective protein degradation machinery. Many intracellular proteins are ubiquitinated and degraded in proteasome, a complex multiprotein enzymatic assembly with several catalytic activities. In neoplastic tissue, proteasome targets participate particularly in the regulation of cell cycle, proliferation, differentiation and apoptosis (Jang, 2018). Therefore, fine tuning of ubiquitin-proteasome degradation pathway is critical for the survival and progression of many tumors. From this developed the idea of targeting the ubiquitin-proteasome system as a rational approach in the treatment of human cancers (Manasanch & Orlowski, 2017; Soave et al., 2017).

3.1 Proteasome inhibitors in multiple myeloma

Haematological malignancies, particularly multiple myeloma (MM), are an extraordinary example of critical dependence on fully functional proteasome (Caravita et al., 2006). MM is a malignancy of immunoglobulin-producing plasma cells that represent the terminal differentiation stage of B-cells. Aberrant plasma cell clones originate from the transformed pro-B-cells that home to the bone marrow (Billadeau et al., 1993; Boyle et al., 2014; Garcés and Simicek et al., 2020). MM cells produce an large quantity of immunoglobulins that can reach up to 30% of the entire proteome (Kumar et al., 2017; Salmon & Smith, 1970). Such a massive production of immunoglobulins generates a huge amount of misfolded proteins, which are subsequently ubiquitinated and targeted for degradation in proteasome (Aronson & Davies, 2012).

Any disruption of the ubiquitin-proteasome system is fatal and leads to the rapid death of MM cells. Therefore, inhibition of proteasome activity has been extensively explored as a successful therapeutic strategy in MM. Soon after, proteasome inhibitors became a cornerstone of anti-myeloma therapy (Gandolfi et al., 2017; Ito, 2020). Introduction of bortezomib, a potent and highly specific proteasome inhibitor, completely revolutionised treatment of MM patients. Although the initial outcomes in many patients are very promising, bortezomib-based therapy eventually leads to the development of resistance (Braggio et al., 2015). An emerging and promising approach to avoid drug resistance is targeting other plasma cells specific components of the ubiquitin-proteasome system (Bianchi et al., 2009).

3.2 Modulation of ubiquitin system to prevent drug resistance in multiple myeloma

Even though the link between immunoglobulin production capacity and sensitivity to proteasome inhibitors was already proposed (Bianchi et al., 2009; Meister et al., 2007), there is very limited experimental and real world evidence connecting these two parameters. We speculated that ability of myeloma cells to produce immunoglobulins might positively correlate with sensitivity to proteasome inhibitors. To evaluate our hypothesis, we quantified amount of intracellular immunoglobulin in a cohort of 25 newly diagnosed MM patients, who later underwent proteasome inhibitor-based treatment. Firstly, aberrant plasma cells were isolated from bone marrow by flow cytometry using a set of unique surface markers. Concentration of intracellular immunoglobulins was further measured by ELISA assay and plotted against the length of progression free survival (PFS) of each patient. As expected, we found a strong correlation between the amount of intracellular immunoglobulin and patient PFS. This correlation was independent of the immunoglobulin chain type (λ *vs* κ). Furthermore, the median concentration of intracellular immunoglobulin was able to stratify MM patients into two groups: 1) immunoglobulin high - proteasome inhibitor responsive; and 2) immunoglobulin low - proteasome inhibitor-resistant (Fig 19).
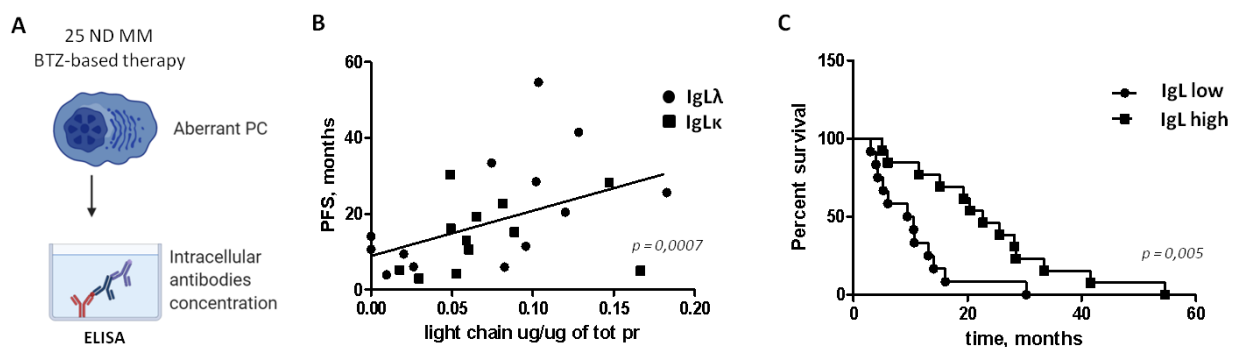
Fig 19: Amount of intracellular immunoglobulin (Ig) correlates with MM patients PFS. *A) Schematic of the experimental set up. B) Correlation analysis of ELISA data with PFS. C) Kapplan-Meier survival analysis of Ig low and Ig high MM patients. ND = new diagnosis, BTZ = bortezomib. Vdovin A. and Simicek M. Unpublished.*

Such a dramatic difference prompted us to identify intrinsic factors that mediate immunoglobulin production in MM cells. To this end, we used RNAseq to explore transcriptome of more than a dozen myeloma patients with different immunoglobulin production capacity. The following bioinformatics analysis together with several filtering steps provided multiple hits. Our attention was attracted particularly by the gene encoding deubiquitinating enzyme OTUD1, which is specifically expressed in B-cells reaching the peak expression in immunoglobulin producing, bone marrow residing plasma cells. Following validation by qPCR analysis confirmed that expression of OTUD1 could distinguish patients with low and high intracellular immunoglobulin. Additionally, we found that myeloma

patients treated with proteasome inhibitors had a significantly worse prognosis when expressing low OTUD1 similarly as patients with low intracellular immunoglobulin levels suggesting on a functional relationship (Fig 20).
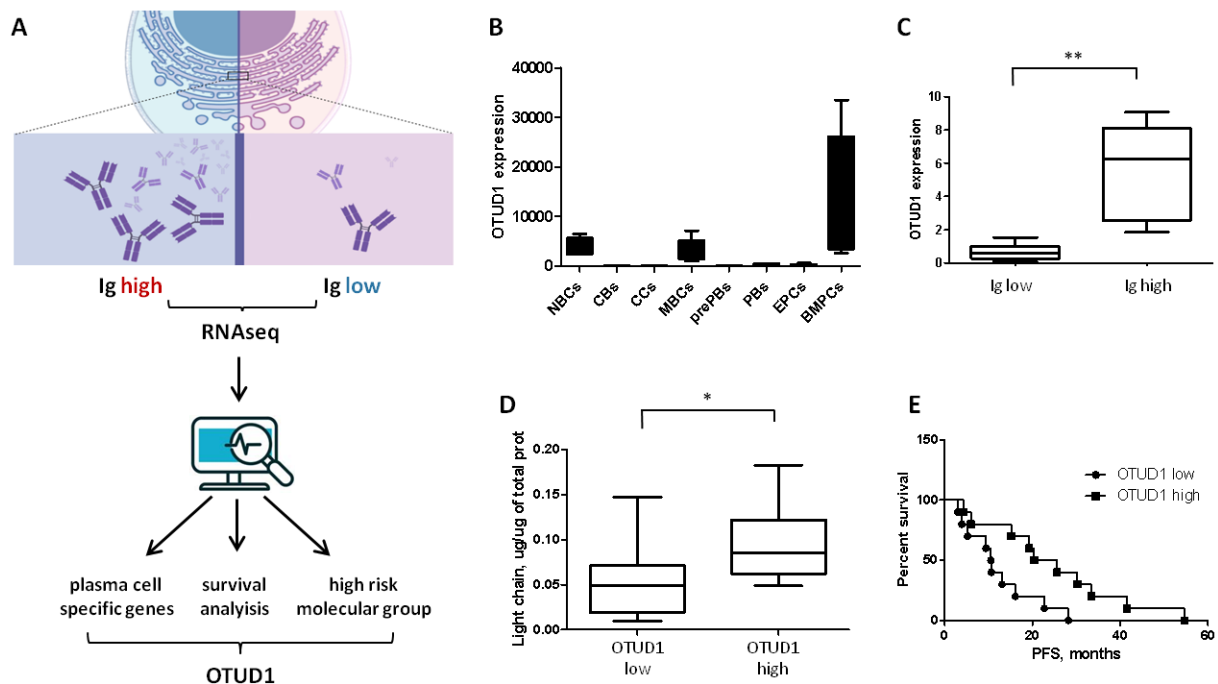
Fig 20: OTUD1 correlates with myeloma capacity to produce immunoglobulins (Ig). *A) Schematic of RNAseq analysis. B) OTUD1 expression during B-cell development. C) OTUD1 expression in Ig low and Ig high MM patient samples. D) Ig quantification in OTUD1 low and OTUD1 MM patient samples. E) Kapplan-Meier survival analysis of MM patients group by OTUD1 expression levels. NBCs - naïve B-cells, CBs - centroblast, CCs - centrocytes, MBC - memory B-cells, prePBs - preplasmablasts, PBs - plasmablasts, EBPs - early plasma cells, BMPCs - bone marrow plasma cells. Vdovin A. and Simicek M. Unpublished.*

To validate results from the RNAseq analysis, we created genetic models of several MM cell lines with doxycycline-inducible OTUD1 overexpression and shRNA-mediated OTUD1 knock down. Similarly to MM patients, cells with OTUD1 overexpression dramatically increased the amount of intracellular immunoglobulin. At the same time, higher expression of OTUD1 potentiated sensitivity to all clinically used proteasome inhibitors. On the contrary, myeloma cells with OTUD1 knock down significantly suppressed intracellular immunoglobulin and become resistant to all three tested classes of clinically used proteasome inhibitors (Fig 21).
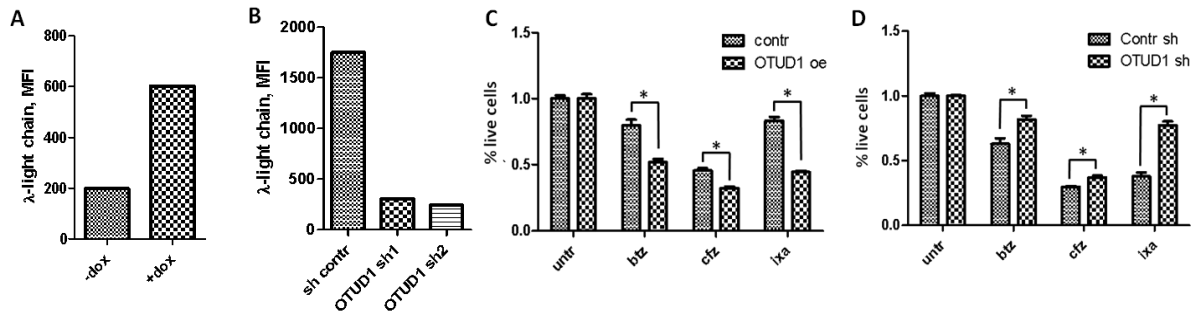
Fig 21: *OTUD1 expression promotes immunoglobulin (Ig) production and sensitizes MM cells to proteasome inhibitors. A) Ig levels in isogennic MM cells with doxycycline-inducible OTUD1. B) Ig levels in MM cells shRNA mediated OTUD1 knock down. C) Viability assay with OTUD1 overexpressing MM cells. D) Viability assay with OTUD1 knock down MM cells. BTZ = bortezomib, CFZ = carfilzomib, IXA = ixazomib. Vdovin A. and Simicek M. Unpublished.*

Our patient data indicated that increased production of immunoglobulin sensitizes myeloma cells to proteasome inhibitors. At the same time, elevated expression of OTUD1 promoted immunoglobulin synthesis and increased proteasome inhibitor-induced cell death. To connect these two phenotypes, we hypothesized that greater immunoglobulin synthesis would also lead to a rise in misfolded, highly ubiquitinated proteins, which would saturate proteasome eventually leading to a higher cytotoxic effect of proteasome inhibitors.

Resistance to proteasome inhibitors might be caused by multiple factors including overexepression of proteasome catalytic 20S subunits, suppression of the regulary 19S proteins or increased enzymatic activity of the chymotrypsin-like protease in the proteasome core (Acosta-Alvear et al., 2015; Allmeroth et al., 2020). To examine these possibilities, we analysed expression of both 19S and 20S subunits. We observed no difference in the amount of proteasome subunits both at mRNA and protein level in MM cells with doxycycline-inducible OTUD1 overexpression. At the same time, analysis of the proteasome core catalytic activity using fluorogenic substrate revealed no changes upon elevated OTUD1 expression (Fig 22).

Fig 22: Expression and activity of proteasome is not affected by OTUD1. *A) qPCR analysis of proteasome subunits mRNA. B) Western blot analysis of proteasome subunits expression. C) Quantitative kinetic analysis of proteasome catalytic activity. Vdovin A. and Simicek M. Unpublished.*

Interestingly, when exploring ubiquitome of myeloma cells, we observed a dramatic increase in the total pool of ubiquitinated proteins in cells with OTUD1 overexpression, while in OTUD1 knock downs t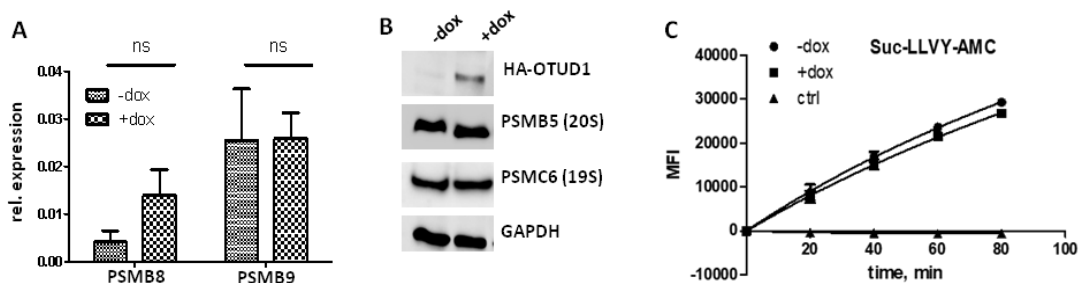he ubiquitin smear almost disappeared. Because immunoglobulins form almost a quarter of all plasma cell proteins, we speculated that the observed changes in ubiquitome are due to differences in OTUD1-mediated immunoglobulin levels. Indeed, when we knocked down immunoglobulin in the OTUD1 overexpressing MM cells, the amount of polyubiquitinated proteins returned to basal state. And finally, the total pool of ubiquitinated proteins correlated with levels of intracellular immunoglobulin in primary samples from the MM patients before application of therapy. Importantly, the selected group of patients later received treatment based on proteasome inhibitors. Analysis of PFS revealed a strong correlation with the amount of polyubiquitinted proteins prior to therapy (Fig 23).
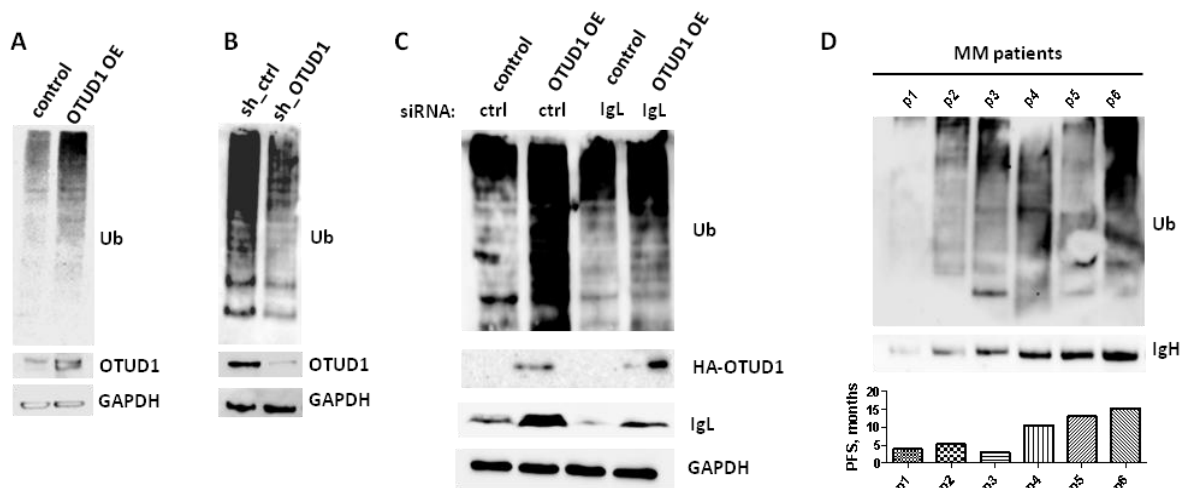
Fig 23: OTUD1 mediated immunoglobulin (Ig) production leads to accumulation of highly ubiquitinated proteins. *A) Ubiquitom analysis in MM cells with OTUD1 overexpression. B) Ubiquitom analysis in MM cells with OTUD1 knock down. C) Ubiquitom analysis of OTUD1 overexpressing cells with Ig knock down. D) Ubiquitom analysis and PFS of primary MM patient samples. Vdovin A. and Simicek M. Unpublished.*

Our previous structural and biochemical data indicated on the potential role of OTUD1 in ubiquitin proteasome system (Fig 10). However, mutation of the RAD23A binding sites in OTUD1 did not revert immunoglobulin levels and related phenotype in myeloma cells. Therefore, we speculated that another OTUD1 binding partner might account for the observed biological effects in MM.

To get a deeper insight in the OTUD1 interactome, we fused OTUD1 to the promiscuous biotin ligase BirA and performed proximity labeling assay. BirA irreversibly attaches biotin only to proteins found in a very small perimeter from the enzyme. Therefore, this approach allows identification of specific, highly dynamic and transient protein-protein interaction in

intact cells. In our system the biotin labeled proteins were isolated by streptavidin pull down. Subsequent mass spectrometry analysis identified several novel OTUD1 interactors. Between the top hits was the endoplasmic reticulum (ER)-resident peroxiredoxin 4 (PRDX4). This enzyme regulates series of redox reactions during disulfide bonds formation, which are critical for the very early steps of the immunoglobulin folding inside the ER. Moreover, we found that PRDX4 expression follows the capacity of B-cells to produce immunoglobulin reaching maximum expression in the bone marrow plasma cells, similarly to OTUD1 (Fig 24).
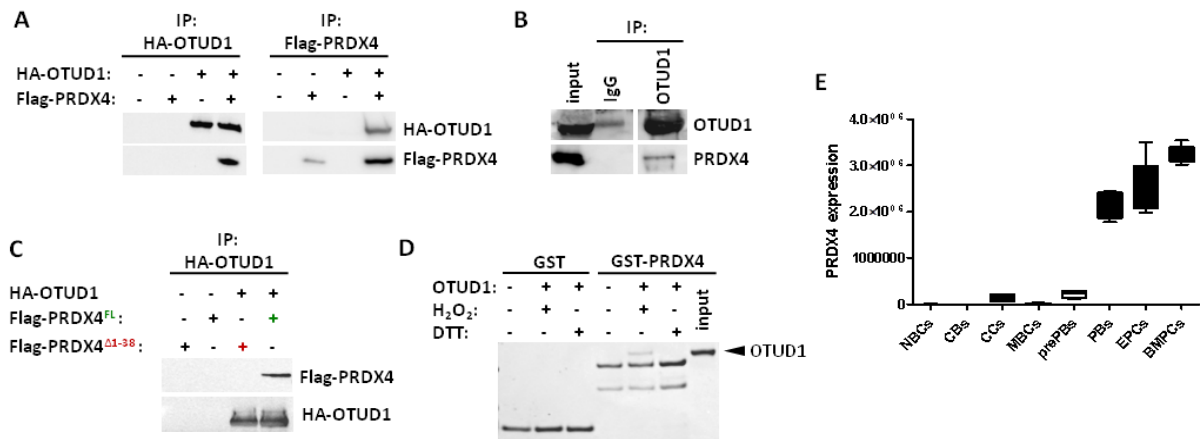
Fig 24: OTUD1 directly interacts with PRDX4 inside the ER. *A) Reciprocal co-immunoprecipitation of OTUD1 and PRDX4. B) Co-immunoprecipitation of endogenous OTUD1 and PRDX4. C) Co-immunoprecipitation of OTUD1 with full length (FL) and cytosolic (Δ1-38) forms of PRDX4. D) In vitro GST-pull down with recombinant OTUD1 and PRDX4. E) PRDX4 expression during B-cell development. NBCs - naïve B-cells, CBs - centroblast, CCs - centrocytes, MBC - memory B-cells, prePBs - preplasmablasts, PBs - plasmablasts, EBPs - early plasma cells, BMPCs - bone marrow plasma cells. Vdovin A. and Simicek M. Unpublished.*

Further biochemical analysis revealed that WT but not the catalytic mutant of OTUD1 was able to deubiquitinate PRDX4 both *in vitro* and *in vivo*. To avoid potential artifacts, we used OTUD1 C320R mutant, which we previously described as the most appropriate substitution model for functional DUB studies (Morrow et al., 2018). Additionally, suppression of OTUD1 in myeloma cells led to a dramatic increase in ubiquitinated form of endogenous PRDX4. Finally, in OTUD1 overexpressing cells PRDX4 was stabilized, while in cells with OTUD1 knock down PRDX4 almost completely disappeared without affecting PRDX4 mRNA levels. These results position OTUD1 as a positive regulator of PRDX4 stability by preventing its ubiquitin-dependent degradation (Fig 25).
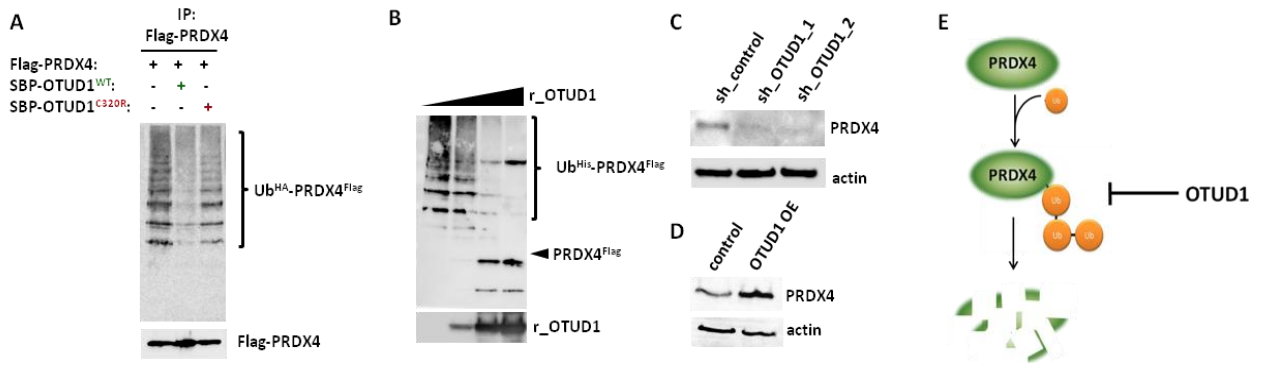
Fig 25: OTUD1 deubiquitinates and stabilises PRDX4. *A) Immunoprecipitation of ubiquitinated PRDX4 in presence of WT or catalytically deficient (C320R) OTUD1. B) In vitro deubiquitination assay with purified endogenously ubiquitinated PRDX4 and recombinant OTUD1. C) PRDX4 levels in OTUD1 knock down MM cells. D) PRDX4 levels in OTUD1 overexpressing MM cells. E) Model of OTUD1 mediated PRDX4 stabilization. Vdovin A. and Simicek M. Unpublished.*

Whether stabilization of PRDX4 is responsible for the phenotypes observed in myeloma cells with altered OTUD1 expression, we performed several rescue experiments by restoring normal PRDX4 levels in MM cells with elevated or suppressed OTUD1. Both in OTUD1 overexpressed and knock down cells restoration of PRDX4 levels almost completely rescued all previously detected phenotypes, i.e. immunoglobulin production, ubiquitin levels and sensitivity to proteasome inhibitors (Fig 26).
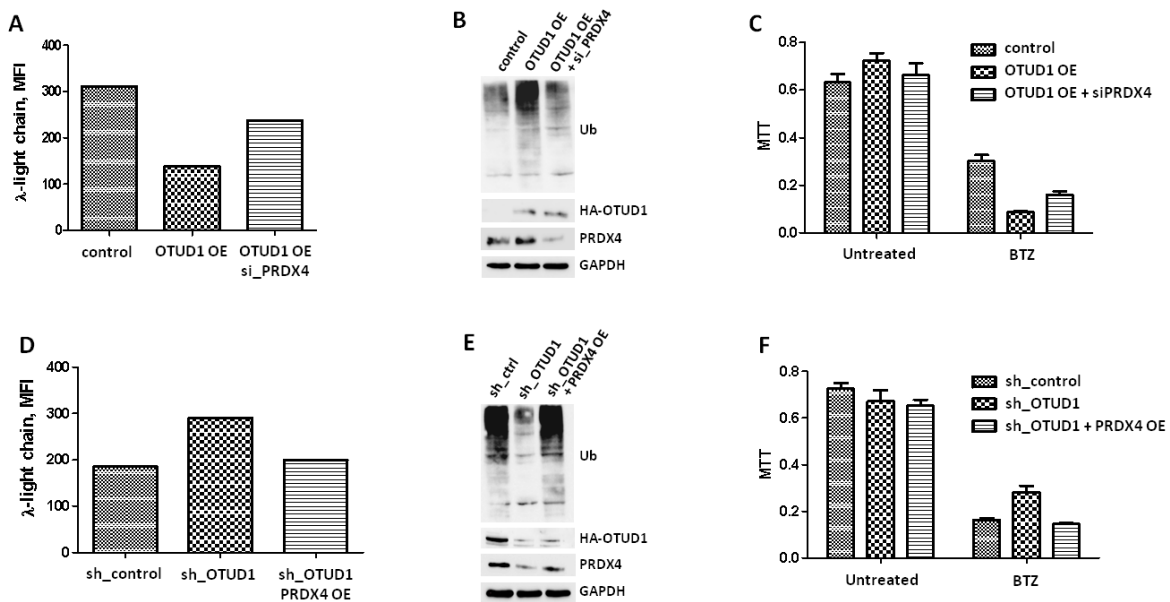
Fig 26: OTUD1 phenotype in MM cells is dependent on PRDX4. *A,D) Immunoglobulin levels in MM cells with altered OTUD1 and PRDX4 levels. B,E) Ubiquitome analysis of cells used in A and D. E,F) Viability assay with cells used in A and D. BTZ = bortezomib. Vdovin A. and Simicek M. Unpublished.*

To summarize the mechanistic part, we have discovered a novel regulatory pathway myeloma cells use to produce a large number of immunoglobulins. In brief, OTUD1 stabilizes PRDX4 which promotes the initial steps of immunoglobulin assembly. Consequently, rapid disulfide bond formation overloads the ER folding capacity. The resulting accumulation of misfolded, highly ubiquitinated immunoglobulins saturates proteasome eventually sensitizing myeloma for proteasome inhibitors. On the other hand, in cells will low OTUD1 levels, PRDX4 is quickly degraded and immunoglobulin folding is slowed down. Therefore, the amount of misfolded immunoglobulins drops leading to lower proteasome occupancy and proteasome inhibitor resistance.

To therapeutically exploit this mechanism, we asked how to re-sensitize the OTUD1 low or in general the immunoglobulin low MM cells. In addition to the already described features, myeloma with increased immunoglobulin synthesis exhibit also high ER stress. This is in a strong contract to MM cells with diminished immunoglobulin production, where ER stress is suppressed. Therefore, we speculated that co-application of selective ER stress inducers together with proteasome inhibitors could revert the negative prognosis of the subset of proteasome inhibitor-resistant myeloma patients with low capacity to produce immunoglobulins. For this reason, we performed a rational screening using several ER-stress inducing drugs including already clinically explored compounds. From the tested chemicals the best performing candidate was the HSP-90 inhibitor tanespimycin (17-N-allylamino-17-demethoxygeldanamycin, 17-AAG), which was able to completely revert proteasome inhibitor (bortezomib) resistance in the OTUD1 low cells with decreased immunoglobulin production capacity. The biochemical analysis confirmed that the mechanism of action of bortezomib in combination with 17-AGG can be attributed to the increase of missfolded, highly ubiquitinated proteins (Fig 27).
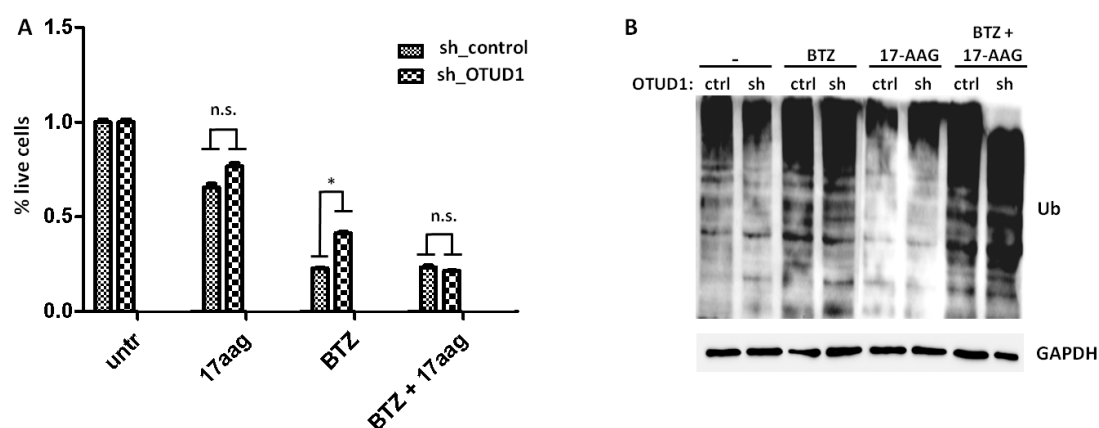
Fig 27: Co-treatment with HSP90 inhibitor resensitises OTUD1 low MM cells to proteasome inhibiton. *A) Viability analysis of control and OTUD1 knock down MM cells treated with HSP90 inhibitor (17-AGG), bortezomib (BTZ) or combination. B) Ubiquitom analysis of the cells used in A. Vdovin A. and Simicek M. Unpublished.*

In conclusion, our study showed that myeloma patients with low expression of OTUD1 have impaired immunoglobulin production due to the destabilization of PRDX4. Lower levels of misfolded, ubiquitinated immunoglobulins in OTUD1 low myeloma cells result in minor occupancy of proteasome and resistance to proteasome inhibitors. The outcome is significantly shorter survival, when treatment is applying exclusively proteasome inhibitors. Based on our results, we propose the combinatory use of proteasome inhibitors with tanespimycin as a novel, promising treatment strategy for myeloma patient with low levels of immunoglobulin (Fig 28). In the future, the intracellular immunoglobulin could be further explored with larger cohorts and might be considered as a robust and easy-to-detect prognostic and treatment stratification marker in MM patients.
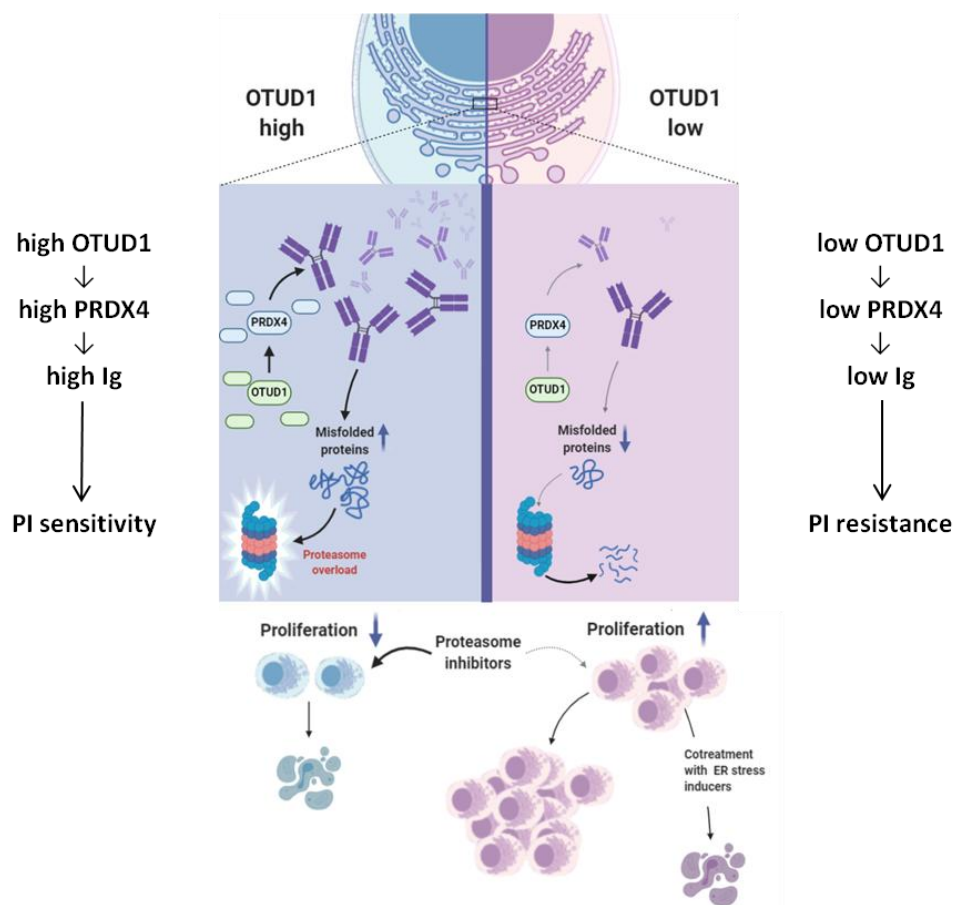
Fig 28: Schematic model of the OTUD1-PRDX4 pathway in MM cells. *In myeloma with high OTUD1 expression PRDX4 is stabilized and promotes formation of immunoglobulins that eventually saturate degradation machinery. Therefore, these cells are highly sensitive to inhibition of proteasome. In myeloma cells with low OTUD1 expression PRDX4 is destabilized and formation of immunoglobulins drops. Thus, protein load on proteasome is diminished and the cells become resistant to proteasome inhibitors. Combinatory use of proteasome inhibitors with the ER-stress inducing drugs, such as HSP90, is a promising strategy to avoid drug resistance in myeloma patient with low immunoglobulins. Vdovin A. and Simicek M. Unpublished.*

Conclusions

Extensive research over the last few decades has uncovered intricate functions of ubiquitin and ubiquitin like proteins in a variety of cellular processes. Numerous publications including our work determined the ubiquitin system as robust and flexible machinery that tightly regulates many delicate and executive cellular events in a spatiotemporal manner. Highly dynamic and complex architecture of ubiquitin moieties ranges from monoubiquitination, multi- monoubiquitination, eight different homotypic chains, yet unresolved number of heterotypic and branched polyubiquitin polymers, mixed ubiquitin chains containing other ubiquitin like proteins up to the second level of posttranslational modification, when ubiquitin itself is modified by phosphorylation and other small chemical groups. As presented in this Thesis, our work and other studies associated many components of the ubiquitin system with human diseases. However, only a limited number of drugs are available. Therefore there is a constant need for further understanding of this extremely complex and sophisticated regulatory apparatus.

Future perspectives

Even though the ubiquitin system has already been extensively studied, many outstanding questions for future research remain. Probably the most difficult and technically challenging will be deciphering the complex myriad of ubiquitin chain types and their function in cell physiology. Breaking down the ubiquitin code will not only improve our understanding of these delicate regulatory entities but especially offer unprecedented possibilities to specifically target unique cellular processes in pathological settings.

Additionally, numerous proteomic studies found tens of thousands of ubiquitination sites in human proteins (Kirkpatrick et al., 2005; Wagner et al., 2011). At the moment, we understand only a very small fraction of these events and for most we completely lack the responsible E3 ligases and DUBs. Sophisticated biochemical approaches such as enzymatic-based proximity labelling and selective ubiquitin binding domains together with modern mass spectrometry might be useful tools to identify the specific enzymes (Baumann, 2012; Q. Liu et al., 2018; Roux et al., 2018; Udeshi et al., 2013).

Drug screening programs offer a plethora of small molecules potentially useful as E3 or DUB inhibitors or activators (Bulatov et al., 2018; Collins et al., 2017; Harrigan et al., 2018; Landré et al., 2014). A brand new direction is a research focused on the development of small molecules that can change the enzyme substrate specificity. Thalidomide derivates, which modulate substrate selection of the E3 ligase Cereblon, represent an excellent example of this class of drugs (Mori et al., 2018). A huge success of these immunomodulatory agents in the treatment of MM (Madan et al., 2011) is encouraging further investigation and rational structure based drug design to target ubiquitin processing enzymes.

Another promising direction is employing the E3 ligase chimeras for targeted degradation of proteins that would be otherwise very difficult or impossible to target by small molecular compounds (Smith et al., 2019). Future research will likely bring new exciting discoveries that will lead to the development of novel tools and approaches for treating human diseases.

List of abbreviations

AMP	adenosine monophosphate
ATP	adenosine triphosphate
BARD1	BRCA1-associated RING domain protein 1
BRCA1	breast cancer 1
CLR	cullin-RING E3 ligase
CYLD	cylindromatosis deubiquitinase
DDR	DNA damage response
DNA	deoxyribonucleic acid
DUB	deubiquitinase
ELISA	enzyme linked immunosorbent assay
ER	endoplasmic reticulum
GAP	GTPase activating protein
GDI	guanosine nucleotide dissociation inhibitor
GDP	guanosin diphosphate
GEF	GTP exchange factor
GTP	guanosin triphosphate
HECT	homologous to the E6-AP carboxyl terminus
HSP-90	heat shock protein 90
IKK	inhibitor of IκB kinase
IL-1R1	interleukin 1 receptor 1
IκB	inhibitor κB
LZTR1	leucine zipper like transcription regulator 1
MAPK	mitogen activated protein kinase
MDC1	mediator of DNA damage checkpoint protein 1
MINDY	motif interacting with Ub-containing novel DUB family
MM	multiple myeloma
NEDD4	neural precursor cell expressed, developmentally down-regulated 4
NF1	neurofibromin 1
NF-κB	nuclear factor κB
NMR	nuclear magnetic resonance spectroscopy
NZF	N-terminal Npl4-like zinc finger
OTU	ovarian tumor protease
PCNA	proliferating cell nuclear antigen
PFS	progression free survival
PINK1	PTEN-induced kinase 1
PRDX4	peroxiredoxin 4
qPCR	quantitative polymerase chain reaction
RABEX5	Rab guanine nucleotide exchange factor 1
RBR	RING-in-between-RING
RING	really interesting new gene
RNF168	RING finger protein 168
RNF8	RING finger protein 8
shRNA	small hairpin ribonucleic acid
SOS1	son of sevenless homolog 1
SPR	surface plasmon resonance

SUMO	small ubiquitin-like modifier
NEDD8	neural precursor cell expressed, developmentally downregulated 8
TCGA	the cancer genome atlas
TLR4	toll-like receptor 4
TNFR1	tumor necrosis factor receptor 1
TRABID	tumor-necrosis factor receptor-associated factor-binding protein domain
TRAF6	TNF receptor associated factor 6
TTC3	tetratricopeptide repeat domain 3
UBA1	ubiquitin activating enzyme 1
UBA6	ubiquitin activating enzyme 6
UBD	ubiquitin-binding domain
Ubl	ubiquitin-like
UCH	ubiquitin C-terminal hydrolyze
USP	ubiquitin-specific protease
WT	wild type
γH2AX	phosphorylated of histone 2AX
17-AAG	17-N-allylamino-17-demethoxygeldanamycin

References

Abdul Rehman, S. A., Kristariyanto, Y. A., Choi, S. Y., Nkosi, P. J., Weidlich, S., Labib, K., Hofmann, K., & Kulathu, Y. (2016). MINDY-1 Is a Member of an Evolutionarily Conserved and Structurally Distinct New Family of Deubiquitinating Enzymes. *Molecular Cell*, *63*(1), 146–155. https://doi.org/10.1016/j.molcel.2016.05.009

Acosta-Alvear, D., Cho, M. Y., Wild, T., Buchholz, T. J., Lerner, A. G., Simakova, O., Hahn, J., Korde, N., Landgren, O., Maric, I., Choudhary, C., Walter, P., Weissman, J. S., & Kampmann, M. (2015). Paradoxical resistance of multiple myeloma to proteasome inhibitors by decreased levels of 19S proteasomal subunits. *ELife*, *4*(September). https://doi.org/10.7554/eLife.08153

Allmeroth, K., Horn, M., Kroef, V., Miethe, S., Müller, R. U., & Denzel, M. S. (2020). Bortezomib resistance mutations in PSMB5 determine response to second-generation proteasome inhibitors in multiple myeloma. *Leukemia*, 1–6. https://doi.org/10.1038/s41375-020-0989-4

Apolloni, A., Prior, I. A., Lindsay, M., Parton, R. G., & Hancock, J. F. (2000). H-ras but Not K-ras Traffics to the Plasma Membrane through the Exocytic Pathway. *Molecular and Cellular Biology*, *20*(7), 2475–2487. https://doi.org/10.1128/mcb.20.7.2475-2487.2000

Aronson, L. I., & Davies, F. E. (2012). DangER: Protein ovERload. Targeting protein degradation to treat myeloma. In *Haematologica* (Vol. 97, Issue 8, pp. 1119–1130). Ferrata Storti Foundation. https://doi.org/10.3324/haematol.2012.064923

Baietti, M. F., Simicek, M., Abbasi Asbagh, L., Radaelli, E., Lievens, S., Crowther, J., Steklov, M., Aushev, V. N., Martínez García, D., Tavernier, J., & Sablina, A. A. (2016). OTUB 1 triggers lung cancer development by inhibiting RAS monoubiquitination . *EMBO Molecular Medicine*, *8*(3), 288–303. https://doi.org/10.15252/emmm.201505972

Baker, R., Wilkerson, E. M., Sumita, K., Isom, D. G., Sasaki, A. T., Dohlman, H. G., & Campbell, S. L. (2013). Differences in the regulation of K-Ras and H-Ras isoforms by monoubiquitination. *Journal of Biological Chemistry*, *288*(52), 36856–36862. https://doi.org/10.1074/jbc.C113.525691

Bard, J. A. M., Goodall, E. A., Greene, E. R., Jonsson, E., Dong, K. C., & Martin, A. (2018). Structure and Function of the 26S Proteasome. *Annual Review of Biochemistry*, *87*(1), 697–724. https://doi.org/10.1146/annurev-biochem-062917-011931

Bartocci, C., & Denchi, E. L. (2013). Put a RING on it: Regulation and inhibition of RNF8 and RNF168 RING finger E3 ligases at DNA damage sites. In *Frontiers in Genetics* (Vol. 4, Issue JUL, p. 128). Frontiers. https://doi.org/10.3389/fgene.2013.00128

Baumann, K. (2012). Technologies: Seeing ubiquitin chains. *Nature Reviews. Molecular Cell Biology*, *13*(9), 540. https://doi.org/10.1038/nrm3413

Bianchi, G., Oliva, L., Cascio, P., Pengo, N., Fontana, F., Cerruti, F., Orsi, A., Pasqualetto, E., Mezghrani, A., Calbi, V., Palladini, G., Giuliani, N., Anderson, K. C., Sitia, R., & Cenci, S. (2009). The proteasome load versus capacity balance determines apoptotic sensitivity of multiple myeloma cells to proteasome inhibition. *Blood*, *113*(13), 3040–3049. https://doi.org/10.1182/blood-2008-08-172734

Billadeau, D., Ahmann, G., Greipp, P., & Ness, B. Van. (1993). The Bone marrow of multiple myeloma patients contains B cell populations at different stages of differentiation that are clonally related to the malignant plasma cell. *Journal of Experimental Medicine*, *178*(3), 1023–1031.

https://doi.org/10.1084/jem.178.3.1023

Biou, V., & Cherfils, J. (2004). Structural principles for the multispecificity of small GTP-binding proteins. In *Biochemistry* (Vol. 43, Issue 22, pp. 6833–6840). https://doi.org/10.1021/bi049630u

Bivona, T. G., Quatela, S. E., Bodemann, B. O., Ahearn, I. M., Soskis, M. J., Mor, A., Miura, J., Wiener, H. H., Wright, L., Saba, S. G., Yim, D., Fein, A., Pérez De Castro, I., Li, C., Thompson, C. B., Cox, A. D., & Philips, M. R. (2006). PKC regulates a farnesyl-electrostatic switch on K-Ras that promotes its association with Bcl-XL on mitochondria and induces apoptosis. *Molecular Cell*, *21*(4), 481–493. https://doi.org/10.1016/j.molcel.2006.01.012

Bos, J. L., Rehmann, H., & Wittinghofer, A. (2007). GEFs and GAPs: Critical Elements in the Control of Small G Proteins. In *Cell* (Vol. 129, Issue 5, pp. 865–877). Cell Press. https://doi.org/10.1016/j.cell.2007.05.018

Boughton, A. J., Krueger, S., & Fushman Correspondence, D. (2020). *Branching via K11 and K48 Bestows Ubiquitin Chains with a Unique Interdomain Interface and Enhanced Affinity for Proteasomal Subunit Rpn1*. https://doi.org/10.1016/j.str.2019.10.008

Boyartchuk, V. L., Ashby, M. N., & Rine, J. (1997). Modulation of ras and a-factor function by carboxyl-terminal proteolysis. *Science*, *275*(5307), 1796–1800. https://doi.org/10.1126/science.275.5307.1796

Boyle, E. M., Davies, F. E., Leleu, X., & Morgan, G. J. (2014). Understanding the multiple biological aspects leading to myeloma. In *Haematologica* (Vol. 99, Issue 4, pp. 605–612). Ferrata Storti Foundation. https://doi.org/10.3324/haematol.2013.097907

Braggio, E., Kort??m, K. M., & Stewart, A. K. (2015). SnapShot: Multiple Myeloma. *Cancer Cell*, *28*(5). https://doi.org/10.1016/j.ccell.2015.10.014

Buday, L., & Downward, J. (2008). Many faces of Ras activation. In *Biochimica et Biophysica Acta - Reviews on Cancer* (Vol. 1786, Issue 2, pp. 178–187). Elsevier. https://doi.org/10.1016/j.bbcan.2008.05.001

Buetow, L., & Huang, D. T. (2016). Structural insights into the catalysis and regulation of E3 ubiquitin ligases. In *Nature Reviews Molecular Cell Biology* (Vol. 17, Issue 10, pp. 626–642). Nature Publishing Group. https://doi.org/10.1038/nrm.2016.91

Bulatov, E., Zagidullin, A., Valiullina, A., Sayarova, R., & Rizvanov, A. (2018). Small molecule modulators of RING-type E3 ligases: MDM and cullin families as targets. In *Frontiers in Pharmacology* (Vol. 9, Issue MAY). Frontiers Media S.A. https://doi.org/10.3389/fphar.2018.00450

Canobbio, I., Trionfini, P., Guidetti, G. F., Balduini, C., & Torti, M. (2008). Targeting of the small GTPase Rap2b, but not Rap1b, to lipid rafts is promoted by palmitoylation at Cys176 and Cys177 and is required for efficient protein activation in human platelets. *Cellular Signalling*, *20*(9), 1662–1670. https://doi.org/10.1016/j.cellsig.2008.05.016

Cappadocia, L., & Lima, C. D. (2018). Ubiquitin-like Protein Conjugation: Structures, Chemistry, and Mechanism. In *Chemical Reviews* (Vol. 118, Issue 3, pp. 889–918). American Chemical Society. https://doi.org/10.1021/acs.chemrev.6b00737

Caravita, T., de Fabritiis, P., Palumbo, A., Amadori, S., & Boccadoro, M. (2006). Bortezomib: Efficacy comparisons in solid tumors and hematologic malignancies. In *Nature Clinical Practice Oncology* (Vol. 3, Issue 7, pp. 374–387). Nat Clin Pract Oncol. https://doi.org/10.1038/ncponc0555

Chen, Z. J., & Sun, L. J. (2009). Nonproteolytic Functions of Ubiquitin in Cell Signaling. In *Molecular Cell* (Vol. 33, Issue 3, pp. 275–286). Elsevier. https://doi.org/10.1016/j.molcel.2009.01.014

Cherfils, J., & Zeghouf, M. (2013). Regulation of small GTPases by GEFs, GAPs, and GDIs. In *Physiological Reviews* (Vol. 93, Issue 1, pp. 269–309). Physiol Rev. https://doi.org/10.1152/physrev.00003.2012

Colicelli, J. (2004). Human RAS superfamily proteins and related GTPases. In *Science's STKE : signal transduction knowledge environment* (Vol. 2004, Issue 250). Sci STKE. https://doi.org/10.1126/stke.2502004re13

Collins, I., Wang, H., Caldwell, J. J., & Chopra, R. (2017). Chemical approaches to targeted protein degradation through modulation of the ubiquitin-proteasome pathway. In *Biochemical Journal* (Vol. 474, Issue 7, pp. 1127–1147). Portland Press Ltd. https://doi.org/10.1042/BCJ20160762

Dantuma, N. P., Heinen, C., & Hoogstraten, D. (2009). The ubiquitin receptor Rad23: At the crossroads of nucleotide excision repair and proteasomal degradation. In *DNA Repair* (Vol. 8, Issue 4, pp. 449–460). DNA Repair (Amst). https://doi.org/10.1016/j.dnarep.2009.01.005

David, Y., Ternette, N., Edelmann, M. J., Ziv, T., Gayer, B., Sertchook, R., Dadon, Y., Kessler, B. M., & Navon, A. (2011). E3 ligases determine ubiquitination site and conjugate type by enforcing specificity on E2 enzymes. *Journal of Biological Chemistry*, *286*(51), 44104–44115. https://doi.org/10.1074/jbc.M111.234559

Deng, L., Meng, T., Chen, L., Wei, W., & Wang, P. (2020). The role of ubiquitination in tumorigenesis and targeted drug discovery. In *Signal Transduction and Targeted Therapy* (Vol. 5, Issue 1, pp. 1–28). Springer Nature. https://doi.org/10.1038/s41392-020-0107-0

Deol, K. K., Lorenz, S., & Strieter, E. R. (2019). Enzymatic Logic of Ubiquitin Chain Assembly. *Frontiers in Physiology*, *10*, 835. https://doi.org/10.3389/fphys.2019.00835

Deshaies, R. J., & Joazeiro, C. A. P. (2009). RING Domain E3 Ubiquitin Ligases. *Annual Review of Biochemistry*, *78*(1), 399–434. https://doi.org/10.1146/annurev.biochem.78.101807.093809

Eliezer, Y., Argaman, L., Kornowski, M., Roniger, M., & Goldberg, M. (2014). Interplay between the DNA damage proteins MDC1 and ATM in the regulation of the spindle assembly checkpoint. *Journal of Biological Chemistry*, *289*(12), 8182–8193. https://doi.org/10.1074/jbc.M113.532739

Emmerich, C. H., Ordureau, A., Strickson, S., Arthur, J. S. C., Pedrioli, P. G. A., Komander, D., & Cohen, P. (2013). Activation of the canonical IKK complex by K63/M1-linked hybrid ubiquitin chains. *Proceedings of the National Academy of Sciences of the United States of America*, *110*(38), 15247–15252. https://doi.org/10.1073/pnas.1314715110

Falsetti, S. C., Wang, D., Peng, H., Carrico, D., Cox, A. D., Der, C. J., Hamilton, A. D., & Sebti, S. M. (2007). Geranylgeranyltransferase I Inhibitors Target RalB To Inhibit Anchorage-Dependent Growth and Induce Apoptosis and RalA To Inhibit Anchorage-Independent Growth. *Molecular and Cellular Biology*, *27*(22), 8003–8014. https://doi.org/10.1128/mcb.00057-07

Gandolfi, S., Laubach, J. P., Hideshima, T., Chauhan, D., Anderson, K. C., & Richardson, P. G. (2017). The proteasome and proteasome inhibitors in multiple myeloma. *Cancer and Metastasis Reviews*, *36*(4), 561–584. https://doi.org/10.1007/s10555-017-9707-8

Garcés, J. J., Simicek, M., Vicari, M., Brozova, L., Burgos, L., Bezdekova, R., Alignani, D., Calasanz, M. J., Growkova, K., Goicoechea, I., Agirre, X., Pour, L., Prosper, F., Rios, R., Martinez-Lopez, J., Millacoy, P., Palomera, L., Del Orbe, R., Perez-Montaña, A., … Paiva, B. (2020). Transcriptional

profiling of circulating tumor cells in multiple myeloma: a new model to understand disease dissemination. *Leukemia*, *34*(2), 589–603. https://doi.org/10.1038/s41375-019-0588-4

Gotoh, T., Tian, X., & Feig, L. A. (2001). Prenylation of Target GTPases Contributes to Signaling Specificity of Ras-Guanine Nucleotide Exchange Factors. *Journal of Biological Chemistry*, *276*(41), 38029–38035. https://doi.org/10.1074/jbc.M104658200

Groettrup, M., Pelzer, C., Schmidtke, G., & Hofmann, K. (2008). Activating the ubiquitin family: UBA6 challenges the field. In *Trends in Biochemical Sciences* (Vol. 33, Issue 5, pp. 230–237). Trends Biochem Sci. https://doi.org/10.1016/j.tibs.2008.01.005

Haglund, K., & Dikic, I. (2012). The role of ubiquitylation in receptor endocytosis and endosomal sorting. In *Journal of Cell Science* (Vol. 125, Issue 2, pp. 265–275). The Company of Biologists Ltd. https://doi.org/10.1242/jcs.091280

Hanahan, D., & Weinberg, R. A. (2011). Hallmarks of cancer: The next generation. In *Cell* (Vol. 144, Issue 5, pp. 646–674). Elsevier. https://doi.org/10.1016/j.cell.2011.02.013

Hancock, J. F. (2003). Ras proteins: Different signals from different locations. In *Nature Reviews Molecular Cell Biology* (Vol. 4, Issue 5, pp. 373–384). Nat Rev Mol Cell Biol. https://doi.org/10.1038/nrm1105

Harrigan, J. A., Jacq, X., Martin, N. M., & Jackson, S. P. (2018). Deubiquitylating enzymes and drug discovery: Emerging opportunities. In *Nature Reviews Drug Discovery* (Vol. 17, Issue 1, pp. 57–77). Nature Publishing Group. https://doi.org/10.1038/nrd.2017.152

Heo, J. M., Ordureau, A., Paulo, J. A., Rinehart, J., & Harper, J. W. (2015). The PINK1-PARKIN Mitochondrial Ubiquitylation Pathway Drives a Program of OPTN/NDP52 Recruitment and TBK1 Activation to Promote Mitophagy. *Molecular Cell*, *60*(1), 7–20. https://doi.org/10.1016/j.molcel.2015.08.016

Hobbs, G. A., Der, C. J., & Rossman, K. L. (2016). RAS isoforms and mutations in cancer at a glance. *Journal of Cell Science*, *129*(7), 1287–1292. https://doi.org/10.1242/jcs.182873

Huang, X., Gollin, S. M., Raja, S., & Godfrey, T. E. (2002). High-resolution mapping of the 11q13 amplicon and identification of a gene, TAOS1, that is amplified and overexpressed in oral cancer cells. *Proceedings of the National Academy of Sciences of the United States of America*, *99*(17), 11369–11374. https://doi.org/10.1073/pnas.172285799

Husnjak, K., & Dikic, I. (2012). Ubiquitin-binding proteins: Decoders of ubiquitin-mediated cellular functions. *Annual Review of Biochemistry*, *81*, 291–322. https://doi.org/10.1146/annurev-biochem-051810-094654

Ikeda, F., & Dikic, I. (2008). Atypical ubiquitin chains: New molecular signals. "Protein Modifications: Beyond the Usual Suspects" Review Series. In *EMBO Reports* (Vol. 9, Issue 6, pp. 536–542). EMBO Rep. https://doi.org/10.1038/embor.2008.93

Ito, S. (2020). Proteasome inhibitors for the treatment of multiple myeloma. In *Cancers* (Vol. 12, Issue 2). MDPI AG. https://doi.org/10.3390/cancers12020265

Jaffe, A. B., & Hall, A. (2005). RHO GTPASES: Biochemistry and Biology. *Annual Review of Cell and Developmental Biology*, *21*(1), 247–269. https://doi.org/10.1146/annurev.cellbio.21.020604.150721

Jang, H. H. (2018). Regulation of Protein Degradation by Proteasomes in Cancer. *Journal of Cancer*

Prevention, *23*(4), 153–161. https://doi.org/10.15430/jcp.2018.23.4.153

Jura, N., Scotto-Lavino, E., Sobczyk, A., & Bar-Sagi, D. (2006). Differential modification of Ras proteins by ubiquitination. *Molecular Cell*, *21*(5), 679–687. https://doi.org/10.1016/j.molcel.2006.02.011

Kane, L. A., Lazarou, M., Fogel, A. I., Li, Y., Yamano, K., Sarraf, S. A., Banerjee, S., & Youle, R. J. (2014). PINK1 phosphorylates ubiquitin to activate parkin E3 ubiquitin ligase activity. *Journal of Cell Biology*, *205*(2), 143–153. https://doi.org/10.1083/jcb.201402104

Karnoub, A. E., & Weinberg, R. A. (2008). Ras oncogenes: Split personalities. In *Nature Reviews Molecular Cell Biology* (Vol. 9, Issue 7, pp. 517–531). Nat Rev Mol Cell Biol. https://doi.org/10.1038/nrm2438

Khan, A. R., & Ménétrey, J. (2013). Structural biology of arf and rab GTPases' effector recruitment and specificity. In *Structure* (Vol. 21, Issue 8, pp. 1284–1297). Structure. https://doi.org/10.1016/j.str.2013.06.016

Kimura, Y., & Tanaka, K. (2010). Regulatory mechanisms involved in the control of ubiquitin homeostasis. In *Journal of Biochemistry* (Vol. 147, Issue 6, pp. 793–798). J Biochem. https://doi.org/10.1093/jb/mvq044

Kirkpatrick, D. S., Denison, C., & Gygi, S. P. (2005). Weighing in on ubiquitin: The expanding role of mass-spectrometry-based proteomics. In *Nature Cell Biology* (Vol. 7, Issue 8, pp. 750–757). Nature Publishing Group. https://doi.org/10.1038/ncb0805-750

Kleiger, G., & Mayor, T. (2014). Perilous journey: A tour of the ubiquitin-proteasome system. In *Trends in Cell Biology* (Vol. 24, Issue 6, pp. 352–359). Elsevier Ltd. https://doi.org/10.1016/j.tcb.2013.12.003

Kliza, K., & Husnjak, K. (2020). Resolving the Complexity of Ubiquitin Networks. In *Frontiers in Molecular Biosciences* (Vol. 7, p. 21). Frontiers Media S.A. https://doi.org/10.3389/fmolb.2020.00021

Komander, D., Clague, M. J., & Urbé, S. (2009). Breaking the chains: Structure and function of the deubiquitinases. In *Nature Reviews Molecular Cell Biology* (Vol. 10, Issue 8, pp. 550–563). Nature Publishing Group. https://doi.org/10.1038/nrm2731

Komander, D., & Rape, M. (2012). The ubiquitin code. *Annual Review of Biochemistry*, *81*, 203–229. https://doi.org/10.1146/annurev-biochem-060310-170328

Kongsema, M., Zona, S., Karunarathna, U., Cabrera, E., Man, E. P. S., Yao, S., Shibakawa, A., Khoo, U. S., Medema, R. H., Freire, R., & Lam, E. F. (2016). Rnf168 cooperates with rnf8 to mediate foxm1 ubiquitination and degradation in breast cancer epirubicin treatment. *Oncogenesis*, *5*(8), 252. https://doi.org/10.1038/oncsis.2016.57

Kravtsova-Ivantsiv, Y., & Ciechanover, A. (2012). Non-canonical ubiquitin-based signals for proteasomal degradation. *Journal of Cell Science*, *125*(3), 539–548. https://doi.org/10.1242/jcs.093567

Kumar, S. K., Rajkumar, V., Kyle, R. A., Van Duin, M., Sonneveld, P., Mateos, M. V., Gay, F., & Anderson, K. C. (2017). Multiple myeloma. *Nature Reviews Disease Primers*, *3*(1), 1–20. https://doi.org/10.1038/nrdp.2017.46

Landré, V., Rotblat, B., Melino, S., Bernassola, F., & Melino, G. (2014). Screening for E3-Ubiquitin ligase inhibitors: Challenges and opportunities. *Oncotarget*, *5*(18), 7988–8013.

https://doi.org/10.18632/oncotarget.2431

Laude, A. J., & Prior, I. A. (2008). Palmitoylation and localisation of RAS isoforms are modulated by the hypervariable linker domain. *Journal of Cell Science*, *121*(4), 421–427. https://doi.org/10.1242/jcs.020107

Lazarou, M., Sliter, D. A., Kane, L. A., Sarraf, S. A., Wang, C., Burman, J. L., Sideris, D. P., Fogel, A. I., & Youle, R. J. (2015). The ubiquitin kinase PINK1 recruits autophagy receptors to induce mitophagy. *Nature*, *524*(7565), 309–314. https://doi.org/10.1038/nature14893

Lee, M. J., Lee, B. H., Hanna, J., King, R. W., & Finley, D. (2011). Trimming of ubiquitin chains by proteasome-associated deubiquitinating enzymes. In *Molecular and Cellular Proteomics* (Vol. 10, Issue 5). Mol Cell Proteomics. https://doi.org/10.1074/mcp.R110.003871

Li, L., Martinez, S. S., Hu, W., Liu, Z., & Tjian, R. (2015). A specific E3 ligase/deubiquitinase pair modulates TBP protein levels during muscle differentiation. *ELife*, *4*(September 2015). https://doi.org/10.7554/eLife.08536

Li, W., Bengtson, M. H., Ulbrich, A., Matsuda, A., Reddy, V. A., Orth, A., Chanda, S. K., Batalov, S., & Joazeiro, C. A. P. (2008). Genome-wide and functional annotation of human E3 ubiquitin ligases identifies MULAN, a mitochondrial E3 that regulates the organelle's dynamics and signaling. *PLoS ONE*, *3*(1). https://doi.org/10.1371/journal.pone.0001487

Liu, J., Cheng, Y., Zheng, M., Yuan, B., Wang, Z., Li, X., Yin, J., Ye, M., & Song, Y. (2021). Targeting the ubiquitination/deubiquitination process to regulate immune checkpoint pathways. In *Signal Transduction and Targeted Therapy* (Vol. 6, Issue 1, pp. 1–11). Springer Nature. https://doi.org/10.1038/s41392-020-00418-x

Liu, Q., Zheng, J., Sun, W., Huo, Y., Zhang, L., Hao, P., Wang, H., & Zhuang, M. (2018). A proximity-tagging system to identify membrane protein–protein interactions. *Nature Methods*, *15*(9), 715–722. https://doi.org/10.1038/s41592-018-0100-5

Lork, M., Verhelst, K., & Beyaert, R. (2017). CYLD, A20 and OTULIN deubiquitinases in NF-κB signaling and cell death: So similar, yet so different. In *Cell Death and Differentiation* (Vol. 24, Issue 7, pp. 1172–1183). Nature Publishing Group. https://doi.org/10.1038/cdd.2017.46

MacGurn, J. A., Hsu, P.-C., & Emr, S. D. (2012). Ubiquitin and Membrane Protein Turnover: From Cradle to Grave. *Annual Review of Biochemistry*, *81*(1), 231–259. https://doi.org/10.1146/annurev-biochem-060210-093619

Madan, S., Lacy, M. Q., Dispenzieri, A., Gertz, M. A., Buadi, F., Hayman, S. R., Detweiler-Short, K., Dingli, D., Zeldenrust, S., Lust, J., Greipp, P. R., Rajkumar, S. V., & Kumar, S. (2011). Efficacy of retreatment with immunomodulatory drugs (IMiDs) in patients receiving IMiDs for initial therapy of newly diagnosed multiple myeloma. *Blood*, *118*(7), 1763–1765. https://doi.org/10.1182/blood-2011-04-350009

Manasanch, E. E., & Orlowski, R. Z. (2017). Proteasome inhibitors in cancer therapy. In *Nature Reviews Clinical Oncology* (Vol. 14, Issue 7, pp. 417–433). Nature Publishing Group. https://doi.org/10.1038/nrclinonc.2016.206

Matsuda, N., Sato, S., Shiba, K., Okatsu, K., Saisho, K., Gautier, C. A., Sou, Y. S., Saiki, S., Kawajiri, S., Sato, F., Kimura, M., Komatsu, M., Hattori, N., & Tanaka, K. (2010). PINK1 stabilized by mitochondrial depolarization recruits Parkin to damaged mitochondria and activates latent Parkin for mitophagy. *Journal of Cell Biology*, *189*(2), 211–221. https://doi.org/10.1083/jcb.200910140

McClellan, A. J., Laugesen, S. H., & Ellgaard, L. (2019). Cellular functions and molecular mechanisms of non-lysine ubiquitination. *Open Biology*, *9*(9), 190147. https://doi.org/10.1098/rsob190147

Meister, S., Schubert, U., Neubert, K., Herrmann, K., Burger, R., Gramatzki, M., Hahn, S., Schreiber, S., Wilhelm, S., Herrmann, M., Jäck, H. M., & Voll, R. E. (2007). Extensive immunoglobulin production sensitizes myeloma cells for proteasome inhibition. *Cancer Research*, *67*(4), 1783–1792. https://doi.org/10.1158/0008-5472.CAN-06-2258

Mevissen, T. E. T., Hospenthal, M. K., Geurink, P. P., Elliott, P. R., Akutsu, M., Arnaudo, N., Ekkebus, R., Kulathu, Y., Wauer, T., El Oualid, F., Freund, S. M. V., Ovaa, H., & Komander, D. (2013). XOTU deubiquitinases reveal mechanisms of linkage specificity and enable ubiquitin chain restriction analysis. *Cell*, *154*(1), 169. https://doi.org/10.1016/j.cell.2013.05.046

Michel, M. A., Elliott, P. R., Swatek, K. N., Simicek, M., Pruneda, J. N., Wagstaff, J. L., Freund, S. M. V., & Komander, D. (2015). Assembly and specific recognition of K29- and K33-linked polyubiquitin. *Molecular Cell*, *58*(1), 95–109. https://doi.org/10.1016/j.molcel.2015.01.042

Michel, M. A., Swatek, K. N., Hospenthal, M. K., & Komander, D. (2017). Ubiquitin Linkage-Specific Affimers Reveal Insights into K6-Linked Ubiquitin Signaling. *Molecular Cell*, *68*(1), 233-246.e5. https://doi.org/10.1016/j.molcel.2017.08.020

Mori, T., Ito, T., Liu, S., Ando, H., Sakamoto, S., Yamaguchi, Y., Tokunaga, E., Shibata, N., Handa, H., & Hakoshima, T. (2018). Structural basis of thalidomide enantiomer binding to cereblon. *Scientific Reports*, *8*(1), 1294. https://doi.org/10.1038/s41598-018-19202-7

Morrow, M. E., Morgan, M. T., Clerici, M., Growkova, K., Yan, M., Komander, D., Sixma, T. K., Simicek, M., & Wolberger, C. (2018). Active site alanine mutations convert deubiquitinases into high-affinity ubiquitin-binding proteins. *EMBO Reports*, *19*(10), e45680. https://doi.org/10.15252/embr.201745680

Nakasone, M. A., Livnat-Levanon, N., Glickman, M. H., Cohen, R. E., & Fushman, D. (2013). Mixed-linkage ubiquitin chains send mixed messages. *Structure*, *21*(5), 727–740. https://doi.org/10.1016/j.str.2013.02.019

Narendra, D. P., Jin, S. M., Tanaka, A., Suen, D. F., Gautier, C. A., Shen, J., Cookson, M. R., & Youle, R. J. (2010). PINK1 is selectively stabilized on impaired mitochondria to activate Parkin. *PLoS Biology*, *8*(1). https://doi.org/10.1371/journal.pbio.1000298

Ohtake, F., Saeki, Y., Sakamoto, K., Ohtake, K., Nishikawa, H., Tsuchiya, H., Ohta, T., Tanaka, K., & Kanno, J. (2015). Ubiquitin acetylation inhibits polyubiquitin chain elongation. *EMBO Reports*, *16*(2), 192–201. https://doi.org/10.15252/embr.201439152

Ohtake, F., Tsuchiya, H., Saeki, Y., & Tanaka, K. (2018). K63 ubiquitylation triggers proteasomal degradation by seeding branched ubiquitin chains. *Proceedings of the National Academy of Sciences of the United States of America*, *115*(7), E1401–E1408. https://doi.org/10.1073/pnas.1716673115

Okatsu, K., Koyano, F., Kimura, M., Kosako, H., Saeki, Y., Tanaka, K., & Matsuda, N. (2015). Phosphorylated ubiquitin chain is the genuine Parkin receptor. *Journal of Cell Biology*, *209*(1), 111–128. https://doi.org/10.1083/jcb.201410050

Ordureau, A., Sarraf, S. A., Duda, D. M., Heo, J. M., Jedrychowski, M. P., Sviderskiy, V. O., Olszewski, J. L., Koerber, J. T., Xie, T., Beausoleil, S. A., Wells, J. A., Gygi, S. P., Schulman, B. A., & Harper, J. W. (2014). Quantitative proteomics reveal a feedforward mechanism for mitochondrial PARKIN translocation and ubiquitin chain synthesis. *Molecular Cell*, *56*(3), 360–375.

https://doi.org/10.1016/j.molcel.2014.09.007

Pasupala, N., Morrow, M. E., Que, L. T., Malynn, B. A., Ma, A., & Wolberger, C. (2018). OTUB1 non-catalytically stabilizes the E2 ubiquitin-conjugating enzyme UBE2E1 by preventing its autoubiquitination. *Journal of Biological Chemistry*, *293*(47), 18285–18295. https://doi.org/10.1074/jbc.RA118.004677

Penengo, L., Mapelli, M., Murachelli, A. G., Confalonieri, S., Magri, L., Musacchio, A., Di Fiore, P. P., Polo, S., & Schneider, T. R. (2006). Crystal Structure of the Ubiquitin Binding Domains of Rabex-5 Reveals Two Modes of Interaction with Ubiquitin. *Cell*, *124*(6), 1183–1195. https://doi.org/10.1016/j.cell.2006.02.020

Pertz, O. (2010). Spatio-temporal Rho GTPase signaling - Where are we now? In *Journal of Cell Science* (Vol. 123, Issue 11, pp. 1841–1850). J Cell Sci. https://doi.org/10.1242/jcs.064345

Pickart, C. M. (2001). Mechanisms underlying ubiquitination. In *Annual Review of Biochemistry* (Vol. 70, pp. 503–533). Annu Rev Biochem. https://doi.org/10.1146/annurev.biochem.70.1.503

Piotrowski, A., Xie, J., Liu, Y. F., Poplawski, A. B., Gomes, A. R., Madanecki, P., Fu, C., Crowley, M. R., Crossman, D. K., Armstrong, L., Babovic-Vuksanovic, D., Bergner, A., Blakeley, J. O., Blumenthal, A. L., Daniels, M. S., Feit, H., Gardner, K., Hurst, S., Kobelka, C., … Messiaen, L. M. (2014). Germline loss-of-function mutations in LZTR1 predispose to an inherited disorder of multiple schwannomas. *Nature Genetics*, *46*(2), 182–187. https://doi.org/10.1038/ng.2855

Piper, R. C., Dikic, I., & Lukacs, G. L. (2014). Ubiquitin-dependent sorting in endocytosis. *Cold Spring Harbor Perspectives in Biology*, *6*(1). https://doi.org/10.1101/cshperspect.a016808

Pohl, C., & Dikic, I. (2019). Cellular quality control by the ubiquitin-proteasome system and autophagy. In *Science* (Vol. 366, Issue 6467, pp. 818–822). American Association for the Advancement of Science. https://doi.org/10.1126/science.aax3769

Prior, I. A., Lewis, P. D., & Mattos, C. (2012). A comprehensive survey of ras mutations in cancer. In *Cancer Research* (Vol. 72, Issue 10, pp. 2457–2467). NIH Public Access. https://doi.org/10.1158/0008-5472.CAN-11-2612

Quatela, S. E., Sung, P. J., Ahearn, I. M., Bivona, T. G., & Philips, M. R. (2008). Analysis of K-Ras Phosphorylation, Translocation, and Induction of Apoptosis. In *Methods in Enzymology* (Vol. 439, pp. 87–102). Methods Enzymol. https://doi.org/10.1016/S0076-6879(07)00407-7

Reyes-Turcu, F. E., Ventii, K. H., & Wilkinson, K. D. (2009). Regulation and cellular roles of ubiquitin-specific deubiquitinating enzymes. In *Annual Review of Biochemistry* (Vol. 78, pp. 363–397). Annual Reviews . https://doi.org/10.1146/annurev.biochem.78.082307.091526

Rosen, E. M. (2013). BRCA1 in the DNA damage response and at telomeres. In *Frontiers in Genetics* (Vol. 4, Issue JUN, p. 85). Frontiers. https://doi.org/10.3389/fgene.2013.00085

Roux, K. J., Kim, D. I., Burke, B., & May, D. G. (2018). BioID: A Screen for Protein-Protein Interactions. *Current Protocols in Protein Science*, *91*(1), 19.23.1-19.23.15. https://doi.org/10.1002/cpps.51

Salmon, S. E., & Smith, B. A. (1970). Immunoglobulin synthesis and total body tumor cell number in IgG multiple myeloma. *J Clin Invest*, *49*(6), 1114–1121. https://doi.org/10.1172/JCI106327

Sasaki, A. T., Carracedo, A., Locasale, J. W., Anastasiou, D., Takeuchi, K., Kahoud, E. R., Haviv, S., Asara, J. M., Pandolfi, P. P., & Cantley, L. C. (2011). Ubiquitination of K-Ras enhances activation and facilitates binding to select downstream effectors. *Science Signaling*, *4*(163).

https://doi.org/10.1126/scisignal.2001518

Schulman, B. A., & Wade Harper, J. (2009). Ubiquitin-like protein activation by E1 enzymes: The apex for downstream signalling pathways. In *Nature Reviews Molecular Cell Biology* (Vol. 10, Issue 5, pp. 319–331). Nat Rev Mol Cell Biol. https://doi.org/10.1038/nrm2673

Schwechheimer, C. (2018). NEDD8 — its role in the regulation of Cullin-RING ligases. In *Current Opinion in Plant Biology* (Vol. 45, Issue Pt A, pp. 112–119). Elsevier Ltd. https://doi.org/10.1016/j.pbi.2018.05.017

Shiba-Fukushima, K., Arano, T., Matsumoto, G., Inoshita, T., Yoshida, S., Ishihama, Y., Ryu, K. Y., Nukina, N., Hattori, N., & Imai, Y. (2014). Phosphorylation of Mitochondrial Polyubiquitin by PINK1 Promotes Parkin Mitochondrial Tethering. *PLoS Genetics*, *10*(12). https://doi.org/10.1371/journal.pgen.1004861

Shiba-Fukushima, K., Ishikawa, K. I., Inoshita, T., Izawa, N., Takanashi, M., Sato, S., Onodera, O., Akamatsu, W., Okano, H., Imai, Y., & Hattori, N. (2017). Evidence that phosphorylated ubiquitin signaling is involved in the etiology of Parkinson's disease. *Human Molecular Genetics*, *26*(16), 3172–3185. https://doi.org/10.1093/hmg/ddx201

Shukla, S., Allam, U. S., Ahsan, A., Chen, G., Krishnamurthy, P. M., Marsh, K., Rumschlag, M., Shankar, S., Whitehead, C., Schipper, M., Basrur, V., Southworth, D. R., Chinnaiyan, A. M., Rehemtulla, A., Beer, D. G., Lawrence, T. S., Nyati, M. K., & Ray, D. (2014). KRAS protein stability is regulated through SMURF2: UBCH5 complex-mediated β-TrCP1 degradation. *Neoplasia (United States)*, *16*(2), 115–128. https://doi.org/10.1593/neo.14184

Shutes, A., & Der, C. J. (2005). Real-time in vitro measurement of GTP hydrolysis. *Methods*, *37*(2), 183–189. https://doi.org/10.1016/j.ymeth.2005.05.019

Shutes, A., & Der, C. J. (2006). Real-Time In Vitro Measurement of Intrinsic and Ras GAP-Mediated GTP Hydrolysis. In *Methods in Enzymology* (Vol. 407, pp. 9–22). Academic Press Inc. https://doi.org/10.1016/S0076-6879(05)07002-3

Simicek, M., Lievens, S., Laga, M., Guzenko, D., Aushev, V. N., Kalev, P., Baietti, M. F., Strelkov, S. V., Gevaert, K., Tavernier, J., & Sablina, A. A. (2013). The deubiquitylase USP33 discriminates between RALB functions in autophagy and innate immune response. *Nature Cell Biology*, *15*(10), 1220–1230. https://doi.org/10.1038/ncb2847

Sit, S. T., & Manser, E. (2011). Rho GTPases and their role in organizing the actin cytoskeleton. In *Journal of Cell Science* (Vol. 124, Issue 5, pp. 679–683). The Company of Biologists Ltd. https://doi.org/10.1242/jcs.064964

Skaug, B., Jiang, X., & Chen, Z. J. (2009). The role of ubiquitin in NF-κB regulatory pathways. In *Annual Review of Biochemistry* (Vol. 78, pp. 769–796). Annu Rev Biochem. https://doi.org/10.1146/annurev.biochem.78.070907.102750

Sloper-Mould, K. E., Jemc, J. C., Pickart, C. M., & Hicke, L. (2001). Distinct Functional Surface Regions on Ubiquitin. *Journal of Biological Chemistry*, *276*(32), 30483–30489. https://doi.org/10.1074/jbc.M103248200

Smith, B. E., Wang, S. L., Jaime-Figueroa, S., Harbin, A., Wang, J., Hamman, B. D., & Crews, C. M. (2019). Differential PROTAC substrate specificity dictated by orientation of recruited E3 ligase. *Nature Communications*, *10*(1), 1–13. https://doi.org/10.1038/s41467-018-08027-7

Soave, C. L., Guerin, T., Liu, J., & Dou, Q. P. (2017). Targeting the ubiquitin-proteasome system for

cancer treatment: discovering novel inhibitors from nature and drug repurposing. *Cancer and Metastasis Reviews*, *36*(4), 717–736. https://doi.org/10.1007/s10555-017-9705-x

Steklov, M., Pandolfi, S., Baietti, M. F., Batiuk, A., Carai, P., Najm, P., Zhang, M., Jang, H., Renzi, F., Cai, Y., Abbasi Asbagh, L., Pastor, T., De Troyer, M., Simicek, M., Radaelli, E., Brems, H., Legius, E., Tavernier, J., Gevaert, K., … Sablina, A. A. (2018). Mutations in LZTR1 drive human disease by dysregulating RAS ubiquitination. *Science*, *362*(6419), 1177–1182. https://doi.org/10.1126/science.aap7607

Stenmark, H. (2009). Rab GTPases as coordinators of vesicle traffic. In *Nature Reviews Molecular Cell Biology* (Vol. 10, Issue 8, pp. 513–525). Nature Publishing Group. https://doi.org/10.1038/nrm2728

Suizu, F., Hiramuki, Y., Okumura, F., Matsuda, M., Okumura, A. J., Hirata, N., Narita, M., Kohno, T., Yokota, J., Bohgaki, M., Obuse, C., Hatakeyama, S., Obata, T., & Noguchi, M. (2009). The E3 Ligase TTC3 Facilitates Ubiquitination and Degradation of Phosphorylated Akt. *Developmental Cell*, *17*(6), 800–810. https://doi.org/10.1016/j.devcel.2009.09.007

Swaney, D. L., Rodríguez-Mias, R. A., & Villén, J. (2015). Phosphorylation of ubiquitin at Ser65 affects its polymerization, targets, and proteome-wide turnover. *EMBO Reports*, *16*(9), 1131–1144. https://doi.org/10.15252/embr.201540298

Swatek, K. N., & Komander, D. (2016). Ubiquitin modifications. In *Cell Research* (Vol. 26, Issue 4, pp. 399–422). Nature Publishing Group. https://doi.org/10.1038/cr.2016.39

Swatek, K. N., Usher, J. L., Kueck, A. F., Gladkova, C., Mevissen, T. E. T., Pruneda, J. N., Skern, T., & Komander, D. (2019). Insights into ubiquitin chain architecture using Ub-clipping. *Nature*, *572*(7770), 533–537. https://doi.org/10.1038/s41586-019-1482-y

Takahashi, T. S., Wollscheid, H.-P., Lowther, J., & Ulrich, H. D. (2020). Effects of chain length and geometry on the activation of DNA damage bypass by polyubiquitylated PCNA. *Nucleic Acids Research*, *48*(6), 3042–3052. https://doi.org/10.1093/nar/gkaa053

Toma-Fukai, S., & Shimizu, T. (2019). Structural insights into the regulation mechanism of small GTPases by GEFs. In *Molecules* (Vol. 24, Issue 18, p. 3308). MDPI AG. https://doi.org/10.3390/molecules24183308

Udeshi, N. D., Mertins, P., Svinkina, T., & Carr, S. A. (2013). Large-scale identification of ubiquitination sites by mass spectrometry. *Nature Protocols*, *8*(10), 1950–1960. https://doi.org/10.1038/nprot.2013.120

Valente, E. M., Abou-Sleiman, P. M., Caputo, V., Muqit, M. M. K., Harvey, K., Gispert, S., Ali, Z., Del Turco, D., Bentivoglio, A. R., Healy, D. G., Albanese, A., Nussbaum, R., González-Maldonado, R., Deller, T., Salvi, S., Cortelli, P., Gilks, W. P., Latchman, D. S., Harvey, R. J., … Wood, N. W. (2004). Hereditary early-onset Parkinson's disease caused by mutations in PINK1. *Science*, *304*(5674), 1158–1160. https://doi.org/10.1126/science.1096284

Vigil, D., Cherfils, J., Rossman, K. L., & Der, C. J. (2010). Ras superfamily GEFs and GAPs: Validated and tractable targets for cancer therapy? In *Nature Reviews Cancer* (Vol. 10, Issue 12, pp. 842–857). Nat Rev Cancer. https://doi.org/10.1038/nrc2960

Wagner, S. A., Beli, P., Weinert, B. T., Nielsen, M. L., Cox, J., Mann, M., & Choudhary, C. (2011). A Proteome-wide, Quantitative Survey of In Vivo Ubiquitylation Sites Reveals Widespread Regulatory Roles. *Molecular & Cellular Proteomics*, *10*(10), M111.013284. https://doi.org/10.1074/mcp.m111.013284

Wauer, T., Simicek, M., Schubert, A., & Komander, D. (2015). Mechanism of phospho-ubiquitin-induced PARKIN activation. *Nature*, *524*(7565), 370–374. https://doi.org/10.1038/nature14879

Wauer, T., Swatek, K. N., Wagstaff, J. L., Gladkova, C., Pruneda, J. N., Michel, M. A., Gersch, M., Johnson, C. M., Freund, S. M., & Komander, D. (2015). Ubiquitin Ser65 phosphorylation affects ubiquitin structure, chain assembly and hydrolysis. *The EMBO Journal*, *34*(3), 307–325. https://doi.org/10.15252/embj.201489847

Wennerberg, K., Rossman, K. L., & Der, C. J. (2005). The Ras superfamily at a glance. *Journal of Cell Science*, *118*(5), 843–846. https://doi.org/10.1242/jcs.01660

Wickliffe, K. E., Lorenz, S., Wemmer, D. E., Kuriyan, J., & Rape, M. (2011). The mechanism of linkage-specific ubiquitin chain elongation by a single-subunit E2. *Cell*, *144*(5), 769–781. https://doi.org/10.1016/j.cell.2011.01.035

Wiener, R., Zhang, X., Wang, T., & Wolberger, C. (2012). The mechanism of OTUB1-mediated inhibition of ubiquitination. *Nature*, *483*(7391), 618–622. https://doi.org/10.1038/nature10911

Wijk, S. J. L., & Timmers, H. T. M. (2010). The family of ubiquitin-conjugating enzymes (E2s): deciding between life and death of proteins. *The FASEB Journal*, *24*(4), 981–993. https://doi.org/10.1096/fj.09-136259

Winborn, B. J., Travis, S. M., Todi, S. V., Scaglione, K. M., Xu, P., Williams, A. J., Cohen, R. E., Peng, J., & Paulson, H. L. (2008). The deubiquitinating enzyme ataxin-3, a polyglutamine disease protein, edits Lys63 linkages in mixed linkage ubiquitin chains. *Journal of Biological Chemistry*, *283*(39), 26436–26443. https://doi.org/10.1074/jbc.M803692200

Woelk, T., Oldrini, B., Maspero, E., Confalonieri, S., Cavallaro, E., Di Fiore, P. P., & Polo, S. (2006). Molecular mechanisms of coupled monoubiquitination. *Nature Cell Biology*, *8*(11), 1246–1254. https://doi.org/10.1038/ncb1484

Wong, E. S. P., Tan, J. M. M., & Lim, K.-L. (2008). Dynamic Role of Ubiquitination in the Management of Misfolded Proteins Associated with Neurodegenerative Diseases. In *Protein Folding and Misfolding: Neurodegenerative Diseases* (pp. 77–95). Springer Netherlands. https://doi.org/10.1007/978-1-4020-9434-7_3

Wu-Baer, F., Lagrazon, K., Yuan, W., & Baer, R. (2003). The BRCA1/BARD1 heterodimer assembles polyubiquitin chains through an unconventional linkage involving lysine residue K6 of ubiquitin. *Journal of Biological Chemistry*, *278*(37), 34743–34746. https://doi.org/10.1074/jbc.C300249200

Xu, L., Lubkov, V., Taylor, L. J., & Bar-Sagi, D. (2010). Feedback regulation of ras signaling by rabex-5-mediated ubiquitination. *Current Biology*, *20*(15), 1372–1377. https://doi.org/10.1016/j.cub.2010.06.051

Yang, M. H., Laurent, G., Bause, A. S., Spang, R., German, N., Haigis, M. C., & Haigis, K. M. (2013). HDAC6 and SIRT2 regulate the acetylation state and oncogenic activity of mutant K-RAS. *Molecular Cancer Research*, *11*(9), 1072–1077. https://doi.org/10.1158/1541-7786.MCR-13-0040-T

Yang, W. L., Wang, J., Chan, C. H., Lee, S. W., Campos, A. D., Lamothe, B., Hur, L., Grabiner, B. C., Lin, X., Darnay, B. G., & Lin, H. K. (2009). The E3 Ligase TRAF6 regulates akt ubiquitination and activation. *Science*, *325*(5944), 1134–1138. https://doi.org/10.1126/science.1175065

Yau, R., & Rape, M. (2016). The increasing complexity of the ubiquitin code. In *Nature Publishing*

Group (Vol. 18, Issue 6). https://doi.org/10.1038/ncb3358

Ye, Y., & Rape, M. (2009). Building ubiquitin chains: E2 enzymes at work. In *Nature Reviews Molecular Cell Biology* (Vol. 10, Issue 11, pp. 755–764). Nat Rev Mol Cell Biol. https://doi.org/10.1038/nrm2780

Zeng, T., Wang, Q., Fu, J., Lin, Q., Bi, J., Ding, W., Qiao, Y., Zhang, S., Zhao, W., Lin, H., Wang, M., Lu, B., Deng, X., Zhou, D., Yin, Z., & Wang, H. R. (2014). Impeded Nedd4-1-Mediated Ras Degradation Underlies Ras-Driven Tumorigenesis. *Cell Reports*, *7*(3), 871–882. https://doi.org/10.1016/j.celrep.2014.03.045

Zhao, S., & Ulrich, H. D. (2010). Distinct consequences of posttranslational modification by linear versus K63-linked polyubiquitin chains. *Proceedings of the National Academy of Sciences of the United States of America*, *107*(17), 7704–7709. https://doi.org/10.1073/pnas.0908764107

Zheng, N., & Shabek, N. (2017). Ubiquitin ligases: Structure, function, and regulation. In *Annual Review of Biochemistry* (Vol. 86, pp. 129–157). Annual Reviews Inc. https://doi.org/10.1146/annurev-biochem-060815-014922

Zinngrebe, J., Montinaro, A., Peltzer, N., & Walczak, H. (2014). Ubiquitin in the immune system. In *EMBO Reports* (Vol. 15, Issue 1, pp. 28–45). Wiley-VCH Verlag. https://doi.org/10.1002/embr.201338025

Appendix

Simicek, M., Lievens, S., Laga, M., Guzenko, D., Aushev, V. N., Kalev, P., Baietti, M. F., Strelkov, S. V., Gevaert, K., Tavernier, J., Sablina, A. A. (2013). The deubiquitylase USP33 discriminates between RALB functions in autophagy and innate immune response. *Nature Cell Biology*, *15*(10), 1220–1230.

Michel, M. A., Elliott, P. R., Swatek, K. N., **Simicek, M.**, Pruneda, J. N., Wagstaff, J. L., Freund, S. M.V., Komander, D. (2015). Assembly and specific recognition of K29- and K33-linked polyubiquitin. *Molecular Cell*, *58*(1), 95–109.

Wauer, T., **Simicek, M.**, Schubert, A., & Komander, D. (2015). Mechanism of phospho-ubiquitin-induced PARKIN activation. *Nature*, *524*(7565), 370–374.

Baietti, M. F.*, **Simicek, M.***, Abbasi Asbagh, L., Radaelli, E., Lievens, S., Crowther, J., Steklov, M., Aushev, V. N., Martínez García, D., Tavernier, J., Sablina, A. A. (2016). OTUB 1 triggers lung cancer development by inhibiting RAS monoubiquitination. *EMBO Molecular Medicine*, *8*(3), 288–303.

Steklov, M., Pandolfi, S., Baietti, M. F., Batiuk, A., Carai, P., Najm, P., Zhang, M., Jang, H., Renzi, F., Cai, Y., Abbasi Asbagh, L., Pastor, T., De Troyer, M., **Simicek, M**., Radaelli, E., Brems, H., Legius, E., Tavernier, J., Gevaert, K., … Sablina, A. A. (2018). Mutations in LZTR1 drive human disease by dysregulating RAS ubiquitination. *Science*, *362*(6419), 1177–1182.

Morrow, M. E., Morgan, M. T., Clerici, M., Growkova, K., Yan, M., Komander, D., Sixma, T. K., **Simicek, M**., & Wolberger, C. (2018). Active site alanine mutations convert deubiquitinases into high-affinity ubiquitin-binding proteins. *EMBO Reports*, *19*(10), e45680.

Garcés, J. J.*, **Simicek, M.***, Vicari, M., Brozova, L., Burgos, L., Bezdekova, R., Alignani, D., Calasanz, M. J., Growkova, K., Goicoechea, I., Agirre, X., Pour, L., Prosper, F., Rios, R., Martinez-Lopez, J., Millacoy, P., Palomera, L., Del Orbe, R., Perez-Montaña, A., … Paiva, B. (2020). Transcriptional profiling of circulating tumor cells in multiple myeloma: a new model to understand disease dissemination. *Leukemia*, *34*(2), 589–603.

The deubiquitylase USP33 discriminates between RALB functions in autophagy and innate immune response

Michal Simicek[1,2], Sam Lievens[3,4], Mathias Laga[3,4], Dmytro Guzenko[5], Vasily N. Aushev[6], Peter Kalev[1,2], Maria Francesca Baietti[1,2], Sergei V. Strelkov[5], Kris Gevaert[3,4], Jan Tavernier[3,4] and Anna A. Sablina[1,2,7]

The RAS-like GTPase RALB mediates cellular responses to nutrient availability or viral infection by respectively engaging two components of the exocyst complex, EXO84 and SEC5. RALB employs SEC5 to trigger innate immunity signalling, whereas RALB–EXO84 interaction induces autophagocytosis. How this differential interaction is achieved molecularly by the RAL GTPase remains unknown. We found that whereas GTP binding turns on RALB activity, ubiquitylation of RALB at Lys 47 tunes its activity towards a particular effector. Specifically, ubiquitylation at Lys 47 sterically inhibits RALB binding to EXO84, while facilitating its interaction with SEC5. Double-stranded RNA promotes RALB ubiquitylation and SEC5–TBK1 complex formation. In contrast, nutrient starvation induces RALB deubiquitylation by accumulation and relocalization of the deubiquitylase USP33 to RALB-positive vesicles. Deubiquitylated RALB promotes the assembly of the RALB–EXO84–beclin-1 complexes driving autophagosome formation. Thus, ubiquitylation within the effector-binding domain provides the switch for the dual functions of RALB in autophagy and innate immune responses.

The RAS family of small GTPases function as molecular switches alternating between inactive GDP-bound and active GTP-bound states[1]. Once activated, RAS GTPases exert their effects through binding and activation of downstream effectors. Each RAS GTPase activates a diverse set of downstream effectors and may propagate multiple signalling pathways. However, the mechanisms that govern specificity of the interactions between RAS GTPases and their downstream effectors are mainly unknown.

Two highly similar RAL proteins, RALA and RALB, constitute a family within the RAS branch of small GTPases. RALA and RALB share the same effector molecules and seem to function in distinct but inter-related biological processes that are largely connected through their interaction with the RALBP1 protein and the components of the hetero-octameric exocyst complex. Two components of the exocyst, SEC5 (EXOC2) and EXO84 (EXOC8), are effector molecules that mediate RAL regulation of dynamic secretory vesicle targeting and tethering processes[2–6].

RALA mobilizes SEC5 and EXO84 to regulate basolateral delivery of membrane proteins in polarized epithelial cells[4,5] and insulin-stimulated GLUT4 delivery to the plasma membrane[7,8]. The binding of RALBP1 to RALA is required for the appropriate mitochondrial fission and accurate distribution of mitochondria between daughter cells[9].

RALB has been demonstrated to mediate an entirely different set of cellular processes. Infection with double-stranded RNA (dsRNA) viruses promotes the formation of the RALB–SEC5 complex that activates the innate immunity signalling kinase TBK1 and the subsequent IRF3 transcription-factor-dependent interferon response[10]. On the other hand, nutrient starvation or double-stranded DNA triggers interaction between RALB and EXO84 driving the assembly of catalytically active ULK1 and the beclin-1–VPS34 autophagy initiation complex[11,12]. These data suggest that RALB and the components of the exocyst complex represent a regulatory hub through bifurcating activation of TBK1 and beclin-1–VPS34 that helps engage coordinated activation of the gene expression and organelle biogenesis responses supporting systemic pathogen recognition and clearance.

The structural data of RAL–effector complexes indicate that the RAL downstream effectors bind overlapping residues of the RAL GTPases and compete for RAL binding[13–16]. It is unclear how specificity pertaining to effector recognition is achieved by the RAL GTPase. Here we found that RALB ubiquitylation at Lys 47, controlled by the
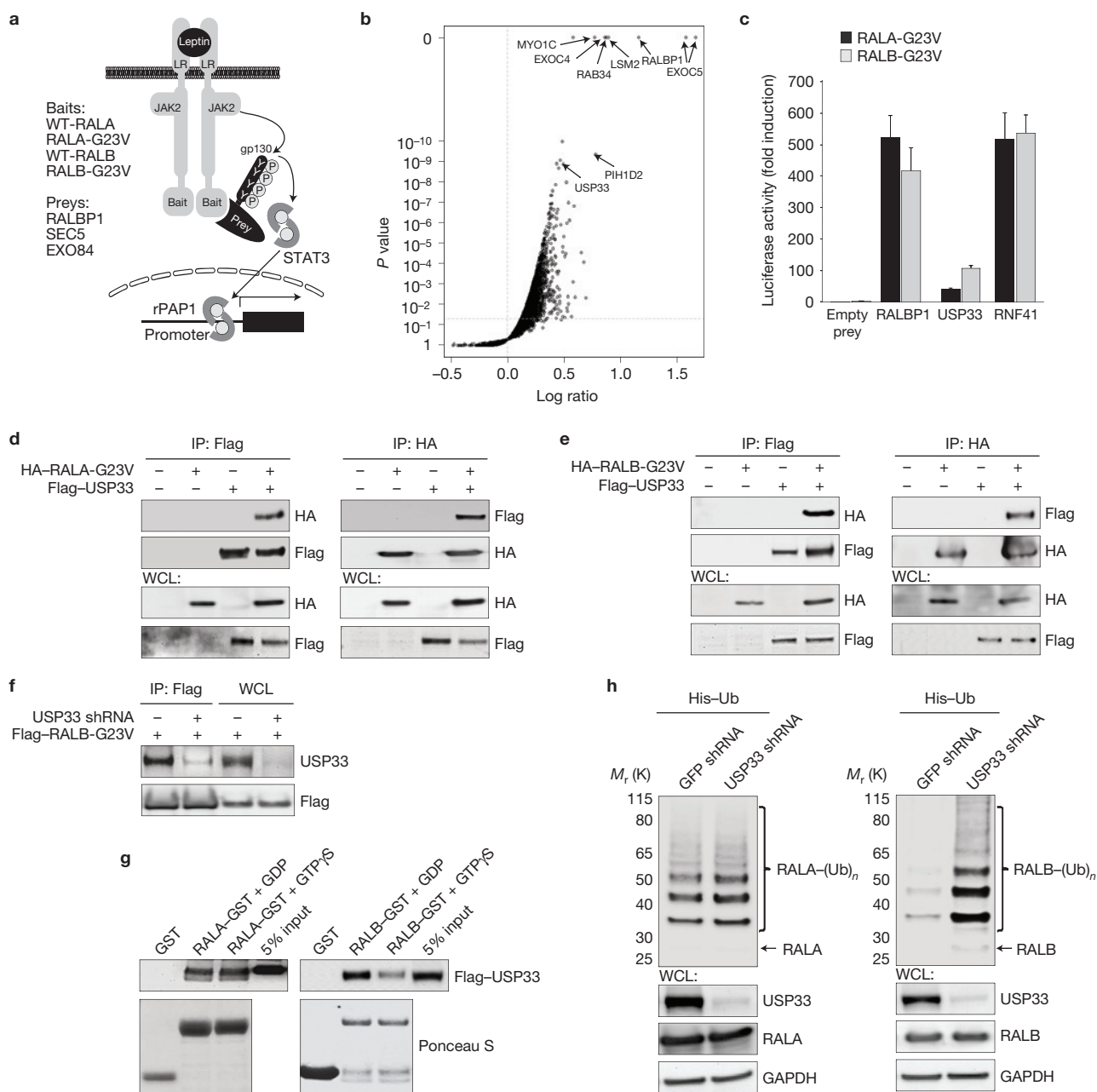
Figure 1 The deubiquitylase USP33 is an interacting partner of the RAL GTPases. (**a**) Schematic outline of the MAPPIT technique. The indicated RAL mutants (baits) were fused to a leptin receptor fragment that is deficient in STAT3 recruitment sites. The RAL downstream effectors (preys) were tethered to a GP130 cytokine receptor fragment containing functional STAT3-docking sites. Association of bait and prey proteins restores a functional leptin receptor complex. On leptin stimulation, STAT3 activation can be monitored by a STAT3-responsive luciferase reporter. WT, wild type. (**b**) MAPPIT screen identified RAL-interacting proteins. A MAPPIT array covering close to 8,500 preys was screened with RALA-G23V as bait. Data are shown in a volcano plot of the log ratio of normalized MAPPIT luciferase activity versus P value Source data can be found in Supplementary Table S1. (**c**) MAPPIT assay confirmed interaction between the RAL proteins and USP33. RALA-G23V or RALB-G23V baits were introduced into HEK293T cells together with the indicated preys. The results are expressed as a mean of normalized luciferase activity $\pm$ s.d (leptin-treated cells versus leptin-untreated cells) for three independent experiments. Statistics source data can be found in Supplementary Table S1. (**d**,**e**) USP33 interacts with both RALA and RALB.

At 48 h post-transfection with tagged USP33 and RAL expression constructs, the indicated proteins were then immunoprecipitated with anti-Flag (M2) or anti-HA–agarose, followed by immunoblotting using anti-Flag or anti-HA antibodies. WCL, whole-cell lysate; IP, immunoprecipitates. (**f**) Endogenous USP33 interacts with RALB. Flag–RALB was immunoprecipitated using anti-Flag (M2) agarose and analysed for co-precipitation with endogenous USP33 using anti-USP33 antibody. Cells expressing USP33 shRNA were used as a negative control. (**g**) GTP binding is not required for interaction between USP33 and the RAL proteins. The GST-tagged RALA and RALB were isolated with glutathione–agarose and mixed with lysates derived from HEK293T cells expressing Flag–USP33 in the presence of GTPγS or excess of GDP followed by immunoblotting with Flag-specific antibody. (**h**) USP33 affects ubiquitylation of RALB, but not RALA. 6xHis-tagged ubiquitin and Flag–RAL-G23V mutants were introduced into HEK293T cells stably expressing GFP shRNA or USP33 shRNA. Ubiquitylated RAL proteins were purified by Co^{2+} metal affinity chromatography and detected by antibodies specific to RALA or RALB. Uncropped images of blots are shown in Supplementary Fig. S7.

deubiquitylase USP33, determines a choice of RALB to form complexes with EXO84 or SEC5 to trigger specific cellular responses.

RESULTS

The deubiquitylase USP33 controls ubiquitylation of the RALB GTPase

To gain insight into the upstream mechanisms of RAL regulation, we employed the two-hybrid mammalian protein–protein interaction trap (MAPPIT) approach (Fig. 1a), which allows one to semi-quantitatively monitor protein–protein interactions in intact mammalian cells[17,18]. We found that GTPase-deficient RAL-G23V baits gave rise to robust MAPPIT signals with each of the tested effector preys, whereas wild-type RAL proteins, used as baits, scored negative in the assay (Supplementary Fig. S1a,b). These results are consistent with previous reports[2,3] that confirm the feasibility of the MAPPIT approach for exploring RAL signalling.

We performed a high-throughput Array MAPPIT screen, in which the RALA-G23V bait was screened against a library of about 8,500 preys[19,20] (Fig. 1b). Importantly, among the top hits we found known RAL interactors, including RALBP1 (ref. 3), MYO1C (ref. 7), and the components of the exocyst complex, SEC10 (EXOC5) and SEC8 (EXOC4; ref. 21). We validated RAB34, LSM2, PIH1D2 and USP33 as potential RALA interactors (Supplementary Fig. S1c).

A recent report has demonstrated that the RAL GTPases undergo reversible mono- and bi-ubiquitylation[22]. As enzymes controlling RAL ubiquitylation warrant further investigation, we focused our further studies on the ubiquitin-specific protease USP33 (refs 23,24). The MAPPIT assay confirmed that both RALA and RALB interact with USP33 (Fig. 1c). When we overexpressed HA-tagged RAL proteins and Flag-tagged USP33, we found that immune complexes isolated using either HA- or Flag-specific antibodies contained both the RAL proteins and USP33 (Fig. 1d,e). We also detected interaction between endogenous USP33 and Flag-tagged RALB (Fig. 1f), further confirming that RALB interacts with USP33.

To assess whether USP33 acts downstream or upstream of the RAL GTPases, we determined whether the interaction between RALs and USP33 is GTP-dependent by performing USP33–RAL pulldown experiments in the presence of guanosine gamma thio-phosphate (GTPγS), a non-hydrolysable GTP analogue, or excess of GDP. We found that RALA interacts with USP33 in a GTP-independent manner. Surprisingly, RALB demonstrated a higher affinity to USP33 in the excess of GDP, indicating that USP33 preferentially interacts with the GDP-bound form of RALB (Fig. 1g). These results reveal that GTP binding is not necessary for USP33–RAL interaction, suggesting that USP33 may serve as an upstream regulator of the RAL GTPases.

To elucidate whether USP33 regulates deubiquitylation of the RAL proteins, we analysed levels of RAL ubiquitylation in USP33-depleted cells. Suppression of USP33 by specific short hairpin RNA (shRNA) (Supplementary Fig. S2a) did not affect levels of ubiquitylated RALA. In contrast, we observed a significant increase of ubiquitylated RALB in USP33-suppressed cells (Fig. 1h). We also investigated whether the deubiquitylase USP20, the closest homologue of USP33, could regulate ubiquitylation of the RAL GTPases. However, USP20 did not affect ubiquitylation of the RAL proteins (Supplementary Fig. S3). Given that we observed an interaction between USP33 and RALB and increased

RALB ubiquitylation in USP33-depleted cells, it seems likely that RALB is a direct target for the deubiquitylase USP33.

RALB ubiquitylation at Lys 47 determines a choice of its downstream effectors

Similar RALB protein levels in cells expressing green fluorescent protein (GFP) shRNA and USP33 shRNA suggest that RALB ubiquitylation plays a regulatory role rather than targeting RALB for degradation (Fig. 1h). We next identified sites of RALB ubiquitylation by mass spectrometry after tandem affinity purification of ubiquitylated RALB from USP33-depleted cells (Fig. 2a). Mass spectrometry analysis revealed six sites of RALB ubiquitylation (Fig. 2b and Supplementary Fig. S4a). We also detected both Lys-48- and Lys-63-linked ubiquitin linkages, indicating that at least some of the bi-ubiquitylated RALB is due to tandem modification. However, a previous report[22] also suggests that the bi-ubiquitylated forms of RALB could consist of two separate monoubiquitylations at different lysine residues on RALB.

The mass spectrometry analysis suggested that ubiquitylation of RALB at Lys 47 and Lys 160 is the most abundant in USP33 knockdown (KD) cells (Fig. 2b). However, whereas we observed rather a slight increase in ubiquitylation of the RALB-K160R mutant, substitution of arginine for Lys 47 markedly reduced the level of RALB ubiquitylation (Fig. 2c). Moreover, USP33 KD did not affect ubiquitylation levels of the RALB-K47R mutant (Fig. 2d), indicating that USP33 regulates RALB deubiquitylation at Lys 47. As USP33 preferentially binds to GDP-bound RALB, we investigated whether RALB ubiquitylation depends on its GDP–GTP status. We found a significantly increased level of ubiquitylation of the GTP-bound RALB-G23V mutant when compared with wild-type RALB (Fig. 2e), indicating that GTP binding and ubiquitylation at Lys 47 are coupled together. We determined that approximately 5% of GTP-bound RALB underwent ubiquitylation, whereas suppression of USP33 led to an increase up to about 14%. (Supplementary Fig. S4b,c).

Mass spectrometry analysis also revealed that ubiquitylated RALB was in complex with SEC5, whereas we did not observe EXO84 peptides (Supplementary Fig. S4d). Consistently, co-immunoprecipitation revealed that substitution of arginine for Lys 47 led to increased interaction of RALB with EXO84 and decreased its binding to SEC5 (Fig. 2f,g). On the other hand, the K47R mutation did not alter the amount of GTP-bound RALB (Fig. 2h). Together, these results suggest that RALB ubiquitylation does not affect RALB activity but modulates RALB–SEC5 and RALB–EXO84 complex formation.

To further determine the effect of Lys 47 ubiquitylation on interactions between RAL and its effectors, we sampled the conformational space of ubiquitin ligated to Lys 47 of RAL using known three-dimensional structures of RALA in complex with RAL-binding domains (RBD) of SEC5 or EXO84 (refs 15,25). By using the Rosetta3 suite[26,27], we found that the scoring confidence index[28] for the decoys with a negative energy of ubiquitylated-RALA–EXO84 simulation is 0.025, indicating that a good binding conformation is unlikely to be identified. The same index for ubiquitylated-RALA–SEC5 is 0.314, indicating that further modelling is required (Fig. 2i). To isolate a possible docking solution for the ubiquitylated-RALA–SEC5 complex, we generated a number of higher-quality decoys for Lys-47-ubiquitylated RALA with and without SEC5-RBD. Assuming that SEC5 binding does not change ubiquitin position significantly, we cross-
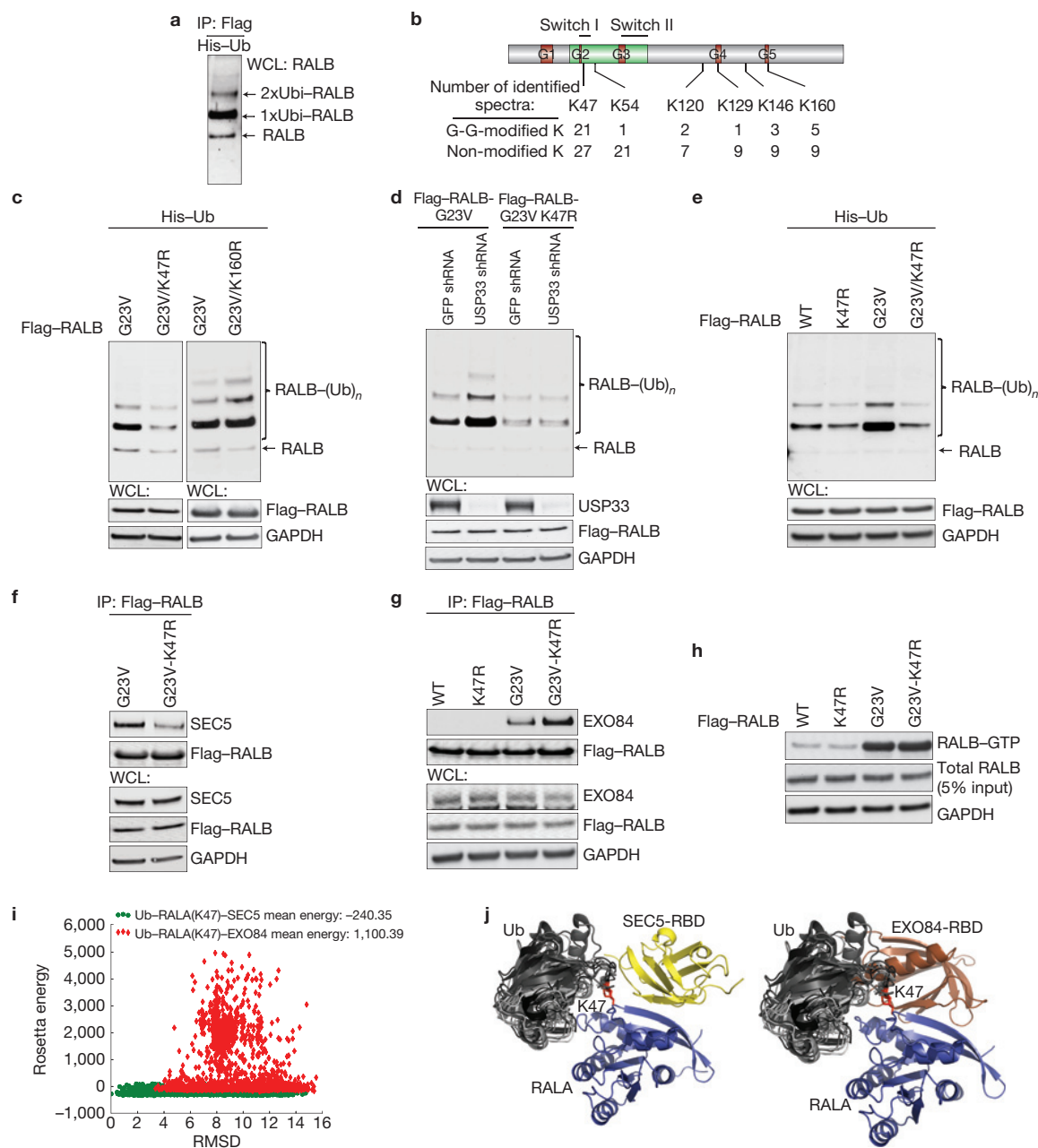
Figure 2 Ubiquitylation of RALB at Lys 47 determines a choice of RALB to interact with SEC5 or EXO84. (**a**) Tandem affinity purification of ubiquitylated RALB. 6xHis–ubiquitin and Flag–RALB-G23V were co-transfected into HEK293T cells, and ubiquitylated RALB was purified using anti-Flag resin followed by Co^{2+} metal affinity chromatography. Isolated RALB was visualized by immunoblotting using anti-RALB antibody. (**b**) RALB undergoes ubiquitylation on multiple sites. Schematic diagram of the RALB domains (upper panel). RALB ubiquitylation sites were identified in two independent tandem mass spectrometry analyses with a total coverage of 63% of the RALB amino acid sequence (Supplementary Fig. S4a). The major identified ubiquitylation sites, Lys 47 and Lys 160, are located in the effector-interacting domain (green) and the G5 box (red), respectively. (**c**) Substitution of arginine for lysine at position 47 significantly inhibits ubiquitylation of RALB. (**d**) USP33 regulates RALB ubiquitylation at Lys 47. (**e**) The GTP–GDP status of RALB affects RALB ubiquitylation at Lys 47. For **c**–**e**, 6xHis-tagged ubiquitin and the indicated RALB mutants were introduced into HEK293T cells expressing GFP shRNA or USP33 shRNA. Ubiquitylated RALB was purified by Co^{2+} metal affinity chromatography and detected by antibodies specific to RALB. WT, wild type. (**f**) Lack of ubiquitylation at Lys 47 inhibits RALB binding

to SEC5. The indicated Flag-tagged RALB mutants were overexpressed in HEK293T cells and then immunoprecipitated with anti-Flag (M2) agarose followed by immunoblotting using anti-SEC5 antibody. (**g**) Ubiquitylation at Lys 47 impairs RALB binding to EXO84. Flag-tagged RALB mutants were overexpressed in HEK293T cells and then immunoprecipitated with anti-Flag (M2) agarose followed by immunoblotting using anti-EXO84 antibody. (**h**) Ubiquitylation at Lys 47 does not affect RALB activity. The activity of RALB mutants was determined by a RALBP1–RBD binding assay. (**i**) The Rosetta v3 protocol described in ref. 26 was used for ubiquitin-docking simulations. The plot represents the energies of the produced decoys distributed by the root-mean-square deviation (RMSD) of ubiquitin position relative to RALA from an arbitrarily chosen decoy. (**j**) Rosetta modelling of ubiquitylated-RALA–SEC5-RBD and ubiquitylated-RALA–EXO84-RBD complexes. Superposition of the top ten refined solutions of ubiquitylated-RALA–SEC5-RBD complex, selected by combined scores of two independent docking simulations of ubiquitylated-RALA–SEC5-RBD and ubiquitylated-RALA (left). Simulated ubiquitin positions linked to Lys 47 of RALA were combined with the RALA–EXO84 complex (right). Uncropped images of blots are shown in Supplementary Fig. S7.
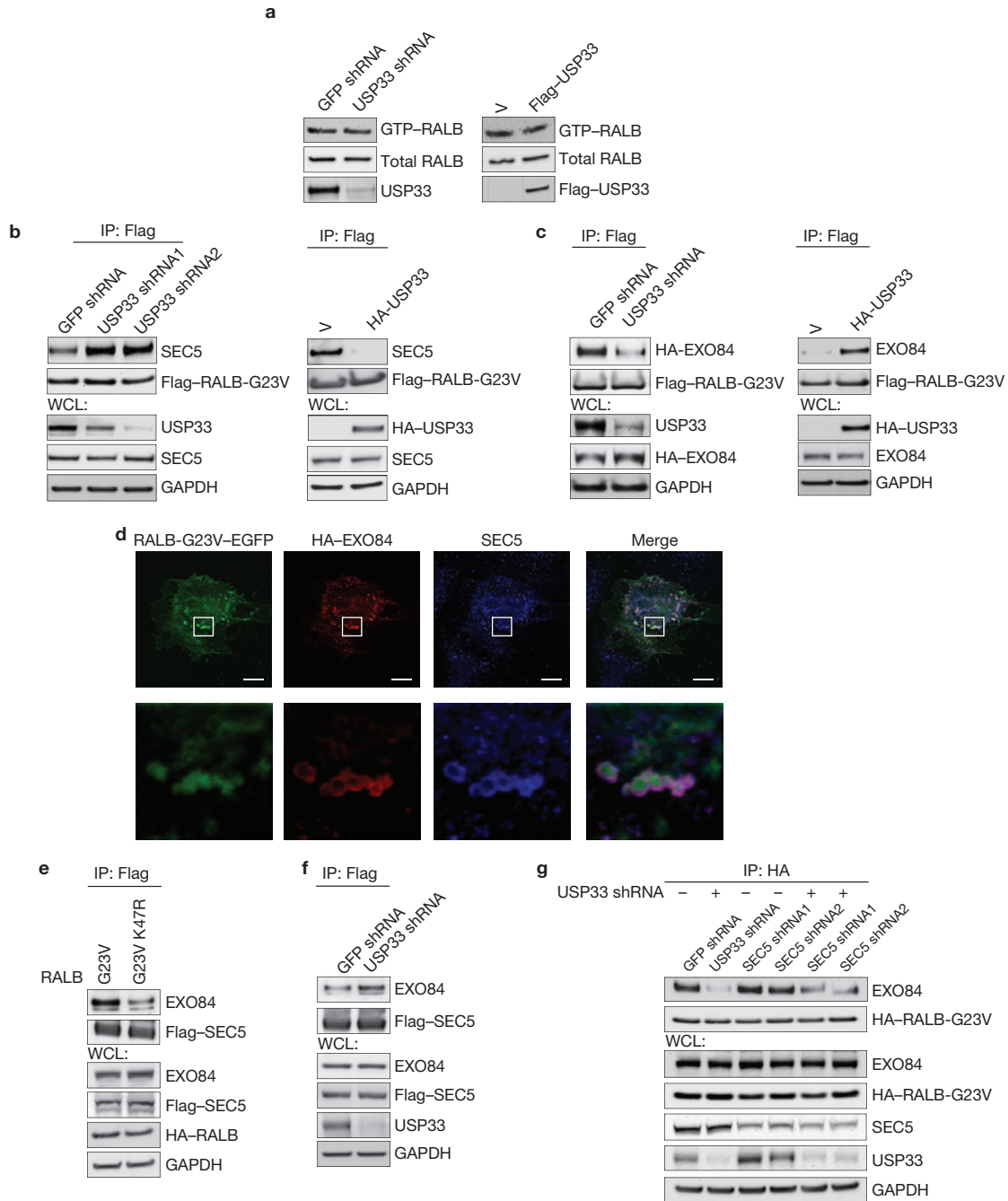
Figure 3 USP33 modulates interactions between RALB and the exocyst proteins by regulating RALB ubiquitylation at Lys 47. (**a**) USP33 does not affect RALB activity. The activity of RALB was determined in HEK293T cells expressing GFP shRNA or USP33 shRNA and empty vector (V) or HA-tagged USP33 by RALBP1–RBD binding assay. (**b**) USP33 modulates interaction between RALB and SEC5. Flag-tagged RALB was overexpressed in HEK293T cells expressing GFP shRNA, USP33 shRNA, empty vector (V) or HA-tagged USP33. The indicated proteins were then immunoprecipitated with anti-Flag (M2) agarose followed by immunoblotting using anti-Flag or anti-SEC5 antibodies. (**c**) USP33 regulates RALB binding to EXO84. Flag-tagged RALB was immunoprecipitated using anti-Flag (M2) agarose from HEK293T cells expressing the indicated constructs. The presence of EXO84 in RALB complexes was analysed by immunoblotting using anti-HA or anti-EXO84 antibody. (**d**) Activated RALB co-localizes with both EXO84 and SEC5. At 24 h after co-transfection with RALB-G23V–EGFP and HA–EXO84, HeLa cells were immunostained with anti-HA and anti-SEC5 antibodies. Scale

bars, 10 μm. The outlined areas are shown at higher magnification in the bottom panels. (**e**) RALB ubiquitylation controls interaction between EXO84 and SEC5. Flag-tagged SEC5 was immunoprecipitated using anti-Flag (M2) agarose from HEK293T cells overexpressing RALB-G23V or RALB-G23V-K47R. The presence of EXO84 in SEC5 complexes was analysed by immunoblotting using anti-EXO84 antibody. (**f**) USP33 regulates EXO84–SEC5 complex formation. Flag-tagged SEC5 was immunoprecipitated using anti-Flag (M2) agarose from HEK293T cells expressing the indicated constructs followed by immunoblotting using anti-EXO84 antibody. (**g**) Suppression of SEC5 affects RALB binding to EXO84. HA-tagged RALB-G23V was immunoprecipitated from HEK293T cells expressing the indicated constructs. The presence of EXO84 in RALB complexes was analysed by immunoblotting using anti-EXO84 antibody. For **a–c,f,g** immunoblotting using antibodies specific for USP33, anti-Flag (M2) or anti-HA determined the levels of USP33 suppression or overexpression. Immunoblot analysis was performed using the indicated antibodies. Uncropped images of blots are shown in Supplementary Fig. S7.

checked the outputs of the simulations. The results suggest a particular position of ubiquitin relative to RALA that allows SEC5 binding but excludes EXO84 binding (Fig. 2j). As the structures of RALA.GMPPNP (ref. 16) and RALB.GMPPNP (ref. 14) are broadly similar, and the residues that interact with effector partners are identical in the RAL proteins, the generated model could be also extrapolated to RALB.

USP33 determines RALB choice of downstream effectors

RALB ubiquitylation at Lys 47 affected both RALB–SEC5 and RALB–EXO84 complex formation but did not affect RALB activity, suggesting that USP33 may regulate interaction between RALB and the exocyst proteins. We corroborated that USP33 expression did not affect the amounts of GTP-bound RALA (Supplementary Fig. S5a) or RALB (Fig. 3a). In consonance with the observation that USP33 suppression did not influence RALA ubiquitylation, we observed no effects of USP33 on the RALA–SEC5 complex formation (Supplementary Fig. S5b). In contrast, USP33 markedly affected interactions between RALB and the exocyst proteins. USP33 overexpression inhibited the interaction between RALB and SEC5, whereas USP33 KD promoted this interaction (Fig. 3b). The MAPPIT assay confirmed that USP33 modulated the interaction between RALB and SEC5 (Supplementary Fig. S5c). Strikingly, USP33 suppression led to about a fivefold increase in SEC5 binding to RALB, indicating that RALB ubiquitylation significantly facilitates RALB–SEC5 complex formation. On the other hand, USP33 overexpression triggered the interaction between RALB and EXO84, whereas USP33 suppression impaired this interaction (Fig. 3c). Taken together, these results strongly indicate that USP33 switches the balance between RALB–SEC5 and RALB–EXO84 complex formation.

Nonetheless, steric inhibition of the interaction between ubiquitylated RALB and EXO84 only partially explains why binding of EXO84 to RALB is abolished in USP33 KD cells, because most of the RALB is still present in the non-ubiquitylated form (Supplementary Fig. S4b,c). Although we did not reveal any redistribution of RALB (Supplementary Fig. S6a) in USP33-depleted cells, we found significant co-localization of EXO84, SEC5 and RALB (Fig. 3d and Supplementary Fig. S6b). This suggests that EXO84 and SEC5 compete for the same intracellular pool of RALB, whereas their interactions with RALB could promote the assembly of specific exocyst subcomplexes.

Given that EXO84 and SEC5 directly interact with each other[5], we examined how RALB ubiquitylation affects EXO84–SEC5 complex formation. We found that overexpression of the RALB-G23V-K47R mutant, which preferentially binds to EXO84 (Fig. 2g), inhibits the interaction between EXO84 and SEC5 (Fig. 3e). In contrast, USP33 suppression, which blocks RALB–EXO84 binding but facilitates RALB–SEC5 interaction, triggered SEC5–EXO84 complex formation (Fig. 3b,f). This suggests that RALB–SEC5 interaction induced by RALB ubiquitylation could additionally hinder EXO84 binding to RALB by sequestering EXO84 to the SEC5-containing exocyst subcomplexes. In fact, suppression of SEC5 (Supplementary Fig. S2c) partially rescued EXO84–RALB interaction, which is completely abolished in USP33-depleted cells (Fig. 3g).

Together, these results imply a two-level model for USP33-mediated regulation of EXO84–RALB interactions, in which RALB ubiquitylation not only sterically excludes binding to EXO84 but also hampers direct RALB–EXO84 interactions by triggering its sequestration to the SEC5-containing subcomplexes.

RALB ubiquitylation at Lys 47 promotes TBK1–IRF3 signalling

Our results suggest that USP33 coordinates the assembly of specific exocyst subcomplexes by regulating RALB ubiquitylation, whereas the differential interaction between RALB and the exocyst proteins has been proposed to represent a regulatory hub through bifurcating activation of TBK1 and beclin-1–VPS34 (refs 10,11). Therefore, we next assessed whether USP33 controls this regulatory hub.

Consistent with our observation that suppression of USP33 facilitated RALB binding to SEC5, we found that TBK1–SEC5 interaction was markedly increased in USP33 KD cells (Fig. 4a). Remarkably, treatment with polyinosine–polycytidylic acid (poly(I:C)), a synthetic analogue of viral dsRNA (ref. 29), triggered accumulation of ubiquitylated RALB (Fig. 4b). Poly(I:C)-induced RALB ubiquitylation led to accumulation of SEC5–RALB complexes (Fig. 4c) and increased phosphorylation of both TBK1 and IRF3 (Fig. 4d). In contrast, such effects were significantly suppressed in cells overexpressing the RALB-G23V-K47R mutant, suggesting that RALB ubiquitylation is essential to regulate IRF3 activation (Fig. 4c,d). These results suggest that viral infection triggers RALB ubiquitylation that, in turn, promotes SEC5–TBK1 complex formation and IRF3 activation.

USP33 triggers the assembly of RALB–EXO84–beclin-1 complexes in response to nutrient deprivation

Recently, it has been shown that under nutrient-rich growth conditions RALB facilitates SEC5–beclin-1 complex formation, while blocking EXO84–beclin-1 complex assembly. In contrast, nutrient deprivation drives the assembly of RALB–EXO84–beclin-1 complexes[11]. Thus, we examined whether USP33 regulates SEC5–beclin-1 and EXO84–beclin-1 complex formation. Consistent with our observation that USP33 KD resulted in the accumulation of RALB–SEC5 complexes, USP33 KD also promoted interactions between SEC5 and beclin 1 (Fig. 5a–d). On the other hand, overexpression of USP33 mediated the assembly of EXO84–beclin-1 complexes, whereas the introduction of a catalytically inactive USP33-C194S-H683Q mutant[30] did not have any effect on EXO84–beclin-1 complex formation (Fig. 5e).

These data suggest that nutrient deprivation should trigger RALB deubiquitylation. Indeed, whereas nutrient deprivation did not change ubiquitylation levels of RALA, we found a marked decrease in RALB ubiquitylation on nutrient starvation (Fig. 5f,g). Remarkably, nutrient deprivation did not affect ubiquitylation levels of the RALB-K47R mutant, suggesting that nutrient starvation triggers RALB deubiquitylation at Lys 47.

To gain insights into the mechanisms underlying RALB deubiquitylation on nutrient deprivation, we assessed USP33 expression and sub-cellular localization under nutrient-poor growth conditions. Immunoblot analysis of USP33 expression revealed that nutrient starvation led to accumulation of endogenous USP33 (Fig. 5h). Consistent with a recent report[31], analysis of USP33–mCherry subcellular distribution revealed conspicuous localization of USP33 in perinuclear structures in the absence of nutrient deprivation. We did not observe marked co-localization of RALB and USP33 under nutrient-rich conditions. On starvation, we observed redistribution of USP33 throughout the cell body. Most RALB-positive vesicular structures became surrounded and co-labelled with USP33 (Fig. 5i).

A recent report has demonstrated that on nutrient withdrawal RALB is recruited to sites of nascent autophagosome formation
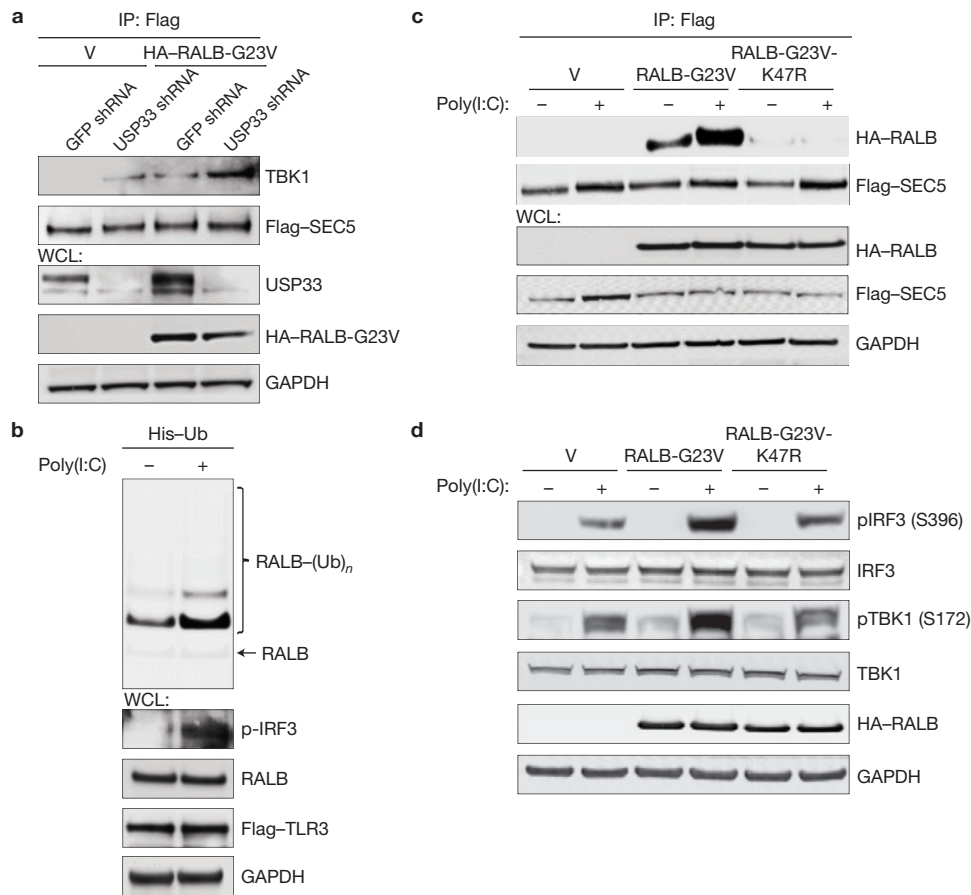
Figure 4 RALB ubiquitylation at Lys 47 activates the TBK1 pathway.
(**a**) Suppression of USP33 facilitates TBK1–SEC5 complex formation.
Flag-tagged SEC5 was introduced into HEK293T cells expressing empty
vector (V) or HA-tagged RALB-G23V together with GFP shRNA or USP33
shRNA as indicated, and then immunoprecipitated with anti-Flag (M2)
agarose followed by immunoblotting using antibody specific for TBK1.
(**b**) RALB undergoes ubiquitylation in response to poly(I:C) treatment. At
48 h after introduction of 6xHis-tagged ubiquitin and Flag–RALB-G23V,
293-hTLR3 cells were treated with $10\,\mu g\,ml^{-1}$ of poly(I:C) for 6 h.
Ubiquitylated RALB was purified by Co^{2+} metal affinity chromatography
and detected by immunoblotting using anti-RALB antibody. (**c**) RALB

ubiquitylation at Lys 47 is crucial for formation of the RALB–SEC5 complex
in response to poly(I:C) treatment. Flag-tagged SEC5 and the indicated
HA-tagged RALB mutants were introduced into 293-hTLR3 cells. At
48 h after transfection cells were treated $100\,\mu g\,ml^{-1}$ of poly(I:C) for
6 h. Flag-tagged SEC5 was immunoprecipitated with anti-Flag (M2), and
analysed for co-precipitation by immunoblotting using anti-HA antibody.
(**d**) RALB ubiquitylation at Lys 47 affects activation of TBK1 and IRF3.
At 48 h after transfection with empty vector (V), Flag–RALB-G23V and
Flag–RALB-G23V–K47R, 293-hTLR3 cells were treated with $10\,\mu g\,ml^{-1}$ of
poly(I:C) for 6 h. Immunoblot analysis was performed using the indicated
antibodies. Uncropped images of blots are shown in Supplementary Fig. S7.

as it is co-localized with beclin 1, ATG5 and LC3 punctae[11].
Consistently, we found marked co-localization of USP33–mCherry
and beclin-1–HA (Fig. 5j). These combined observations indicate that
nutrient deprivation triggers accumulation and relocalization of USP33
to RALB-containing vesicles that results in RALB deubiquitylation and
the assembly of RALB–EXO84–beclin-1 complexes, suggesting that
USP33 plays an essential role in autophagy regulation.

USP33 controls autophagy by regulating RALB deubiquitylation

We next examined the role of USP33 in nutrient-starvation-induced
autophagy. We analysed the conversion of the autophagy marker
light chain 3 (LC3) to the lower migrating phosphatidylethanolamine-
conjugated LC3 form (LC3-II). In consonance with the observation that
depletion of USP33 switches the balance towards RALB–SEC5–beclin-1
complexes, we found that USP33 KD inhibited accumulation of
LC3–lipid conjugates under both nutrient-rich and nutrient-starved

conditions (Fig. 6a). This inhibition is probably associated with a
decreased autophagic flux as we observed decreased levels of LC3-II in
USP33-depleted cells in the presence of chloroquine, an inhibitor of
autophagosome turnover (Fig. 6a).

Immunostaining of endogenous LC3 also revealed that USP33 deple-
tion significantly impaired both LC3 puncta formation, whereas overex-
pression of a USP33-shRNA-resistant form of USP33 (Supplementary
Fig. S2b) in USP33-depleted cells completely rescued this phenotype
(Fig. 6b–d). In contrast, USP33 overexpression resulted in accumula-
tion of LC3 puncta even in the absence of nutrient limitation, suggesting
that USP33 overexpression is sufficient to increase the autophagic flux
(Fig. 6b–d). We also found accumulation of the autophagy substrate of
p62 (SQSTM1) in USP33-depleted cells (Fig. 6e). Taken together, these
data strongly suggest a role for USP33 in the control of autophagy.

To further confirm the role of RALB ubiquitylation in
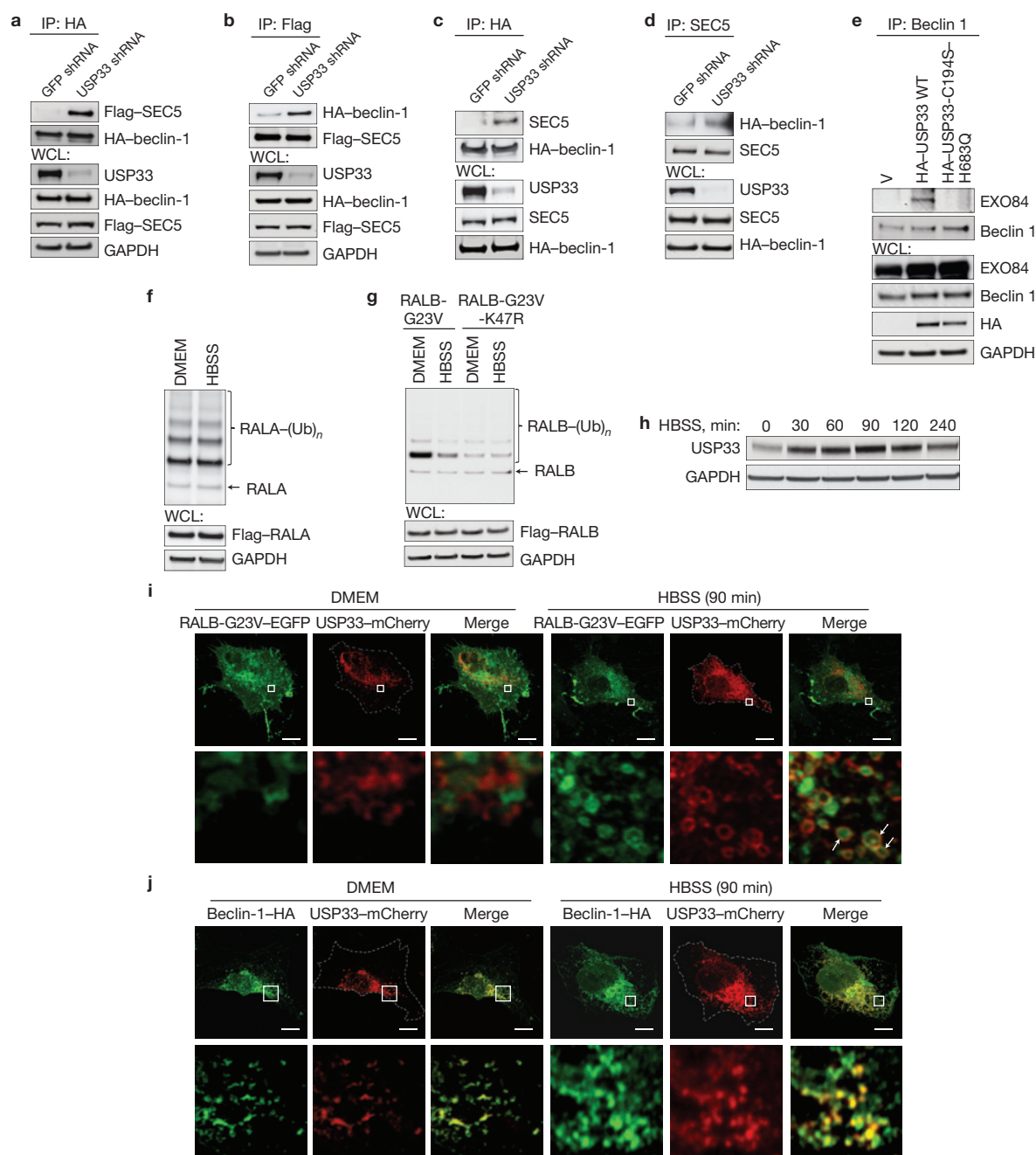autophagocytosis, we assessed how overexpression of the RALB-G23V

Figure 5 USP33 triggers RALB–EXO84–beclin-1 complex formation in response to nutrient starvation. (**a**–**d**) USP33 inhibits assembly of SEC5–beclin-1 complexes. The indicated proteins were immunoprecipitated from cells expressing GFP shRNA or USP33 shRNA with anti-Flag (M2), anti-HA or anti-SEC5 antibody and analysed for co-precipitation by immunoblotting using specific antibodies as indicated. (**e**) USP33 potentiates the interaction between EXO84 and beclin 1. Endogenous beclin 1 was immunoprecipitated from HEK293T cells, expressing either empty vector (V), HA–USP33 wild type (WT) or the catalytically inactive mutant C194S-H683Q, using anti-beclin 1 antibody. Immunoprecipitates were analysed for co-precipitation by immunoblotting using anti-EXO84 or anti-beclin 1 antibodies. (**f**,**g**) RALB but not RALA undergoes deubiquitylation under nutrient deprivation. 6xHis-tagged ubiquitin and the indicated RAL mutants were overexpressed in HEK293T cells. At 48 h after transfection cells were deprived of nutrients and incubated in Hank's buffered salt solution (HBSS) medium for 90 min. Ubiquitylated RAL proteins were purified by Co^{2+} metal affinity chromatography and analysed by immunoblotting using anti-RALA or anti-RALB antibodies. (**h**) Nutrient starvation results in the accumulation of USP33. HEK TE cells were incubated in HBSS medium for the indicated periods of time. Immunoblotting was performed using anti-USP33 antibody. (**i**) USP33 co-localizes with RALB-positive vesicles in the absence of nutrients. At 48 h after co-transfection with RALB-G23V–EGFP and USP33–mCherry, HeLa cells were incubated in HBSS medium for 90 min. Cells were imaged for EGFP and mCherry fluorescence. Scale bars, 10 μm. The outlined areas are shown at higher magnification in the bottom panels. Arrows indicate USP33 co-localization to RALB-positive vesicles. (**j**) Beclin 1 co-localizes with USP33. HeLa cells were transfected with beclin-1–HA and USP33–mCherry. At 48 h after transfection, cells were incubated in HBSS medium for 90 minutes and treated as in **i**. Scale bars, 10 μm. The outlined areas are shown at higher magnification in the bottom panels. Uncropped images of blots are shown in Supplementary Fig. S7.
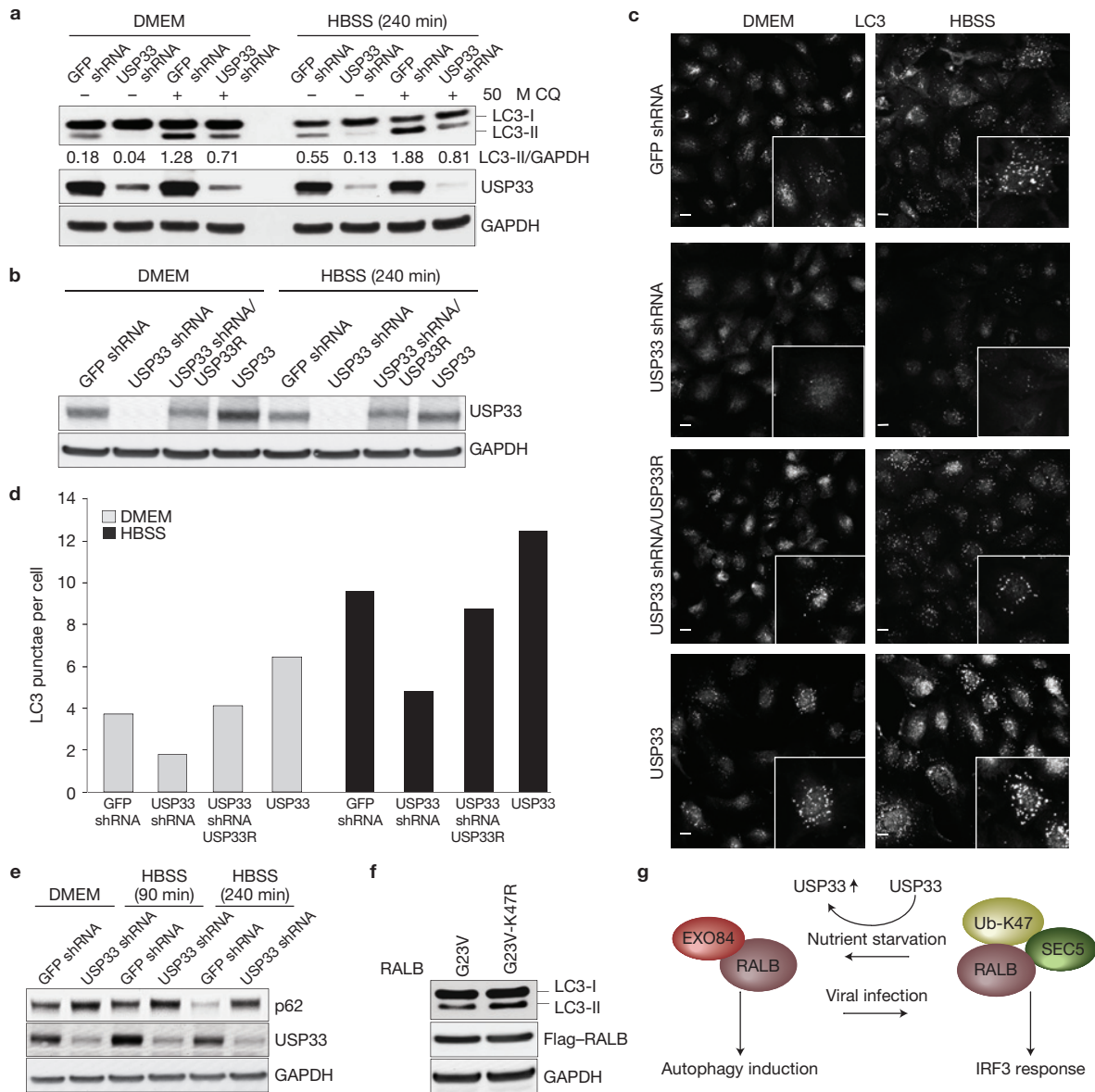
Figure 6 USP33 regulates autophagy. (**a**) USP33 depletion inhibits accumulation of LC3–lipid conjugates. HEK TE cells stably expressing GFP shRNA or USP33 shRNA were incubated with DMEM or HBSS medium for 4 h, in the presence or absence of $50\,\mu M$ of chloroquine (CQ). Cells were then assayed for the relative accumulation of LC3-I and LC3-II by immunoblotting analysis using anti-LC3 antibody. LC3-II/GAPDH ratios have been calculated using ImageJ densitometric analysis. (**b–d**) USP33 expression levels affect the accumulation of LC3 punctae. Wild-type USP33 or a USP33-shRNA-resistant USP33 mutant (USP33R) was introduced into HEK TE cells stably expressing GFP shRNA or USP33 shRNA. The generated cells were incubated in HBSS medium for 4 h. USP33 was analysed by immunoblotting using anti-USP33 antibody (**b**). Representative images of LC3 immunostaining are shown (**c**). Endogenous LC3 punctae were quantified using the In Cell Analyser 2000 automatic imaging system and IN Cell Investigator software. The mean distribution of LC3 punctae per cell is represented as the mean of two independent experiments. Statistics source data for **d**

can be found in Supplementary Table S1 (**d**). (**e**) USP33 depletion leads to increased levels of p62. HEK TE cells expressing GFP shRNA or USP33 shRNA were incubated in HBSS medium for the indicated periods of time. Immunoblotting was performed using the indicated antibodies. (**f**) Overexpression of the RALB-G23V-K47R mutant leads to accumulation of LC3–lipid conjugates. HEK293T cells overexpressing the RALB-G23V or RALB-G23V-K47R mutants were assayed for the relative accumulation of LC3-I and LC3-II by immunoblotting using anti-LC3 antibody. (**g**) Ubiquitylation of RALB at Lys 47 determines a choice of specific pathways to mediate particular cellular functions. dsRNA, mimicking viral infection, triggers ubiquitylation of RALB. RALB ubiquitylated at Lys 47 preferentially binds SEC5 that drives SEC5–TBK1 complex formation and activation of IRF3 signalling. In contrast, nutrient deprivation induces stabilization and relocalization of USP33 that deubiquitylates RALB at Lys 47. Deubiquitylation of RALB mediates assembly of the RALB–EXO84–beclin-1 complex that initiates autophagy. Uncropped images of blots are shown in Supplementary Fig. S7.

or RALB-G23V-K47R mutants affects the amount of LC3-II. Although RALB-G23V expression induces autophagy[11], we found that overexpression of the RALB-G23V-K47R mutant led to further

accumulation of phosphatidylethanolamine-conjugated LC3 (Fig. 6f), indicating that both GTP binding and deubiquitylation at Lys 47 are essential to trigger autophagosome formation.

DISCUSSION

As for all members of the GTPase family, RAL proteins cycle between the active GTP- and inactive GDP-bound states. The cycling between the GDP- and GTP-bound forms is regulated by guanine nucleotide exchange factors and GTPase-activating proteins (GAPs). A recent study revealed that K-RAS monoubiquitylation at Lys 147, which is located within the conserved guanine-nucleotide-binding motif, disrupts regulation of RAS by GAPs that leads to the increased amount of the GTP-bound form and enhanced ability to bind its downstream effectors, PI3K and Raf (ref. 28). We also observed ubiquitylation of RALB at Lys 160, which corresponds to Lys 147 of K-RAS, suggesting that reversible ubiquitylation of RALB at Lys 160 could also promote RALB activity.

Once activated, RALB GTPase exerts its effects through activation of downstream effectors, EXO84 and SEC5. Previous reports demonstrated that the binding sites for EXO84 and SEC5 on RAL GTPases are partially overlapping and that both effectors compete for interaction with RAL proteins *in vitro*[13–16]. Here we describe ubiquitylation at Lys 47 as a crucial regulator of RALB substrate specificity towards exocyst proteins. Our findings are consistent with a model in which GTP binding is crucial to turn on RALB activity, whereas RALB ubiquitylation at Lys 47 serves to tune its activity towards a particular effector. A higher affinity of USP33 to a GDP-bound form of RALB may explain why RALB ubiquitylation at Lys 47 and GTP binding are coupled together. It is possible that, on GTP hydrolysis, GDP-bound ubiquitylated RALB could be more efficiently deubiquitylated by USP33.

Ubiquitylation of RALB at Lys 47, which is located within the RALB effector-binding domain, sterically hinders RALB–EXO84 interaction but promotes the assembly of RALB–SEC5 complexes. It has been predicted that SEC5 is composed of α-helical bundles[32], which are often present in ubiquitin-binding domains[33], suggesting that ubiquitin may provide additional surface area for ubiquitylated-RALB–SEC5 interaction. Enhanced RALB binding to SEC5 mediated by RALB ubiquitylation also triggers EXO84 sequestration to the SEC5-containing subcomplexes that further impedes direct RALB–EXO84 interaction.

By controlling RALB ubiquitylation at Lys 47, USP33 provides a regulatory switch to coordinate RALB cellular functions (Fig. 6g). Virus infection stimulates RALB ubiquitylation and formation of the RALB–SEC5–TBK1 complexes leading to activation of the innate immunity signalling kinase TBK1 and the subsequent IRF3 activation. In contrast, nutrient starvation triggers RALB deubiquitylation that, in turn, mediates formation of RALB–EXO84–beclin-1 complexes and induction of autophagy. We can speculate that viral infection and nutrient starvation may modulate the activity of either RALB-specific ubiquitin ligases or USP33 to promote respectively ubiquitylation or deubiquitylation of RALB. In concordance with this idea, we found that nutrient deprivation triggers accumulation and relocalization of USP33 to RALB-containing vesicles. However, further investigation is required to uncover the mechanisms regulating the activity of USP33 or RALB-specific ubiquitin ligases in response to diverse stimuli.

Our results suggest that the binding specificity of the small GTPases could be regulated by ubiquitylation within the effector-binding domain. These data strongly indicate that, in addition to guanine nu-cleotide exchange factors or GAPs, ubiquitylation or deubiquitylation of the RAL GTPases by specific E3 ubiquitin ligases and deubiquitylases seems to play a crucial role in pertaining specificity of the RAL signalling. Further studies are necessary to identify E3 ligases and deubiquitylases responsible for ubiquitylation or deubiquitylation of the RAL proteins and to elucidate their contribution to regulation of the RAL signalling pathways. □

METHODS

Methods and any associated references are available in the online version of the paper.

AUTHOR CONTRIBUTIONS

M.S. and A.A.S. conceived of the study. M.S. performed most of the experiments; S.L. and J.T. designed and performed the MAPPIT screen; M.L. and K.G. performed the mass spectrometry analysis; D.G. and S.V.S. carried out the Rosetta docking; P.K. and M.F.B. assisted with the fluorescence microscopy. V.N.A. assisted with ubiquitylation experiments. A.A.S. wrote the manuscript. All authors discussed results and commented on the manuscript.

COMPETING FINANCIAL INTERESTS
The authors declare no competing financial interests.

1. Colicelli, J. Human RAS superfamily proteins and related GTPases. *Sci. STKE* **2004**, re13 (2004).
2. Bodemann, B. O. & White, M. A. Ral GTPases and cancer: linchpin support of the tumorigenic platform. *Nat. Rev. Cancer* **8**, 133–140 (2008).
3. Feig, L. A. Ral-GTPases: approaching their 15 minutes of fame. *Trends Cell Biol.* **13**, 419–425 (2003).
4. Moskalenko, S. *et al.* The exocyst is a Ral effector complex. *Nat. Cell Biol.* **4**, 66–72 (2002).
5. Moskalenko, S. *et al.* Ral GTPases regulate exocyst assembly through dual subunit interactions. *J. Biol. Chem.* **278**, 51743–51748 (2003).
6. Sugihara, K. *et al.* The exocyst complex binds the small GTPase RalA to mediate filopodia formation. *Nat. Cell Biol.* **4**, 73–78 (2002).
7. Chen, X. W., Leto, D., Chiang, S. H., Wang, Q. & Saltiel, A. R. Activation of RalA is required for insulin-stimulated Glut4 trafficking to the plasma membrane via the exocyst and the motor protein Myo1c. *Dev. Cell* **13**, 391–404 (2007).
8. Nozaki, S., Ueda, S., Takenaka, N., Kataoka, T. & Satoh, T. Role of RalA downstream of Rac1 in insulin-dependent glucose uptake in muscle cells. *Cell Signal.* **24**, 2111–2117 (2012).
9. Kashatus, D. F. *et al.* RALA and RALBP1 regulate mitochondrial fission at mitosis. *Nat. Cell Biol.* **13**, 1108–1115 (2011).
10. Chien, Y. *et al.* RalB GTPase-mediated activation of the IkappaB family kinase TBK1 couples innate immune signaling to tumor cell survival. *Cell* **127**, 157–170 (2006).
11. Bodemann, B. O. *et al.* RalB and the exocyst mediate the cellular starvation response by direct activation of autophagosome assembly. *Cell* **144**, 253–267 (2011).
12. Shi, C. S. *et al.* Activation of autophagy by inflammatory signals limits IL-1beta production by targeting ubiquitinated inflammasomes for destruction. *Nature Immunol.* **13**, 255–263 (2012).
13. Fenwick, R. B. *et al.* The RalB-RLIP76 complex reveals a novel mode of ral-effector interaction. *Structure* **18**, 985–995 (2010).
14. Fenwick, R. B. *et al.* Solution structure and dynamics of the small GTPase RalB in its active conformation: significance for effector protein binding. *Biochemistry* **48**, 2192–2206 (2009).
15. Jin, R. *et al.* Exo84 and Sec5 are competitive regulatory Sec6/8 effectors to the RalA GTPase. *EMBO J.* **24**, 2064–2074 (2005).
16. Nicely, N. I., Kosak, J., de Serrano, V. & Mattos, C. Crystal structures of Ral-GppNHp and Ral-GDP reveal two binding sites that are also present in Ras and Rap. *Structure* **12**, 2025–2036 (2004).

17. Eyckerman, S. *et al.* Design and application of a cytokine-receptor-based interaction trap. *Nat. Cell Biol.* **3,** 1114–1119 (2001).

18. Lievens, S., Peelman, F., De Bosscher, K., Lemmens, I. & Tavernier, J. MAPPIT: a protein interaction toolbox built on insights in cytokine receptor signaling. *Cytokine Growth Factor Rev.* **22,** 321–329 (2011).

19. Lievens, S. *et al.* Array MAPPIT: high-throughput interactome analysis in mammalian cells. *J. Proteome Res.* **8,** 877–886 (2009).

20. Lievens, S., Vanderroost, N., Defever, D., Van der Heyden, J. & Tavernier, J. ArrayMAPPIT: a screening platform for human protein interactome analysis. *Methods Mol. Biol.* **812,** 283–294 (2012).

21. Brymora, A., Valova, V. A., Larsen, M. R., Roufogalis, B. D. & Robinson, P. J. The brain exocyst complex interacts with RalA in a GTP-dependent manner: identification of a novel mammalian Sec3 gene and a second Sec15 gene. *J. Biol. Chem.* **276,** 29792–29797 (2001).

22. Neyraud, V. *et al.* RalA and RalB proteins are ubiquitinated GTPases, and ubiquitinated RalA increases lipid raft exposure at the plasma membrane. *J. Biol. Chem.* **287,** 29397–29405 (2012).

23. Li, Z. *et al.* Identification of a deubiquitinating enzyme subfamily as substrates of the von Hippel-Lindau tumor suppressor. *Biochem. Biophys. Res. Commun.* **294,** 700–709 (2002).

24. Li, Z. *et al.* Ubiquitination of a novel deubiquitinating enzyme requires direct binding to von Hippel-Lindau tumor suppressor protein. *J. Biol. Chem.* **277,** 4656–4662 (2002).

25. Fukai, S., Matern, H. T., Jagath, J. R., Scheller, R. H. & Brunger, A. T. Structural basis of the interaction between RalA and Sec5, a subunit of the sec6/8 complex. *EMBO J.* **22,** 3267–3278 (2003).

26. Baker, R. *et al.* Site-specific monoubiquitination activates Ras by impeding GTPase-activating protein function. *Nat. Struct. Mol. Biol.* **20,** 46–52 (2013).

27. Leaver-Fay, A. *et al.* ROSETTA3: an object-oriented software suite for the simulation and design of macromolecules. *Methods Enzymol.* **487,** 545–574 (2011).

28. Zavodszky, M. I., Stumpff-Kane, A. W., Lee, D. J. & Feig, M. Scoring confidence index: statistical evaluation of ligand binding mode predictions. *J. Comput. Aided Mol. Des.* **23,** 289–299 (2009).

29. Chien, Y. & White, M. A. Characterization of RalB–Sec5–TBK1 function in human oncogenesis. *Methods Enzymol.* **438,** 321–329 (2008).

30. Shenoy, S. K. *et al.* Beta-arrestin-dependent signaling and trafficking of 7-transmembrane receptors is reciprocally regulated by the deubiquitinase USP33 and the E3 ligase Mdm2. *Proc. Natl Acad. Sci. USA* **106,** 6650–6655 (2009).

31. Thorne, C., Eccles, R. L., Coulson, J. M., Urbe, S. & Clague, M. J. Isoform-specific localization of the deubiquitinase USP33 to the Golgi apparatus. *Traffic* **12,** 1563–1574 (2011).

32. Croteau, N. J., Furgason, M. L., Devos, D. & Munson, M. Conservation of helical bundle structure between the exocyst subunits. *PloS One* **4,** e4443 (2009).

33. Dikic, I., Wakatsuki, S. & Walters, K.J. Ubiquitin-binding domains—from structures to functions. *Nat. Rev. Mol. Cell Biol.* **10,** 659–671 (2009).

METHODS

MAPPIT screen. Microtitre plates for the ArrayMAPPIT screen containing prey and reporter reverse transfection mixtures were prepared as described previously[20]. Each of the preys was present on the plates in 4 replicates. The prey collection screened in this report corresponds to a subset of close to 10,000 full-length human ORF preys selected from the human ORFeome collection version 5.1 (http://horfdb.dfci.harvard.edu/hv5/). The screen for RALA-G23V-interacting preys was performed as described previously[20]. Briefly, HEK293T cells were transfected in bulk with the pCLG–RALA–G23V bait-expressing plasmid, and 24 h after transfection, cells were plated to the array screening plates. Twenty-four hours later, duplicate wells were supplemented with medium with or without 100 ng ml^{-1} leptin, and 24 h after stimulation, luciferase activity was measured. MAPPIT signals were calculated as the ratio between the average values of the two leptin-stimulated and the two unstimulated samples. Preys were ranked according to MAPPIT signal intensity and within-experiment variation applying a one-sided balanced test[34].

Cell culture and lentiviral transduction. 293-hTLR3 cells (Invivogen), HeLa cells (ATCC), human embryonic kidney cells immortalized by stable expression of SV40 LT antigen and hTERT (HEK TE), and HEK293T cells (a gift from W. Hahn, DFCI) were cultured in Dulbecco's modified Eagle's medium supplemented with 10% FBS and penicillin/streptomycin. All cells were tested for mycoplasma contamination every two weeks using a Mycoplasma Detection Kit (Lonza). Transient transfections were performed using Lipofectamine LTX (Life Technologies) or XtremeGene9 (Roche). Lentiviral infections were performed as described previously[35].

Plasmids. Lentiviral pLA–CMV–Flag and pLA–CMV–HA vectors were used to generate Flag/HA-tagged constructs. The pLKO.1–puro–GFP-shRNA, pLKO.1–puro–luciferase-shRNA and pLKO.1–puro vectors containing shRNAs targeting USP33, USP20 or SEC5 (Sigma-Aldrich) were tested as described in Supplementary Figs S2 and S3. A shRNA-resistant silent mutant of USP33 was generated as described in Supplementary Fig. S2b. Complementary DNA of RALA (#71078), RALB (#661), RALBP1 (#2384) and EXO84 (#10122) originated from the Orfeome collection (DFCI). SEC5 cDNA (sc111916) was from Origene; Flag–TLR3 (#13084), pcDNA4–beclin-1–HA (#24399) and Flag–HA–USP20 (#22573) were from Addgene. For MAPPIT experiments, the RAL baits without the carboxy-terminal CCIL motif were cloned into the pCLG vector; full-length cDNAs of preys were subcloned into the pMG2 vector. For GST pulldown, wild-type RALs without the C-terminal CCIL motif were subcloned into the pGEX-2T4 vector. The pMT107–6xHis–ubiquitin plasmid was a generous gift from D. Bohmann (University of Rochester, USA). pcDNA3–HA–Usp33–C214S-H683Q plasmid was a generous gift from S. K. Shenoy (Duke University, USA). Point mutations were introduced by using site-directed mutagenesis.

Antibodies. Antibodies were from commercial sources: mouse monoclonal anti-Flag (Sigma-Aldrich, M2), anti-USP33 (Sigma-Aldrich, 5B5), anti-TBK1 (Imgenex, 108A429), anti-beclin 1 (Cell Signaling, 2A4), anti-RALB (Millipore, 25), anti-RALA (BD Biosciences, 8/RALA), anti-GAPDH (Sigma-Aldrich, GAPDH-71.1); rabbit monoclonal anti-beclin 1 (Cell Signaling, D40C5), anti-phospho-IRF3 (S396; Cell Signaling, 4D4G), anti-IRF3 (Cell Signaling, D6I4C); anti-p62 (Cell Signaling, D5E2), anti-LC3B (Cell Signaling, D11), anti-phospho-TBK1 (S172; Cell Signaling, D52C2); rat monoclonal anti-HA tag (Roche, 3F10); rabbit polyclonal anti-DYKDDDDK (Cell Signaling), anti-HA (Abcam), anti-USP33 (Bethyl Laboratories), anti-SEC5 (ProteinTech), anti-EXO84 (LifeSpan Biosciences), anti-TBK1 (Cell Signaling), anti-USP20 (Bethyl Laboratories), anti-SEC5 (Sigma-Aldrich) and anti-EXO84 (Sigma-Aldrich). See Supplementary Table S1 for more information on antibodies.

GTS pulldown. BL21 RP *Escherichia coli* cells expressing GST–RALs were resuspended in GST buffer (50 mM Tris, at pH 7.5, 100 mM NaCl, 5 mM β-ME, 10% glycerol and protease inhibitor cocktail (Roche)). After binding to glutathione beads, GST-bound proteins were washed with 10 mM EDTA and incubated with 10 mM GDP or 100 mM GTPγS. GTP/GDP loading was terminated by 50 mM MgCl$_2$. The beads were washed three times with buffer A (20 mM Tris, at pH 7.5, 137 mM NaCl, 1% NP-40, 1 mM MgCl$_2$ and protease inhibitor cocktail (Roche)).

HEK293T cells overexpressing Flag–USP33 were lysed in buffer A, pre-cleared with GST-bound glutathione beads, and then incubated with the GST–RALA or GST–RALB coupled beads. The beads were washed in buffer A, and proteins were subjected to SDS–PAGE and immunoblotted.

RAL activation assay. Cells were lysed in RAL activation buffer (50 mM Tris–HCl, at pH 7.5, 250 mM NaCl, 1% NP-40, 10 mM MgCl$_2$ and 0.5 mM DTT), mixed with RALBP1-RBD agarose (Millipore) and incubated for 30 min at 4 °C. The beads were washed with RAL activation buffer, and proteins were subjected to SDS–PAGE and immunoblotted.

Immunoblotting and immunoprecipitation. Cells were lysed in co-immunoprecipitation buffer (50 mM Tris, at pH 7.5, 137 mM NaCl, 1% NP-40, 5 mM MgCl$_2$, 10% glycerol and protease inhibitor cocktail (Roche)). For detection of ubiquitylated RALB, 50 µMPR-619 (LifeSensors) and 10 mM *N*-ethylmaleimide (Sigma-Aldrich) were added to the lysis buffer.

Tagged proteins were immunoprecipitated with anti-Flag (M2) agarose or anti-HA agarose (Sigma-Aldrich) and then eluted with 3 × Flag or HA peptides. For immunoprecipitation of endogenous proteins, cell lysates were incubated with primary antibodies overnight, and then mixed with protein G-agarose (Roche) or protein A-Sepharose (GE Healthcare) for 1 h. The beads were washed with co-immunoprecipitation buffer, and proteins were then eluted with LDS sample buffer. Image quantification was done using ImageJ software.

Purification of ubiquitylated proteins. HEK293T cells were co-transfected with 6xHis–ubiquitin and Flag–RALs. Ubiquitylated proteins were purified as described previously[22]. Briefly, cells were lysed in co-immunoprecipitation buffer containing EDTA-free protease inhibitor cocktail (Roche). Cell lysates were mixed with His-buffer A (PBS, at pH 8.0, 6 M guanidinium-HCl, 0.1% NP-40 and 1 mM β-ME) at proportion 1:10 and added to TALON beads (Clontech). After binding, the resin was washed with His-buffer B (PBS, at pH 8.0, 0.1% NP-40, 5% glycerol and 20 mM imidazole), and proteins were eluted in LDS sample buffer.

For TAP purification, HEK293T cells were co-transfected with Flag–RALB and 6xHis–ubiquitin. Cell were lysed in RAL activation buffer, and Flag–RALB was immunoprecipitated using anti-Flag (M2) agarose (Sigma-Aldrich), washed twice with lysis buffer, once with buffer containing 50 mM Tris, at pH 7.5, 100 mM LiCl, and eluted with 3xFlag peptide. Ubiquitylated Flag–RALB was then purified using TALON beads (Clontech) as described above.

Mass spectrometry analysis. The RALB-containing beads were washed with 25 mM ammonium bicarbonate, re-suspended in 25 mM (NH$_4$)HCO$_3$ and incubated with trypsin (Promega) for 16 h at 37 °C. The supernatant was dried and peptides were re-dissolved in solvent A (2% acetonitrile and 0.1% trifluoroacetic acid). The peptides were introduced into a liquid chromatography–tandem mass spectrometry system, an Ultimate 3000 RSLC nano (Dionex) in-line connected to an LTQ Orbitrap Velos mass spectrometer (Thermo Fisher Scientific). The sample was loaded on a trapping column, and after back-flushing from the trapping column, on a reverse-phase column (made in-house, 75 µm inner diameter × 150 mm length, 3 µm C18 Reprosil-HD beads, Maisch). Peptides were loaded with solvent A at a flow rate of 10 µl min^{-1}, and separated with a linear gradient from 2% of solvent A′ (0.1% formic acid in 2% acetonitrile) to 50% of solvent B′ (0.1% formic acid in 80% acetonitrile) at a flow rate of 300 nl min^{-1} followed by a steep increase to 100% of solvent B.

The Orbitrap Velos mass spectrometer was operated in data-dependent mode, selecting for the ten most abundant peaks in a mass spectrum. From the tandem mass spectrometry data in each liquid chromatography run, Mascot Generic Files were created using the Mascot Distiller software (version 2.4, Matrix Science). The generated peak lists were searched using Mascot Daemon (version 2.4, Matrix Science) against the Swiss-Prot database (version 2012_10 of UniProtKB/Swiss-Prot protein database). Methionine oxidation, protein amino-terminal acetylation, pyroglutamate formation, and diglycine modification of lysine side chains were set as variable modifications. Mass tolerance on precursor peptide ions was set to ±10 ppm, and on fragment ions to ±0.5 dalton. The peptide charge was set to 1+, 2+ or 3+ and the instrument setting used was ESI-TRAP. Enzyme was set to trypsin, allowing for one missed cleavage. Only peptides that were ranked first and scored above the identity threshold score, set at 99% confidence, were withheld.

Rosetta docking. The UBQ_Gp_LYX-Cterm protocol of the Rosetta v3.4 suite[26] was used for docking simulations. As base models, we used ubiquitin (PDB 3NS8), RALA (PDB 1U8Z), RALA–EXO84 (PDB 1ZC3) and RALA–SEC5 (PDB 1UAD). RALA–EXO84 and RALA–SEC5 complexes as docking partners were treated as one rigid body. The draft runs for initial sampling had 'score' and 'SASA' filters disabled and the number of refinement cycles reduced to 500. Two thousand initial decoys were produced for ubiquitylated-RALA–EXO84 and ubiquitylated-RALA–SEC5

complexes, of which 1,945 and 636 respectively had a negative energy score and were used for calculating the scoring confidence index.

Three hundred and thirteen decoys for ubiquitylated-RALA and 103 decoys for ubiquitylated-RALA–SEC5 were produced with the recommended high-quality parameters. To rank the solutions, taking into account information from both sets, a 'match score' has been calculated as

$$M(x_i) = \min_j \frac{E(x_i) + E(y_j)}{\mathrm{RMSD}(x_i, y_j)}$$

where x_i is a decoy from the ubiquitin–RALA–SEC5 simulation, y_j is one from ubiquitin–RALA, E is the Rosetta energy score, and RMSD is the root-mean-square deviation of ubiquitin localization between the decoys. The reasoning is that a good solution would have a good score $E(x_i)$ and a close counterpart in the other set (with low RMSD($x_i y_j$)), which also has a good score $E(y_j)$.

All RMSD calculations in all cases were performed between ubiquitin positions.

Immunofluorescence. Cells were grown on coverslips or non-coated eight-well chamber slides (Nalge Nunc International). Twenty-four hours after transfection, cells were fixed with 4% paraformaldehyde and permeabilized with 0.1% Triton X-100 in PBS. For HA–beclin-1 immunostaining, samples were blocked with 5% goat serum, and incubated with anti-HA antibody (Abcam) followed by goat Alexa488-coupled anti-rabbit antibody (Jackson Immunoresearch). For analysis of RALB–EXO84–SEC5 intracellular localization, cells were incubated with 0.1 M glycine, at pH 7.4 and blocked with 1% BSA and 10% goat serum in PBS. Primary antibodies and goat secondary antibodies, Alexa488-coupled anti-mouse antibody (Invitrogen), Alexa594-coupled anti-rat antibody (Invitrogen), and Alexa647-coupled anti-rabbit antibody (Invitrogen) were applied diluted in a blocking buffer. To avoid antibody cross-reactivity, secondary anti-mouse antibodies were pre-blocked with 10% rat serum. Confocal images were taken using a Leica TCS SP5 II microscope.

For LC3 immunostaining, cells were grown in μ Clear 96-well plate and fixed in ice-cold methanol. After blocking in 5% goat serum, samples were incubated with anti-LC3 antibody and labelled with Alexa488-coupled anti-rabbit antibody. Images were automatically acquired using IN Cell Analyser 2000 (GE Healthcare) and then analysed using IN Cell Investigator software (GE Healthcare).
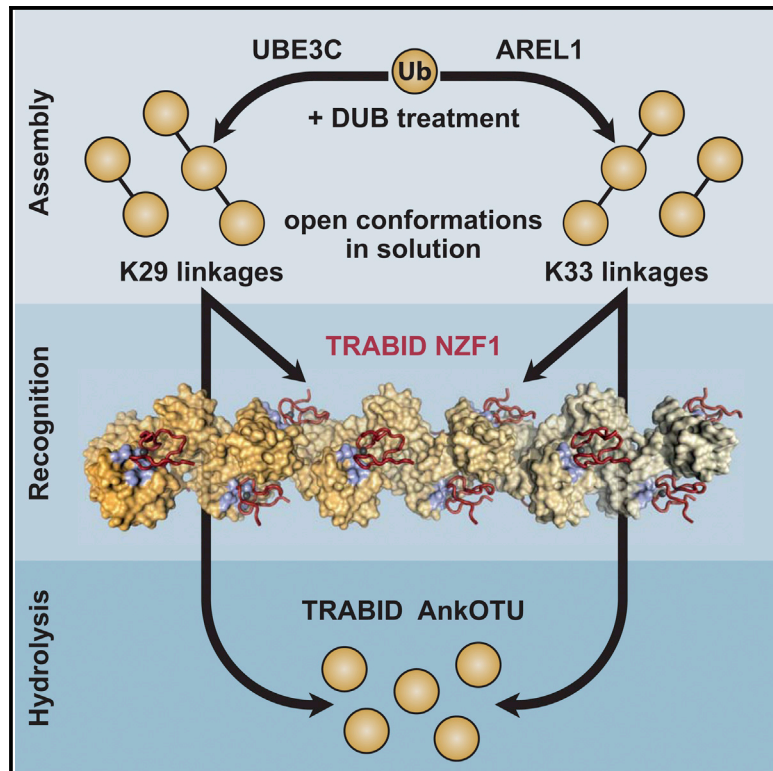
Statistical analysis. P values were calculated by two-tailed t-test. All data were analysed using Graphpad Prism 5 or Excel.

34. Moerkerke, B. & Goetghebeur, E. Selecting 'significant' differentially expressed genes from the combined perspective of the null and the alternative. *J. Comput. Biol.* **13,** 1513–1531 (2006).

35. Sablina, A. A. *et al.* The tumor suppressor PP2A Abeta regulates the RalA GTPase. *Cell* **129,** 969–982 (2007).

Assembly and Specific Recognition of K29- and K33-Linked Polyubiquitin

Graphical Abstract

Highlights

- The HECT E3 ligases UBE3C and AREL1 assemble K29- and K33-linked polyubiquitin, respectively

- K29- and K33-linked chains adopt open conformations in solution

- The N-terminal NZF1 domain of TRABID specifically recognizes K29/K33-diubiquitin

- A structure of a K33 filament bound to NZF1 domains explains TRABID specificity

Authors

Martin A. Michel, Paul R. Elliott, ..., Stefan M.V. Freund, David Komander

Correspondence

dk@mrc-lmb.cam.ac.uk

In Brief

Michel et al. reveal that UBE3C and AREL1 assemble K29- and K33-linked polyubiquitin, respectively, on substrates and as unanchored chains. They further identify a K29/K33-specific ubiquitin binding domain in TRABID and structurally characterize how TRABID recognizes K29/K33 filaments.

Accession Numbers

5AF4
5AF5
5AF6

CellPress

Article

Assembly and Specific Recognition of K29- and K33-Linked Polyubiquitin

Martin A. Michel,[1,2] Paul R. Elliott,[1,2] Kirby N. Swatek,[1] Michal Simicek,[1] Jonathan N. Pruneda,[1] Jane L. Wagstaff,[1] Stefan M.V. Freund,[1] and David Komander[1,*]
[1]Medical Research Council Laboratory of Molecular Biology, Francis Crick Avenue, Cambridge CB2 0QH, UK
[2]Co-first author
*Correspondence: dk@mrc-lmb.cam.ac.uk
http://dx.doi.org/10.1016/j.molcel.2015.01.042

SUMMARY

Protein ubiquitination regulates many cellular processes via attachment of structurally and functionally distinct ubiquitin (Ub) chains. Several atypical chain types have remained poorly characterized because the enzymes mediating their assembly and receptors with specific binding properties have been elusive. We found that the human HECT E3 ligases UBE3C and AREL1 assemble K48/K29- and K11/K33-linked Ub chains, respectively, and can be used in combination with DUBs to generate K29- and K33-linked chains for biochemical and structural analyses. Solution studies indicate that both chains adopt open and dynamic conformations. We further show that the N-terminal Npl4-like zinc finger (NZF1) domain of the K29/K33-specific deubiquitinase TRABID specifically binds K29/K33-linked diUb, and a crystal structure of this complex explains TRABID specificity and suggests a model for chain binding by TRABID. Our work uncovers linkage-specific components in the Ub system for atypical K29- and K33-linked Ub chains, providing tools to further understand these unstudied posttranslational modifications.

INTRODUCTION

Protein ubiquitination is an important posttranslational modification that affects virtually every cellular process. Its best-studied function is the degradation of proteins by the proteasome (Hershko and Ciechanover, 1998). However, ubiquitination also regulates alternative degradation pathways, such as ER-associated degradation, autophagy, and mitophagy (Christianson and Ye, 2014; Shaid et al., 2013). In addition, ubiquitination has many non-degradative roles in protein kinase signaling, DNA damage response, intracellular trafficking, transcription, and translation (Komander and Rape, 2012).

During ubiquitination, the 76-amino acid protein ubiquitin (Ub) is attached via its C terminus to, most commonly, Lys residues on substrate proteins. The versatility of Ub in regulating cellular processes arises from its ability to form a wide variety of polyUb

chains (Komander and Rape, 2012). Ub has seven internal Lys residues and an N-terminal amino group, all of which can be ubiquitinated, leading to the formation of polyUb chains. Proteomic analyses have revealed that all Ub chain linkages exist simultaneously in cells (Kim et al., 2011; Wagner et al., 2011; Xu et al., 2009). Chains can be homotypic, in which only one linkage type is present, but also heterotypic, in which multiple linkages form mixed and branched structures (Komander and Rape, 2012). Importantly, different linkage types have distinct cellular roles. K48-linked Ub chains are proteasomal degradation signals, whereas K63-linked Ub chains are mainly non-degradative. For the remaining six "atypical" linkage types, cellular roles are less clear. K11-linked chains are important in cell-cycle regulation, where they seem to constitute an alternative proteasomal degradation signal (Wickliffe et al., 2011) but also have other roles (Bremm and Komander, 2011), whereas M1-linked chains have independent non-degradative roles, in particular during NFκB activation and apoptosis (Iwai et al., 2014). For the remaining four chain types, linked via K6, K27, K29, and K33, very little is known, and proteins generating and recognizing these chains in eukaryotic cells are still elusive (Kulathu and Komander, 2012).

The process of ubiquitination is facilitated by an enzymatic cascade in which an E1 Ub-activating enzyme transfers Ub onto the active-site Cys of an E2 Ub-conjugating enzyme (Schulman and Harper, 2009; Ye and Rape, 2009). The E2 enzyme can directly discharge its Ub onto substrates, usually with the help of a RING or U-box E3 ligase (Deshaies and Joazeiro, 2009). Alternatively, a subset of E2 enzymes can perform a transthiolation reaction by transferring Ub onto the active-site Cys of a HECT or RBR E3 ligase. When charged with Ub, HECT and RBR E3 ligases modify substrates in an E2-independent manner (Berndsen and Wolberger, 2014). Importantly, a number of E2 enzymes as well as several HECT and RBR E3 ligases are known to assemble polyUb in a linkage-specific fashion (Kulathu and Komander, 2012; Mattiroli and Sixma, 2014). Based on this knowledge, we have previously described enzymatic assembly systems for K11- and K6-linked chains using a modified E2- and a HECT-like E3 ligase, respectively (Bremm et al., 2010; Hospenthal et al., 2013).

When polyUb chains are generated, they are recognized by Ub binding domains (UBDs), some of which bind polyUb chains in a linkage-specific manner (Husnjak and Dikic, 2012). Linkage-specific UBDs for M1-linked chains have been described (e.g., Sato
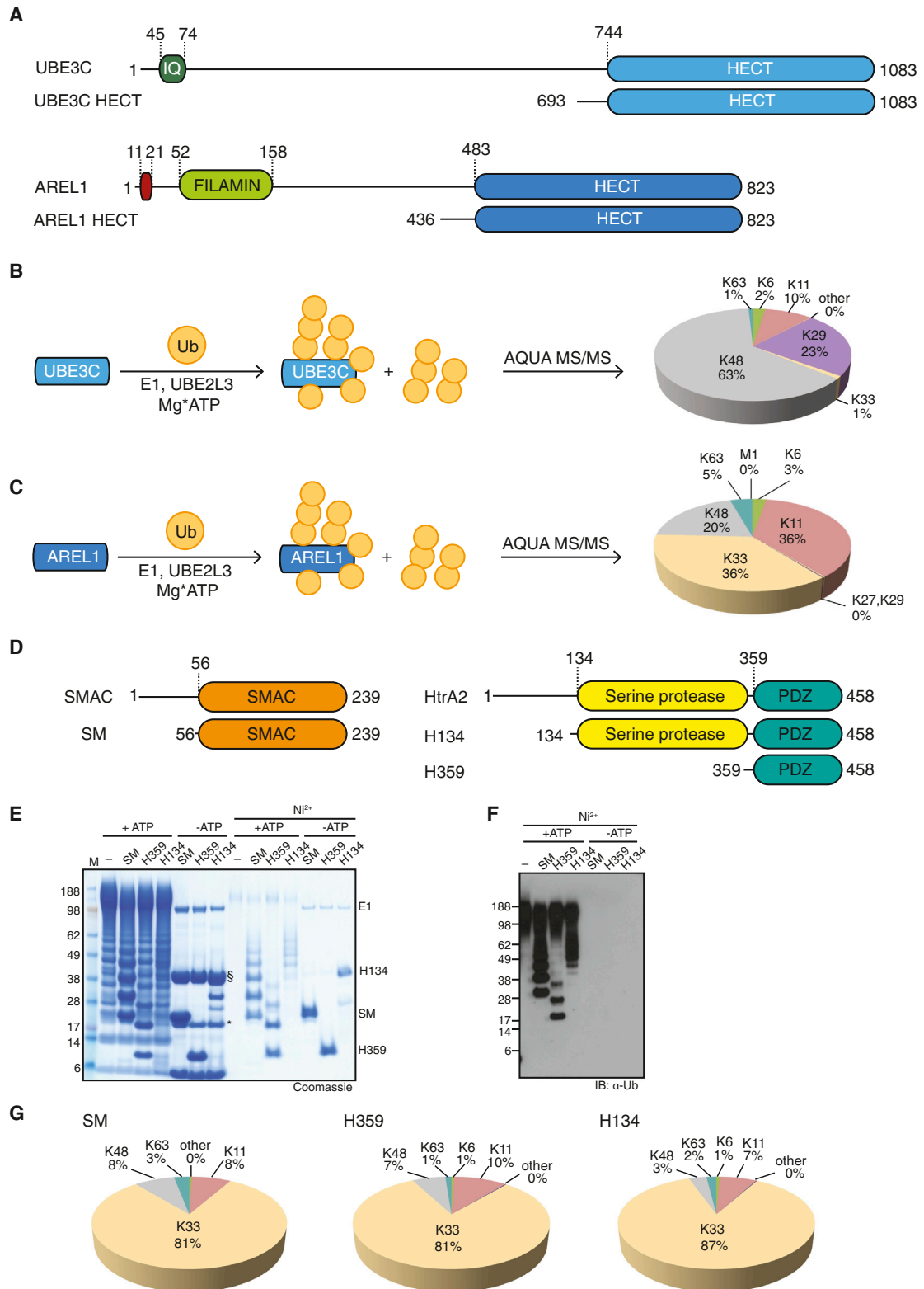
Figure 1. Role of HECT E3 Ligases in Assembling Atypical Ub Chains

(A) Domain structures of UBE3C and AREL1 (KIAA0317) (top) and constructs used in this study (bottom).

(B) Schematic of an assembly reaction with UBE3C, UBE2L3 (UbcH7), E1, and WT Ub (left). The linkage composition in the reaction mixture was analyzed by AQUA-based MS/MS (right).

(legend continued on next page)

et al., 2011) but are unknown for the remaining atypical chain types. Deubiquitinases (DUBs) hydrolyze Ub chains, in some cases with linkage preference (Clague et al., 2013; Komander et al., 2009). Characterization of the ovarian tumor (OTU) DUB family has revealed enzymes to hydrolyze atypical chain types specifically (Keusekotten et al., 2013; Licchesi et al., 2012; Mevissen et al., 2013; Ritorto et al., 2014; Rivkin et al., 2013).

In our search for assembly systems of atypical Ub chain types, we confirmed an earlier report showing that UBE3C primarily assembles K29- and K48-linked chains (You and Pickart, 2001) and further discovered that the HECT E3 ligase apoptosis-resistant E3 ubiquitin protein ligase 1 (AREL1), also known as KIAA0317 (Kim et al., 2013), assembles atypical K11- and K33-linked chains in autoubiquitination reactions and predominantly K33-linkages in free chains and on reported substrates. Treatment of assembly reactions with linkage-specific DUBs enabled purification of K29- and K33-linked polyUb in quantities suitable for biophysical and structural studies. This enabled the structural characterization of the polymers and of the K29/K33 linkage-specific OTU family DUB TRABID (Licchesi et al., 2012). DiUb of both linkage types adopt open conformations in solution, similar to K63-linked polyUb. We found that the TRABID N terminus, which contains three Npl4-type zinc finger (NZF) UBDs, specifically binds K29- and K33-linked diUb, and specificity can be attributed to the first NZF domain (NZF1). A crystal structure of NZF1 bound to K33-linked diUb reveals an intriguing filamentous structure for K33 polymers in which NZF1 binds each Ub-Ub interface. A similar binding mode is observed for K29-linkages in solution studies, together suggesting a model for TRABID interaction with atypical chains. Inactive TRABID localizes to Ub-rich puncta in cells, and this is attenuated when the K29/K33-specific binding mode is disrupted by point mutations. Our work unlocks K29- and K33-linked Ub chains for biochemical studies and provides a launching point for future discoveries related to these atypical Ub signals.

RESULTS

HECT E3 Ligases Assemble Atypical Ub Chains

The HECT family of E3 ligases contains 28 members, many of which have important cellular functions (Rotin and Kumar, 2009). Much research has focused on the first discovered member, E6AP (Scheffner et al., 1993), and on the NEDD4 family, which comprises Rsp5 in yeast and nine enzymes in humans (Rotin and Kumar, 2009). Interestingly, although E6AP assembles K48-linked chains, the NEDD4 family specifically assembles K63 linkages in vitro. Elegant biochemical and structural work has identified many features important for linkage specificity (Kamadurai et al., 2009, 2013; Kim and Huibregtse, 2009; Maspero et al., 2013). Because of their ability to dictate linkage specificity and many hints in the literature (Tran et al., 2013; You and Pick-

art, 2001), we characterized human HECT E3 ligases to investigate their ability to assemble atypical chains.

One way to assess which linkage types are assembled is to utilize a panel of Ub mutants in which each Lys is mutated to Arg either inclusively (K0) or with the exception of one position (Kx-only) (Figure S1A). This analysis reproduced K63 specificity of NEDD4L (amino acids [aa] 576–955) (Figure S1B) and indicated a broader specificity of the unstudied HECT E3 ligase AREL1 (aa 436–823, Figure 1A; Figure S1C), which seemed to assemble K33 linkages efficiently.

Using Ub mutants for chain assembly has multiple caveats. To understand which linkage types are assembled in E3 ligase reactions with wild-type (WT) Ub, we used absolute quantification (AQUA)-based mass spectrometry (Kirkpatrick et al., 2006). For this, tryptic digests of chain assembly reactions are spiked with isotope-labeled GlyGly-modified standard peptides derived from each potential linkage site, allowing absolute quantification of all chain types (Kirkpatrick et al., 2006). NEDD4L assembled K63 chains almost exclusively (96%) (Figure S1D), whereas UBE3C assembled K48 (63%), K29 (23%), and K11 linkages (10%) (Figure 1B), as reported previously (Maspero et al., 2013; You and Pickart, 2001). Interestingly, AREL1 assembled 36% of K33, 36% of K11, 20% of K48, and small amounts of K63 and K6 linkages (Figure 1C). The high abundance of K11 linkages in AREL1 reactions contrasts with the finding from K11-only Ub that was incorporated poorly into chains (Figure S1C), suggesting that mutated Lys residues are crucial for assembly of this linkage type by AREL1. Abrogating K11 linkage production by AREL1 using Ub K11R led to 71% of K33 and 24% of K48 linkages (Figure S1E). The fact that K48 linkages stayed relatively constant indicated that this chain type is assembled as a constant byproduct of AREL1.

A recent characterization of AREL1 function (Kim et al., 2013) has suggested that the pro-apoptotic proteins SMAC, HtrA2, and ARTS are among its substrates and further indicated that they interact via the AREL1 HECT domain (rather than an auxiliary N-terminal domain). We expressed fragments of SMAC and HtrA2 (Figure 1D) and used these proteins as in vitro AREL1 substrates. AREL1 ubiquitinated all proteins efficiently (Figures 1E and 1F). Strikingly, AQUA analysis of modified substrates showed that AREL1 had assembled >80% of K33 linkages in the polyUb chains on all three substrates (Figure 1G).

Generating K29- and K33-Linked PolyUb

AREL1 and UBE3C also assembled free Ub chains. Precipitation of enzymes by perchloric acid in an assembly reaction enriched free polyUb chains of varying lengths (see gel in Figure 2A). AREL1 assembled WT Ub into di- and triUb with (for triUb) 75% of K33-linkages and only 13% of K11-linked and 7% of K63-linked chains (Figure 2A). Using K11R Ub, we generated up to 86% of K33 linkages in triUb (Figure 2A). To generate

(C) Reaction as in (B) with AREL1, UBE2L3, E1, and WT Ub.

(D) Domain structures of the pro-apoptotic proteins SMAC and HtrA2 (top) and the expressed constructs used in this work (bottom).

(E) AREL1 is able to assemble chains onto SMAC and HtrA2 in an in vitro ubiquitination reaction that depends on ATP. Ubiquitinated, His6-tagged substrates are enriched following Ni^{2+} affinity binding. SM, SMAC (56–239); H359, HtrA2 (359–458); H134, HtrA2 (134–458); §, AREL1; *, UBE2L3.

(F) Western blot against Ub of the Ni^{2+}-enriched reaction from (E).

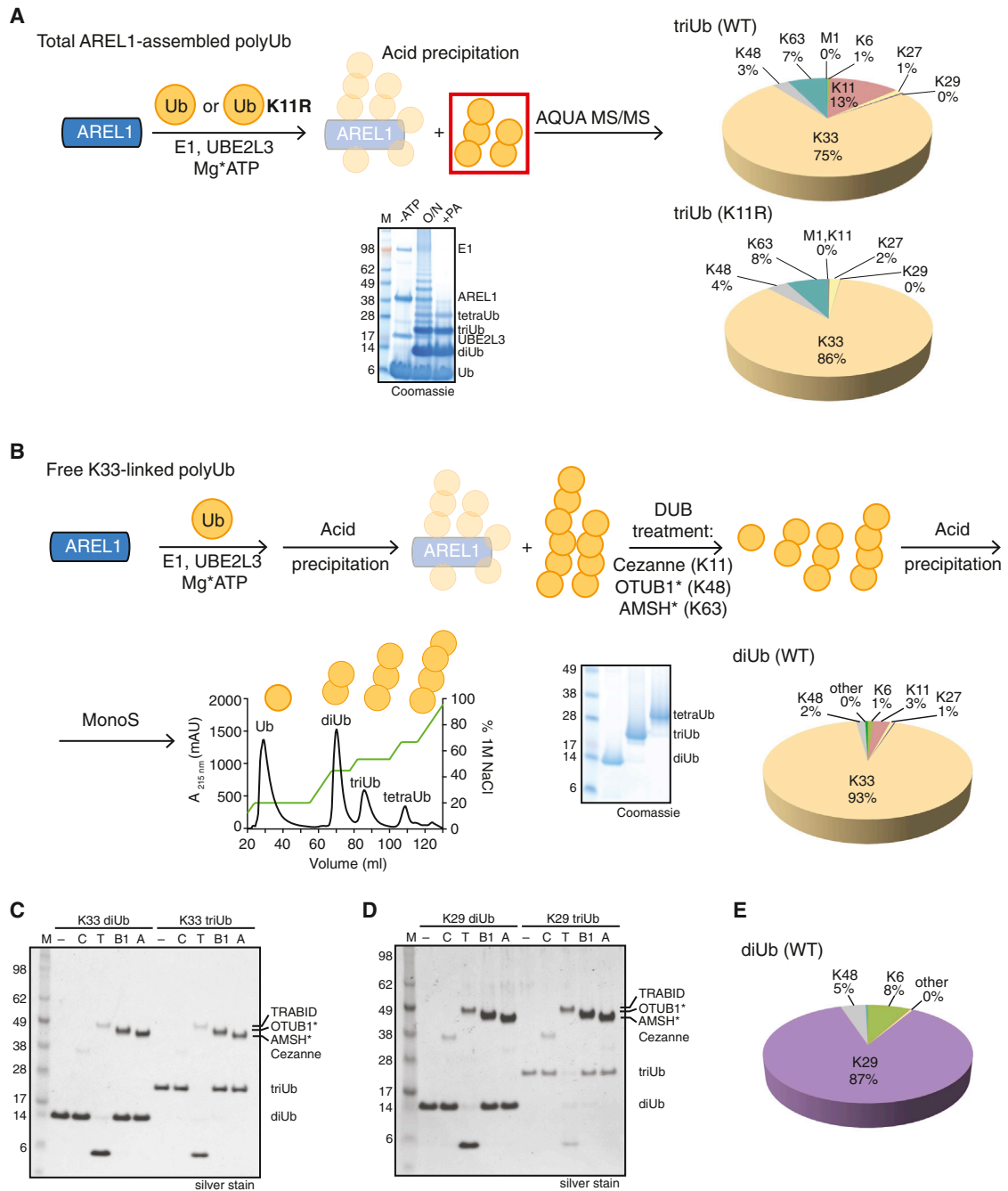(G) AQUA MS/MS profiles of the ubiquitinated substrates purified from (E).

Figure 2. Purification of Unanchored K29/K33 PolyUb Chains

(A) Schematic of the assembly of K33-linked Ub chains using either WT or K11R Ub (top). AQUA profiles of triUb using either WT (top right) or K11R Ub (bottom right; K6 linkage was excluded from the quantitative analysis because of the K11R substitution). Bottom: corresponding SDS-PAGE gel for assembly of free chains. −ATP, initial reaction without ATP addition; O/N, overnight incubation of the assembly reaction; +PA, perchloric acid treatment of the assembly reaction.

(B) Schematic representation of the purification of K33-linked polyUb chains. Following the assembly reaction, perchloric acid treatment removes the ubiquitinated and unmodified forms of E1, E2, and E3. Linkage-selective DUBs are then used to remove undesired Ub linkages. An additional perchloric acid step is required to inactivate the DUBs prior to cation exchange chromatography (bottom), which resolves the homotypic chains based on linkage length. Bottom center: SDS-PAGE of purified K33-linked di-, tri-, and tetraUb. Bottom right: AQUA MS/MS of purified K33-linked diUb.

(C) Deubiquitinase assay of purified K33-linked di- and triUb. −, no DUB; C, 200 nM Cezanne (K11-specific); T, 350 nM TRABID (K29/K33-specific); B1, 1 μM OTUB1* (K48-specific); A, 1 μM AMSH* (K63-specific).

(D) K29-linked polyUb chains can be purified analogous to the schematic shown in (B). Purified K29-linked di- and triUb were treated with DUBs as in (C).

(E) AQUA mass spectrometry profile of purified K29 diUb.

Table 1. Data Collection Statistics

	K33 diUb	K33 triUb	TRABID NZF1-K33 diUb
Data Collection			
Beamline	Diamond I03	Diamond I24	Diamond I24
Space group	*I* 4	*P* 2$_1$ 2$_1$ 2$_1$	*C* 2
a, *b*, *c* (Å)	113.08, 113.08, 103.90	28.42, 42.48, 50.52	98.38, 126.51, 78.09
α, β, γ (°)	90.00, 90.00, 90.00	90.00, 90.00, 90.00	90.00, 103.38, 90.00
Wavelength	0.9763	0.9686	0.9686
Resolution (Å)	45.47–1.85 (1.89–1.85)[a]	23.62–1.68 (1.72–1.68)	38.59–3.40 (3.67–3.40)
R_{merge}	4.5 (44.3)	5.1 (77.6)	10.9 (56.2)
$I/\sigma I$	11.9 (2.5)	19.9 (2.7)	6.6 (2.0)
Completeness (%)	99.8 (100)	99.8 (99.5)	99.9 (100)
Redundancy	3.5 (3.5)	7.3 (7.7)	3.4 (3.4)
Refinement			
Resolution (Å)	45.47–1.85	23.62–1.68	38.59–3.40
No. of reflections	55,562	7,363	12,783
R_{work}/R_{free}	22.9/27.1	19.4/22.5	18.0/22.2
No. of Atoms			
Protein	4,788	596	4,076
Ligand/ion	84		5
Water	128	49	
B Factors			
Wilson *B*	33.77	26.49	83.17
Protein	70.20	35.00	106.68
Ligand/ion	67.50		83.84
Water	45.90	43.17	
RMSDs			
Bond lengths (Å)	0.005	0.002	0.002
Bond angles (°)	0.930	0.748	0.603
Ramachandran statistics (favored /allowed/outliers)	99.0/1.0/0.0	100.0/0.0/0.0	98.8/1.2/0.0

[a]Numbers in brackets are for the highest-resolution bin.

pure K29 and K33 chains from WT Ub, we acid-precipitated the reaction and treated the free chains with a panel of linkage-specific DUBs consisting of K11-specific Cezanne (Mevissen et al., 2013) as well as enhanced versions of K48-specific OTUB1* (an UBE2D2-OTUB1 fusion) and K63-specific AMSH* (a STAM2-AMSH fusion) (Figure 2B; Figures S2A and S2B; Supplemental Experimental Procedures). The resulting K29- and K33-linked polyUb chains were purified by cation exchange and were 87% and 93% pure, respectively; uncleavable by Cezanne, OTUB1*, or AMSH*; but hydrolyzed efficiently by the K29/K33-specific DUB TRABID (Licchesi et al., 2012) (Figures 2C–2E; Figures S2C and S2D; also see below).

K29- and K33-Linked diUbs Adopt Open Conformations in Solution

With new linkage types at hand, we set out to understand their structural features. We crystallized K33-linked di- and triUbs (Figure S3). The K33-linked diUb crystallized in space group *I*4, not observed previously for Ub, and a structure to 1.85 Å resolution revealed eight molecules forming four identical Ub dimers

with clear electron density for the K33 linkages (Figures S3A and S3B; Table 1). In this structure, K33-linked diUb is compact, and distal and proximal Ub moieties interact symmetrically via their Ile36 hydrophobic patches (Figure S3A). The symmetric interface did not provide a model for the conformation of a longer K33 chain.

A second crystal structure for K33-linked triUb was obtained at 1.68 Å in space group *P*2$_1$2$_1$2$_1$ with similar unit cell dimensions as the Ub reference structure (1ubq; Vijay-Kumar et al., 1987), and also contains only one Ub molecule per asymmetric unit (Table 1). Examination of adjacent asymmetric units only allowed one possibility for K33 chain formation (Figure S3C), although the C termini and isopeptide linkages were poorly ordered and not built in the model (Figure S3D). The Ub moieties in K33 chains were related by translational symmetry and, in contrast to the compact diUb structure, adopted an open conformation in which Ub moieties do not interact with each other except by two polar side chain contacts (Figure S3C). The distinct conformations of di- and triUb could be due to differences in crystallization conditions but highlight the underlying problem that crystallization
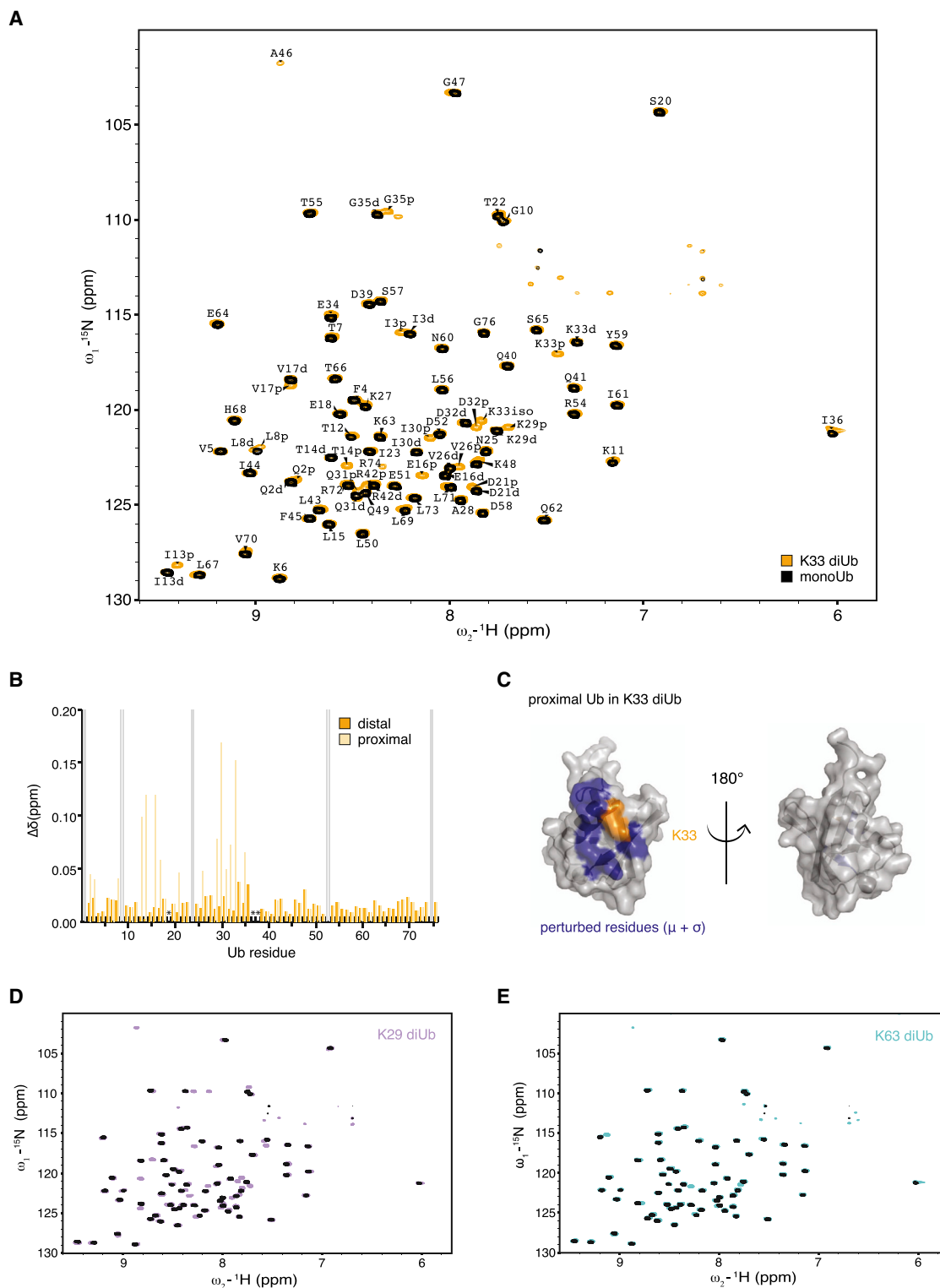
Figure 3. NMR Analysis of K29/K33 Chains

(A) BEST-TROSY spectra for ^{15}N-K33 diUb (orange) and ^{15}N-monoUb (black). Complete assignment of resonances from the proximal (p) or distal (d) moieties from a ^{13}C, ^{15}N-K33 diUb sample are shown.

(B) Chemical shift perturbation of distal (orange) and proximal (beige) resonances with respect to monoUb. Grey bars, exchange-broadened resonances; asterisks, proline residues.

(legend continued on next page)

may present an incomplete picture of the dynamic states of free polyUb in solution.

We therefore turned to nuclear magnetic resonance (NMR), which is better suited to analyze dynamic Ub chains. When Ub polymers adopt open conformations in solution, the spectra resemble free monoUb, showing a small number of perturbations surrounding the isopeptide linkage. The best example for this is K63-linked Ub (Varadan et al., 2004) which does not form a defined interface in solution (Ye et al., 2012). Contrasting this are compact conformations in which defined interfaces are formed. In K48-linked diUb (Varadan et al., 2002), resonances of proximal and distal Ub moieties adopt distinctly different chemical shift positions (splitting) because of their different chemical environment.

We assembled K33-linked diUb from ^{13}C, ^{15}N-labeled monoUb and measured 2D band-selective excitation short transient transverse relaxation-optimized spectroscopy (BEST-TROSY) spectra, revealing well dispersed peaks similar to monoUb (Figure 3A). Assignment of the spectra revealed splitting of 16 resonances. The small chemical shift perturbations (CSPs) in all split resonances could be attributed to the proximal Ub, whereas the distal Ub was unperturbed (Figure 3B). Mapping of the perturbed residues on Ub revealed a small region surrounding the isopeptide bond at K33 (Figure 3C). Almost identical spectra were obtained for ^{15}N-labeled, K29-linked diUb, in which 19 resonances were split and mildly perturbed (Figure 3D). Both diUb spectra resembled the K63 diUb spectrum (Varadan et al., 2004; Figure 3E). Together, this indicates that both K29- and K33-linked diUb do not form defined interfaces in solution but, rather, exist in open conformations.

TRABID K29/K33 DUB Specificity Is Retained with Longer Chains

TRABID, a DUB from the OTU family, is the only known protein to date that acts specifically on K29- and K33-linked Ub chains (Licchesi et al., 2012; Mevissen et al., 2013; Figure 4A). In TRABID, a C-terminal OTU domain of the A20 subfamily is preceded by an ankyrin repeat Ub binding domain (AnkUBD) that enables a non-specific OTU domain to preferentially cleave K29- and K33-linked diUb (Licchesi et al., 2012). This construct hydrolyzes K63-linked chains with 40-fold lower activity compared to K29 chains (Virdee et al., 2010). Because of the necessity for chemical synthesis of K27, K29, and K33 linkages, these experiments were so far confined to diUb cleavage. We now confirm that the specificity of TRABID AnkOTU also holds true for longer tetraUb chains. TRABID cleaved K33-linked tetraUb with a significantly higher activity compared with K63-linked chains (Figures 2C, 2D, and 4B; Figure S4A).

TRABID NZF1 Specifically Binds K29- and K33-Linked Chains

In addition to the C-terminal AnkOTU catalytic domain, TRABID contains three N-terminal NZF domains (Figure 4A) that bind polyUb and are important, together with the AnkUBD, for

TRABID localization to characteristic punctate structures in cells (Licchesi et al., 2012). Surprisingly, analyzing the preference of the N-terminal NZF domains in pull-down experiments revealed the specificity of the 3xNZF module (aa 1–263 or 1–178) for K29- and K33-linked diUb, whereas K63-diUb binding was barely detectable (Figure 4C; Figure S4B). This resembled the cleavage specificity of the AnkOTU catalytic domain (Figure 4B; Licchesi et al., 2012). Pull-down experiments with individual NZF domains showed that K29/K33 specificity could be attributed entirely to the N-terminal NZF1 domain (aa 1–33), which bound these chains as well as the 3xNZF modules but did not interact with K63-linked diUb.

To measure affinities, we established a surface plasmon resonance (SPR)-based binding assay in which monoUb and all types of diUb were immobilized, and NZF1 binding was detected by SPR (Figure 4D). Of the nine datasets, seven were fitted to a one-site binding model with NZF1 affinities between 190–370 μM (Figures S4C and S4D). For K29- and K33-linked diUb, fitting to a one-site model resulted in high residuals, and data were fitted to a two-site binding model, revealing significantly higher affinities (K_d^{high} 3.6 and 4.9 μM, respectively, and 180/200 μM affinities for K_d^{low}) (Figure S4C). The high binding affinities of K29- and K33-linked diUb were consistent with the pull-down experiments (Figure 4C).

Curiously, NZF2 and NZF3 did not bind diUb in pull-down assays. To understand whether these domains can bind Ub, binding studies were performed by NMR using ^{15}N-labeled Ub. NZF1 interacts with monoUb, leading to chemical shift perturbation maps that show the characteristic profile for interactions via the Ub Ile44 patch (Figure 4E; Figure S4E). This is consistent with the known binding mode of NZF domains first derived for Npl4 (Alam et al., 2004), and mapping of perturbed residues on Ub suggests similar interactions (Figure S4E). Titrations of NZF2 and NZF3 resulted in similar CSP profiles (Figure 4F; Figure S4E). Using NMR titration experiments, we derived binding constants for the monoUb-NZF interactions, with K_d values of ~440 μM for NZF1, ~1 mM for NZF2, and ~540 μM for NZF3 (Figures S4F and S4G), which is in a typical range for monoUb binding to small UBDs. Although this showed that all NZF domains are functional in Ub binding, it did not explain why only NZF1 showed K29/K33 specificity.
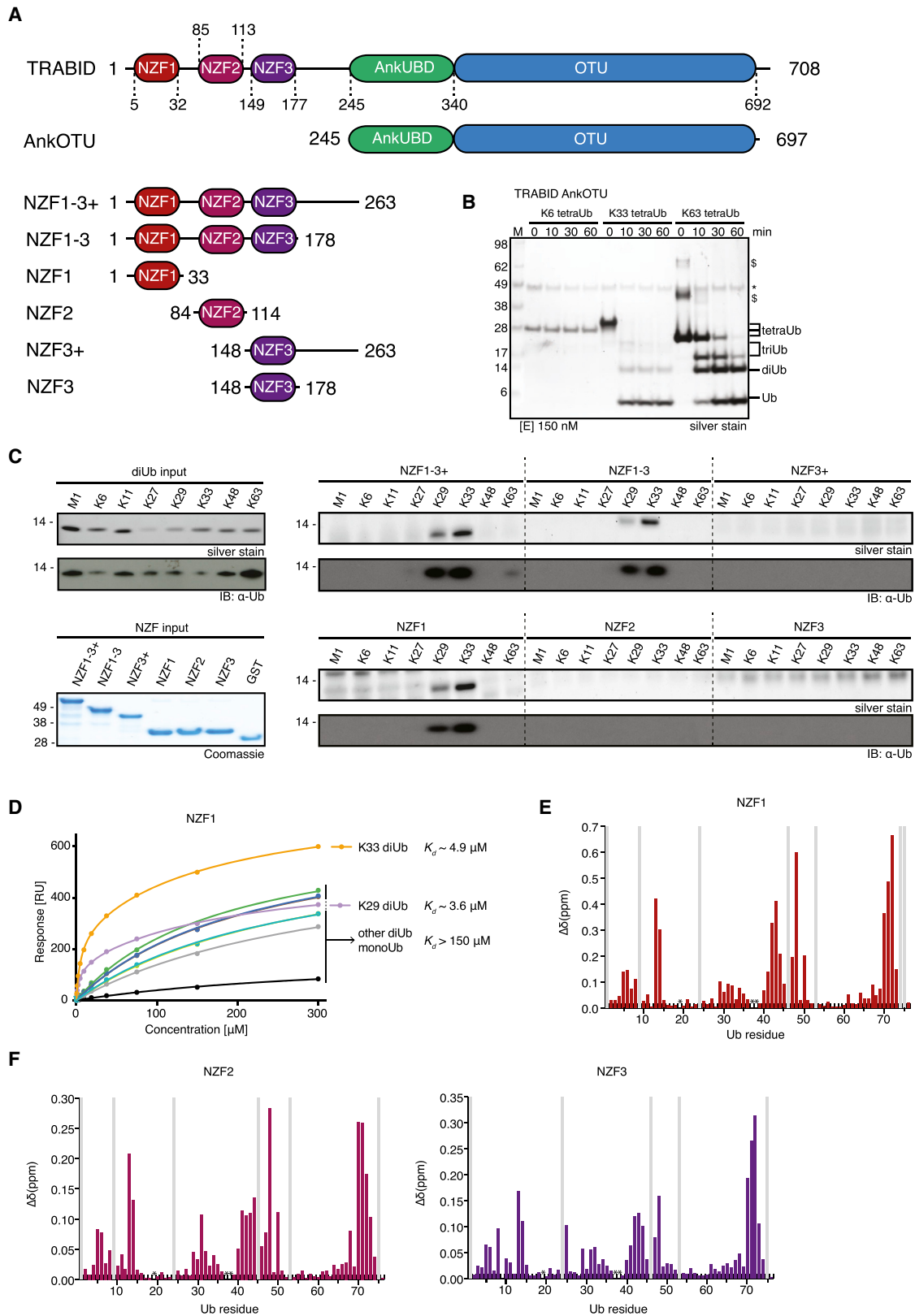
Structure of a K33-Linked Ub Polymer Bound to TRABID NZF1

To understand the underlying molecular basis for the K29/K33 specificity of TRABID NZF1, we crystallized the complex with K33-diUb and determined a structure to 3.4 Å resolution. High solvent content (67%, Matthews coefficient ~ 3.8) led to high-contrast maps (Figure S5A) and allowed building of a complete model with good statistics (Table 1). It was immediately apparent that the arrangement of Ub molecules in the crystal lattice generated seemingly infinite helical polymers (Figures 5A and 5B; Figure S5B). The K33-filament forms a helix with 5-fold

(C) Resonances that display a perturbation of more than 1 σ are mapped onto the surface of monoUb (purple) and cluster around the K33 residue (orange). No significant perturbations were observed on the distal Ub moiety, consistent with an open conformation of K33 diUb.
(D) BEST-TROSY spectra for ^{15}N K29 diUb (purple) and monoUb (black).
(E) BEST-TROSY spectra for ^{15}N K63 diUb (cyan) and monoUb (black).

A

TRABID

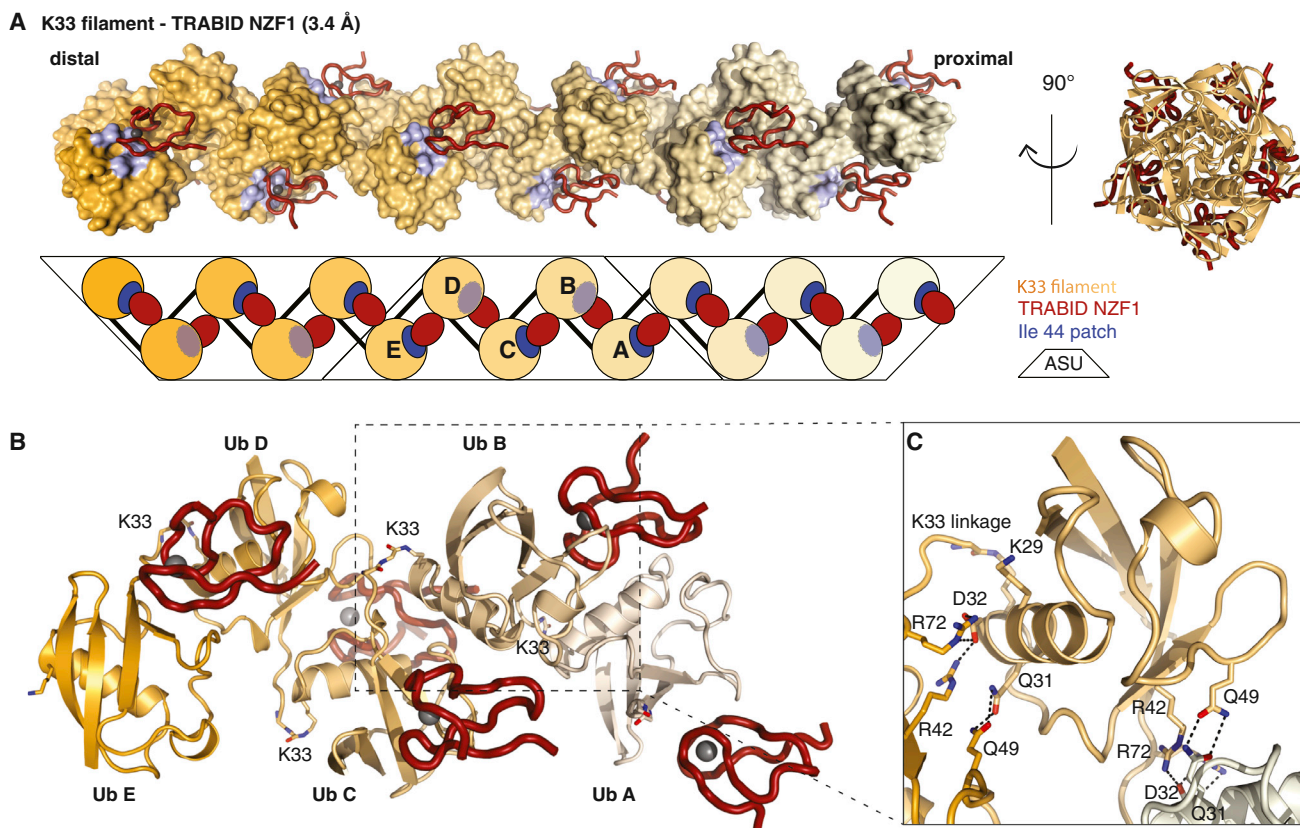AnkOTU

NZF1-3+

NZF1-3

NZF1

NZF2

NZF3+

NZF3

B TRABID AnkOTU

C

D

NZF1

E

NZF1

F

NZF2   NZF3

(legend on next page)

A K33 filament - TRABID NZF1 (3.4 Å)

distal / proxial

90°

K33 filament
TRABID NZF1
Ile 44 patch
ASU

B

Ub D / Ub B
K33
Ub E / Ub C / Ub A

C

K33 linkage
K29
D32
R72
Q31
R42 / Q49
R42
Q49
R72
D32
Q31

Figure 5. Structure of K33 Filaments Bound to NZF1

(A) Structure of the K33-linked Ub filament as observed in the crystal, showing three adjacent asymmetric units (black outline). Ub molecules are shown as a surface representation with a gradient from orange (distal) to beige (proximal), and Ile44 patches are indicated in blue. NZF1 is shown as a red ribbon with gray Zn^{2+} atoms. A schematic is shown below. Right: view of the filament down the 5-fold symmetry axis. ASU, asymmetric unit.

(B) Content of the asymmetric unit, colored as in (A). K33 isopeptide linkages are shown as stick representations; see Figure S5C for electron density.

(C) Close-up view of one Ub in the filament, showing interacting residues as a stick representation. Hydrogen bonds are shown as black dashed lines. The K33 and K29 side chains are also shown.

symmetry. The helix turns twice between the first and sixth molecule (Figure 5A). The asymmetric unit contains five Ub molecules and five NZF domains (Figures 5A and 5B). The electron density for K33 linkages can be discerned for one isopeptide bond (Figure S5C). The electron density for the isopeptide bonds is weak because of flexibility but also because diUb was crystallized, and each linkage in the asymmetric unit is only at half occupancy. K29 is in close proximity to the tail of the distal Ub, and it is conceivable that K29-linked polymers interact with TRABID

NZF1 in a similar manner and can form similar filaments. This was supported by NMR experiments where NZF1 was added to either ^{15}N-labeled K33- or K29-linked diUb. NZF1 binding leads to chemical shift perturbations along the same face of the proximal Ub moieties, indicating that the overall orientation of the proximal Ub is similar (Figure S5D).

Interactions between Ub molecules are identical along the filament and involve exclusively polar contacts (Figure 5C). A distal Ub interacts with the Ub helix of a proximal Ub, forming hydrogen

Figure 4. Characterization of TRABID Specificity

(A) Domain structure of human TRABID. The AnkOTU fragment has been characterized in detail in Licchesi et al. (2012). Boundaries of the NZF domain fragments analyzed here are shown.

(B) Deubiquitination assay of TRABID AnkOTU against K6-, K33-, and K63-linked tetraUb. See Figure S4A for a reaction at a lower DUB concentration.

(C) Pull-down analysis of NZF fragments with a panel of diUb covering all linkage types. Left: the input chains and GST-NZF constructs used. Right: pull-down analysis shown by silver stain and anti-Ub western blot. See Figure S4B for additional controls.

(D) SPR binding experiment of NZF1 to monoUb and the eight different diUb species with error bars representing SEs. K_d values derived from two experiments are shown. See Figure S4C for best-fit parameters and values of SEs.

(E) NMR analysis of isolated NZF1 binding to ^{15}N-labeled monoUb. The chemical shift perturbation for Ub from binding to 600 μM of NZF1 is shown. Grey bars, exchange-broadened residues; asterisks, proline residues. See Figures S4E–S4G for titration data.

(F) NMR analyses as in (E) but for NZF2 and NZF3.

bonds between Gln49 (distal Ub) and Gln31 (proximal Ub) and charged interactions between Arg42 and Arg72 (distal Ub) and Asp32 (proximal Ub) (Figure 5C). This exposes the hydrophobic Ile44 and Ile36 patches of each Ub molecule and enables binding of one NZF domain to each Ile44 patch along the filament (Figure 5A).

Explaining the Specificity of TRABID NZF1 for K33 Linkages

Consistent with other linkage-specific NZF domains, NZF1 of TRABID forms a bidentate interaction across the distal and proximal Ub moieties (Figures 5B and 6A). This has been seen previously for the TAB2 and HOIL-1L NZF domains, which interact specifically with K63- and M1-linked diUb, respectively (Figure 6B; Figure S6A; Kulathu et al., 2009; Sato et al., 2009, 2011), and can be superimposed with TRABID NZF1 with low root-mean-square deviations (RMSDs) (0.5–0.6 Å). TRABID NZF1 binds the distal Ub at the Ile44 patch via the canonical NZF interaction involving Thr14, Tyr15, and Met26 (Figure 6A). This binding mode through the T-Y/F-Φ motif is conserved in all NZF interactions described to date (Figure S6B; Alam et al., 2004) and is consistent with the NMR interaction data in Figures 4E and 4F (see above). The proximal Ub is bound by TRABID NZF1 in an unusual way, at a binding site involving the start of the Ub α helix and two nearby loop regions (Figure 6A). In this interaction, Ub Glu24 makes key interactions with a complementary pocket on NZF1 formed by Tyr15, Asn17, Trp18, and Thr25. The Ub Glu24 side chain can form hydrogen bonds with side chains of these four residues (Figure 6A). In addition, the solvent-exposed TRABID NZF1 Trp18 side chain forms apolar contacts with the Asp52-Gly53 loop of the proximal Ub, and NZF1 Ser20 forms a hydrogen bond with the Gly53 carbonyl group (Figure 6A). All interacting residues in NZF1 are conserved in evolution (Figure 6C).

A comparison of the TAB2 and HOIL-1L diUb complexes reveals how NZF domains have achieved their specificity. Although the canonical interaction with a distal Ub is conserved, the proximal Ub is rotated in each complex to form distinct interactions with a second patch on the NZF domain. In the case of TAB2, the second interaction with a proximal Ub is also via the Ile44 patch (Kulathu et al., 2009; Sato et al., 2009; Figure 6B). In HOIL-1L, a short helical NZF extension contributes the secondary contacts, which are mediated by the Phe4 patch of the proximal Ub (Sato et al., 2011; Figure S6A). Superposition of structures reveals why TAB2 is unable to bind the K33 filament: Glu685 would clash directly with Glu24 of the proximal Ub (Figure S6C). Similarly, TRABID NZF1 Trp18 clashes with the proximal Ub when the TAB2-K63 diUb complex is superimposed (Figure S6D) (although mutation of this residue did not enable high-affinity K63 diUb binding; see below). Finally, the structure also reveals why TRABID NZF2 and NZF3 are unable to bind K33 polymers: Ser20 in NZF1 is replaced by Lys or Arg residues in NZF2/3 (Figure S6E), which affects binding (Figure 6E; see below). However, mutation of Lys165 in NZF3 to Ser did not enhance binding to K29/K33 chains (data not shown), suggesting that the remaining differences play a role as well. It is fascinating that, given their small size, NZF domains have evolved so many distinct binding modes to recognize different linkage types.

Validation of the TRABID-K33 Chain Interaction

To validate the interaction between TRABID NZF1 and K33-diUb biochemically, we mutated residues in the interfaces. We assembled K33-linked diUb from a Ub K11R/E24R mutant that would abrogate its interactions with the proximal interface of TRABID NZF1. Indeed, TRABID NZF1 is unable to pull down K11R/E24R diUb (Figure 6D), confirming that this Ub residue, which has not been implicated in any other Ub interaction known to us, is important for TRABID NZF1 binding.

Next, NZF1 was mutated (Figures 6E–6G; Figure S6F). NZF1 W18A and T25D were unable to interact with K33-linked diUb in pull-down experiments, and Y15F and S20R significantly weakened binding compared with wild-type NZF1 (Figure 6E). SPR measurements for these mutants interacting with K29- or K33-linked diUb revealed that, although Y15F had to be fitted to a two-site binding model with a lower K_d^{high} (11 μM), W18A and T25D fit well with a one-site binding model, indicating that they interacted only via the Ub Ile44 patch (Figures 6F and 6G; Figure S6F; Supplemental Experimental Procedures). No binding could be detected when mutating the canonical Thr14/Tyr15 (to Leu/Val, termed TY14LV), consistent with disruption of the Ile44 patch interaction.

This shows the importance of these residues for NZF1 Ub interactions, validates the observed binding mode in the structure for K33-diUb, and further confirms a similar binding mode for K29-linked chains (Figures 5 and 6). Moreover, this emphasizes that conserved residues on previously unknown proximal binding sites in NZF domains (and perhaps other small UBDs) can furnish UBDs with chain preference.

Localization of Inactive TRABID to Ub-Rich Puncta Relies on NZF1 Binding to Atypical Ub Chains

Catalytically inactive TRABID C443S (ciTRABID) localizes to Ub-rich punctate structures in cells, and this depends on its Ub-binding capability (Licchesi et al., 2012; Tran et al., 2008). TRABID contains at least six independent Ub binding interfaces: at least four in the 3xNZF module, one in the AnkUBD, and at least one in the catalytic domain. Because our biochemical analysis indicated that NZF1 provides TRABID with high-affinity binding for K29/K33 chains, we assessed how important individual NZF domains are for ciTRABID localization to puncta (Figure 7).

Mutation of the canonical Ub binding site in NZF1 (NZF1*; Figure 7A) led to a diffuse (mostly nuclear) ciTRABID localization without puncta (Figure 7B). In contrast, the same mutation in NZF2 or NZF3 (NZF2* and NZF3*, respectively) showed identical punctate pattern as ciTRABID, with a similar number of dots (Figures 7B and 7C; Figure S7A). This shows that Ub binding by NZF1 is crucial for forming punctate structures in the ciTRABID background. We also tested whether the identified mutants in the proximal Ub binding site of NZF1 are defective in punctum formation. ciTRABID W18A and ciTRABID T25D showed a reduction in the number of puncta per cell (Figures 7B and 7C; Figure S7A). This is consistent with the distal Ub binding site still being intact and maintaining residual low-affinity Ub binding capability. However, the significant reduction of dots with ciTRABID W18A suggests that the NZF1:K29/K33 interface promotes punctum formation (Figure 7D).
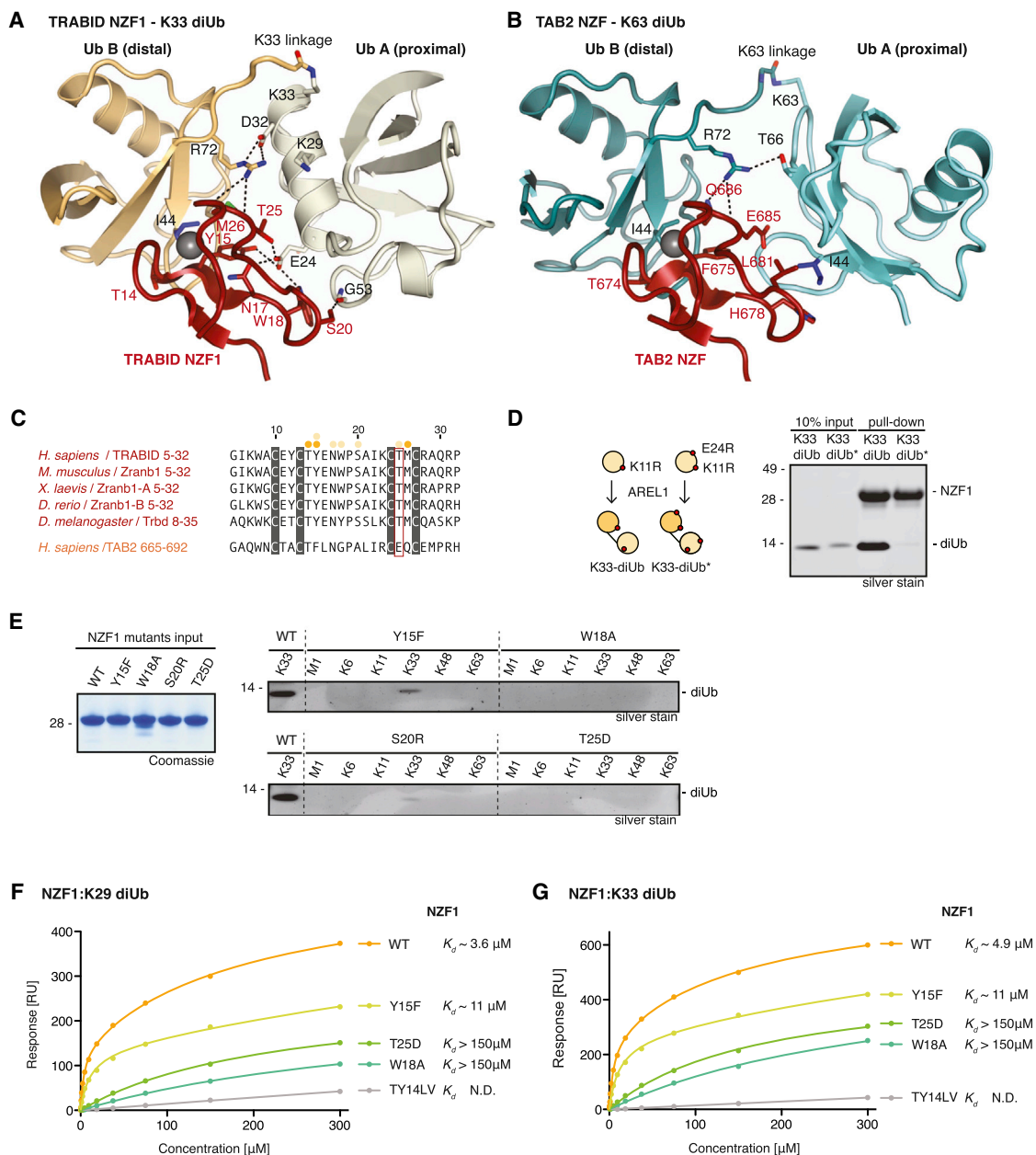
Figure 6. Explaining the K29/K33 Specificity of TRABID NZF1

(A) Detailed view of the interactions between TRABID NZF1 (red) and K33-linked diUb (orange/beige). Interacting residues are labeled, and hydrogen bonds are shown as black dashed lines.

(B) As in (A) for the TAB2 NZF interaction with K63-linked diUb (cyan).

(C) Sequence alignment of TRABID NZF1 from a diverse range of species and human TAB2 NZF domains. Interacting residues are indicated with orange (distal Ub) and beige (proximal Ub) dots. Thr25 in TRABID NZF1 is replaced with Glu685 in TAB2 NZF, which would prevent K29/K33 binding in TAB2 NZF.

(D) Left: Ub chains were assembled into K33 diUb with AREL1 using K11R or K11R/E24R Ub. Right: pull-down assays with TRABID NZF1 and diUb variants.
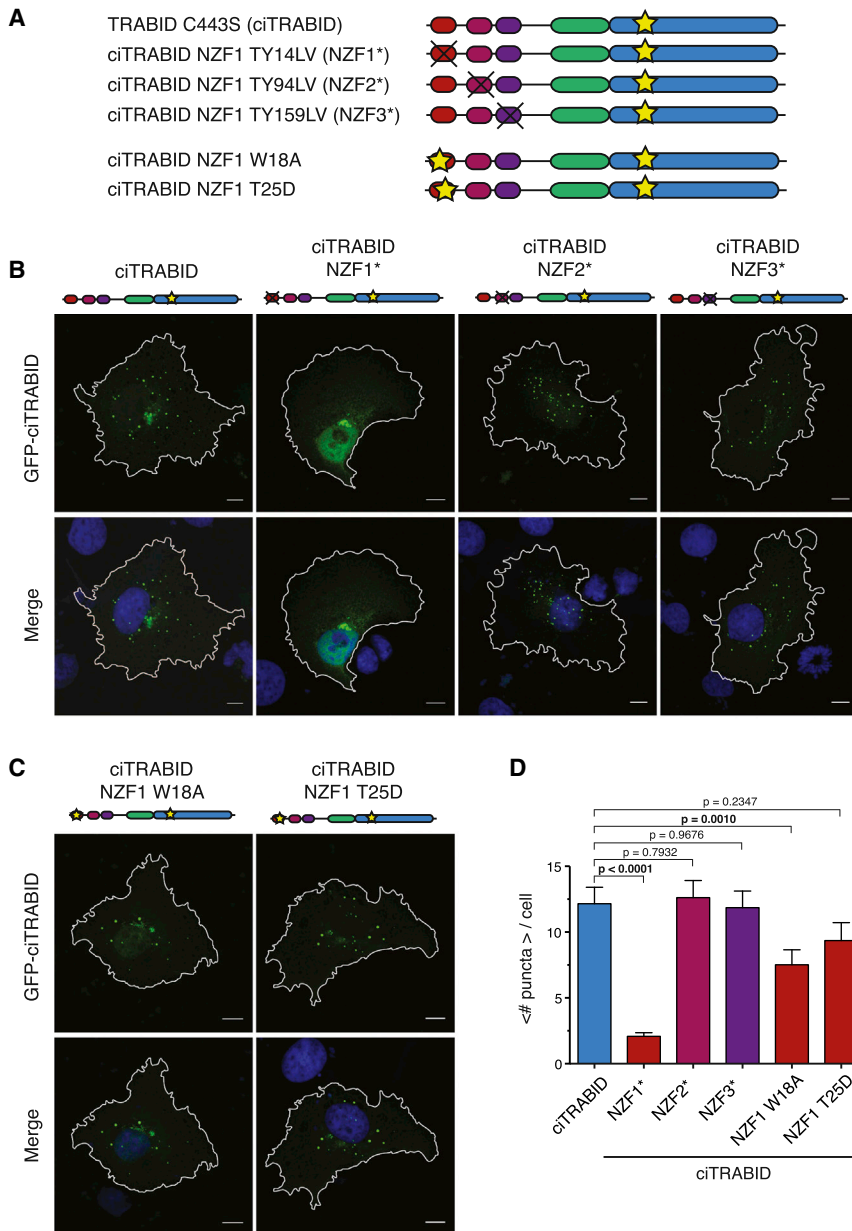
(E) Pull-down assays as in Figure 4C for TRABID NZF1 mutants.

(F and G) SPR binding experiment of NZF1 and its mutants against K29 diUb (F) and K33 diUb (G) with the respective K_d values indicated. SEs from two experiments are shown as error bars. See Figure S6F for values of SEs and best-fit parameters.

DISCUSSION

Chain linkage profiling by AQUA mass spectrometry is a powerful strategy to discover the missing ligases for atypical chains and to provide mechanistic insights into Ub chain assembly. Because of their mechanism of E2-independent linkage determination, HECT E3 ligases are good candidates to assemble atypical chains, and, although several have been suggested to

Figure 7. Localization of Catalytically Inactive TRABID Mutants in Cells

(A) Constructs used in localization experiments for GFP-TRABID fusions. Yellow stars indicate single amino acid substitutions, whereas black crosses denote two amino acid substitutions that abrogate Ub binding in the respective domain.

(B) Localization of catalytically inactive full-length GFP-TRABID (ciTRABID) constructs. GFP-ci-TRABID localizes to distinct puncta in COS-7 cells. Mutations in this background that abrogate Ub binding of NZF1 (NZF1*) lead to a significant decrease in the number of dots, whereas the equivalent mutations in NZF2 (NZF2*) or NZF3 (NZF3*) do not lead to a change in the number of puncta. Cartoon representations of the constructs are shown as in (A). Scale bars, 10 μm.

(C) The same experiment with single amino acid substitutions in the proximal Ub binding site of NZF1.

(D) Statistical analysis of experiments in (B) and (C) with an average number of puncta per cell for the different mutants and corresponding SEs. p Values are given in reference to the ciTRABID mutant, and significant values ($\alpha < 0.05$) are shown in boldface. Error bars represent SEs.

(UbiCRest) analysis (Mevissen et al., 2013), this highlights the utility of linkage-specific DUBs in studying the Ub system.

K29- and K33-linked chains are flexible and able to adopt multiple conformations, much like the remaining chain types (Ye et al., 2012). Although the diUb crystal structure has captured a compact conformation of K33-linked diUb, solution studies suggest open conformations for both chain types without formation of defined interfaces, as reported for chemically assembled K33-linked chains (Dixon et al., 2013).

Ub binding proteins can stabilize chain conformations (Ye et al., 2012), and it is therefore important to understand how polyUb is recognized by UBDs in a linkage-specific fashion. Our discovery of K29/K33 specificity in the N-terminal TRABID NZF1 domain enabled further insights into linkage-specific UBDs. NZF domains are small zinc-binding folds with remarkable linkage specificity that is achieved by bidentate interactions, whereby the ~30-aa NZF fold intercalates between and interacts with two Ub molecules. The TRABID NZF1 contacts the canonical Ile44 hydrophobic patch on the distal Ub and an unusual surface on the proximal Ub surrounding Glu24 of the Ub helix. The observed binding mode is validated by mutational analysis, which indicates that it may be shared between K29- and K33-linked chains, explaining TRABID NZF1 cross-specificity. The structure also explains why TAB2 or TRABID NZF2 and NZF3 are unable to bind K29/K33-linked chains in a similar manner.

assemble atypical linkages, only a subset have been characterized biochemically (Tran et al., 2013; You and Pickart, 2001). We show here that AREL1 predominantly assembles K33 linkages in free chains and on substrate proteins. Together with UBE3C, which has been reported to generate K48 and K29 linkages (You and Pickart, 2001), we provide a protocol to generate pure K29- and K33-linked polyUb enzymatically for in vitro analysis.

Our protocol to generate WT K29- or K33-linked polyUb relies on the recently discovered linkage specificity in DUBs, and we used these enzymes preparatively to remove unwanted linkage types in chains. Our redesigned forms of K48-specific OTUB1 and K63-specific AMSH are highly active and have proven to be useful for this purpose. Together with Ub chain restriction

A remarkable feature of the structure is the assembly of the K33 diUb with NZF1 into filaments that make up the entire crystal. In these filaments, each Ub-Ub contact is identical, each NZF domain binds two Ub molecules, and each Ub binds two NZF domains. The helical Ub filament bound to NZF1 domains provides an immediate model for interactions with the TRABID 3xNZF module, which, despite the lack of K29/K33 specificity in NZF2 and NZF3, could assemble on a Ub filament (Figure S7B). This is enabled by flexible linkers that vary in sequence and length but have a minimal length of 35 aa (NZF1-NZF2) and 28 aa (NZF2-NZF3) throughout evolution (Figure S7C). Such linkers would easily be able to bridge the space between adjacent NZF domains when binding a K29/K33 filament (Figure S7B).

Further studies by complementary techniques will be required to see whether K29- and K33-linked chains indeed form filaments in the presence of NZF1 in vivo. We have previously described the accumulation of catalytically inactive TRABID into characteristic Ub-containing puncta in cells, which depends on functional NZF domains (Licchesi et al., 2012). Here we extend these studies to show that, indeed, NZF1 and its K29/K33-specific binding mode are important for punctum formation. The cellular structures covered with K29/K33 chains that lead to punctum formation are intriguing and require further investigation.

Nonetheless, some new roles of K33-linked chains are emerging. AREL1 has been reported to ubiquitinate cytosolic inhibitor of apoptosis (IAP) antagonists, including SMAC, HtrA2, and ARTS, which leads to their proteasomal degradation (Kim et al., 2013). We show here that AREL1 polyubiquitinates SMAC and HtrA2 with >80% of K33 linkages in vitro. It will be interesting to see whether K33-linked chains can be linked to antiapoptotic signaling.

In cells, K33 chains have been found on AMPK kinases (together with K29-linked chains; Al-Hakim et al., 2008), on T cell receptor (TCR) ζ (Huang et al., 2010), and on Coronin-7 (Yuan et al., 2014). The latter study used an elegant Ub replacement strategy where cells express Ub K33R instead of WT Ub and revealed roles of this chain type in post-Golgi transport (Yuan et al., 2014). Interestingly, these reports and our previous work on TRABID (Licchesi et al., 2012) agreed that K33-linked chains are likely non-degradative, which is consistent with this chain type not being significantly enriched upon proteasomal inhibition (Kim et al., 2011). The ability of K33 chains to act as a proteasomal degradation signal requires further study.

Such in vivo studies of atypical chain types can now be supplemented with powerful biochemical tools reported here. The TRABID NZF1 domain could serve as an excellent tool in future studies, e.g., when used as a Ub chain sensor (Sims et al., 2012; van Wijk et al., 2012) or as a K29/K33-specific affinity reagent (Hjerpe et al., 2009). The availability of K29- and K33-linked polymers and new affinity reagents will enable a better understanding of these uncharacterized Ub signals.

EXPERIMENTAL PROCEDURES

Please see the Supplemental Experimental Procedures for more detailed information.

Protein Production

The His6-SUMO-AREL1 (436–823) and His6-SUMO-UBE3C (693–1083) constructs (both from the pOPIN-S vector) and the His6-GST-TRABID NZF construct (from the pOPIN-K vector) were expressed in Rosetta2 (DE3) pLacI cells and purified by affinity chromatography. Tags were removed by incubation with SENP1 or 3C protease. Further purification was performed by anion exchange and/or size exclusion chromatography.

Ub Chain Composition Mass Spectrometry Analysis

Ub chains were separated on a NuPAGE 4%–12% gradient gel (Invitrogen) before in-gel digestion with trypsin and the addition of Ub AQUA peptide internal standards according to Kirkpatrick et al. (2006). 10 μl of each sample was directly injected onto an EASY-Spray reverse-phase column (C18, 3 μm, 100 Å, 75 μm × 15 cm) using a Dionex UltiMate 3000 high-pressure liquid chromatography system (Thermo Fisher Scientific) and analyzed on a Q-Exactive mass spectrometer (Thermo Fisher Scientific) using parallel reaction monitoring (PRM), similar to Tsuchiya et al. (2013). Data were analyzed further according to Kirkpatrick et al. (2006).

K29 Chain Generation

K29-linked polyUb was assembled from 3 mM Ub, 1 μM E1, 10 μM UBE2L3, and 32 μM His6-SUMO UBE3C (aa 693–1083) in buffer containing 10 mM ATP, 10 mM MgCl₂, 40 mM Tris (pH 8.5), 100 mM NaCl, 0.6 mM DTT, and 10% (v/v) glycerol overnight at 37°C. After precipitation of enzymes by perchloric acid (0.25% [v/v]), unanchored chains were buffer-exchanged into 50 mM Tris (pH 7.4), 150 mM NaCl, and 4 mM DTT and treated with OTUB1* (1 μM), AMSH* (1 μM), and Cezanne (400 nM) for 60 min at 37°C. A second round of acid precipitation and cation exchange chromatography was used for purification.

K33 Chain Generation

K33-linked polyUb was assembled like K29-linked chains from a reaction that contained 36 μM AREL1 (aa 436–823) instead of UBE3C. The addition of 10% (v/v) glycerol in the reaction buffer prevented AREL1 precipitation during the reaction.

Pull-Down Assays

Pull-down assays were performed as described previously (Kulathu et al., 2009). Proteins were visualized by silver staining using the Silver Stain Plus kit (BioRad) according to manufacturer's protocols or by western blotting using a rabbit anti-Ub antibody (Millipore).

Nuclear Magnetic Resonance Studies

NMR experiments were performed in NMR PBS (18 mM Na₂HPO₄, 7 mM NaH₂PO₄ (pH 7.2), and 150 mM NaCl) with 5% D₂O added as a lock solvent. NMR acquisition was carried out at 298 K on a Bruker Avance III 600 MHz spectrometer equipped with a cryogenic triple resonance TCI probe. Topspin (Bruker) and Sparky (Goddard & Kneller, University of California San Francisco; http://www.cgl.ucsf.edu/home/sparky/) software packages were used for data processing and analysis, respectively. ^{1}H,^{15}N 2D BEST-TROSY experiments (Favier and Brutscher, 2011) allowed the calculation of weighted chemical shift perturbation using the equation $\sqrt{(\Delta^1H)^2+((\Delta^{15}N)^2/5)}$. K_d values for NZF-Ub interactions were determined according to Williamson (2013).

Crystallization, Data Collection, and Refinement

Crystals of K33-linked diUb, triUb, and of the TRABID NZF1-K33 diUb complex were grown by sitting drop vapor diffusion. Diffraction data were collected at Diamond Light Source beamlines I03 and I24, and the structures were solved by molecular replacement and refined to the final statistics in Table 1.

ACCESSION NUMBERS

Coordinates and structure factors for K33-linked di- and triUb and for TRABID NZF1-K33 diUb have been deposited with the protein data bank under accession codes 5AF4, 5AF5, and 5AF6.

REFERENCES

Al-Hakim, A.K., Zagorska, A., Chapman, L., Deak, M., Peggie, M., and Alessi, D.R. (2008). Control of AMPK-related kinases by USP9X and atypical Lys(29)/Lys(33)-linked polyubiquitin chains. Biochem. J. *411*, 249–260.

Alam, S.L., Sun, J., Payne, M., Welch, B.D., Blake, B.K., Davis, D.R., Meyer, H.H., Emr, S.D., and Sundquist, W.I. (2004). Ubiquitin interactions of NZF zinc fingers. EMBO J. *23*, 1411–1421.

Berndsen, C.E., and Wolberger, C. (2014). New insights into ubiquitin E3 ligase mechanism. Nat. Struct. Mol. Biol. *21*, 301–307.

Bremm, A., and Komander, D. (2011). Emerging roles for Lys11-linked polyubiquitin in cellular regulation. Trends Biochem. Sci. *36*, 355–363.

Bremm, A., Freund, S.M.V., and Komander, D. (2010). Lys11-linked ubiquitin chains adopt compact conformations and are preferentially hydrolyzed by the deubiquitinase Cezanne. Nat. Struct. Mol. Biol. *17*, 939–947.

Christianson, J.C., and Ye, Y. (2014). Cleaning up in the endoplasmic reticulum: ubiquitin in charge. Nat. Struct. Mol. Biol. *21*, 325–335.

Clague, M.J., Barsukov, I., Coulson, J.M., Liu, H., Rigden, D.J., and Urbé, S. (2013). Deubiquitylases from genes to organism. Physiol. Rev. *93*, 1289–1315.

Deshaies, R.J., and Joazeiro, C.A.P. (2009). RING domain E3 ubiquitin ligases. Annu. Rev. Biochem. *78*, 399–434.

Dixon, E.K., Castañeda, C.A., Kashyap, T.R., Wang, Y., and Fushman, D. (2013). Nonenzymatic assembly of branched polyubiquitin chains for structural and biochemical studies. Bioorg. Med. Chem. *21*, 3421–3429.

Favier, A., and Brutscher, B. (2011). Recovering lost magnetization: polarization enhancement in biomolecular NMR. J. Biomol. NMR *49*, 9–15.

Hershko, A., and Ciechanover, A. (1998). The ubiquitin system. Annu. Rev. Biochem. *67*, 425–479.

Hjerpe, R., Aillet, F., Lopitz-Otsoa, F., Lang, V., England, P., and Rodriguez, M.S. (2009). Efficient protection and isolation of ubiquitylated proteins using tandem ubiquitin-binding entities. EMBO Rep. *10*, 1250–1258.

Hospenthal, M.K., Freund, S.M.V., and Komander, D. (2013). Assembly, analysis and architecture of atypical ubiquitin chains. Nat. Struct. Mol. Biol. *20*, 555–565.

Huang, H., Jeon, M.-S., Liao, L., Yang, C., Elly, C., Yates, J.R., 3rd, and Liu, Y.-C. (2010). K33-linked polyubiquitination of T cell receptor-zeta regulates proteolysis-independent T cell signaling. Immunity *33*, 60–70.

Husnjak, K., and Dikic, I. (2012). Ubiquitin-binding proteins: decoders of ubiquitin-mediated cellular functions. Annu. Rev. Biochem. *81*, 291–322.

Iwai, K., Fujita, H., and Sasaki, Y. (2014). Linear ubiquitin chains: NF-κB signalling, cell death and beyond. Nat. Rev. Mol. Cell Biol. *15*, 503–508.

Kamadurai, H.B., Souphron, J., Scott, D.C., Duda, D.M., Miller, D.J., Stringer, D., Piper, R.C., and Schulman, B.A. (2009). Insights into ubiquitin transfer cascades from a structure of a UbcH5B approximately ubiquitin-HECT(NEDD4L) complex. Mol. Cell *36*, 1095–1102.

Kamadurai, H.B., Qiu, Y., Deng, A., Harrison, J.S., Macdonald, C., Actis, M., Rodrigues, P., Miller, D.J., Souphron, J., Lewis, S.M., et al. (2013). Mechanism of ubiquitin ligation and lysine prioritization by a HECT E3. eLife *2*, e00828–e00828.

Keusekotten, K., Elliott, P.R., Glockner, L., Fiil, B.K., Damgaard, R.B., Kulathu, Y., Wauer, T., Hospenthal, M.K., Gyrd-Hansen, M., Krappmann, D., et al. (2013). OTULIN antagonizes LUBAC signaling by specifically hydrolyzing Met1-linked polyubiquitin. Cell *153*, 1312–1326.

Kim, H.C., and Huibregtse, J.M. (2009). Polyubiquitination by HECT E3s and the determinants of chain type specificity. Mol. Cell. Biol. *29*, 3307–3318.

Kim, W., Bennett, E.J., Huttlin, E.L., Guo, A., Li, J., Possemato, A., Sowa, M.E., Rad, R., Rush, J., Comb, M.J., et al. (2011). Systematic and quantitative assessment of the ubiquitin-modified proteome. Mol. Cell *44*, 325–340.

Kim, J.B., Kim, S.Y., Kim, B.M., Lee, H., Kim, I., Yun, J., Jo, Y., Oh, T., Jo, Y., Chae, H.D., and Shin, D.Y. (2013). Identification of a novel anti-apoptotic E3 ubiquitin ligase that ubiquitinates antagonists of inhibitor of apoptosis proteins SMAC, HtrA2, and ARTS. J. Biol. Chem. *288*, 12014–12021.

Kirkpatrick, D.S., Hathaway, N.A., Hanna, J., Elsasser, S., Rush, J., Finley, D., King, R.W., and Gygi, S.P. (2006). Quantitative analysis of in vitro ubiquitinated cyclin B1 reveals complex chain topology. Nat. Cell Biol. *8*, 700–710.

Komander, D., and Rape, M. (2012). The ubiquitin code. Annu. Rev. Biochem. *81*, 203–229.

Komander, D., Clague, M.J., and Urbé, S. (2009). Breaking the chains: structure and function of the deubiquitinases. Nat. Rev. Mol. Cell Biol. *10*, 550–563.

Kulathu, Y., and Komander, D. (2012). Atypical ubiquitylation - the unexplored world of polyubiquitin beyond Lys48 and Lys63 linkages. Nat. Rev. Mol. Cell Biol. *13*, 508–523.

Kulathu, Y., Akutsu, M., Bremm, A., Hofmann, K., and Komander, D. (2009). Two-sided ubiquitin binding explains specificity of the TAB2 NZF domain. Nat. Struct. Mol. Biol. *16*, 1328–1330.

Licchesi, J.D.F., Mieszczanek, J., Mevissen, T.E.T., Rutherford, T.J., Akutsu, M., Virdee, S., El Oualid, F., Chin, J.W., Ovaa, H., Bienz, M., and Komander, D. (2012). An ankyrin-repeat ubiquitin-binding domain determines TRABID's specificity for atypical ubiquitin chains. Nat. Struct. Mol. Biol. *19*, 62–71.

Maspero, E., Valentini, E., Mari, S., Cecatiello, V., Soffientini, P., Pasqualato, S., and Polo, S. (2013). Structure of a ubiquitin-loaded HECT ligase reveals the molecular basis for catalytic priming. Nat. Struct. Mol. Biol. *20*, 696–701.

Mattiroli, F., and Sixma, T.K. (2014). Lysine-targeting specificity in ubiquitin and ubiquitin-like modification pathways. Nat. Struct. Mol. Biol. *21*, 308–316.

Mevissen, T.E.T., Hospenthal, M.K., Geurink, P.P., Elliott, P.R., Akutsu, M., Arnaudo, N., Ekkebus, R., Kulathu, Y., Wauer, T., El Oualid, F., et al. (2013). OTU deubiquitinases reveal mechanisms of linkage specificity and enable ubiquitin chain restriction analysis. Cell *154*, 169–184.

Ritorto, M.S., Ewan, R., Perez-Oliva, A.B., Knebel, A., Buhrlage, S.J., Wightman, M., Kelly, S.M., Wood, N.T., Virdee, S., Gray, N.S., et al. (2014).

Screening of DUB activity and specificity by MALDI-TOF mass spectrometry. Nat. Commun. *5*, 4763.

Rivkin, E., Almeida, S.M., Ceccarelli, D.F., Juang, Y.-C., MacLean, T.A., Srikumar, T., Huang, H., Dunham, W.H., Fukumura, R., Xie, G., et al. (2013). The linear ubiquitin-specific deubiquitinase gumby regulates angiogenesis. Nature *498*, 318–324.

Rotin, D., and Kumar, S. (2009). Physiological functions of the HECT family of ubiquitin ligases. Nat. Rev. Mol. Cell Biol. *10*, 398–409.

Sato, Y., Yoshikawa, A., Yamashita, M., Yamagata, A., and Fukai, S. (2009). Structural basis for specific recognition of Lys 63-linked polyubiquitin chains by NZF domains of TAB2 and TAB3. EMBO J. *28*, 3903–3909.

Sato, Y., Fujita, H., Yoshikawa, A., Yamashita, M., Yamagata, A., Kaiser, S.E., Iwai, K., and Fukai, S. (2011). Specific recognition of linear ubiquitin chains by the Npl4 zinc finger (NZF) domain of the HOIL-1L subunit of the linear ubiquitin chain assembly complex. Proc. Natl. Acad. Sci. USA *108*, 20520–20525.

Scheffner, M., Huibregtse, J.M., Vierstra, R.D., and Howley, P.M. (1993). The HPV-16 E6 and E6-AP complex functions as a ubiquitin-protein ligase in the ubiquitination of p53. Cell *75*, 495–505.

Schulman, B.A., and Harper, J.W. (2009). Ubiquitin-like protein activation by E1 enzymes: the apex for downstream signalling pathways. Nat. Rev. Mol. Cell Biol. *10*, 319–331.

Shaid, S., Brandts, C.H., Serve, H., and Dikic, I. (2013). Ubiquitination and selective autophagy. Cell Death Differ. *20*, 21–30.

Sims, J.J., Scavone, F., Cooper, E.M., Kane, L.A., Youle, R.J., Boeke, J.D., and Cohen, R.E. (2012). Polyubiquitin-sensor proteins reveal localization and linkage-type dependence of cellular ubiquitin signaling. Nat. Methods *9*, 303–309.

Tran, H., Hamada, F., Schwarz-Romond, T., and Bienz, M. (2008). Trabid, a new positive regulator of Wnt-induced transcription with preference for binding and cleaving K63-linked ubiquitin chains. Genes Dev. *22*, 528–542.

Tran, H., Bustos, D., Yeh, R., Rubinfeld, B., Lam, C., Shriver, S., Zilberleyb, I., Lee, M.W., Phu, L., Sarkar, A.A., et al. (2013). HectD1 E3 ligase modifies adenomatous polyposis coli (APC) with polyubiquitin to promote the APC-axin interaction. J. Biol. Chem. *288*, 3753–3767.

Tsuchiya, H., Tanaka, K., and Saeki, Y. (2013). The parallel reaction monitoring method contributes to a highly sensitive polyubiquitin chain quantification. Biochem. Biophys. Res. Commun. *436*, 223–229.

van Wijk, S.J.L., Fiskin, E., Putyrski, M., Pampaloni, F., Hou, J., Wild, P., Kensche, T., Grecco, H.E., Bastiaens, P., and Dikic, I. (2012). Fluorescence-based sensors to monitor localization and functions of linear and K63-linked ubiquitin chains in cells. Mol. Cell *47*, 797–809.

Varadan, R., Walker, O., Pickart, C., and Fushman, D. (2002). Structural properties of polyubiquitin chains in solution. J. Mol. Biol. *324*, 637–647.

Varadan, R., Assfalg, M., Haririnia, A., Raasi, S., Pickart, C., and Fushman, D. (2004). Solution conformation of Lys63-linked di-ubiquitin chain provides clues to functional diversity of polyubiquitin signaling. J. Biol. Chem. *279*, 7055–7063.

Vijay-Kumar, S., Bugg, C.E., and Cook, W.J. (1987). Structure of ubiquitin refined at 1.8 A resolution. J. Mol. Biol. *194*, 531–544.

Virdee, S., Ye, Y., Nguyen, D.P., Komander, D., and Chin, J.W. (2010). Engineered diubiquitin synthesis reveals Lys29-isopeptide specificity of an OTU deubiquitinase. Nat. Chem. Biol. *6*, 750–757.

Wagner, S.A., Beli, P., Weinert, B.T., Nielsen, M.L., Cox, J., Mann, M., and Choudhary, C. (2011). A proteome-wide, quantitative survey of in vivo ubiquitylation sites reveals widespread regulatory roles. Mol Cell Proteomics, M111.013284.

Wickliffe, K.E., Williamson, A., Meyer, H.-J., Kelly, A., and Rape, M. (2011). K11-linked ubiquitin chains as novel regulators of cell division. Trends Cell Biol. *21*, 656–663.

Williamson, M.P. (2013). Using chemical shift perturbation to characterise ligand binding. Prog. Nucl. Magn. Reson. Spectrosc. *73*, 1–16.

Xu, P., Duong, D.M., Seyfried, N.T., Cheng, D., Xie, Y., Robert, J., Rush, J., Hochstrasser, M., Finley, D., and Peng, J. (2009). Quantitative proteomics reveals the function of unconventional ubiquitin chains in proteasomal degradation. Cell *137*, 133–145.

Ye, Y., and Rape, M. (2009). Building ubiquitin chains: E2 enzymes at work. Nat. Rev. Mol. Cell Biol. *10*, 755–764.

Ye, Y., Blaser, G., Horrocks, M.H., Ruedas-Rama, M.J., Ibrahim, S., Zhukov, A.A., Orte, A., Klenerman, D., Jackson, S.E., and Komander, D. (2012). Ubiquitin chain conformation regulates recognition and activity of interacting proteins. Nature *492*, 266–270.

You, J., and Pickart, C.M. (2001). A HECT domain E3 enzyme assembles novel polyubiquitin chains. J. Biol. Chem. *276*, 19871–19878.

Yuan, W.-C., Lee, Y.-R., Lin, S.-Y., Chang, L.-Y., Tan, Y.P., Hung, C.-C., Kuo, J.-C., Liu, C.-H., Lin, M.-Y., Xu, M., et al. (2014). K33-Linked Polyubiquitination of Coronin 7 by Cul3-KLHL20 Ubiquitin E3 Ligase Regulates Protein Trafficking. Mol. Cell *54*, 586–600.

LETTER

Mechanism of phospho–ubiquitin–induced PARKIN activation

Tobias Wauer[1], Michal Simicek[1], Alexander Schubert[1] & David Komander[1]

The E3 ubiquitin ligase PARKIN (encoded by *PARK2*) and the protein kinase PINK1 (encoded by *PARK6*) are mutated in autosomal-recessive juvenile Parkinsonism (AR-JP) and work together in the disposal of damaged mitochondria by mitophagy[1–3]. PINK1 is stabilized on the outside of depolarized mitochondria and phosphorylates polyubiquitin[4–8] as well as the PARKIN ubiquitin-like (Ubl) domain[9,10]. These phosphorylation events lead to PARKIN recruitment to mitochondria, and activation by an unknown allosteric mechanism[4–12]. Here we present the crystal structure of *Pediculus humanus* PARKIN in complex with Ser65-phosphorylated ubiquitin (phosphoUb), revealing the molecular basis for PARKIN recruitment and activation. The phosphoUb binding site on PARKIN comprises a conserved phosphate pocket and harbours residues mutated in patients with AR-JP. PhosphoUb binding leads to straightening of a helix in the RING1 domain, and the resulting conformational changes release the Ubl domain from the PARKIN core; this activates PARKIN. Moreover, phosphoUb-mediated Ubl release enhances Ubl phosphorylation by PINK1, leading to conformational changes within the Ubl domain and stabilization of an open, active conformation of PARKIN. We redefine the role of the Ubl domain not only as an inhibitory[13] but also as an activating element that is restrained in inactive PARKIN and released by phosphoUb. Our work opens up new avenues to identify small-molecule PARKIN activators.

The RING-between-RING E3 ligase PARKIN contains a RING1 domain that binds ubiquitin-charged E2 enzymes, and transfers ubiquitin from the E2 to an active site Cys residue in the RING2 domain and subsequently to a substrate. Cytosolic PARKIN exists in an autoinhibited, 'closed' conformation[13–16], in which binding to E2 is blocked by the amino-terminal Ubl domain as well as by a 'repressor' element (REP), and access to the RING2 active site Cys is blocked by the unique PARKIN domain (UPD, also known as RING0) (Extended Data Fig. 1). PhosphoUb binding and/or PARKIN Ubl phosphorylation are presumed to induce conformational domain rearrangements to activate PARKIN[13–16]; however, the mechanism and sequence of events are unclear. Once activated, PARKIN ubiquitinates numerous mitochondrial and cytosolic proteins[17], eventually triggering mitophagy.

To understand how phosphoUb induces PARKIN activation, we used PINK1-phosphorylated 'ubiquitin suicide probes'[18] that can modify Cys residues near a ubiquitin binding site *in vitro*[19] (Fig. 1a and Extended Data Fig. 1d). Probes could not modify a previously crystallized construct of human PARKIN lacking the Ubl domain[14] (*Hs*PARKIN(ΔUbl), amino acids 137–465) (Fig. 1b). Unexpectedly, a similar fragment of *Pediculus humanus corporis* (human body louse) PARKIN (amino acids 140–461, hereafter referred to as *Ph*PARKIN) was modified by a subset of phosphoUb (pUb) suicide probes (Fig. 1b), enabling purification of the *Ph*PARKIN–pUb complex and determination of a crystal structure at 2.6 Å resolution (Fig. 1c, Methods and
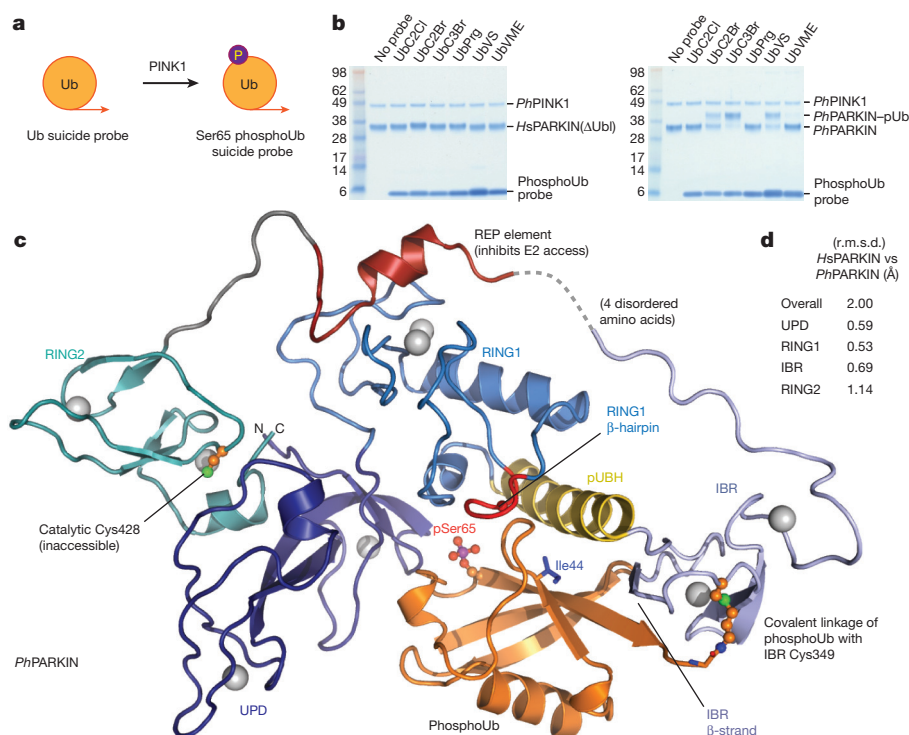

Figure 1 | Generation and structure of *Ph*PARKIN–phosphoUb complex. a, Schematic of the generation of phosphoUb suicide probes used in this study. **b,** *Hs*PARKIN(ΔUbl) (left, amino acids 137–465) and *Ph*PARKIN (right, amino acids 140–461) were incubated with indicated ubiquitin suicide probes[18] for 1 h in the presence of *Ph*PINK1 (Methods and Extended Data Fig. 1d) and resolved on Coomassie-stained SDS–PAGE gels. UbC2Cl, Ub chloroethylamine; UbC2Br, Ub bromoethylamine; UbC3Br, Ub bromopropylamine; UbPrg, Ub propargyl; UbVS, Ub vinylmethylsulfone; UbVME, Ub vinylmethylester. The experiment was performed three times with consistent results. Molecular weight markers are in kDa. **c,** Structure of the *Ph*PARKIN–pUb complex with domains coloured from blue to cyan (UPD, RING1, IBR, RING2), grey zinc atoms, red REP, yellow phosphoUb binding helix (pUBH), and orange phosphoUb. The catalytic Cys in RING2, and key phosphoUb residues, are indicated. **d,** Root mean squared deviation (r.m.s.d.) values for *Ph*PARKIN in comparison to *Hs*PARKIN (Protein Data Bank (PDB) accession 4BM9 (ref. 14)).

[1]Medical Research Council Laboratory of Molecular Biology, Francis Crick Avenue, Cambridge CB2 0QH, UK.

Extended Data Figs 1e and 2a). *Ph*PARKIN–pUb resembles autoinhibited structures of *Hs*PARKIN (Fig. 1c, d and Extended Data Fig. 2e), with key differences as described below. The phosphoUb suicide probe had modified Cys349 in the *Ph*PARKIN in-between-RING (IBR) domain (Figs 1c and 2a), which in *Hs*PARKIN corresponds to probe-unreactive Gln347. Notably, *Hs*PARKIN Q347C is modified by phosphoUb suicide probes (Fig. 2b), indicating a similar binding mode of phosphoUb in *Hs*PARKIN. Hence, our complex structure serves as model for phosphoUb binding to *Hs*PARKIN.

PhosphoUb forms an extended interface (1,150 Å², 25% of ubiquitin surface) with the RING1 and IBR domains in *Ph*PARKIN, and also

interacts with side chains of the UPD (Fig. 2a and Extended Data Fig. 3). Key interactions are formed (1) via the phosphate group, which is located in a pocket formed by His304, Arg307 and Tyr314 of *Ph*PARKIN (Fig. 2c); (2) via the hydrophobic Ile44 patch of phosphoUb, which binds to an extended helix in the RING1 domain (amino acids 311–329, hereafter referred to as phosphoUb binding helix (pUBH)); (3) via a conserved surface β-hairpin loop (amino acids 280–288) in RING1 that harbours AR-JP mutations; and (4) via the phosphoUb carboxy terminus, which forms an intermolecular parallel β-sheet with a β-strand of the IBR domain (Figs 1c and 2a). Most residues forming phosphoUb interactions in *Ph*PARKIN are
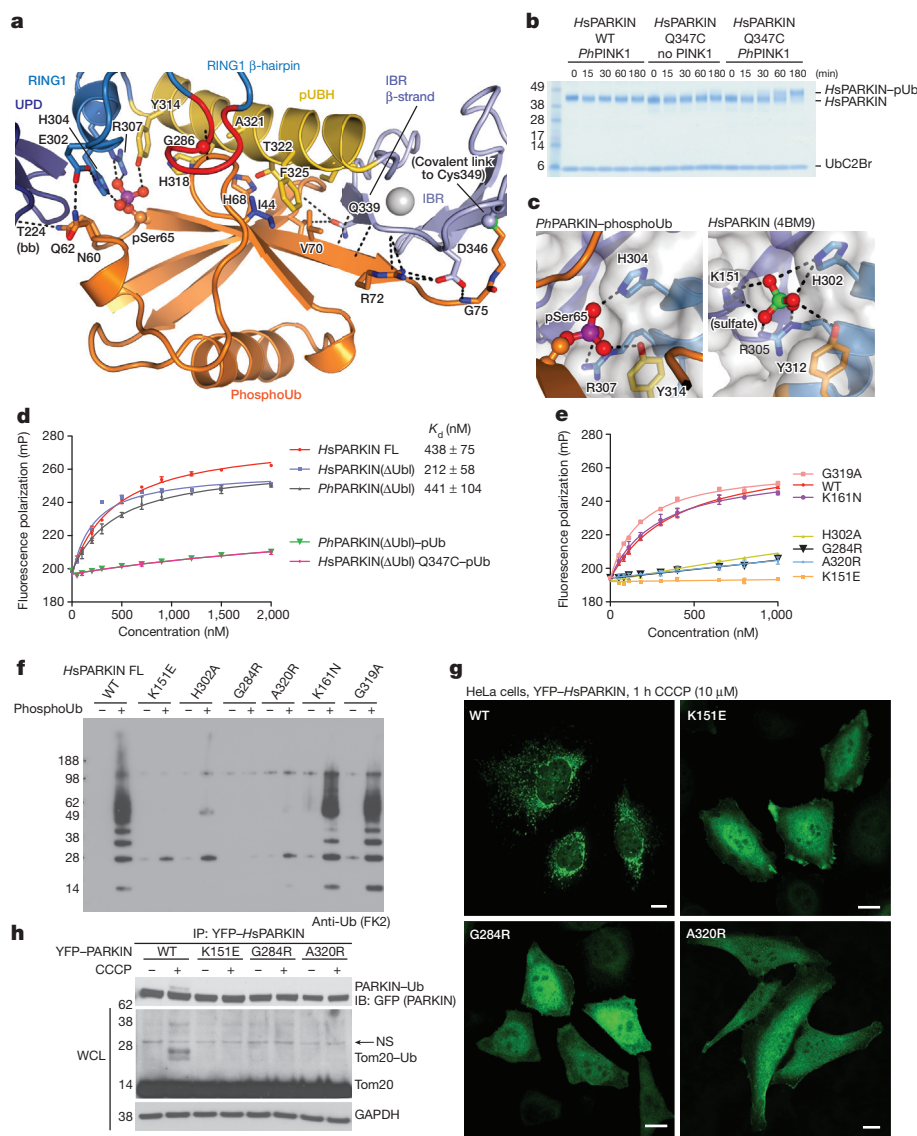

Figure 2 | PhosphoUb binding to PARKIN. a, PhosphoUb binding site on *Ph*PARKIN as in Fig. 1c. Dotted lines indicate hydrogen bonds. The RING1 β-hairpin that harbours patient mutations is highlighted in red. bb, backbone contacts. **b**, PhosphoUb suicide probe reactions as in Fig. 1b with UbC2Br and GST–*Ph*PINK1. The experiment was performed three times with consistent results. **c**, Occupied Ser65 phosphate pocket in *Ph*PARKIN (left); identical pocket in *Hs*PARKIN occupied by a sulfate ion in PDB 4BM9 (ref. 14) (right). **d**, Fluorescence polarization experiments characterizing the binding of FlAsH-tagged phosphoUb to PARKIN variants. Measurements were performed in triplicate and error bars represent standard deviation from the mean. mP, milli-polarization unit. **e**, Binding assays as in **d** with full-length *Hs*PARKIN and mutants in the phosphoUb binding site. Binding curves were compiled from experiments shown in Extended Data Fig. 3d. Measurements were performed in triplicate and error bars represent standard deviation from the mean.

f, Activity assays of full-length *Hs*PARKIN variants with and without phosphoUb. After 2 h, reactions were resolved by SDS–PAGE and polyubiquitin visualized by anti-polyubiquitin western blotting (FK2, Millipore). PARKIN protein normalization is shown in Extended Data Fig. 3e. The experiment was performed three times with consistent results. **g**, YFP–*Hs*PARKIN wild type or mutants were transfected into HeLa cells, treated with CCCP (10 μM) for 1 h and visualized by immunofluorescence. See Extended Data Fig. 4 for controls and quantification. Scale bars, 10 μm. **h**, HeLa cell lysates expressing YFP–*Hs*PARKIN wild type or mutants were western blotted for PARKIN (after immunoprecipitation (IP)) and Tom20 (in whole-cell lysate (WCL)). NS, non-specific band. The experiment was performed at least twice as biological replicate for every mutant with consistent results. See Extended Data Fig. 4d and Supplementary Information. Molecular weight markers are in kDa for **b**, **f**, **h**.

conserved in *Hs*PARKIN (Extended Data Fig. 3a–c), and in our previous *Hs*PARKIN structure[14] the phosphate pocket is occupied by a sulfate molecule from the crystallization condition (Fig. 2c).

A fluorescence-polarization-based phosphoUb binding assay revealed sub-micromolar interactions of phosphoUb with full-length *Hs*PARKIN, *Hs*PARKIN(ΔUbl) and *Ph*PARKIN (Fig. 2d). Modification with phosphoUb suicide probes of *Ph*PARKIN or *Hs*PARKIN Q347C (*Hs*PARKIN Q347C–pUb) abrogated phosphoUb binding (Fig. 2d), indicating that the covalently bound phosphoUb molecule satisfied the major phosphoUb binding site.

Mutations in the predicted phosphoUb interface in *Hs*PARKIN reduced or abrogated phosphoUb binding (Fig. 2e and Extended Data Fig. 3d). *Hs*PARKIN K151E (in the phosphate pocket; Fig. 2c, Ala152 in *Ph*PARKIN), A320R (pUBH, Thr322 in *Ph*PARKIN, Fig. 2a) or G284R (β-hairpin, Gly286 in *Ph*PARKIN, Fig. 2a) abrogated phosphoUb binding (Fig. 2e). *Hs*PARKIN G284R is an AR-JP-derived patient mutation, and our data provide a rationale for how this mutation leads to defects in PARKIN function (see below). Similarly, AR-JP mutation L283P (ref. 20) and cancer-associated H279P (ref. 21) in this region might also disrupt this loop and affect phosphoUb binding to *Hs*PARKIN.

PARKIN activity can be assessed in autoubiquitination assays[4–7,14]. *Hs*PARKIN was activated by phosphoUb, whereas *Hs*PARKIN K151E, H302A, A320R or G284R showed impaired phosphoUb-induced activation (Fig. 2f). *Hs*PARKIN K161N (an AR-JP mutation on the UPD[14], see below) and *Hs*PARKIN G319A (see below) bound to and were activated by phosphoUb (Fig. 2e, f and Extended Data Fig. 3d, e).

In HeLa cells, carbonyl cyanide *m*-chlorophenyl hydrazone (CCCP)-mediated depolarization of mitochondria led to rapid mitochondrial localization of yellow fluorescent protein (YFP)-tagged *Hs*PARKIN, while phosphoUb-binding mutants did not show mitochondrial localization (Fig. 2g and Extended Data Fig. 4a–c). Moreover, wild-type *Hs*PARKIN ubiquitinated endogenous Tom20 after CCCP treatment, while phosphoUb-binding mutants showed no apparent activity (Fig. 2h and Extended Data Fig. 4d).

Hence, we reveal that the phosphoUb binding site in PARKIN, which is conserved in divergent species, harbours AR-JP patient mutations and is important for PARKIN localization in cells (Fig. 2). This provides the molecular basis for PARKIN translocation to mitochondrial phosphoUb[7,11,22] (Extended Data Fig. 3g).

Next we addressed the question of how phosphoUb activates PARKIN. PhosphoUb binds to a straight helix, pUBH, in *Ph*PARKIN (Figs 2 and 3). In previous PARKIN structures[14–16] this helix is kinked at Gly319 (Ala321 in *Ph*PARKIN). The distinct conformation of the pUBH does not originate from this sequence difference; a crystal structure of *Hs*PARKIN(ΔUbl) G319A still shows a kinked pUBH conformation (Extended Data Figs 1e and 5) and *Hs*PARKIN wild type and G319A have similar biochemical properties (Fig. 2e, f and Extended Data Fig. 3d, e). Notably, RING1 of the RBR E3 ligase HHARI (ref. 23) also features a kinked helix in the autoinhibited state (see Extended Data Fig. 5e–h). A kinked helix would be unable to bind phosphoUb, leading to a model in which the pUBH is dynamic and straightens upon phosphoUb binding. pUBH straightening hardly affects RING1 (Extended Data Fig. 6a) but impacts on the position of the IBR domain (Figs 2 and 3a, b), which rotates and moves by >20 Å as compared to full-length rat PARKIN (*Rn*PARKIN)[16] (Fig. 3a). The conformational change stretches the IBR–REP linker (14–15 amino acids, Extended Data Fig. 2a) from spanning 31 Å in *Rn*PARKIN to cover a distance of 43 Å in *Ph*PARKIN–pUb (Fig. 3b and Extended Data Fig. 6b). This appears to destabilize inhibitory interactions of REP and RING2 as suggested by increased B-factors for these domains in *Ph*PARKIN–pUb (Extended Data Fig. 6c, d).

More importantly, phosphoUb binding also destabilizes the interface between the PARKIN Ubl domain and the RBR core, due to displacement of the IBR domain and reorganization of the IBR–REP linker that no longer spans the Ubl surface (Fig. 3b). Using isothermal titration calorimetry (ITC), we detected binding of isolated *Hs*PARKIN Ubl (amino acids 1–72) to *Hs*PARKIN(ΔUbl) in *trans* (Fig. 3c, dissociation constant (K_d) ~40 μM). Notably, binding is undetectable in the
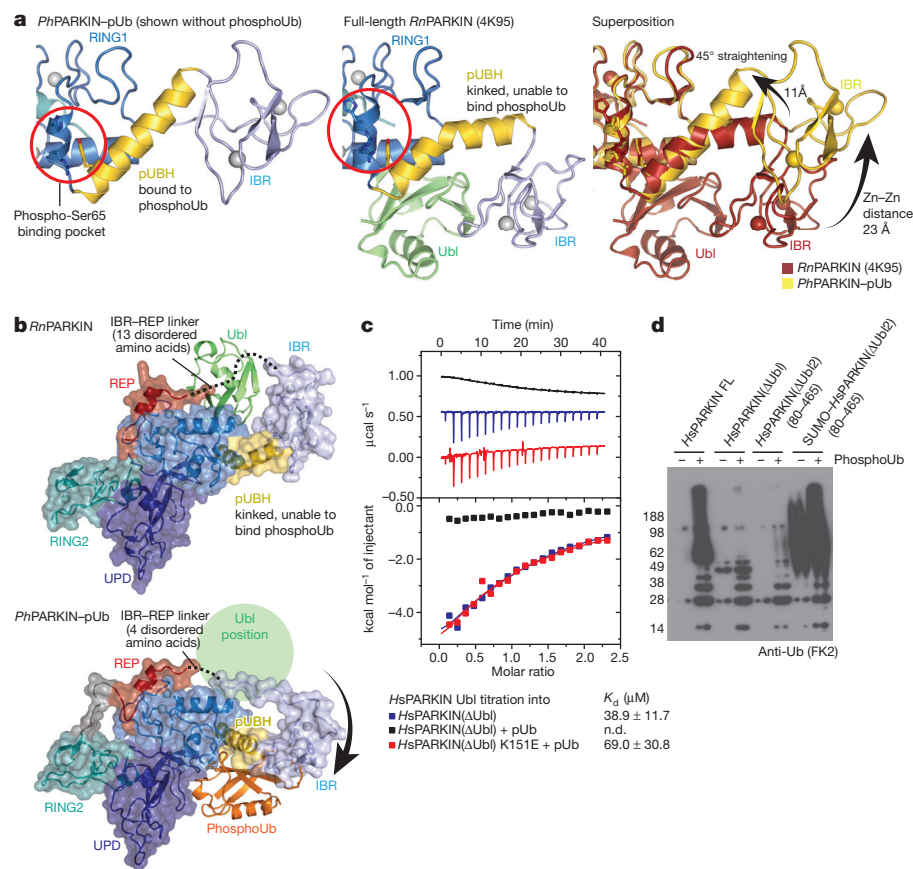

Figure 3 | Conformational changes due to phosphoUb binding. a, Straight pUBH in *Ph*PARKIN–pUb (left) versus kinked pUBH in previous PARKIN structures (middle; shown is full-length *Rn*PARKIN, PDB 4K95 (ref. 16)). Superposition indicating IBR repositioning by >20 Å (right). **b**, Full-length *Rn*PARKIN (top) with core domains under a transparent surface and Ubl as green cartoon, and *Ph*PARKIN–pUb (bottom), with a green circle indicating the putative Ubl binding site; phosphoUb is in orange. **c**, ITC experiment titrating *Hs*PARKIN Ubl domain into *Hs*PARKIN(ΔUbl) without phosphoUb (blue curve, K_d ~39 μM), with phosphoUb present (black curve, K_d not detectable (n.d.)), and *Hs*PARKIN K151E with phosphoUb present (red curve, K_d ~69 μM). Heat release curves (top panel) were shifted in their *y*-axis position for better visibility. Dissociation constant and curve fitting errors are indicated. All measurements were performed three times with consistent results. **d**, Activity of full-length *Hs*PARKIN, *Hs*PARKIN(ΔUbl) (137–465), *Hs*PARKIN(ΔUbl2) (80–465) and SUMO-tagged *Hs*PARKIN(ΔUbl2) (80–465) with or without phosphoUb for 1 h (see Fig. 2f and Extended Data Fig. 3f). Experiments were performed three times with consistent results. Molecular weight markers are in kDa.

presence of phosphoUb, but recovered with phosphoUb-binding-deficient *Hs*PARKIN(ΔUbl) K151E mutant (Fig. 3c). Hence, phosphoUb binding releases the Ubl from the PARKIN RBR core.

PARKIN variants lacking the Ubl domain are still autoinhibited[14–16] and less well activated by phosphoUb in comparison to full-length PARKIN[7] (Fig. 3d). This indicates that the presence of the Ubl domain is important for full PARKIN activity. Interestingly, replacing the Ubl domain (amino acids 1–79) with SUMO, which lacks a Ubl-like hydrophobic patch and would not bind RING1, activates PARKIN constitutively, even in the absence of phosphoUb. This suggests that the released Ubl domain actively helps to unravel the autoinhibited PARKIN conformation. This, together with destabilization of the REP and RING2 autoinhibitory interactions, enables RING1 to bind and discharge E2–Ub conjugates[4], and explains how PARKIN is activated by phosphoUb.

An alternative mechanism to activate PARKIN is PINK1-mediated phosphorylation of Ser65 in the Ubl domain[7,9,10], which was also sug-

gested to release the Ubl domain from the PARKIN core[9,24]. In the closed conformation of PARKIN, the Ubl domain binds via its Ile44 patch to RING1 (refs 13, 16) (Fig. 4a and Extended Data Fig. 1). Importantly, PINK1 did not phosphorylate *Hs*PARKIN Ubl I44A (or ubiquitin I44A) efficiently (Extended Data Fig. 7a, b). This suggests that PARKIN and PINK1 utilize overlapping binding sites on the Ubl domain, and that the Ubl domain has to be released from the PARKIN core for PINK1 to access and phosphorylate it.

Consistently, using a phosphospecific antibody against PARKIN phospho-Ser65 (anti-pSer65 PARKIN), we found that PARKIN phosphorylation is significantly enhanced when phosphoUb is added to the reaction, and this depends on ubiquitin phosphorylation and phosphoUb binding (Fig. 4c and Extended Data Fig. 7c, d). Induced release of the Ubl domain by mutating the binding site on RING1 (*Hs*PARKIN L266R, Fig. 4a) leads to phosphorylation by PINK1 in the absence of phosphoUb (Fig. 4c and Extended Data Fig. 7c, d),
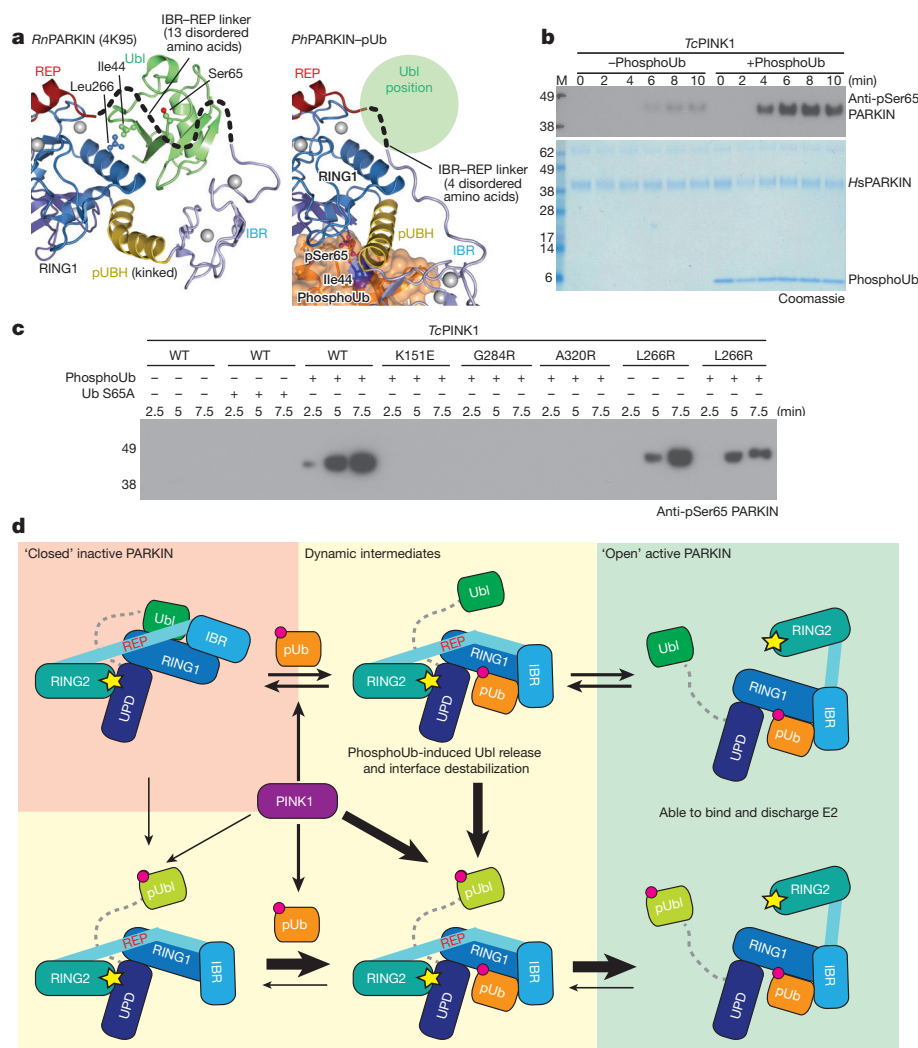

Figure 4 | PhosphoUb induces PARKIN Ubl phosphorylation and model of PARKIN activation. **a**, Detail of the Ubl position on PARKIN. Ubl Ile44 and interacting Leu266 on RING1 are highlighted. The mostly disordered IBR–REP linker hovers above Ser65 and moves out of the way in *Ph*PARKIN–pUb (compare Fig. 3b). **b**, Time course of phosphorylation of *Hs*PARKIN by GST–*Tc*PINK1 (*Tribolium castaneum* PINK1), in the absence and presence of phosphoUb at 37 °C, visualized with anti-pSer65 PARKIN antibody (Abcam catalogue number ab154995) (top) and Coomassie (bottom). The experiment was performed three times with consistent results. **c**, Experiment as in **b** but performed at 22 °C with lower phosphoUb concentration (5.8 μM). The experiment was performed three times with consistent results. Also see Extended Data Fig. 7c, d. **d**, Model of PARKIN activation. PARKIN

is autoinhibited (top left) by multiple mechanisms (Extended Data Fig. 1). Inactive PARKIN can interact with phosphoUb, which releases the Ubl domain, destabilizes inhibitory interactions and 'opens' PARKIN (top row). This process is reversible. PARKIN can also be phosphorylated by PINK1, either directly (bottom left) or with improved kinetics after phosphoUb binding (bottom middle). Phosphorylated Ubl undergoes a conformational change (Extended Data Fig. 8), probably preventing it from reverting back to the autoinhibited state. Phosphorylation of PARKIN hence stabilizes an open, active conformation (bottom right). Thickness of arrows indicates preferred routes. Further information on the role of Ubl phosphorylation is in Extended Data Figs 9 and 10. Molecular weight markers are in kDa for **b** and **c**.

indicating that Ubl release is crucial for enhanced phosphorylation. These results reveal a new function for phosphoUb, namely to enable phosphorylation of the Ubl domain (Fig. 4). However, PINK1 can phosphorylate PARKIN in the absence of phosphoUb *in vitro* (albeit inefficiently, Fig. 4b) and in cells[7,25], showing that PARKIN is a dynamic molecule (Fig. 4d) in which the Ubl domain is partially accessible by PINK1.

We next examined consequences of Ubl phosphorylation in *Hs*PARKIN. Nuclear magnetic resonance measurements reveal that the Ubl domain undergoes significant changes when phosphorylated, in particular in the Ser65 loop and the Ile44 patch (Extended Data Fig. 8). Disruption of the Ile44 patch prevents re-binding of the Ubl domain to RING1[13,24], and probably stabilizes a more open, active conformation of PARKIN. Moreover, this may also explain why the phosphorylated Ubl domain cannot compete with phosphoUb for the phosphoUb binding site (Extended Data Fig. 9). Phosphorylated *Hs*PARKIN does not impede binding of phosphoUb, but rather enhances it[7] (Extended Data Fig. 9).

Together, this completes our model of PARKIN activation (Fig. 4d). Autoinhibited PARKIN (Fig. 4d, top left) responds to phosphoUb on mitochondria, which releases the Ubl to activate PARKIN in a reversible manner (Fig. 4d, top row). PINK1 phosphorylates PARKIN preferentially when the Ubl domain is released (Fig. 4d, bottom middle), and this leads to irreversible PARKIN activation (Fig. 4d, bottom right). Alternatively, inactive PARKIN may be phosphorylated by PINK1 directly[7,25] (Fig. 4d, bottom left); this improves phosphoUb binding, retains PARKIN on mitochondria, and irreversibly activates PARKIN (Fig. 4d, bottom row).

The conformation of fully active PARKIN remains elusive. Phosphorylated PARKIN but not phosphoUb-activated PARKIN exposes its active site Cys residue[7] (Extended Data Fig. 10), further indicating that PARKIN phosphorylation leads to 'opening' of PARKIN. Notably, mutations in a putative second phosphate pocket in the UPD, which we reported previously[14] and which is distinct from the pocket involved in phosphoUb binding, prevents phospho-Ubl-induced PARKIN opening and activation (Extended Data Fig. 10c, d). The functional link between PARKIN phosphorylation and a putative phosphate-binding pocket in the UPD may suggest that the phosphorylated Ubl domain binds back to the UPD; however, alternative activation mechanisms or the involvement of the Ubl–UPD linker cannot be excluded.

Our work is consistent with suggested models of PARKIN-mediated mitophagy[7,25–28] and provides a structural understanding for phosphoUb binding and allosteric PARKIN activation. We refine the role of the PARKIN Ubl domain as an essential activating element that is restrained in autoinhibited PARKIN. The model ensures tight temporal and spatial regulation of PARKIN activity, and incorporates a commitment step whereby PARKIN phosphorylation locks PARKIN in the active, open conformation. Our insights may prove useful pharmacologically, since small molecules that dislodge the PARKIN Ubl domain from the PARKIN core may activate PARKIN and benefit patients with Parkinson's disease.

Online Content Methods, along with any additional Extended Data display items and Source Data, are available in the online version of the paper; references unique to these sections appear only in the online paper.

1. Youle, R. J. & Narendra, D. P. Mechanisms of mitophagy. *Nature Rev. Mol. Cell Biol.* **12,** 9–14 (2011).
2. Corti, O., Lesage, S. & Brice, A. What genetics tells us about the causes and mechanisms of Parkinson's disease. *Physiol. Rev.* **91,** 1161–1218 (2011).
3. Corti, O. & Brice, A. Mitochondrial quality control turns out to be the principal suspect in parkin and PINK1-related autosomal recessive Parkinson's disease. *Curr. Opin. Neurobiol.* **23,** 100–108 (2013).
4. Koyano, F. *et al.* Ubiquitin is phosphorylated by PINK1 to activate parkin. *Nature* **510,** 162–166 (2014).
5. Kane, L. A. *et al.* PINK1 phosphorylates ubiquitin to activate Parkin E3 ubiquitin ligase activity. *J. Cell Biol.* **205,** 143–153 (2014).
6. Kazlauskaite, A. *et al.* Parkin is activated by PINK1-dependent phosphorylation of ubiquitin at Ser65. *Biochem. J.* **460,** 127–139 (2014).
7. Ordureau, A. *et al.* Quantitative proteomics reveal a feedforward mechanism for mitochondrial PARKIN translocation and ubiquitin chain synthesis. *Mol. Cell* **56,** 360–375 (2014).
8. Wauer, T. *et al.* Ubiquitin Ser65 phosphorylation affects ubiquitin structure, chain assembly and hydrolysis. *EMBO J.* **34,** 307–325 (2015).
9. Kondapalli, C. *et al.* PINK1 is activated by mitochondrial membrane potential depolarization and stimulates Parkin E3 ligase activity by phosphorylating serine 65. *Open Biol.* **2,** 120080 (2012).
10. Shiba-Fukushima, K. *et al.* PINK1-mediated phosphorylation of the Parkin ubiquitin-like domain primes mitochondrial translocation of Parkin and regulates mitophagy. *Sci. Rep.* **2,** 1002 (2012).
11. Shiba-Fukushima, K. *et al.* Phosphorylation of mitochondrial polyubiquitin by PINK1 promotes Parkin mitochondrial tethering. *PLoS Genet.* **10,** e1004861 (2014).
12. Okatsu, K. *et al.* Phosphorylated ubiquitin chain is the genuine Parkin receptor. *J. Cell Biol.* **209,** 111–128 (2015).
13. Chaugule, V. K. *et al.* Autoregulation of Parkin activity through its ubiquitin-like domain. *EMBO J.* **30,** 2853–2867 (2011).
14. Wauer, T. & Komander, D. Structure of the human Parkin ligase domain in an autoinhibited state. *EMBO J.* **32,** 2099–2112 (2013).
15. Riley, B. E. *et al.* Structure and function of Parkin E3 ubiquitin ligase reveals aspects of RING and HECT ligases. *Nature Commun.* **4,** 1982 (2013).
16. Trempe, J.-F. *et al.* Structure of parkin reveals mechanisms for ubiquitin ligase activation. *Science* **340,** 1451–1455 (2013).
17. Sarraf, S. A. *et al.* Landscape of the PARKIN-dependent ubiquitylome in response to mitochondrial depolarization. *Nature* **496,** 372–376 (2013).
18. Borodovsky, A. *et al.* Chemistry-based functional proteomics reveals novel members of the deubiquitinating enzyme family. *Chem. Biol.* **9,** 1149–1159 (2002).
19. Wang, T. *et al.* Evidence for bidentate substrate binding as the basis for the K48 linkage specificity of otubain 1. *J. Mol. Biol.* **386,** 1011–1023 (2009).
20. Macedo, M. G. *et al.* Genotypic and phenotypic characteristics of Dutch patients with early onset Parkinson's disease. *Mov. Disord.* **24,** 196–203 (2009).
21. Veeriah, S. *et al.* Somatic mutations of the Parkinson's disease-associated gene *PARK2* in glioblastoma and other human malignancies. *Nature Genet.* **42,** 77–82 (2010).
22. Zheng, X. & Hunter, T. Parkin mitochondrial translocation is achieved through a novel catalytic activity coupled mechanism. *Cell Res.* **23,** 886–897 (2013).
23. Duda, D. M. *et al.* Structure of HHARI, a RING-IBR-RING ubiquitin ligase: autoinhibition of an ariadne-family E3 and insights into ligation mechanism. *Structure* **21,** 1030–1041 (2013).
24. Caulfield, T. R. *et al.* Phosphorylation by PINK1 releases the UBL domain and initializes the conformational opening of the E3 ubiquitin ligase Parkin. *PLOS Comput. Biol.* **10,** e1003935 (2014).
25. Ordureau, A. *et al.* Defining roles of PARKIN and ubiquitin phosphorylation by PINK1 in mitochondrial quality control using a ubiquitin replacement strategy. *Proc. Natl Acad. Sci. USA* **112,** 6637–6642 (2015).
26. Kazlauskaite, A. & Muqit, M. M. K. PINK1 and Parkin — mitochondrial interplay between phosphorylation and ubiquitylation in Parkinson's disease. *FEBS J.* **282,** 215–223 (2015).
27. Pickrell, A. M. & Youle, R. J. The roles of PINK1, Parkin, and mitochondrial fidelity in Parkinson's disease. *Neuron* **85,** 257–273 (2015).
28. Koyano, F. & Matsuda, N. Molecular mechanisms underlying PINK1 and Parkin catalyzed ubiquitylation of substrates on damaged mitochondria. *Biochim. Biophys. Acta.* http://dx.doi.org/10.1016/j.bbamcr.2015.02.009 (2015).

Author Contributions T.W. and D.K. designed the research, and T.W. performed all experiments. M.S. performed cell-based studies. A.S. contributed to characterization of Ubl and ubiquitin phosphorylation. T.W. and D.K. analysed the data and wrote the manuscript with help from all authors.

Author Information Coordinates and structure factors for the *Ph*PARKIN–pUb complex and *Hs*PARKIN(ΔUbl) G319A have been deposited with the Protein Data Bank under accession codes 5CAW and 5C9V, respectively. Reprints and permissions information is available at www.nature.com/reprints. The authors declare competing financial interests: details are available in the online version of the paper. Readers are welcome to comment on the online version of the paper. Correspondence and requests for materials should be addressed to D.K. (dk@mrc-lmb.cam.ac.uk).

METHODS

No statistical methods were used to predetermine sample size.

Protein expression and purification. *Hs*PARKIN full length, *Hs*PARKIN(ΔUbl) (amino acids 137–465), *Ph*PARKIN (amino acids 140–461), *Ph*PINK1 (amino acids 115–575) as well as *Tribolium castaneum* PINK1 (*Tc*PINK1, amino acids 128–570) were expressed as GST fusion proteins in Rosetta2 pLacI cells from pOPIN-K vectors as described[14]. In short, PARKIN cultures were induced by adding 200 μM ZnCl₂ and 50 μM IPTG, whereas PINK1 variants and the *Hs*PARKIN Ubl domain (amino acids 1–72) were induced with 150 μM IPTG followed by 12 h expression at 18 °C. After collection, the cell pellet was lysed by sonication in lysis buffer (270 mM sucrose, 10 mM glycerol 2-phosphate disodium, 50 mM NaF, 14 mM β-mercaptoethanol, 50 mM Tris (pH 8.0)), in the presence of lysozyme, DNase I and EDTA-free protease inhibitors. The suspension was centrifuged and the supernatant applied to Glutathione Sepharose 4B beads (GE Healthcare). After 1 h of agitation at 4 °C the beads were washed with high salt buffer (500 mM NaCl, 10 mM DTT, 25 mM Tris (pH 8.5)) and equilibrated in low salt buffer (200 mM NaCl, 10 mM DTT, 25 mM Tris (pH 8.5)). GST-tagged proteins were either eluted from beads with low salt buffer containing 40 mM glutathione and purified by gel filtration (Superdex 200, GE Life Sciences), or cleaved on beads by incubating with GST-3C protease for 12 h at 4 °C before further purification by gel filtration (Superdex 75, GE Life Sciences) in low salt buffer as a final step. When improved purity was required, such as for *Ph*PARKIN used in crystallization, an anion exchange step (RESOURCE Q, GE Life Sciences) using a linear gradient of 75–600 mM NaCl in 10 mM DTT, 25 mM Tris (pH 8.5) was included before final gel filtration.

N-terminally His6-SUMO-tagged *Hs*PARKIN(ΔUbl2) (amino acids 80–465) was expressed as described above and lysed in His6-lysis buffer (200–300 mM NaCl, 4 mM β-mercaptoethanol, 25 mM Tris (pH 8.5)). After centrifugation, the protein was affinity purified with Talon Superflow resin (GE Healthcare) and eluted in 200 mM NaCl, 4 mM β-mercaptoethanol, 25 mM Tris (pH 8.5) containing 200–250 mM imidazole. Eluted protein was directly applied to gel filtration (Superdex 75, GE Life Sciences) in low salt buffer. Protein for SUMO-tag cleavage was dialysed overnight in 200 mM NaCl, 4 mM β-mercaptoethanol, 25 mM Tris (pH 8.5) containing His6-tagged SENP1. The sample was reapplied to Talon resin, and the flow-through purified by gel filtration (Superdex 75, GE Life Sciences) in low salt buffer.

Phospho-*Hs*PARKIN for biochemical assays was generated by incubating 32–37 μM *Hs*PARKIN, 5.4 μM GST–*Ph*PINK1 and 10 mM ATP with 1× ligation buffer (40 mM Tris pH 7.4, 10 mM MgCl₂, 0.6 mM DTT) for 1 h at room temperature. GST–*Ph*PINK1 was removed with Glutathione Sepharose 4B resin (GE Healthcare) and *Hs*PARKIN was re-purified by gel filtration (Superdex 75, GE Life Sciences). Consistent phosphorylation levels were checked by western blot analysis using an anti-pSer65 PARKIN antibody (Abcam cat no. ab154995).

Modification with ubiquitin-based suicide probes. Probe reactions for biochemical assays were performed by incubating 5 μM PARKIN with 40 μM indicated ubiquitin suicide probe (Figs 1b and 2b) or 20 μM Ub-VS (Extended Data Fig. 10), 1 μM *Ph*PINK1 where indicated and 5 μM phosphoUb where indicated in the presence of 1× reaction buffer (50 mM Tris pH 7.4, 200 mM NaCl, 10 mM DTT, 10 mM MgCl₂). The reaction took place at room temperature after adding 10 mM ATP and was quenched by adding LDS sample buffer at the indicated time points. Samples were applied on NuPAGE 4–12% Bis-Tris gels (Invitrogen) and stained with Instant Blue SafeStain (Expedeon).

To generate the covalent *Ph*PARKIN–pUb complex for crystallization, 46 μM *Ph*PARKIN (amino acids 140–461) was reacted with 230 μM UbC3Br probe and 23 μM GST–*Ph*PINK1 in the presence of 1× reaction buffer. The coupling was initiated by adding 10 mM ATP and incubated for 6 h at room temperature. The complex was purified by gel filtration (Superdex 75, GE Life Sciences) in low salt buffer. Fractions containing *Ph*PARKIN–pUb were pooled, concentrated and used for crystallization without freezing.

Crystallization, data collection and refinement. *Ph*PARKIN–pUb was crystallized in sitting-drop vapour diffusion at a concentration of ~5.3 mg ml⁻¹ at 18 °C. Crystals were grown in 100 nl protein solution mixed with 100 nl mother liquor (2% (v/v) PEG400, 2 M ammonium sulfate, 0.1 M HEPES pH 7.5). Before vitrification, crystals were soaked in 1.7% (v/v) PEG400, 15% (v/v) glycerol, 1.7 M ammonium sulfate, 0.085 M HEPES (pH 7.5) for cryo-protection. Diffraction data were collected at the Diamond Light Source (Harwell, UK), beamline I-04, at 100 K and a wavelength of 0.97949 Å, to a resolution of 2.62 Å.

The *Hs*PARKIN(ΔUbl) (amino acids 137–465) G319A mutant was crystallized at a concentration of 2.4 mg ml⁻¹ by mixing 400 nl protein solution with 400 nl mother liquor (1.8 M lithium sulfate, 0.01 M MgCl₂, 0.05 M MES pH 5.6) in a sitting-drop vapour diffusion set-up at 18 °C. Before vitrification in liquid nitrogen the crystals were briefly soaked in 1.6 M lithium sulfate, 0.01 M MgCl₂, 0.05 M

MES pH 5.4 containing 15% (v/v) glycerol. Diffraction data were collected at the Diamond Light Source (Harwell, UK), beamline I04-1, at 100 K and a wavelength of 0.91730 Å, to a resolution of 2.35 Å.

Phasing of the *Ph*PARKIN–pUb data set was performed by molecular replacement with Phaser[29] using isolated domains of *Hs*PARKIN(ΔUbl) (PDB 4BM9 (ref. 14)) and ubiquitin (PDB 1UBq (ref. 30)) as search models. The structure of *Hs*PARKIN(ΔUbl) G319A was solved by using *Hs*PARKIN(ΔUbl) (PDB 4BM9 (ref. 14)) as a refinement model. For both structures, subsequent rounds of model building in Coot[31] and refinement in Phenix[32] resulted in final models with statistics shown in Extended Data Fig. 1e. The *Hs*PARKIN(ΔUbl) G319A structure was refined with simulated annealing to reduce model bias. Both structures were refined with TLS, using different protein chains as individual TLS groups. Final Ramachandran statistics were 95.3%/4.7%/0.0% (favoured/allowed/outliers) for the *Hs*PARKIN G319A mutant structure, and 96.7%/3.2%/0.1% for the *Ph*PARKIN–pUb structure. Structure figures were generated with PyMol (http://www.pymol.org).

Fluorescence polarization phosphoUb binding assays. N-terminally FlAsH-tagged ubiquitin was phosphorylated and purified as described for phosphoUb[8] with buffers supplemented with β-mercaptoethanol. Labelling was performed overnight at 4 °C with 60 μM FlAsH-tagged phosphoUb at a ratio of 37.5:1 (v/v) with Lumio Green (Invitrogen) in 1× FlAsH dilution buffer (50 mM Tris (pH 7.4), 1 mM β-mercaptoethanol). Buffer exchange was performed with PD-10 desalting columns (GE Healthcare) in 50 mM Tris (pH 7.4), 2 mM β-mercaptoethanol and samples were concentrated to ~8 μM FlAsH-labelled phosphoUb. For binding studies in 384-well low volume plates (Corning), 10 μl of 100 nm labelled phosphoUb was mixed with 10 μl of PARKIN serial dilutions in FlAsH buffer (20 mM Tris (pH 7.4), 100 mM NaCl, 2 mM β-mercaptoethanol, 0.1 mg ml⁻¹ bovine serum albumin). Fluorescence polarization (FP = (I∥ − I⊥)/(I∥ + I⊥)) was measured using a PheraStar plate reader (BMB Labtech) with the optic module set to λ_ex = 485 nm and λ_em = 520 nm. Measurements were performed in triplicate and error bars are given as the standard deviation from the mean. A least square fit for one binding site was performed using the following equation

$$FP = (B_{max} \times X/(K_d + X)) + NS \times X + background$$

with FP being fluorescence polarization and X the concentration of the titrant, B_{max} is the maximum specific binding, K_d is the equilibrium dissociation constant and NS the slope for nonspecific binding, which was restricted to values greater than 0.

PARKIN activity assays. Spin-filtered *Hs*PARKIN (2 μM) was pre-incubated for 0.5 h at 30 °C with 10 mM ATP, 1× ligation buffer (40 mM Tris pH 7.5, 10 mM magnesium chloride, 0.6 mM dithiothreitol (DTT)), a total concentration of 0.5 mg ml⁻¹ ubiquitin and 0.05 mg ml⁻¹ phosphoUb or 0.1 μM GST–*Tc*PINK1 where indicated. Ubiquitination was initiated by adding 0.1 μM E1 and 1 μM UBE2L3 (Fig. 2f and Extended Data Fig. 10d) or 0.2 μM E1 and 2 μM UBE2L3 (Fig. 3d). The reaction was quenched with LDS sample buffer containing DTT and iodoacetamide to prevent forming of disulfide bridges. NuPAGE 4–12% gradient Bis-Tris gels were used for separation, and proteins were transferred on a nitrocellulose membrane with subsequent detection using an anti-polyubiquitin FK2 antibody (Millipore).

Immunofluorescence. HeLa cells (originating from ATCC) were nucleofected with N-terminally tagged eYFP–*Hs*PARKIN (gift from the J. Kittler laboratory) and grown on coverslips for 24–48 h. After treatment with DMSO or CCCP (10 μM) for 1 h, cells were fixed with 4% paraformaldehyde, washed with 0.1 M glycine in phosphate buffered saline (PBS), at pH 7.4, briefly permeabilized with 0.2% Triton X-100 in PBS and blocked with a blocking solution containing 10% goat serum and 0.5% BSA. Samples were further incubated with anti-Tom20 antibody (FL-145, Santa Cruz) followed by goat Alexa647-coupled anti-rabbit antibody (Life Technologies). Confocal images were taken using a Zeiss LSM780 microscope.

Immunoblotting and immunoprecipitation. HeLa cells (originating from ATCC) were transfected with eYFP–*Hs*PARKIN. After 24–48 h, cells were treated with DMSO or CCCP as before, and lysed in cell lysis buffer (50 mM Tris (pH 7.4), 150 mM NaCl, 1% (v/v) NP-40) supplemented with EDTA-free protease inhibitor cocktail (Roche), PhosphoSTOP (Roche), as well as 10 mM N-ethylmaleimide (Sigma-Aldrich) and 10 mM chloracetamide (Sigma-Aldrich) for better detection of ubiquitinated proteins. For immunoprecipitation of eYFP–*Hs*PARKIN, 500 μg of cell lysate was incubated with GFP–Trap agarose (Chromotek) for 1 h. The beads were washed three times with cell lysis buffer, and proteins were eluted with 1× LDS buffer. Cells were regularly checked for the absence of mycoplasma infection using the MycoAlert Kit (Lonza). Antibodies were from commercial sources: goat anti-GFP (ab6673, Abcam), rabbit anti-Tom20 (FL-145, Santa Cruz), mouse anti-GAPDH (6C5, Ambion).

Isothermal titration calorimetry. Isothermal titration calorimetry (ITC) experiments were performed in a MicroCal iTC200 machine (GE Healthcare) at 20 °C with the sample and the ligand in low salt buffer. The cell contained 35 μM of

*Hs*PARKIN(ΔUbl) and 400 μM *Hs*PARKIN Ubl was injected in 2 μl injections at 120 s intervals. Protein sample as well as ligand were in low salt buffer and *Hs*PARKIN(ΔUbl) was mixed with phosphoUb at a 1:1.2 molar ratio as indicated. Binding curves were integrated and fitted to a one-site binding model by using the MicroCal ITC Analysis plug-in for Origin (Malvern).

Phosphorylation assays. PARKIN phosphorylation was performed by incubating 5 μM *Hs*PARKIN with 0.5 μM GST–*Tc*PINK1, 10 mM ATP, 1 × reaction buffer and phosphoUb (14 μM unless stated differently). The reaction was quenched at the given time points with LDS sample buffer and proteins were separated on a NuPAGE 4–12% gradient Bis-Tris gel, transferred on nitrocellulose membrane and detected with anti-pSer65 PARKIN antibody (Abcam cat no. ab154995). Phosphorylation assays of *Hs*PARKIN Ubl domain (amino acids 1–72) and ubiquitin were performed as described above with 20 μM of *Hs*PARKIN Ubl domain and ubiquitin, respectively. For the ubiquitin phosphorylation assay, the GST–*Tc*PINK1 concentration was increased to 1.5 μM. The reaction was quenched at the given time points with LDS sample buffer and proteins were separated on a 15% SuperSep Phos-tag gel (Wako Chemicals) and stained with Instant Blue SafeStain (Expedeon).

Phosphorylation of the PARKIN Ubl domain for NMR analysis. Isotope-labelled *Hs*PARKIN Ubl domain (amino acids 1–72) was expressed in M9 minimal media supplemented with 4 g l^{-1} ^{13}C-glucose, 2 g l^{-1} ^{15}N-NH$_4$Cl, trace elements and BME vitamins (Sigma-Aldrich) and purified as described above. The final gel filtration was performed in NMR buffer (18 mM Na$_2$HPO$_4$, 7 mM NaH$_2$PO$_4$ (pH 7.2), 150 mM NaCl, 5 mM TCEP). Isotope-labelled *Hs*PARKIN Ubl was phosphorylated at room temperature by incubating 80 μM *Hs*PARKIN Ubl with 2.5 μM *Ph*PINK1, 1 mM ATP and 1 × ligation buffer which was adjusted to 332.5 μl with NMR buffer, before addition of 17.5 μl D$_2$O as lock solvent. The reaction was monitored by consecutive ^{1}H,^{15}N 2D BEST-TROSY (band selective excitation short transients transverse relaxation optimized spectroscopy) experiments and quenched with apyrase.

Solution studies of the phosphorylated PARKIN Ubl domain. NMR acquisition was performed at 298 K on a Bruker Avance III 600 MHz spectrometer

equipped with a cryogenic triple resonance TCI probe. The software packages Topspin3.2 (Bruker) and Sparky (Goddard & Kneller, UCSF; http://www.cgl.ucsf.edu/home/sparky/) were used for data processing and analysis, respectively. ^{1}H,^{15}N 2D BEST-TROSY experiments[33] were conducted with in-house optimized Bruker pulse sequences that contained a recycling delay of 400 ms and 512 × 64 complex points in the ^{1}H,^{15}N dimension, respectively.

Standard HSQC-based Bruker triple resonance pulse sequences were used to generate backbone chemical shift assignments. CBCACONH and HNCACB spectra were collected with 50% non-uniform sampling (NUS) of 1,024 × 32 × 55 complex points in the ^{1}H, ^{15}N and ^{13}C dimensions. HNCO and HNCACO experiments were acquired using NUS at a rate of 50% with 1,024 × 32 × 48 complex points in the ^{1}H, ^{15}N and ^{13}C dimensions, respectively. Data set processing was performed with compressed sensing using the MddNMR software package[34]. Weighted chemical shift perturbation calculations were completed using the equation $\sqrt{((\Delta^1H)^2 + (\Delta^{15}N/5)^2)}$.

29. McCoy, A. J. *et al.* Phaser crystallographic software. *J. Appl. Crystallogr.* **40,** 658–674 (2007).
30. Vijay-Kumar, S., Bugg, C. E. & Cook, W. J. Structure of ubiquitin refined at 1.8 Å resolution. *J. Mol. Biol.* **194,** 531–544 (1987).
31. Emsley, P., Lohkamp, B., Scott, W. G. & Cowtan, K. Features and development of Coot. *Acta Crystallogr. D* **66,** 486–501 (2010).
32. Adams, P. D. *et al.* The Phenix software for automated determination of macromolecular structures. *Methods* **55,** 94–106 (2011).
33. Favier, A. & Brutscher, B. Recovering lost magnetization: polarization enhancement in biomolecular NMR. *J. Biomol. NMR* **49,** 9–15 (2011).
34. Kazimierczuk, K. & Orekhov, V. Y. Accelerated NMR spectroscopy by using compressed sensing. *Angew. Chem. Int. Edn Engl.* **50,** 5556–5559 (2011).
35. Dou, H., Buetow, L., Sibbet, G. J., Cameron, K. & Huang, D. T. BIRC7–E2 ubiquitin conjugate structure reveals the mechanism of ubiquitin transfer by a RING dimer. *Nature Struct. Mol. Biol.* **19,** 876–883 (2012).
36. Sakata, E. *et al.* Parkin binds the Rpn10 subunit of 26S proteasomes through its ubiquitin-like domain. *EMBO Rep.* **4,** 301–306 (2003).
37. Kelsall, I. R. *et al.* TRIAD1 and HHARI bind to and are activated by distinct neddylated Cullin-RING ligase complexes. *EMBO J.* **32,** 2848–2860 (2013).

OTUB1 triggers lung cancer development by inhibiting RAS monoubiquitination

Maria Francesca Baietti[1,2,‡], Michal Simicek[1,2,†,‡], Layka Abbasi Asbagh[1,2], Enrico Radaelli[1,2],
Sam Lievens[3,4], Jonathan Crowther[1,2], Mikhail Steklov[1,2], Vasily N Aushev[1,2,5], David Martínez García[1,2],
Jan Tavernier[3,4] & Anna A Sablina[1,2,*]

Abstract

Activation of the RAS oncogenic pathway, frequently ensuing from mutations in RAS genes, is a common event in human cancer. Recent reports demonstrate that reversible ubiquitination of RAS GTPases dramatically affects their activity, suggesting that enzymes involved in regulating RAS ubiquitination may contribute to malignant transformation. Here, we identified the de-ubiquitinase OTUB1 as a negative regulator of RAS mono- and di-ubiquitination. OTUB1 inhibits RAS ubiquitination independently of its catalytic activity resulting in sequestration of RAS on the plasma membrane. OTUB1 promotes RAS activation and tumorigenesis in wild-type RAS cells. An increase of OTUB1 expression is commonly observed in non-small-cell lung carcinomas harboring wild-type KRAS and is associated with increased levels of ERK1/2 phosphorylation, high Ki67 score, and poorer patient survival. Our results strongly indicate that dysregulation of RAS ubiquitination represents an alternative mechanism of RAS activation during lung cancer development.

Introduction

The RAS small GTPases (HRAS, NRAS, and KRAS) are essential regulators of diverse eukaryotic cellular processes, such as cell proliferation, cytoskeletal assembly and organization, and intracellular membrane trafficking [for review (Colicelli, 2004)]. The RAS family members function as molecular switches alternating between an inactive GDP-bound and active GTP-bound state. The transition between GDP- and GTP-bound forms is tightly regulated by guanine nucleotide exchange factors (GEF) and GTPase-activating proteins (GAP).

The RAS small GTPases play a major role in the development of human cancer. Oncogenic RAS mutations occur in up to 30% of non-small-cell lung carcinomas (NSCLC), mostly adenocarcinomas (Karnoub & Weinberg, 2008). The intrinsic GTP hydrolysis activity of RAS is the predominant target of most common somatic mutations found in the oncogenic variants of RAS alleles (Pylayeva-Gupta et al, 2011). KRAS-mutant lung adenocarcinomas have higher levels of the MAPK pathway activation than wild-type (wt) KRAS tumors. However, the MAPK cascade is also hyperactivated in a significant proportion of wt KRAS tumors, suggesting that RAS proteins may be frequently activated by alternative mechanisms not yet fully elucidated (Network, 2014).

Beyond oncogenic mutations of RAS, up-regulation of RAS-specific GEFs and functional loss of GAPs also have been shown to contribute to cancer development and progression (Vigil et al, 2010). In addition, several post-translational modifications, such as phosphorylation (Bivona et al, 2006), lipidation (Hancock, 2003), and acetylation (Yang et al, 2013), are known to regulate the functions of RAS GTPases. RAS stability is controlled by the E3 ubiquitin ligases, β-TrCP1, and Nedd4-1, that directly polyubiquitinate RAS proteins triggering degradation (Shukla et al, 2014; Zeng et al, 2014). In addition, we and others have recently demonstrated that RAS family members can undergo reversible mono- and di-ubiquitination (Jura et al, 2006; Xu et al, 2010; Sasaki et al, 2011; Baker et al, 2013a; Simicek et al, 2013). However, how reversible ubiquitination affects RAS activity and its tumorigenic properties remains very much controversial.

Earlier studies reported that reversible ubiquitination restricts the activity of HRAS and NRAS, but not that of KRAS, whereas more recent reports demonstrated that KRAS can also undergo mono- and di-ubiquitination (Jura et al, 2006). Xu et al (2010) demonstrated that di-ubiquitination of HRAS and NRAS by the E3 ubiquitin ligase RABEX5 (RABGEF1) induces their re-localization to the endomembranes,

1 Center for the Biology of Disease, VIB, Leuven, Belgium
2 Center for Human Genetics, KU Leuven, Leuven, Belgium
3 Department of Medical Protein Research, VIB, Leuven, Belgium
4 Department of Biochemistry, Gent University, Gent, Belgium
5 Institute of Carcinogenesis, Blokhin Russian Cancer Research Center, Moscow, Russia
  *Corresponding author. Tel: +32 16330790; Fax: +32 16330145; E-mail: anna.sablina@cme.vib-kuleuven.be
  ‡ These authors equally contributed to this work
  † Present address: PNAC, MRC, LMB, Cambridge, UK

leading to a decrease in RAS activity and downstream signaling. On the other hand, two other groups demonstrated that monoubiquiti-nation of HRAS at Lys117 accelerates intrinsic nucleotide exchange and promotes GTP loading, whereas monoubiquitination of KRAS at Lys147 impaired NF1-mediated GTP hydrolysis (Sasaki *et al*, 2011; Baker *et al*, 2013a,b). Moreover, the KRAS gene fusion with the ubiquitin-conjugating enzyme UBE2L3 has been identified in meta-static prostate cancer. The UBE2L3-KRAS fusion protein is highly ubiquitinated and exhibits transforming activity via specific activa-tion of AKT and p38 MAPK pathways (Wang *et al*, 2011).

Taken together, these studies strongly highlight the importance of reversible ubiquitination of RAS-like GTPases governing down-stream signaling. These results also suggest that enzymes involved in RAS ubiquitination may contribute to tumorigenic transformation by modulating RAS activity. In this study, we focused on the identi-fication of specific RAS de-ubiquitinating enzymes (DUBs) and their role in cancer development and progression. We found that OTUB1 up-regulation contributes specifically to the development of wt KRAS lung adenocarcinomas by inhibiting reversible ubiquitination of RAS proteins.

Results

OTUB1 controls RAS ubiquitination

To identify DUBs involved in the control of RAS ubiquitination, we utilized a targeted mammalian protein–protein interaction (MAPPIT) screen, a two-hybrid technology for the detection of protein-protein interactions in intact mammalian cells (Lievens *et al*, 2009, 2012). As a proof of concept, we applied the MAPPIT system to examine the interactions between HRAS and its known downstream effectors (Fig EV1). GTPase-deficient HRAS G12V-mutant bait gave rise to the robust MAPPIT signals with each of the tested effector preys (Fig EV1), confirming the feasibility of the MAPPIT approach to identify novel RAS regulators.

A targeted MAPPIT screen, in which the HRAS G12V bait was screened against a library of 55 DUBs, identified four DUBs, USP12,

JOSD2, UCHL5, and OTUB1, as potential interactors of HRAS G12V (Fig 1A). We next assessed whether the candidate DUBs could also interact with KRAS G12V and NRAS Q61K. The MAPPIT assay revealed that, in contrast to other tested DUBs, OTUB1 demon-strated a much higher affinity for both NRAS and KRAS compared to random non-specific baits, MAL and eDHFR (Fig 1B). Altogether, the MAPPIT experiments identified OTUB1 (OTU de-ubiquitinase, ubiquitin aldehyde binding 1), a member of the ovarian tumor domain protease (OTU) family of DUBs (Wang *et al*, 2009; Iglesias-Gato *et al*, 2015), as a putative binding partner of RAS proteins (Fig 1A and B).

Using a set of reciprocal immunoprecipitations, we confirmed that OTUB1 interacted with RAS proteins (Fig 1C–F). We found that OTUB1 formed a complex with either wt NRAS or constitutively active form of NRAS Q61K (Fig 1D). Consistently with this observa-tion, both inactive GDP-bound and active GTP-γ-S-bound forms of NRAS interacted with OTUB1 (Fig 1E), indicating that GTP binding does not significantly affect the interaction between RAS and OTUB1. Furthermore, immunofluorescence analysis revealed that OTUB1 and wt KRAS co-localized at the plasma membrane (Fig 1G). These results strongly indicate that OTUB1 interacts with RAS proteins in a GTP-independent manner, suggesting that OTUB1 is an upstream regulator of RAS GTPases.

We next investigated whether OTUB1 is implicated in the regula-tion of RAS ubiquitination. Consistently with previous reports (Jura *et al*, 2006; Sasaki *et al*, 2011), we found that all RAS proteins undergo mono- and di-ubiquitination (Fig 2A–D). Suppression of OTUB1 with two different shRNAs resulted in increased levels of NRAS monoubiq-uitination (Fig 2A), whereas overexpression of wt OTUB1 almost completely abolished ubiquitination of RAS proteins (Fig 2B–D).

OTUB1 has recently emerged as a unique DUB that binds to several classes of E2s, including Ubc13 and UbcH5C, and inhibits ubiquitination independently of its proteolytic activity (Nakada *et al*, 2010; Juang *et al*, 2012; Sato *et al*, 2012; Wiener *et al*, 2012). Therefore, we tested whether the catalytic activity of OTUB1 is essential to promote RAS de-ubiquitination. We found that catalyti-cally inactive OTUB1 C91S-mutant (Edelmann *et al*, 2009) as well as wt OTUB1 dramatically decreased the ubiquitination levels of

---

Figure 1.   The de-ubiquitinase OTUB1 interacts with the RAS GTPases.

A   A targeted MAPPIT screen identifies several DUBs as putative RAS interactors. A MAPPIT array containing DUB prey library was screened with HRAS G12V as bait. pSEL (+2L)-HRAS G12V was expressed in HEK293T cells together with the indicated prey. BRAF served as a positive control. Each measurement was done in triplicate. The results are expressed as a mean of normalized luciferase activity (leptin-treated cells *vs* leptin-untreated cells). The overall mean value + 2 s.d. served as a threshold.

B   MAPPIT assay confirms the interaction between OTUB1 and RAS proteins. pSEL(+2L) vectors coding RAS proteins were expressed in HEK293T cells together with the indicated prey. Empty vector and two random baits, MAL and eDHFR, were used as negative controls. REM2 and EFHA1 preys that bind to the bait receptor itself were used to evaluate the expression of the RAS baits. The results are expressed as a mean of normalized luciferase activity ± s.e.m (leptin-treated cells *vs* leptin-untreated cells), *n* = 3.

C   NRAS Q61K mutant co-immunoprecipitates with OTUB1. At 48 h post-transfection with Flag-tagged NRAS Q61K and HA-tagged OTUB1 expression constructs, HA-tagged OTUB1 was immunoprecipitated with anti-HA-agarose followed by immunoblotting using anti-Flag or anti-HA antibodies.

D   OTUB1 interacts with wt NRAS and active NRAS-mutant. Flag-tagged NRAS proteins were immunoprecipitated using anti-Flag (M2) agarose from HEK293T cells overexpressing HA-tagged OTUB1 or empty vector (V).

E   GTP binding does not affect the complex formation between NRAS and OTUB1. Recombinant Flag-tagged NRAS was incubated with lysates derived from HEK293T cells expressing HA-tagged OTUB1 in the excess of GTP-γ-S or GDP, followed by immunoblotting with the indicated antibodies.

F   OTUB1 interacts with wt KRAS. Flag-tagged KRAS was immunoprecipitated using anti-Flag (M2) agarose from HEK293T cells overexpressing HA-tagged OTUB1 or empty vector (V).

G   OTUB1 co-localizes with KRAS at the plasma membrane. At 24 h after co-transfection with GFP-tagged KRAS and HA–tagged OTUB1, HeLa cells were immunostained with anti-HA antibody. The outlined areas are shown at higher magnification at the top of each image. Scale bar, 10 μm.

Data information: (C–F) IP, immunoprecipitates; WCL, whole cell lysate.
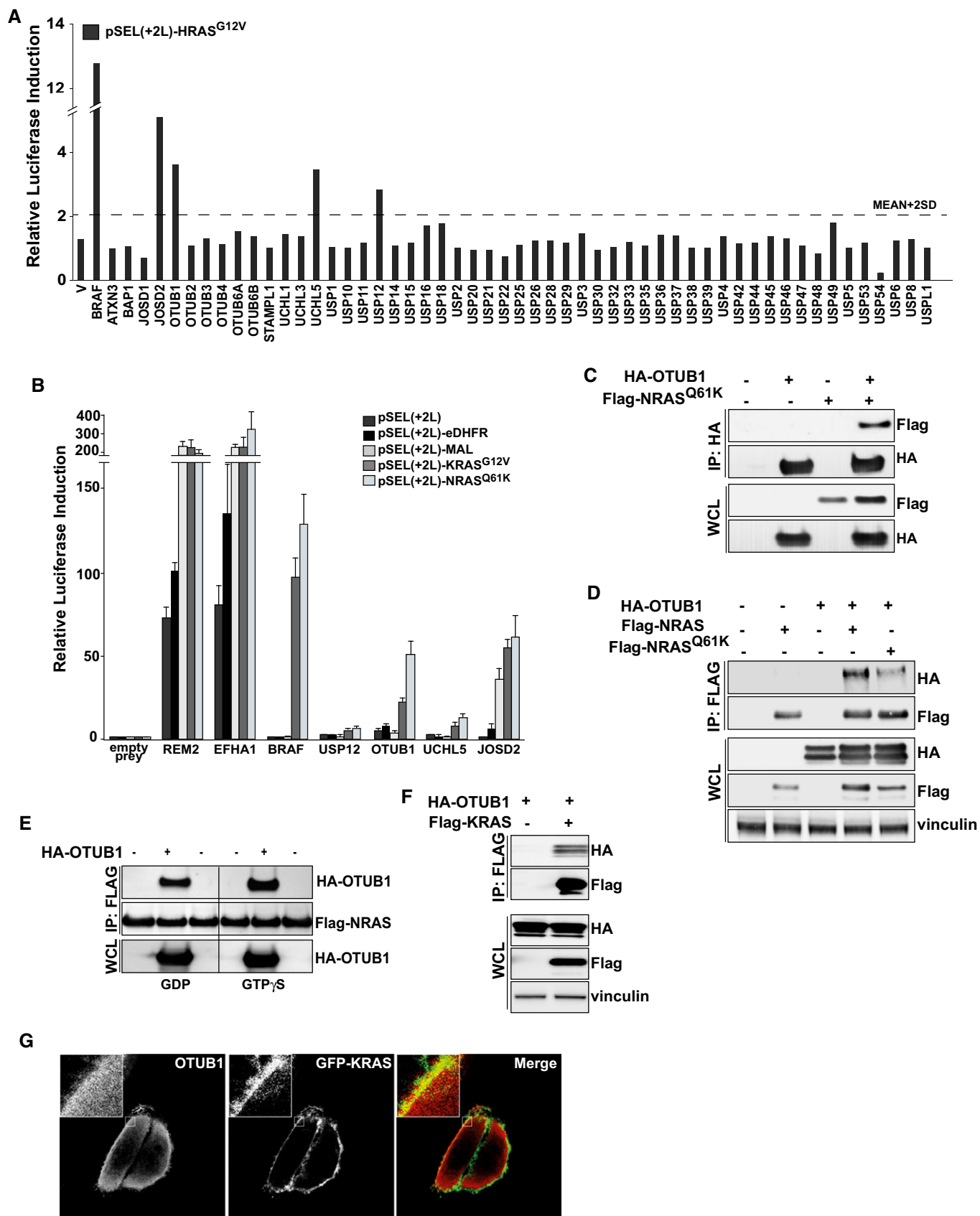Source data are available online for this figure.
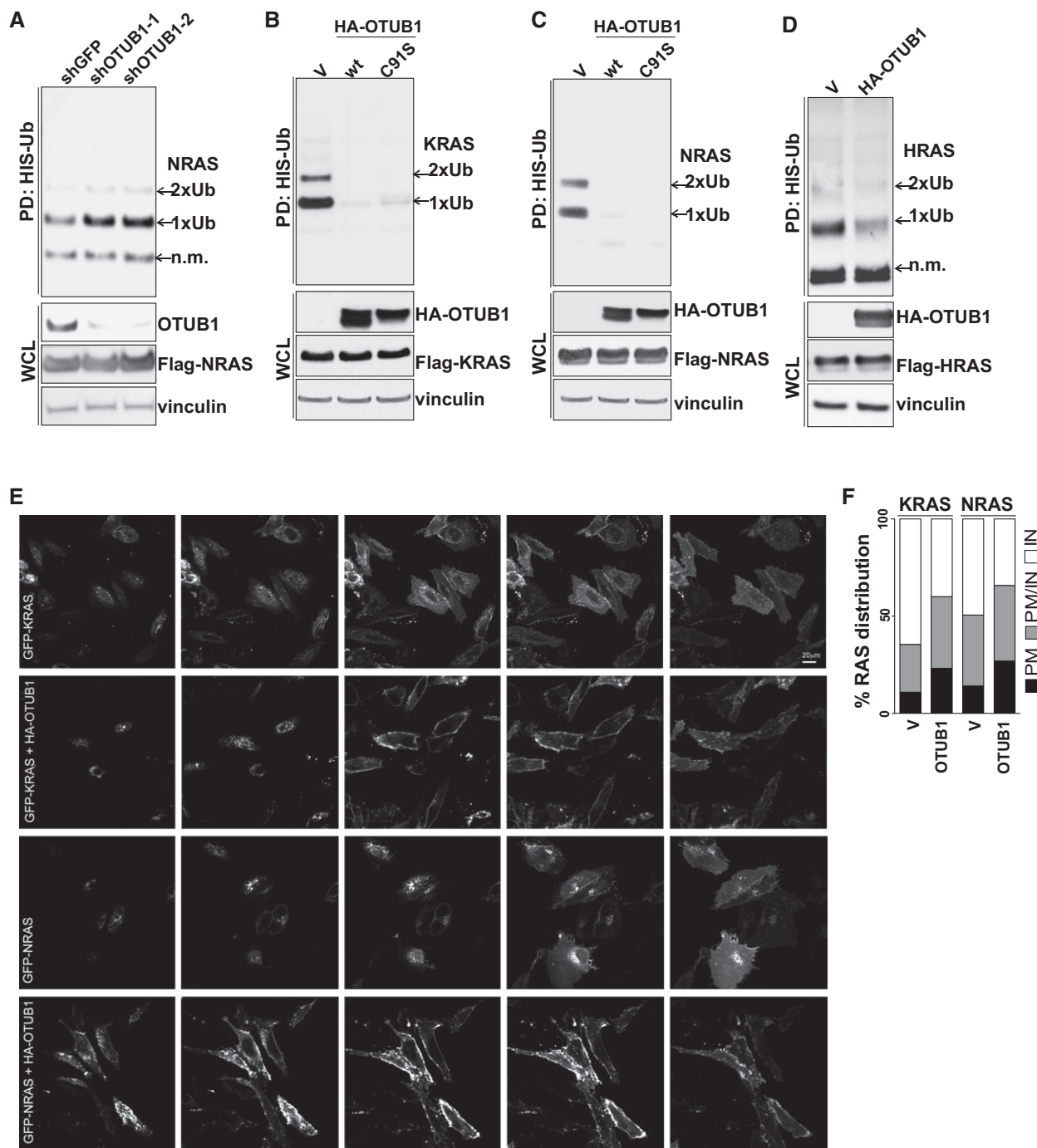
Figure 1.

Figure 2. OTUB1 triggers membrane localization of RAS ubiquitination by inhibiting its ubiquitination.

A   Suppression of OTUB1 expression increases NRAS mono- and di-ubiquitination. 6×His-tagged ubiquitin and Flag-NRAS were introduced into HEK293T cells expressing shGFP or shRNAs against OTUB1. Ubiquitinated NRAS was purified by Co^{2+} metal affinity chromatography and detected by anti-Flag antibody.

B–D Catalytic activity of OTUB1 is not required to inhibit RAS ubiquitination. 6×His-tagged ubiquitin and RAS expression constructs were introduced into HEK293T cells expressing wt HA-OTUB1, the catalytically dead mutant HA-OTUB1 C91S, or empty vector (V). Ubiquitinated RAS was purified by Co^{2+} metal affinity chromatography and detected by anti-Flag antibody.

E   OTUB1 induces membrane RAS re-localization. Confocal imaging of HeLa cells expressing the indicated constructs. For each sample, z-stacks obtained by scanning the sample from the apical to the basal layer. Step-size, 2 μm. Scale bar, 20 μm.

F   RAS cellular distribution expressed as percentage of cells with specific RAS localization. For quantification of RAS localization, cells were randomly imaged using IN Cell Analyzer. RAS localization (> 200 cells) was scored as intracellular and diffused (IN), mostly at the plasma membrane (PM), or both intracellular and plasma membrane (PM/IN). *P*-value = 0.0005 as determined by chi-squared test, *n* = 3. Representative images of HeLa cells expressing GFP-tagged KRAS are shown in Appendix Fig S1. pull-down, PD. whole cell lysate, WCL. not modified, n.m.

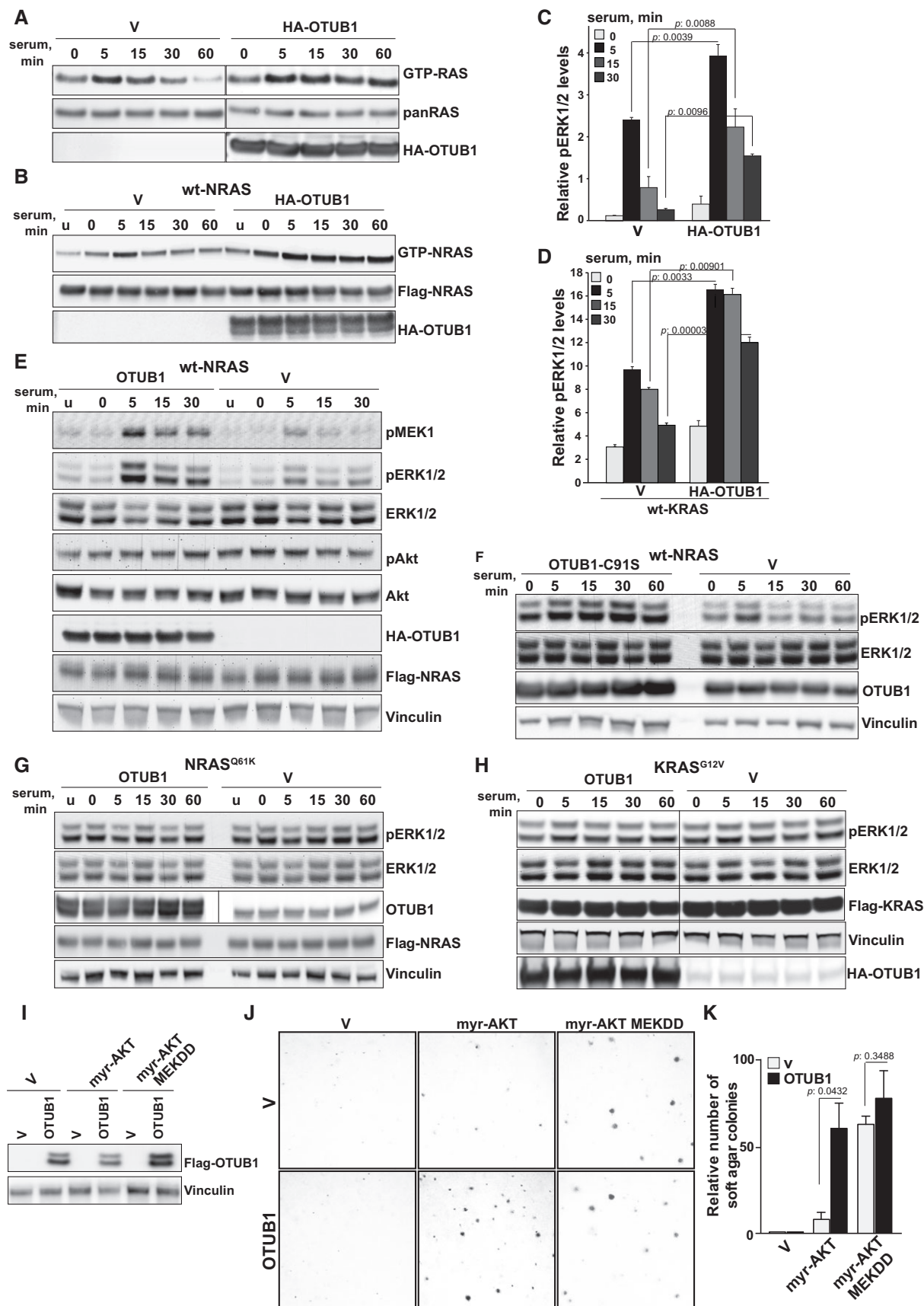Source data are available online for this figure.

Figure 3.

◄

Figure 3.   OTUB1 increases RAS activity and enhances MAPK activation in wt RAS cells.

A, B   OTUB1 overexpression promotes serum-induced activation of endogenous wt RAS (A) or wt NRAS (B). GTP-bound RAS was pulled down from HEK293T cells expressing HA-tagged OTUB1 or empty vector (V) using recombinant RAF1 RBD conjugated to agarose beads. Input was controlled by immunoblotting using anti-panRAS or anti-Flag antibodies.

C, D   OTUB1 enhances serum-induced ERK1/2 phosphorylation in endogenous wt RAS (C) or wt KRAS (D). Levels of phosphorylated ERK1/2 and total ERK1/2 in HEK293T cells expressing HA-tagged OTUB1 or empty vector (V) were analyzed by Meso Scale assay. The results are expressed as a mean of pERK1/2 levels relative to total ERK1/2 ± s.e.m. $n = 2$. P-values were determined by two-sided t-Test.

E, F   Overexpression of wt OTUB1 (E) or the catalytically dead mutant OTUB1 C91S (F) promotes serum-induced MAPK activation in cell expressing wt NRAS. Whole cell lysates were analyzed by immunoblotting using the indicated antibodies.

G, H   Overexpression of OTUB1 has no effect on serum-induced MAPK activation in cell expressing mutant NRAS Q61K or KRAS G12V. Whole cell lysates were analyzed by immunoblotting using antibodies as indicated.

I   Immunoblot of OTUB1 overexpression in immortalized human embryonic kidney epithelial cells (HEK TEST), expressing empty vector (V), myristoylated AKT1 (myr-AKT), MEK1 D218, D222-mutant (MEKDD).

J, K   OTUB1 cooperates with active AKT1 to promote anchorage-independent growth. Representative images of soft-agar colonies formed by HEK TEST cells expressing the indicated constructs. The number of soft agar colonies formed by cells expressing OTUB1 compared to cells expressing an empty vector. Data are presented as mean ± s.e.m. P-values were determined by two-sided t-Test, $n = 2$.

Data information: (A–H) Serum-starved HEK293T cells expressing the indicated constructs were stimulated with 10% serum for the indicated time periods.
Source data are available online for this figure.

RAS, suggesting that OTUB1 may affect RAS ubiquitination by inhibiting the E2 ubiquitin-conjugating enzymes (Fig 2B and C). In fact, *in vitro* ubiquitination of RAS was abolished by wt OTUB1, but not by deltaN(1-30) OTUB1-mutant lacking binding to E2 (Fig EV2A). In contrast, incubation of ubiquitinated RAS with wt OTUB1 did not decrease levels of RAS ubiquitination, thus supporting the premise that OTUB1 functions via E2 inhibition independent of its catalytic activity (Fig EV2B).

Since previous reports demonstrated that reversible ubiquitination of RAS promotes its endosomal association (Jura *et al*, 2006), we tested whether OTUB1 affects the subcellular localization of RAS. Consistent with the observation that OTUB1 inhibits RAS ubiquitination, analysis of RAS localization revealed that OTUB1 overexpression augmented the presence of RAS proteins on the plasma membrane (Fig 2E and F; Appendix Fig S1). Hence, by inhibiting RAS ubiquitination, OTUB1 functions to hinder RAS re-localization from the plasma membrane thereby contributing to the spatial control of RAS-dependent cellular responses.

OTUB1 triggers RAS activity and downstream signaling

We next analyzed how OTUB1 affects RAS activity and signaling. We found that overexpression of OTUB1 in HEK293T cells led to hyperactivation of wt RAS upon serum stimulation (Fig 3A and B). In concordance with this result, OTUB1 overexpression triggered a significant increase in phospho-ERK1/2 levels at different time points after addition of serum (Fig 3C–E). We observed a similar overactivation of the MAPK pathway, when we overexpressed catalytically inactive OTUB1 C91S-mutant, indicating that catalytic activity of OTUB1 is not necessary to induce the MAPK pathway activation (Fig 3F). In contrast, OTUB1 overexpression did not dramatically affect phosphorylation levels of AKT1 (Appendix Fig S2A and B). The latter observation could be due to OTUB1-mediated inhibition of TRAF6 (Li *et al*, 2010) that plays a crucial role in AKT activation (Yang *et al*, 2009).

On the other hand, when we overexpressed OTUB1 in HEK293T cells expressing constitutively active RAS-mutants, NRAS Q61K or KRAS G12V, we did not observe any significant up-regulation of ERK1/2 phosphorylation, most likely because the MAPK pathway was already optimally active due to the introduction of the active

RAS-mutants (Fig 3G and H). We also did not observe OTUB1-induced hyperactivation of the MAPK kinase pathway when we overexpressed a dominant-negative KRAS S17N-mutant, indicating that the effect of OTUB1 overexpression is RAS dependent (Appendix Fig S2C). Taken together, these data indicate that OTUB1 up-regulation leads to activation of wt RAS signaling.

OTUB1 triggers cell transformation by inducing the MAPK cascade activation

Hyperactivation of the MAPK signaling by OTUB1 overexpression suggests that OTUB1 overexpression may promote tumorigenic transformation. Multiple studies have demonstrated that the co-expression of the telomerase catalytic subunit (hTERT), the SV40 Large T (LT) and small t (ST) oncoproteins, and an activated allele of RAS (RAS G12V) renders a wide range of human cells tumorigenic (Zhao *et al*, 2004), while co-activation of the MAPK and PI3K pathways suffices to replace RAS G12V in human cell transformation (Boehm *et al*, 2007). We used immortalized, but non-malignant human embryonic kidney epithelial cells expressing hTERT, LT, and ST (HEK TEST cells) as a model to assess tumorigenic potential of OTUB1 (Boehm *et al*, 2007). Given that OTUB1 overexpression up-regulated the MAPK pathway, but did not affect AKT signaling, we hypothesized that OTUB1 could cooperate with myristoylated (myr) and therefore the constitutively active allele of AKT1 (myr-AKT) to promote cell transformation. In fact, overexpression of OTUB1 together with myr-AKT1 dramatically induced anchorage-independent growth, whereas OTUB1 alone was not sufficient to trigger soft agar colony formation (Fig 3I–K). On the other hand, OTUB1 did not further accelerate anchorage-independent colony formation of HEK TE cells overexpressing both a constitutively active MEK1 D218, D222 allele (MEKDD) and myr-AKT, further confirming that OTUB1 overexpression promotes tumorigenic transformation by inducing the MAPK cascade activation.

OTUB1 is more frequently up-regulated in wt KRAS non-small-cell lung carcinomas

Our results suggest that increased OTUB1 expression could be an alternative mechanism of RAS activation superseding that of RAS

Figure 4. *OTUB1* expression is up-regulated in wt KRAS lung tumors.

A   Gains of OTUB1 and KRAS mutation are mutually exclusive in lung adenocarcinomas. OncoPrint showing the distribution of KRAS somatic mutations and OTUB1 copy number alterations in TCGA lung adenocarcinomas and squamous cell carcinomas obtained from cBioPortal (Cerami *et al*, 2012; Gao *et al*, 2013). Co-occurrence analysis showing significant mutual exclusivity between KRAS mutation and OTUB1 gain.

B, C   *OTUB1* overexpression in TCGA lung carcinomas is associated with 11q13.1 copy number alteration. Pearson correlation of *OTUB1* copy number (log2 ratio) with *OTUB1* mRNA levels (RNAseq normalized read counts, log2 transformed) was analyzed.

D–F   *OTUB1* expression in TCGA lung adenocarcinoma (LUAD) and lung squamous cell carcinoma (SCC) patients. Patients were stratified according to their *OTUB1* mRNA levels and/or their KRAS status as described in Materials and Methods. Box whisker plots represent *OTUB1* mRNA expression levels in TCGA lung carcinoma patients determined by RNAseq analysis. *P*-values were determined by two-sided *t*-Test. Total number of patients, n.

G   Gain of 11q13.1 locus is an early event in lung adenocarcinoma development. TCGA lung adenocarcinoma patients with diploid or gain of the *OTUB1* locus were stratified according tumor stages (T1–T4). Total numbers of patients, n. Statistical comparison of the sample distributions were compared using Chi-square test.

H   *OTUB1* mRNA overexpression is an early event in lung adenocarcinoma development. TCGA lung adenocarcinoma patients were stratified by tumor stages (T1–T4) and *OTUB1* expression levels as described in Materials and Methods. Total numbers of patients, n. Statistical comparison of the sample distributions were compared using Chi-square test.

I   KRAS mutation is a late event in lung adenocarcinoma progression. TCGA lung adenocarcinoma patients with different KRAS mutation status were stratified by tumor stages (T1–T4). Total numbers of patients, *n*. Statistical comparison of the sample distributions were compared using Chi-square test.

activating mutations. Analysis of The Cancer Genome Atlas (TCGA) revealed that gain of the 11q13.1 locus, where the *OTUB1* gene resides, was commonly observed in both lung adenocarcinomas and lung squamous cell carcinomas (SCC) (Figs 4A and EV3A). Correlation analysis revealed a strong association between copy number variation of 11q13.1 locus and *OTUB1* expression levels, suggesting that *OTUB1* is commonly up-regulated in lung tumors due to gain of the 11q13 locus (Figs 4B and C, and EV3A and B). *OTUB1* mRNA expression was also significantly up-regulated in about 50% of adenocarcinomas and about 80% of SCC compared to normal tissue samples (Fig 4D–F). These observations are further consolidated by the increase of *OTUB1* in a majority of tumorigenic lesions compared to their respective matched normal samples (Fig EV3C and D).

We also observed a higher proportion of wt KRAS lung adenocarcinomas with medium/high levels of OTUB1 expression compared to mutant KRAS tumors (Fig 4D and F). Correlation analysis revealed that increased expression of OTUB1 (co-occurrence log odds ratio: −1.478; *P*-value: 0.014) or a gain of the OTUB1 locus (co-occurrence log odds ratio: −0.796; *P*-value: 0.017) and the mutation status of KRAS were mutually exclusive (Fig 4A), suggesting that OTUB1 overexpression may play a crucial role in tumorigenesis especially in lung adenocarcinomas harboring wt KRAS.

Furthermore, either 11q13.1 gain or moderate OTUB1 overexpression is observed at early stages in lung adenocarcinomas with no increase in frequency in higher tumor stages (Fig 4G and H). In contrast, the frequency of KRAS mutations significantly increased with tumor stage predominantly associated with later stages of adenocarcinoma progression (Fig 4I). Taken together, these results suggest the role of OTUB1 up-regulation in promoting cancer development in wt KRAS lung tumors.

OTUB1 enhanced tumorigenic growth of lung adenocarcinomas

Next we assessed the contribution of OTUB1 to tumorigenic transformation of non-small-cell lung carcinoma (NSCLC) cells. To examine whether OTUB1 is essential for growth, we suppressed OTUB1 expression in lung adenocarcinoma cell lines using OTUB1 shRNAs (Fig 5A). Meso Scale analysis revealed that suppression of OTUB1 in A549 cell line led to decreased ERK1/2 phosphorylation upon serum stimulation (Fig 5B). Stable knockdown of OTUB1 also decreased anchorage-independent growth of several NSCLC cell lines and dramatically suppressed the xenograft growth of A549 cells in immunocompromised mice (Fig 5C–E). Taken together, these data strongly indicate that OTUB1 expression is essential for NSCLC tumor growth.

To further elucidate tumorigenic activity of OTUB1, we generated stable cell lines expressing Flag-tagged OTUB1. In the generated cell lines, we observed approximately 1.5- to 2-fold increase of OTUB1 expression with respect to endogenous protein levels that corresponds to an increase of OTUB1 expression triggered by 11q13.1 gain (Appendix Fig S3). OTUB1 overexpression in the H1993 cell line harboring wt KRAS led to a higher and more sustained activation of ERK1/2 phosphorylation (Fig 6A), whereas the introduction of OTUB1 into KRAS-mutant A549 cells only slightly increased the activity of the MAPK pathway (Fig 6B). These results are concordant with the effect of OTUB1 overexpression on the MAPK cascade activation in HEK293T cells expressing wt RAS or constitutively active RAS-mutants (Fig 3C–H).

We found that overexpression of OTUB1 in wt KRAS cell lines, H838, H1437, H1993, and HOP92, increased their ability to form colonies in soft agar (Fig 6C–E). In contrast, OTUB1 expression did not significantly affect anchorage-independent growth in KRAS-mutant cell lines, H2009, HOP62, and A427. A sole mutant KRAS A549 cell line had increased colony formation in response to OTUB1 overexpression (Fig 6C–E); however, *in vivo* tumor growth of A549 was not affected upon OTUB1 overexpression (Fig 6F). This indicates that even though OTUB1 is essential to maintain the activity of mutant RAS, up-regulation of OTUB1 expression does not further prompt tumorigenic properties of constitutively active RAS-mutants. Notably, OTUB1 expression in wt KRAS H1993 and H1437 cells significantly enhanced xenograft growth (Fig 6G). Taken together, these results suggest that an increase in OTUB1 expression accelerated tumorigenic transformation of wt KRAS NSCLCs.

OTUB1 up-regulation is associated with increased ERK1/2 activity in a subset of wt KRAS non-small-cell lung carcinomas

To confirm the contribution of OTUB1 to lung cancer development, we performed immunohistochemistry analysis of a NSCLC tissue array. OTUB1 immunoreactivity was scored as negative/low, medium, and high (Fig 7A). We found that more than 70% of
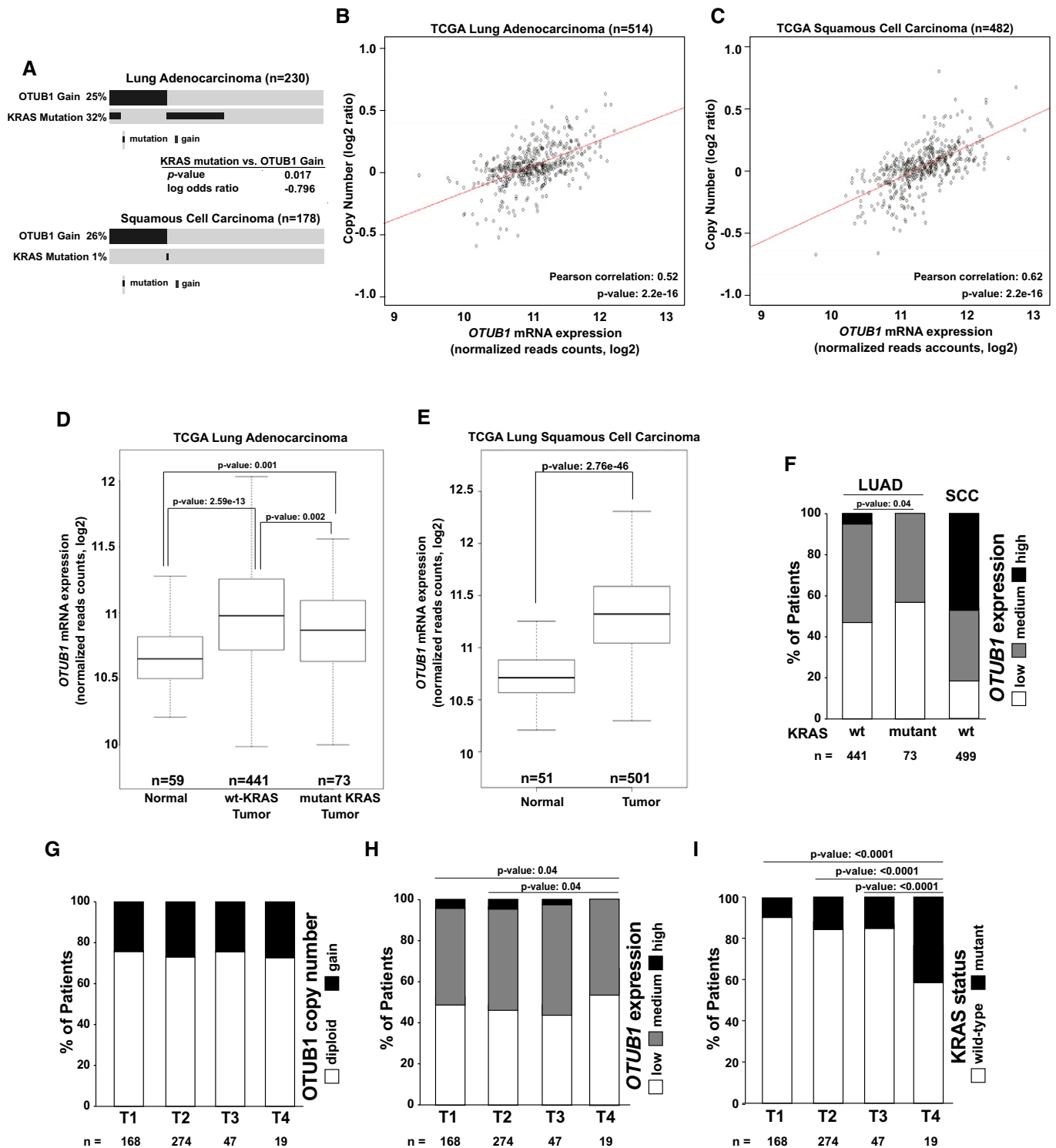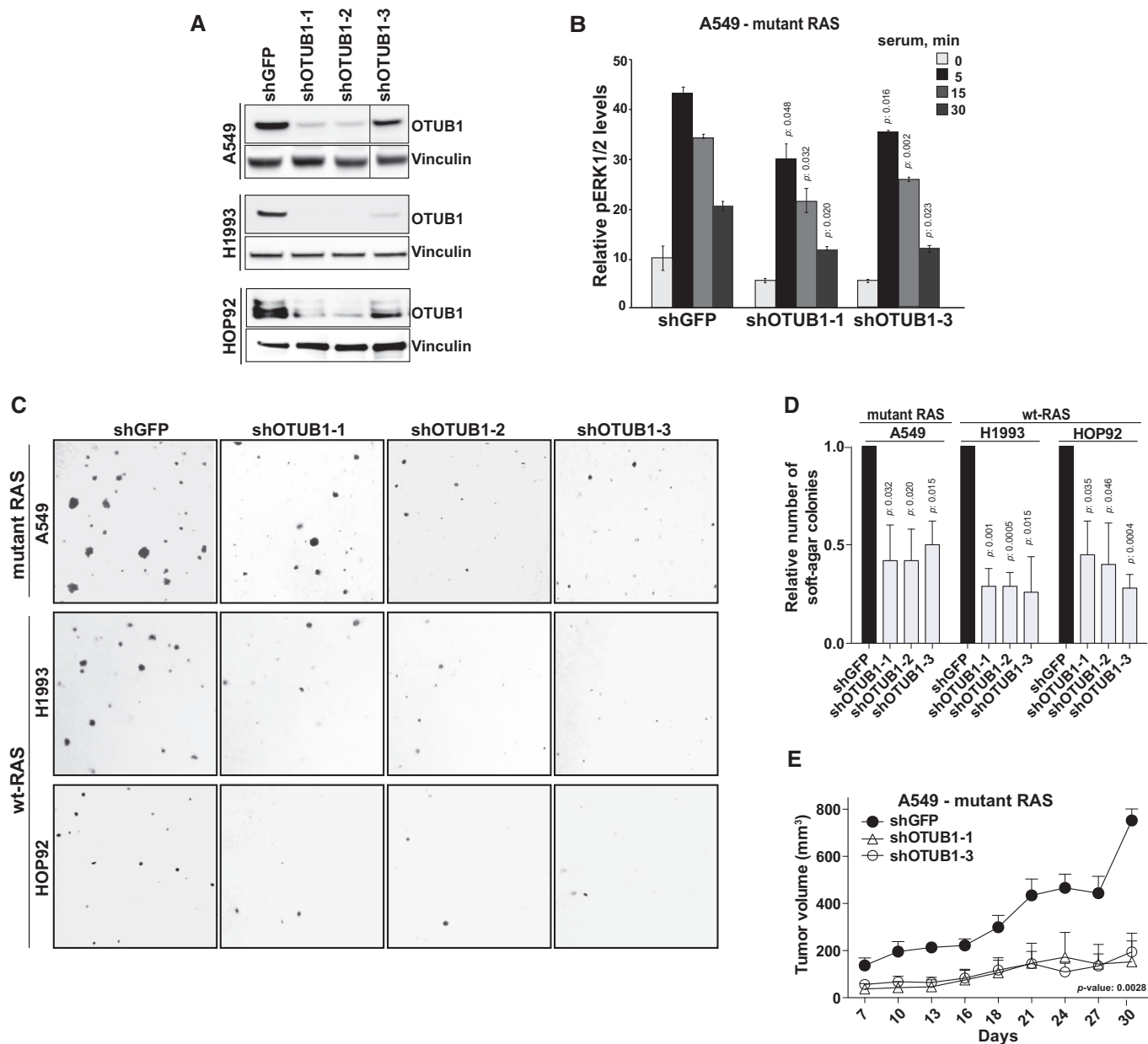
Figure 4.

adenocarcinomas and about 25% of squamous cell carcinomas exhibited intermediate or strong cytoplasmic OTUB1 positivity (Figs 7B and EV4A). Consistent with our TCGA data analysis, OTUB1 positivity was already observed in early stages of lung adenocarcinomas with strong immunoreactivity found in stages T2/T3 (Fig 7C). We also stratified the patients according to their

KRAS mutation status. Unfortunately, the low number of mutant KRAS samples ($n = 19$) did not permit statistical evaluation of this subgroup of patients (Fig 7B).

Consistently with our observation that OTUB1 overexpression induces the MAPK cascade activation in cells with wt RAS, we found that higher levels of OTUB1 significantly correlated with

Figure 5. OTUB1 is essential for tumorigenicity of lung cancer cells.

A   Suppression of OTUB1 expression in NSCLC cell lines by specific shRNAs against OTUB1 was confirmed by immunoblotting using antibody against OTUB1.

B   OTUB1 suppression decreases serum-induced ERK1/2 phosphorylation. Serum-starved A549 cells expressing shRNAs against OTUB1 or GFP were stimulated with 10% serum for the indicated time periods. Levels of phosphorylated ERK1/2 and total ERK1/2 were analyzed by Meso Scale assay. The results are expressed as a mean of pERK1/2 levels relative to total ERK1/2 ± s.e.m; *P*-values were determined by two-sided *t*-Test, *n* = 2.

C, D   OTUB1 suppression impairs the anchorage-independent growth of lung cancer cell lines. Representative images of soft-agar colonies formed by lung cells expressing shRNAs against OTUB1 or GFP. The number of soft agar colonies formed by cells expressing shOTUB1 compared to cells expressing shGFP. Data are presented as mean ± s.e.m. *P*-values were determined by two-sided *t*-Test, *n* = 3.

E   Xenograft tumor growth of A549 cells expressing shRNAs against GFP or OTUB1 subcutaneously injected into nude mice. Data are presented as mean ± s.e.m. *P*-value was determined by 2-way ANOVA, *n* = 4.

Source data are available online for this figure.

increased levels of ERK1/2 phosphorylation in lung adenocarcinomas harboring wt KRAS (Pearson's coefficient: 0.352; *P*-value: 0.013) (Fig 7D and E), while mutant KRAS tumors exhibited in general higher levels of ERK1/2 phosphorylation (Fig 7D and E).

We also observed that, in wt KRAS tumors, intermediate OTUB1 immunoreactivity has a tendency to display a higher proliferative score, as detected by Ki67 staining (Figs 7F and EV4B). On the other hand, high OTUB1 expression is mostly associated with
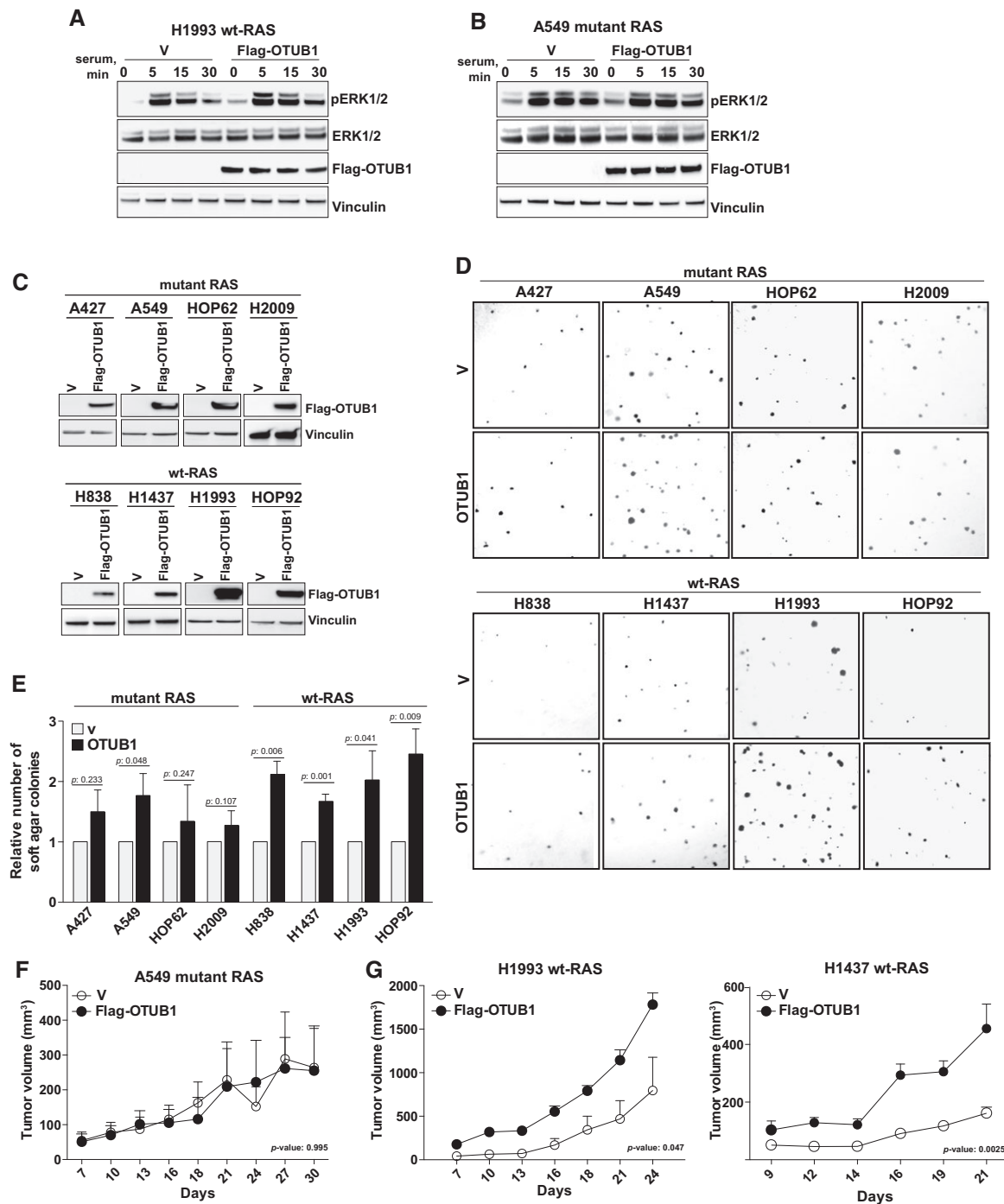
Figure 6. OTUB1 promotes tumorigenicity of wt KRAS cells.

A   OTUB1 overexpression promotes serum-induced MAPK activation in wt KRAS H1993 lung adenocarcinoma cells.

B   OTUB1 overexpression does not affect serum-induced MAPK activation in mutant KRAS A549 lung adenocarcinoma cells.

C   Representative immunoblots of Flag-tagged OTUB1 overexpression in lung adenocarcinoma cell lines.

D, E OTUB1 overexpression affects anchorage-independent growth of lung adenocarcinoma cell lines. Representative images of soft-agar colonies formed by the indicated cells expressing Flag-OTUB1 or empty vector (V). The number of soft agar colonies formed by OTUB1-expressing cells compared to cells expressing an empty vector. Data are presented as mean $\pm$ s.e.m. *P*-values were determined by two-sided *t*-Test, *n* = 3.

F, G Xenograft tumor growth of A549, H1993 or H1437 cells expressing Flag-OTUB1 or an empty vector (V) subcutaneously injected into nude mice. Data are presented as mean $\pm$ s.e.m. *P*-values were determined by 2-way ANOVA, *n* = 4.

Data information: (A, B) Serum-starved lung cells expressing Flag-OTUB1 or an empty vector (V) were stimulated with 10% serum for the indicated time periods. Whole cell lysates were analyzed by immunoblotting using antibodies against pERK1/2, ERK1/2, Flag, and vinculin.

Source data are available online for this figure.
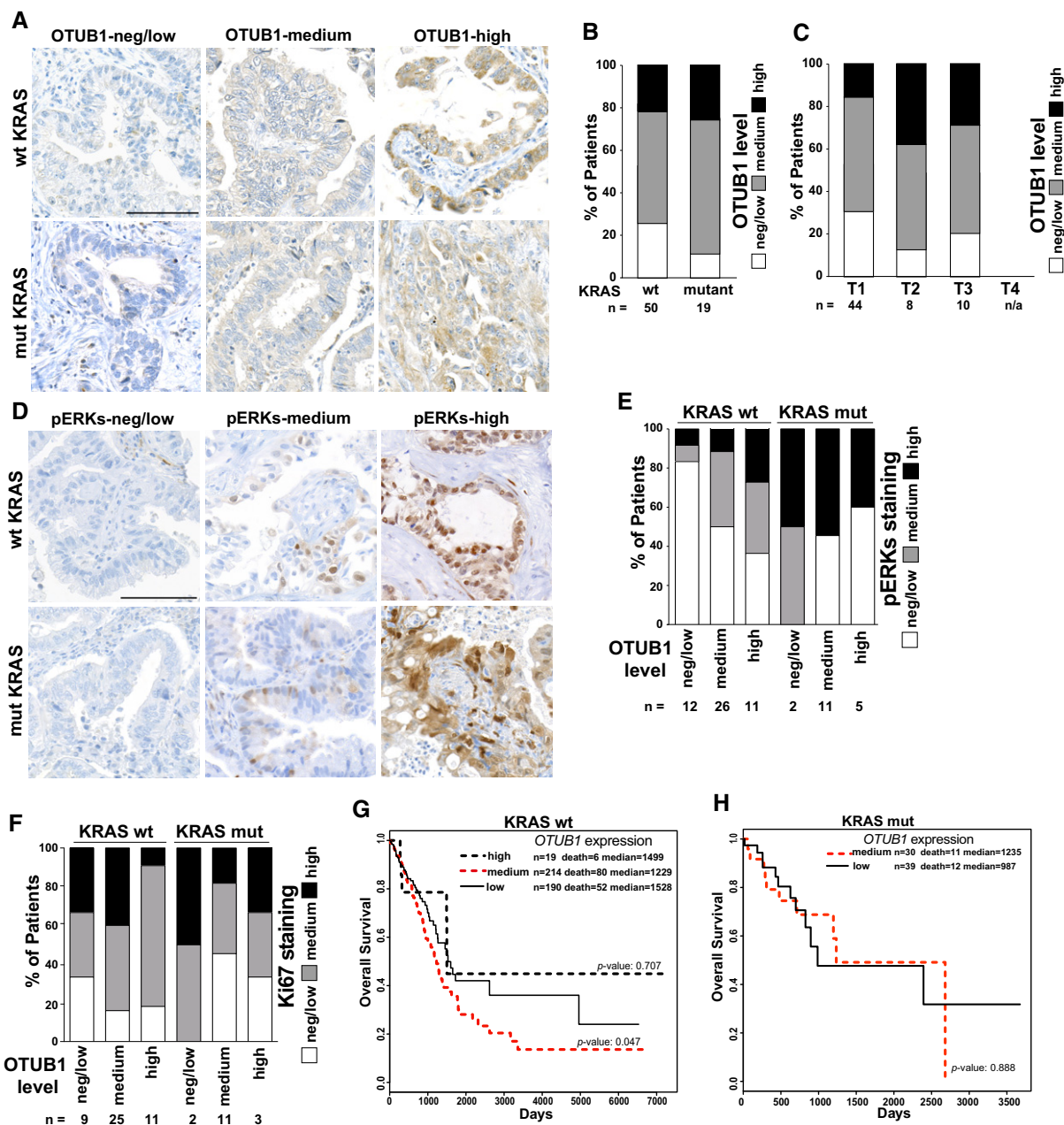
Figure 7. OTUB1 up-regulation in wt KRAS lung adenocarcinomas correlates with increased MAPK signaling and poorer patient survival.

A Representative examples of OTUB1 immunostaining in lung adenocarcinomas. Samples were scored as negative/low, medium, or high staining as described in Materials and Methods. Scale bar, 100 μm.

B OTUB1 expression in lung non-small-cell carcinomas with different KRAS mutation status. OTUB1 expression was assessed in TMA samples by IHC.

C OTUB1 up-regulation is an early event in lung adenocarcinoma development. Lung adenocarcinoma patients expressing different levels of OTUB1 were stratified by tumor stages (T1–T4). Total number of patients, n.

D Representative examples of phosphorylated-ERK1/2 immunostaining in lung adenocarcinomas. Samples were scored as negative/low, medium, or high staining as described in Material and Methods. Scale bar, 100 μm.

E OTUB1 levels correlates with increased levels of phosphorylated-ERK1/2 in wt KRAS lung adenocarcinomas. Association between OTUB1 and pERK1/2 expression levels was assessed in the same tumor samples by IHC.

F Ki67 expression in lung adenocarcinomas expressing different levels of OTUB1. Ki67 expression was assessed by IHC. The percentage of Ki67-positive cells was counted, and the samples were scored as negative/low, < 10%; medium, between 10 and 40%; and high, > 40%. See Fig EV4, for representative images of Ki67 staining.

G Wt KRAS lung adenocarcinoma TCGA patients with medium *OTUB1* expression have poorer overall survival.

H *OTUB1* expression levels are not associated with survival rate of KRAS-mutant lung adenocarcinoma TCGA patients.

Data information: (G, H) Patients were stratified according to their OTUB1 mRNA levels and/or their KRAS status as described in Materials and Methods. Overall survival of lung adenocarcinoma patients expressing different levels of OTUB1 mRNA as measured by Kaplan–Meier curves. *P*-values were determined by log-rank test.

intermediate Ki67 staining (Figs 7F and EV4B). This could be explained by several observations that sustained hyperactivation of the MAPK pathway may result in growth inhibition rather than cell proliferation (Pumiglia & Decker, 1997; Ravi *et al*, 1998).

Multiple reports revealed that the expression of Ki67 in patients with stages T1–T3 NSCLC is a poor prognostic factor for survival (Martin *et al*, 2004). Consistently with these observations, we found that a moderate up-regulation of OTUB1 is significantly associated with poorer overall survival in TCGA lung adenocarcinoma patients with wt KRAS compared to low-expressing OTUB1 (Fig 7G). On the contrary, moderate OTUB1 expression levels do not affect the survival of patients harboring KRAS mutation (Fig 7H). Together, these results support that up-regulation of OTUB1 may play a crucial role in tumorigenic transformation of cells harboring wt KRAS by promoting RAS-induced ERK activation.

Discussion

Our study identifies OTUB1 as a key player in the pathogenesis of wt KRAS lung cancers. Previously, OTUB1 has been implicated in the regulation of several physiological and pathological processes independently of its de-ubiquitinase activity. OTUB1 has been reported to regulate T-cell anergy by enhancing the degradation of the E3 ligase GRAIL (gene related to anergy in lymphocytes) (Lin *et al*, 2009), to augment TGF-β signaling by inhibiting degradation of phosphorylated SMAD2/3 (Herhaus *et al*, 2013), and to suppress DNA-damage-dependent chromatin ubiquitination (Nakada *et al*, 2010) and MDM2-mediated ubiquitination of the tumor suppressor p53 (Sun *et al*, 2012). Here we found that OTUB1 promotes tumorigenic transformation of wt RAS cells by triggering the RAS/MAPK pathway. Several lines of evidences support this conclusion. First, OTUB1 promotes hyperactivation of the MAPK cascade only when overexpressed in a wt RAS background. Second, OTUB1 replaces activated MEK1-mutant in an experimental model of human cell transformation. Furthermore, higher levels of OTUB1 expression are observed specifically in lung adenocarcinomas harboring wt KRAS compared to mutated RAS tumors. Finally, OTUB1 drives tumorigenic growth of wt RAS, but not mutant KRAS tumors.

OTUB1 triggers activation of the MAPK pathway by inhibiting RAS ubiquitination. Consistently with these observations, previous reports demonstrated that ubiquitination of HRAS and NRAS modulates their ability to activate the MAPK pathway (Xu *et al*, 2010; Yan *et al*, 2010). The RAS-specific E3 ligase RABEX5 may act as a tumor suppressor by regulating MAPK cascade activation. Rabex5-deficient mast cells exhibit enhanced and prolonged activation of Ras under basal conditions (Tam *et al*, 2004). A *Drosophila* Rabex5 hypomorphic mutation results in giant larvae or pupae, which often contain melanotic tumors (Yan *et al*, 2010). This phenotype is also attributed to dysregulation of RAS signaling (Zettervall *et al*, 2004; Yan *et al*, 2010).

In contrast to these studies and our results, some reports suggest that ubiquitination of KRAS at Lys117 and Lys147, which contribute to the formation of a GDP/GTP-binding pocket of RAS, increases its ability to activate downstream signaling and promote KRAS tumorigenic properties (Sasaki *et al*, 2011). However, the conclusions of these studies are mostly based on the analysis of Lys117 and Lys147-mutants (Baker *et al*, 2013a,b), whereas amino acid substitutions within the GDP/GTP-binding pocket have been shown to augment the flexibility of the pocket, leading to increased guanine nucleotide dissociation and higher GTP loading. Identification of E3 ubiquitin ligases that could ubiquitinate RAS proteins specifically at Lys117/Lys147 will help to resolve this apparent conundrum.

Whereas down-regulation or loss of function of RABEX5 in human cancers has not been reported, we found that OTUB1 expression is commonly up-regulated in a substantial subset of NSCLCs harboring wt KRAS. Recent studies also report increased expression of OTUB1 in prostate, colorectal, and breast cancers that are associated with poor survival, high metastatic potential, and chemotherapeutic drug resistance (Liu *et al*, 2014; Zhou *et al*, 2014; Iglesias-Gato *et al*, 2015; Karunarathna *et al*, 2015). Importantly, TCGA data analysis revealed that, similarly to lung adenocarcinomas, OTUB1 overexpression in colorectal cancer is mutually exclusive with KRAS mutations (co-occurrence log odds ratio: −3; *P*-value: 0.003), whereas RAS genes are rarely mutated in prostate and breast cancers (Karnoub & Weinberg, 2008). This further confirms that OTUB1 up-regulation may contribute to the development of different tumor types harboring wt RAS. Compellingly, a moderate up-regulation of OTUB1 decreases the overall survival of lung adenocarcinoma patients with wt KRAS, suggesting that only medium levels of OTUB1 confers advantage to cancer cells and/or could affect their chemotherapeutic resistance. On the other hand, the lack of effect of high OTUB1 expression levels on patients' survival could be further explained by the alternative interactions of OTUB1 beyond RAS that for instance were reported to lead to the stabilization of p53 (Sun *et al*, 2012) or CK2-mediated OTUB1 nuclear translocation to affect DNA repair (Herhaus *et al*, 2015).

Oncogenic mutations of the RAS GTPases have been observed in about one-third of human cancers (Karnoub & Weinberg, 2008). However, the high prevalence of RAS pathway activation strongly suggests the existence of alternative mechanisms of RAS/MAPK activation. Recently, RAS GAPs have emerged as an expanding new class of tumor suppressor genes that contribute to malignant transformation by triggering RAS activity (Maertens & Cichowski, 2014). Our data suggest that dysregulation of RAS ubiquitination represents an alternative mechanism to activate RAS during NSCLC development. Advancing knowledge on the regulatory hub controlling RAS ubiquitination and thus targeting RAS up-regulation could be clinically exploited as a strategy to inhibit the activation of wt RAS in lung cancers.

Materials and Methods

Cell culture and lentiviral transduction

HEK293T, HeLa, H838, H2009, H1437, A549, and A427 cells were cultured in DMEM-F12 medium (GIBCO); H1993, HOP62, and HOP92 were grown in RMPI 1640 medium (GIBCO). All media were supplemented with 10% fetal bovine serum and 1% penicillin/streptomycin. Embryonic kidney epithelial cells (HEK TEST) immortalized by hTERT, SV40 LT, and SV40 ST and expressing either empty vector, myristoylated AKT1 (myr-AKT), or MEK1 D218,

D222-mutant (MEKDD) were a gift from Dr. Hahn (Dana-Farber Cancer Institute, USA) (Boehm *et al*, 2007).

Transient transfections were performed using Turbofect, Lipofectamine LTX (Life Technologies), or XtremeGene9 (Roche). Lentiviral infections were performed as described by the RNAi Consortium (TRC). Infected cells were selected by treatment with 1–2 µg puromycin (InvivoGen) for 2 days.

Expression vectors and antibodies

Full-length OTUB1 expression constructs were purchased from ORIGENE. Point mutations to generate OTUB1 C91S were obtained by QuickChange site-directed mutagenesis PCR (Stratagene, La Jolla). Lentiviral pLA-CMV-N-Flag or pLA-CMV-N-HA vectors were used to generate Flag/HA-tagged constructs. The pMT107–6×His–ubiquitin plasmid was a generous gift from Dr. Bohmann (University of Rochester, USA). pLKO.1-puro shGFP and pLKO.1-puro vectors containing shRNAs targeting OTUB1 (pLKO.1-shOTUB1_1 (TRCN0000004211), pLKO.1-shOTUB1_2 (TRCN0000004213), pLKO.1-shOTUB1_3 (TRCN0000004215)) were purchased from Sigma-Aldrich.

The antibodies used: mouse monoclonal anti-FLAG (Sigma-Aldrich, M2), anti-RAS (Millipore, Clone 10), anti-vinculin (Sigma-Aldrich, clone hVIN-1), anti-GAPDH (Sigma-Aldrich, GAPDH-71.1), anti-p44/42 MAPK (Erk1/2) (Thr202/Tyr204) (Cell Signaling, 3A7, #9107), anti-AKT (Cell Signaling, 40D4); rat monoclonal anti-HA (Roche, 3F10); rabbit monoclonal anti-phospho-p44/42 MAPK (Erk1/2) (Thr202/Tyr204) (IHC) (Cell Signaling, D13.14.4E, #4370), anti-Ki67 (Thermo Scientific #RM-9106-S, clone SP6); rabbit polyclonal anti-DYKDDDDK (Cell Signaling), anti-OTUB1 (Bethyl Laboratories), anti-OTUB1 (IHC) (Sigma-Aldrich, HPA039176), anti-phospho-p44/42 MAPK (Erk1/2) (Thr202/Tyr204) (Cell Signaling, #9101), anti-pAKT (Cell Signaling, D9E), anti-RABEX5 (Sigma-Aldrich).

MAPPIT screen

MAPPIT experiments were performed as described previously (Lemmens *et al*, 2015). RAS proteins, expressed through a pSEL(+2L) vector, served as bait and DUB ORFs were cloned as prey in the pMG1 vector. The prey collection screened was selected from the human ORFeome collection versions 5.1 and 8.1 (http://horfdb.dfci.harvard.edu/hv5/). In brief, 293T cells were transfected with the bait and prey expressing plasmids combined with the STAT3-dependent pXP2d2-rPAPI-luciferase reporter plasmid. Twenty-four hours later, triplicate wells were supplemented with medium with or without 10 ng/ml erythropoietin. Twenty-four hours after leptin stimulation, luciferase activity was measured. MAPPIT signals were calculated as the ratio between the average values of the leptin-stimulated and the unstimulated samples.

Immunoprecipitation, immunoblotting, and Meso Scale analysis

Cells were washed twice in cold PBS and scraped on ice in lysis buffer (50 mM Tris–HCl pH 7.5, 150 mM NaCl, 1% NP-40) containing protease inhibitor and phosphatase inhibitor cocktails (Roche). Samples were subsequently cleared by centrifugation for 10 min 16,000 *g* at 4°C. For immunoprecipitation assays, cells

were lysed in co-immunoprecipitation buffer [50 mM Tris–HCl, at pH 7.5, 137 mM NaCl, 1% NP-40, 5 mM MgCl$_2$, 10% glycerol, and protease inhibitor cocktail (Roche)]. Tagged proteins were immunoprecipitated using anti-Flag (M2) or anti-HA agarose beads (Sigma-Aldrich) for 2 h at 4°C, washed five times with cold co-immunoprecipitation and finally eluted with 3 × Flag or HA peptides according to the manufacture's protocol. For immunoblotting, equivalent amounts of cell lysates were separated on 4–12% gradient gels (Invitrogen), transferred to nitrocellulose membranes, and incubated with the indicated antibodies. The signal was visualized with chemiluminescence detection reagent (Amersham Pharmacia Biotech) using an automated digital developer.

Meso Scale Discovery 96-well multispot plates were used for quantitative phospho/total ERK1/2(K15107D) and AKT1 (K15100A3) analyses according to the manufacturer's instructions (Meso Scale Diagnostics). Plates were analyzed using MESO QuickPlex SQ120 multiplex imager (Meso Scale Diagnostics).

RAS activation assay

The RAS activation assay was conducted according to the manufacturer's protocol (Millipore). Briefly, cells were washed with cold PBS and lysed in lysis/wash buffer (Millipore). Equal amounts of clarified cell lysates were mixed with Raf-1-RBD agarose beads (Millipore) and incubated for 45 min at 4°C. The beads were washed with lysis/wash buffer three times and eluted by boiling in 2 × SDS buffer. Eluted proteins were subjected to SDS–PAGE and immunoblotted.

Purification of ubiquitinated proteins

HEK293T cells were co-transfected with 6×His–ubiquitin and Flag–RASs. Ubiquitinated proteins were purified as described previously (Simicek *et al*, 2013). Briefly, cells were lysed in co-immunoprecipitation buffer containing EDTA-free protease inhibitor cocktail (Roche). Cell lysates were mixed with His-buffer A (PBS, at pH 8.0, 6 M guanidinium–HCl, 0.1% NP-40 and 1 mM β-ME) and added to TALON beads (Clontech). After binding, the resin was washed with His-buffer B (PBS, at pH 8.0, 0.1% NP-40, 5% glycerol and 20 mM imidazole), and proteins were eluted in sample buffer.

For *in vitro* ubiquitination assay, purified proteins were incubated in the reaction buffer (20 mM Tris, pH 7.4; 50 mM NaCl; 100 µM ZnCl$_2$; 8 mM MgCl$_2$; 4 mM ATP) for 2 h at 30°C. The final protein concentrations in the reaction mix were as follows: UBE1 (80 nM), UbcH5C (400 nM), ubiquitin (16 µM), RABEX5 (1-76) (3 µM), Flag–NRAS (2.5 µM), and OTUB1 (3 µM). The reaction was quenched with 20 mM EDTA, and NRAS ubiquitination was analyzed by immunoblotting using anti-Flag M2 antibody.

Fluorescence microscopy

For immunostaining, 2×10^4 HeLa cells were plated on 8-well chamber glass slide (Nalge Nunc International) and fixed 24 h after transfection with 4% PFA. Immunostaining was performed as described previously (Simicek *et al*, 2013). Briefly, cells were permeabilized in PBS-0.15% Triton and blocked with 1% BSA and 10% goat serum. Primary antibodies and goat Alexa-conjugated

secondary antibodies were applied by diluting in blocking buffer before mounting in Citifluor. Images were obtained by using a confocal Leica SPII microscope (63× magnification) (Leica Microsystems, Wetzlar, Germany).

Cellular distribution of RAS proteins was determined by automatic imaging using the IN Cell Analyzer 2000 system. Data analysis and image quantification were performed using ImageJ (National Institutes of Health USA).

TCGA analysis

To generate the OncoPrint of OTUB1 gain and KRAS mutation status in lung adenocarcinoma (LUAD) and lung squamous cell carcinoma (LUSC), cBioPortal (http://www.cbioportal.org) (Cerami *et al*, 2012; Gao *et al*, 2013) was queried over all completed tumors from TCGA provisional datasets using the Onco Query Language (OQL), "OTUB1:GAIN; KRAS: MUT".

Additionally, clinico-pathological, gene expression, and copy number alteration data were downloaded from the TCGA data portal (https://tcga-data.nci.nih.gov/tcga/) for both datasets. For analysis of *OTUB1* expression, OTUB1 read counts from RNASeq analysis were normalized across all patient samples and log2-transformed. To determine the copy number status of OTUB1, the mean copy number segments overlapping the OTUB1 locus were extracted using a Perl script. OTUB1 gain was determined as samples with a log2 ratio > 0.1. Pearson correlation between *OTUB1* expression and copy number was performed and plotted in the R statistical package (Version 3.2.0). *Z*-score normalization of OTUB1 expression in tumors compared to matched normals revealed three levels of expression, negative/low (< 1 s.d.), medium (1–3 s.d.), and high (> 3 s.d.). Kaplan–Meier survival plots were generated in R comparing the overall survival for each level of OTUB1 expression in both KRAS wt and KRAS-mutated LUAD using the log-rank test.

Immunohistochemistry

Non-small-cell lung cancer tissue micro-array slides (TristarGroup, US) were immunostained for OTUB1, Ki67, and pERKs on a Discovery Ventana automated staining platform. OTUB1 and phospho-ERKs immunohistochemistry was evaluated using a semi-quantitative approach that combines intensity and distribution of immunoreactivity in the epithelial tumor cells. Each single TMA spot was annotated using the same criteria applied in the HUMAN PROTEIN ATLAS project (http://www.proteinatlas.org/). Arrays were scored in a blinded manner on an intensity scale of 0–3 (0, no staining; 1, low staining; 2, moderate staining; 3, strong staining) and on a distribution scale of 0–3 (0, none; 1, < 25% tumor area; 2, between 25% and 75% tumor area; 3, > 75% tumor area). Data were then analyzed combining the intensity and distribution values in a scale of no/low staining (neg/low), moderate staining (medium), and strong staining (high). For Ki67 analysis, the percentage of positive cells was counted and the samples scored on a positivity scale as neg/low, < 10%; medium, between 10 and 40%; and high, > 40%.

Anchorage-independent growth and tumor xenograft assays

Anchorage-independent growth in soft agar was performed as previously described in Boehm *et al* (2007). About 10^4 cells were plated

in triplicates in 0.35% Noble agar over a 0.5% agar bottom layer. Three weeks after plating, several random areas were imaged and colonies were quantified using ImageJ software.

For tumor xenograft assays, 2.0×10^6 cells were injected subcutaneously into the lower flanks of 6-week-old female NMRI-nu (nu/nu) nude mice (Janvier). Tumor growth was monitored 3 times per week, and volumes were calculated using the following formula: volume = (tumor width^2 × tumor length)/2.

Statistical analysis

Meso Scale measurements, RAS cellular distribution, and colony quantifications were calculated as percentages from at least three independent experiments. The error bars indicate the standard error of the mean (s.e.m.). *P*-values were calculated by two-tailed *t*-Test. All data were analyzed using GraphPad Prism for Apple Mac (version 6.0f). For the TCGA analysis, two-sided *t*-Tests determined the significant differences between groups means based on the expression levels. Two-way ANOVA was used to analyze xenograft experiments.

Study approval

The ethical committee of the KU Leuven approved the animal study (declaration P166/2013).

Acknowledgements

The paper explained

Problem
Hyperactivation of the RAS-MAPK oncogenic pathway is a common event in lung cancer. Despite many efforts to inhibit the RAS proteins, selective inhibition of RAS remains a considerable challenge; thus, a better understanding of the RAS pathway is urgently required to establish new treatment strategies.

Results
Recent reports demonstrate that reversible ubiquitination of RAS dramatically affects its activity, suggesting that enzymes involved in regulating RAS ubiquitination may contribute to malignant transformation. Our results strongly indicate that dysregulation by RAS monoubiquitination represents an alternative mechanism of RAS activation during lung cancer development. Specifically, we found that the deubiquitinase OTUB1 promotes lung cancer formation and correlates with poorer patient prognosis.

Impact
The development of small-molecule modulators of deubiquitinases has recently attracted the attention of the biomedical industry, rendering them promising targets for cancer treatment. The results of our study not only advance our understanding of RAS signaling, but also subsequently could lead to novel therapeutic approaches.

Author contributions

Conflict of interest

References

Baker R, Lewis SM, Sasaki AT, Wilkerson EM, Locasale JW, Cantley LC, Kuhlman B, Dohlman HG, Campbell SL (2013a) Site-specific monoubiquitination activates Ras by impeding GTPase-activating protein function. *Nat Struct Mol Biol* 20: 46 – 52

Baker R, Wilkerson EM, Sumita K, Isom DG, Sasaki AT, Dohlman HG, Campbell SL (2013b) Differences in the regulation of K-Ras and H-Ras isoforms by monoubiquitination. *J Biol Chem* 288: 36856 – 36862

Bivona TG, Quatela SE, Bodemann BO, Ahearn IM, Soskis MJ, Mor A, Miura J, Wiener HH, Wright L, Saba SG *et al* (2006) PKC regulates a farnesyl-electrostatic switch on K-Ras that promotes its association with Bcl-XL on mitochondria and induces apoptosis. *Mol Cell* 21: 481 – 493

Boehm JS, Zhao JJ, Yao J, Kim SY, Firestein R, Dunn IF, Sjostrom SK, Garraway LA, Weremowicz S, Richardson AL *et al* (2007) Integrative genomic approaches identify IKBKE as a breast cancer oncogene. *Cell* 129: 1065 – 1079

Cerami E, Gao J, Dogrusoz U, Gross BE, Sumer SO, Aksoy BA, Jacobsen A, Byrne CJ, Heuer ML, Larsson E *et al* (2012) The cBio cancer genomics portal: an open platform for exploring multidimensional cancer genomics data. *Cancer Discov* 2: 401 – 404

Colicelli J (2004) Human RAS superfamily proteins and related GTPases. *Sci STKE* 2004: RE13.

Edelmann MJ, Iphofer A, Akutsu M, Altun M, di Gleria K, Kramer HB, Fiebiger E, Dhe-Paganon S, Kessler BM (2009) Structural basis and specificity of human otubain 1-mediated deubiquitination. *Biochem J* 418: 379 – 390

Gao J, Aksoy BA, Dogrusoz U, Dresdner G, Gross B, Sumer SO, Sun Y, Jacobsen A, Sinha R, Larsson E *et al* (2013) Integrative analysis of complex cancer genomics and clinical profiles using the cBioPortal. *Sci Signal* 6: pl1.

Hancock JF (2003) Ras proteins: different signals from different locations. *Nat Rev Mol Cell Biol* 4: 373 – 384

Herhaus L, Al-Salihi M, Macartney T, Weidlich S, Sapkota GP (2013) OTUB1 enhances TGF beta signalling by inhibiting the ubiquitylation and degradation of active SMAD2/3. *Nat Commun* 4: 2519

Herhaus L, Perez-Oliva AB, Cozza G, Gourlay R, Weidlich S, Campbell DG, Pinna LA, Sapkota GP (2015) Casein kinase 2 (CK2) phosphorylates the deubiquitylase OTUB1 at Ser16 to trigger its nuclear localization. *Sci Signal* 8: ra35

Iglesias-Gato D, Chuan YC, Jiang N, Svensson C, Bao J, Paul I, Egevad L, Kessler BM, Wikstrom P, Niu Y *et al* (2015) OTUB1 de-ubiquitinating enzyme promotes prostate cancer cell invasion in vitro and tumorigenesis in vivo. *Mol Cancer* 14: 8

Juang YC, Landry MC, Sanches M, Vittal V, Leung CC, Ceccarelli DF, Mateo AR, Pruneda JN, Mao DY, Szilard RK *et al* (2012) OTUB1 co-opts Lys48-linked ubiquitin recognition to suppress E2 enzyme function. *Mol Cell* 45: 384 – 397

Jura N, Scotto-Lavino E, Sobczyk A, Bar-Sagi D (2006) Differential modification of Ras proteins by ubiquitination. *Mol Cell* 21: 679 – 687

Karnoub AE, Weinberg RA (2008) Ras oncogenes: split personalities. *Nat Rev Mol Cell Biol* 9: 517 – 531

Karunarathna U, Kongsema M, Zona S, Gong C, Cabrera E, Gomes AR, Man EP, Khongkow P, Tsang JW, Khoo US *et al* (2015) OTUB1 inhibits the ubiquitination and degradation of FOXM1 in breast cancer and epirubicin resistance. *Oncogene*. doi: 10.1038/onc.2015.208

Lemmens I, Lievens S, Tavernier J (2015) MAPPIT, a mammalian two-hybrid method for in-cell detection of protein-protein interactions. *Methods Mol Biol* 1278: 447 – 455

Li S, Zheng H, Mao AP, Zhong B, Li Y, Liu Y, Gao Y, Ran Y, Tien P, Shu HB (2010) Regulation of virus-triggered signaling by OTUB1- and OTUB2-mediated deubiquitination of TRAF3 and TRAF6. *J Biol Chem* 285: 4291 – 4297

Lievens S, Vanderroost N, Van der Heyden J, Gesellchen V, Vidal M, Tavernier J (2009) Array MAPPIT: high-throughput interactome analysis in mammalian cells. *J Proteome Res* 8: 877 – 886

Lievens S, Vanderroost N, Defever D, Van der Heyden J, Tavernier J (2012) ArrayMAPPIT: a screening platform for human protein interactome analysis. *Methods Mol Biol* 812: 283 – 294

Lin JT, Lineberry NB, Kattah MG, Su LL, Utz PJ, Fathman CG, Wu LD (2009) Naive CD4 T Cell Proliferation Is Controlled by Mammalian Target of Rapainaycin Regulation of GRAIL Expression. *J Immunol* 182: 5919 – 5928

Liu X, Jiang WN, Wang JG, Chen H (2014) Colon cancer bears overexpression of OTUB1. *Pathol Res Pract* 210: 770 – 773

Maertens O, Cichowski K (2014) An expanding role for RAS GTPase activating proteins (RAS GAPs) in cancer. *Adv Biol Regul* 55: 1 – 14

Martin B, Paesmans M, Mascaux C, Berghmans T, Lothaire P, Meert AP, Lafitte JJ, Sculier JP (2004) Ki-67 expression and patients survival in lung cancer: systematic review of the literature with meta-analysis. *Br J Cancer* 91: 2018 – 2025

Nakada S, Tai I, Panier S, Al-Hakim A, Iemura S, Juang YC, O'Donnell L, Kumakubo A, Munro M, Sicheri F *et al* (2010) Non-canonical inhibition of DNA damage-dependent ubiquitination by OTUB1. *Nature* 466: 941 – 946

Network CGAR (2014) Comprehensive molecular profiling of lung adenocarcinoma. *Nature* 511: 543 – 550

Pumiglia KM, Decker SJ (1997) Cell cycle arrest mediated by the MEK/mitogen-activated protein kinase pathway. *Proc Natl Acad Sci USA* 94: 448 – 452

Pylayeva-Gupta Y, Grabocka E, Bar-Sagi D (2011) RAS oncogenes: weaving a tumorigenic web. *Nat Rev Cancer* 11: 761 – 774

Ravi RK, Weber E, McMahon M, Williams JR, Baylin S, Mal A, Harter ML, Dillehay LE, Claudio PP, Giordano A *et al* (1998) Activated Raf-1 causes growth arrest in human small cell lung cancer cells. *J. Clin. Invest.* 101: 153 – 159

Sasaki AT, Carracedo A, Locasale JW, Anastasiou D, Takeuchi K, Kahoud ER, Haviv S, Asara JM, Pandolfi PP, Cantley LC (2011) Ubiquitination of K-Ras enhances activation and facilitates binding to select downstream effectors. *Sci Signal* 4: ra13

Sato Y, Yamagata A, Goto-Ito S, Kubota K, Miyamoto R, Nakada S, Fukai S (2012) Molecular Basis of Lys-63-linked Polyubiquitination Inhibition by the Interaction between Human Deubiquitinating Enzyme OTUB1 and Ubiquitin-conjugating Enzyme UBC13. *J Biol Chem* 287: 25860 – 25868

Shukla S, Allam US, Ahsan A, Chen G, Krishnamurthy PM, Marsh K, Rumschlag M, Shankar S, Whitehead C, Schipper M *et al* (2014) KRAS

protein stability is regulated through SMURF2: UBCH5 complex-mediated β-TrCP1 degradation. *Neoplasia* 16: 115−128

Simicek M, Lievens S, Laga M, Guzenko D, Aushev VN, Kalev P, Baietti MF, Strelkov SV, Gevaert K, Tavernier J *et al* (2013) The deubiquitylase USP33 discriminates between RALB functions in autophagy and innate immune response. *Nat Cell Biol* 15: 1220−1230

Sun XX, Challagundla KB, Dai MS (2012) Positive regulation of p53 stability and activity by the deubiquitinating enzyme Otubain 1. *EMBO J* 31: 576−592

Tam SY, Tsai M, Snouwaert JN, Kalesnikoff J, Scherrer D, Nakae S, Chatterjea D, Bouley DM, Galli SJ (2004) RabGEF1 is a negative regulator of mast cell activation and skin inflammation. *Nat Immunol* 5: 844−852

Vigil D, Cherfils J, Rossman KL, Der CJ (2010) Ras superfamily GEFs and GAPs: validated and tractable targets for cancer therapy? *Nat Rev Cancer* 10: 842−857

Wang T, Yin L, Cooper EM, Lai MY, Dickey S, Pickart CM, Fushman D, Wilkinson KD, Cohen RE, Wolberger C (2009) Evidence for bidentate substrate binding as the basis for the K48 linkage specificity of otubain 1. *J Mol Biol* 386: 1011−1023

Wang XS, Shankar S, Dhanasekaran SM, Ateeq B, Sasaki AT, Jing X, Robinson D, Cao Q, Prensner JR, Yocum AK *et al* (2011) Characterization of KRAS rearrangements in metastatic prostate cancer. *Cancer Discov* 1: 35−43

Wiener R, Zhang XB, Wang T, Wolberger C (2012) The mechanism of OTUB1-mediated inhibition of ubiquitination. *Nature* 483: 618−U143

Xu L, Lubkov V, Taylor LJ, Bar-Sagi D (2010) Feedback regulation of Ras signaling by Rabex-5-mediated ubiquitination. *Curr Biol* 20: 1372−1377

Yan H, Jahanshahi M, Horvath EA, Liu HY, Pfleger CM (2010) Rabex-5 Ubiquitin Ligase Activity Restricts Ras Signaling to Establish Pathway Homeostasis in Drosophila. *Curr Biol* 20: 1378−1382

Yang WL, Wang J, Chan CH, Lee SW, Campos AD, Lamothe B, Hur L, Grabiner BC, Lin X, Darnay BG *et al* (2009) The E3 ligase TRAF6 regulates Akt ubiquitination and activation. *Science* 325: 1134−1138

Yang MH, Laurent G, Bause AS, Spang R, German N, Haigis MC, Haigis KM (2013) HDAC6 and SIRT2 regulate the acetylation state and oncogenic activity of mutant K-RAS. *Mol Cancer Res* 11: 1072−1077

Zeng T, Wang Q, Fu J, Lin Q, Bi J, Ding W, Qiao Y, Zhang S, Zhao W, Lin H *et al* (2014) Impeded nedd4-1-mediated ras degradation underlies ras-driven tumorigenesis. *Cell Rep* 7: 871−882

Zettervall CJ, Anderl I, Williams MJ, Palmer R, Kurucz E, Ando I, Hultmark D (2004) A directed screen for genes involved in Drosophila blood cell activation. *Proc Natl Acad Sci USA* 101: 14192−14197

Zhao JJ, Roberts TM, Hahn WC (2004) Functional genetics and experimental models of human cancer. *Trends Mol Med* 10: 344−350

Zhou Y, Wu J, Fu X, Du W, Zhou L, Meng X, Yu H, Lin J, Ye W, Liu J *et al* (2014) OTUB1 promotes metastasis and serves as a marker of poor prognosis in colorectal cancer. *Mol Cancer* 13: 258

SIGNAL TRANSDUCTION

Mutations in LZTR1 drive human disease by dysregulating RAS ubiquitination

M. Steklov[1,2]*, S. Pandolfi[1,2]*, M. F. Baietti[1,2]*, A. Batiuk[1,2], P. Carai[3], P. Najm[1,2],
M. Zhang[4], H. Jang[4], F. Renzi[1,2], Y. Cai[1,2], L. Abbasi Asbagh[1,2], T. Pastor[1,2],
M. De Troyer[1,2], M. Simicek[1,2], E. Radaelli[5], H. Brems[5], E. Legius[5], J. Tavernier[6,7],
K. Gevaert[6,7], F. Impens[8], L. Messiaen[5,9], R. Nussinov[4,10], S. Heymans[3,11,12],
S. Eyckerman[6,7], A. A. Sablina[1,2]†

The leucine zipper–like transcriptional regulator 1 (LZTR1) protein, an adaptor for cullin
3 (CUL3) ubiquitin ligase complex, is implicated in human disease, yet its mechanism
of action remains unknown. We found that Lztr1 haploinsufficiency in mice
recapitulates Noonan syndrome phenotypes, whereas LZTR1 loss in Schwann cells
drives dedifferentiation and proliferation. By trapping LZTR1 complexes from intact
mammalian cells, we identified the guanosine triphosphatase RAS as a substrate for the
LZTR1-CUL3 complex. Ubiquitome analysis showed that loss of Lztr1 abrogated Ras
ubiquitination at lysine-170. LZTR1-mediated ubiquitination inhibited RAS signaling
by attenuating its association with the membrane. Disease-associated *LZTR1* mutations
disrupted either LZTR1-CUL3 complex formation or its interaction with RAS proteins.
RAS regulation by LZTR1-mediated ubiquitination provides an explanation for the
role of LZTR1 in human disease.

Mutations concurrent with loss of heterozygosity at leucine zipper–like transcriptional regulator 1 (*LZTR1*) are associated with glioblastoma and schwannomatosis (*1–3*). LZTR1 mutations predispose for pediatric neoplasms and are increased over background in liver and testicular cancers (*4, 5*). The most recurrent LZTR1 mutation in cancer is an inactivating splice-site mutation at codon 217 (fig. S1) (*4, 6*). LZTR1 constitutes to Noonan syndrome caused by dysregulation of the guanosine triphosphatase RAS (*7–9*). However, how LZTR1 contributes to human disease is not known.

To uncover Lztr1 disease mechanisms, we used an Lztr1 deletion mouse model. We found that loss of Lztr1 is lethal between embryonic day 17.5 (E17.5) and birth (fig. S2A). *Lztr1*^{+/−} male mice exhibited decreased weight (fig. S2, B to D) and facial dysmorphia (Fig. 1A). *Lztr1*^{+/−} mice, both male and female, displayed heart malformations, including decreased left ventricular systolic function, increased diastolic dimensions, eccentric hypertrophy, increased cardiomyocyte area, and reduced longevity (Fig. 1, B and C, and fig. S2, E and F). Collectively, our results show that *Lztr1*^{+/−} mice recapitulate some phenotypes of human Noonan syndrome patients, indicating that LZTR1 function is evolutionary conserved.

We engineered several cellular models of LZTR1 loss: mouse embryo fibroblasts (MEFs) derived from *Lztr1*^{+/+} and *Lztr1*^{−/−} mouse embryos, primary human Schwann cells expressing short hairpin green fluorescent protein (shGFP) or shLZTR1, and immortalized human Schwann cells and HeLa cells with CRISPR-Cas9–mediated LZTR1-indels (fig. S3). In all tested models, LZTR1 loss increased growth rate (Fig. 1D and fig. S4, A to C). Overexpression of wild-type LZTR1 (wt-LZTR1), but not of LZTR1 mutants, reduced the enhanced growth rate (Fig. 1E and fig. S4, D and E). Loss of LZTR1 in Schwann cells enhanced two-dimensional colony and anchorage-independent (AI) growth (Fig. 1F and fig. S4, F to H), and overexpression of wt-LZTR1, but not of disease-associated
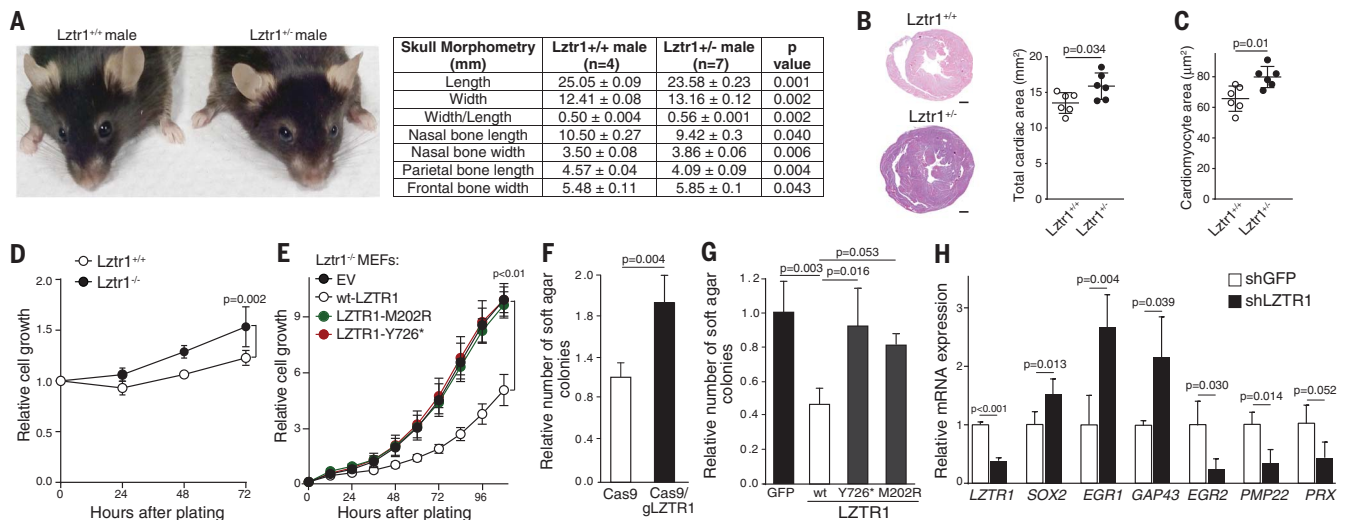
Fig. 1. LZTR1 loss recapitulates disease phenotypes. (**A**) Morphometric characteristics of the skulls of 12-month-old *Lztr1*^{+/+} and *Lztr1*^{+/−} male mice. (**B**) Haematoxylin and eosin–stained heart ventricular sections. Scale bar, 0.5 mm. The total cardiac area was quantified by Fiji. In the graph, horizontal lines represent means ± SD. (**C**) A mean area of 200 cardiomyocytes measured in laminin-stained heart sections of *Lztr1*^{+/+} and *Lztr1*^{+/−} mice. Horizontal lines represent means ± SD. (**D**) Growth rate of early-passage MEFs isolated from three *Lztr1*^{+/+} and three *Lztr1*^{−/−} embryos. (**E**) Growth rate of *Lztr1*^{−/−} MEFs expressing an empty vector (EV), wt-LZTR1, or LZTR1 mutants. *n* = 3. (**F**) AI growth of Schwann cells expressing Cas9 or Cas9/gLZTR1 (gLZTR1, guide RNA targeting LZTR1). *n* = 3. (**G**) AI growth of LZTR1-indel Schwann cells expressing the indicated constructs. *n* = 3. M202R, Met[202]→Arg. (**H**) Quantitative real time polymerase chain reaction (qRT-PCR) analysis of mRNA expression in primary human Schwann cells expressing shGFP or pooled shLZTR1. *n* = 3. For (D) to (H), values are means ± SEM. For (A) to (C) and (F) to (H), *P* values are from a two-sided Student's *t* test. For (D) and (E), *P* values were detected by two-way analysis of variance (ANOVA).

LZTR1 mutants, suppressed AI growth in LZTR1-indel cells (Fig. 1G). Furthermore, depletion of LZTR1 in Schwann cells showed a gene expression signature (Fig. 1H) resembling that of proliferating Schwann cells during nerve regeneration (10). These data suggest that LZTR1 loss drives Schwann cells from quiescent, myelinating cells into proliferating cells.

LZTR1 acts a substrate adaptor for cullin 3 (CUL3) ubiquitin ligase complexes (11). To identify candidate LZTR1 substrates, we used a mass spectrometry (MS) Virotrap method, which allowed the trapping of protein complexes from intact mammalian cells (fig. S5A) (12). The screen with LZTR1 as bait detected CUL3, Harvey rat sarcoma viral oncogene homolog (HRAS), and neuroblastoma RAS viral oncogene homolog (NRAS) among the top hits (Fig. 2A). The reciprocal Virotrap screen with the HRAS-deltaCAAX mutant, which lacks the last four amino acids, confirmed the complex formation with LZTR1 and identified CUL3 (Fig. 2B). Furthermore, a panRAS antibody that recognizes all RAS isoforms coimmunoprecipitated with hemagglutinin (HA)–tagged LZTR1. Similarly, Flag-tagged LZTR1 coimmunoprecipitated with endogenous RAS proteins, but not RAC1 (fig. S5B). Moreover, we introduced a Halo-tag HiBiT (13) to the LZTR1 locus in HeLa cells and MEFs (Fig. 2C and fig. S5, C and D). panRAS antibody coimmunoprecipitated with endogenous RAS and endogenous HiBiT-LZTR1 (Fig. 2C and fig. S5E). Reciprocal coimmunoprecipitations (co-IPs) demonstrated that LZTR1 interacted with each of the three Flag-RAS isoforms (fig. S5F). Together, these results indicate that LZTR1, CUL3, and RAS form a complex.

To test whether the LZTR1-CUL3 complex might control RAS ubiquitination, we performed an in vitro ubiquitination reaction. We observed ubiquitination of wt-HRAS specifically in the presence of the LZTR1-CUL3 complex (fig. S6A). Coexpression of LZTR1 and CUL3 in human embryonic kidney (HEK) 293T cells increased amounts of ubiquitinated RAS (Fig. 2D and fig. S6B). By contrast, treatment with the cullin

[1]VIB-KU Leuven Center for Cancer Biology, VIB, 3000 Leuven, Belgium. [2]Department of Oncology, KU Leuven, Herestraat 49, 3000 Leuven, Belgium. [3]Department of Cardiovascular Sciences, Centre for Molecular and Vascular Biology, KU Leuven, Herestraat 49, 3000 Leuven, Belgium. [4]Cancer and Inflammation Program, Leidos Biomedical Research, Inc., Frederick National Laboratory for Cancer Research, National Cancer Institute at Frederick, Frederick, MD 21702, USA. [5]Department of Human Genetics, KU Leuven, Herestraat 49, 3000 Leuven, Belgium. [6]VIB Medical Biotechnology Center, Albert Baertsoenkaai 3, 9000 Ghent, Belgium. [7]Department of Biochemistry, Ghent University, Albert Baertsoenkaai 3, 9000 Ghent, Belgium. [8]VIB Proteomics Core, Albert Baertsoenkaai 3, 9000 Ghent, Belgium. [9]Department of Genetics, University of Alabama, Birmingham, AL 35294, USA. [10]Department of Human Molecular Genetics and Biochemistry, Sackler School of Medicine, Tel Aviv University, Tel Aviv 69978, Israel. [11]Department of Cardiology, CARIM School for Cardiovascular Diseases Faculty of Health, Medicine and Life Sciences, Maastricht University, Netherlands. [12]The Netherlands Heart Institute, NI-HI, Utrecht, Netherlands.
*These authors equally contributed to this work.
†Corresponding author. Email: anna.sablina@kuleuven.vib.be

Fig. 2. The LZTR1-CUL3 complex ubiquitinates RAS proteins. (**A** and **B**) Virotrap screens performed in HEK293T cells using group-specific antigen (GAG)–LZTR1 (A) or GAG-HRAS–deltaCAAX (deltaC) (B) as baits. *Escherichia coli* dihydrofolate reductase (eDHFR) fused to GAG was used as a negative control. (**C**) A scheme for the generation of cells expressing in-frame HiBiT-LZTR1 protein. RAS was immunoprecipitated from the HiBiT-LZTR1 edited HeLa cell lysates with panRAS antibody. Luminescent signal was generated by LgBiT. nt, nucleotide. (**D**) Ubiquitinated RAS was purified from HEK293T cells expressing the indicated constructs by Co^{2+} metal affinity chromatography and detected by immunoblotting. Numbers on the left are molecular masses in kDa. 2xUb, two Ub; 1xUb, one Ub; EV, empty vector, WCL, whole-cell lysate; ns, nonspecific. (**E**) A workflow for the ubiquitome analysis. LC-MS/MS, liquid chromatography–tandem mass spectrometry. (**F**) A heatmap showing differentially ubiquitinated peptides in *Lztr1*^{+/+} and *Lztr1*^{−/−} MEFs. The scale shows *Z*-scored site intensity values. (**G**) The quantification of the PLA analysis of Schwann cells expressing Cas9 or Cas9/gLZTR1 using antibodies against panRAS and Ub. Values are means ± SEM; *n* = 3. *P* values are from a two-sided Student's *t* test. Single-letter abbreviations for the amino acid residues are as follows: A, Ala; C, Cys; D, Asp; E, Glu; F, Phe; G, Gly; H, His; I, Ile; K, Lys; L, Leu; M, Met; N, Asn; P, Pro; Q, Gln; R, Arg; S, Ser; T, Thr; V, Val; W, Trp; and Y, Tyr.

neddylation inhibitor MLN4924 or loss of LZTR1 led to decreased ubiquitination of all Flag-tagged RAS protein isoforms (fig. S6, C to F). Thus, the LZTR1-CUL3 complex can promote ubiquitination of RAS.

To investigate the role of LZTR1 in ubiquitination of endogenous RAS, we characterized ubiquitination profiles of $Lztr1^{+/+}$ and $Lztr1^{-/-}$ MEFs by MS (Fig. 2E). Ubiquitome analysis revealed that ubiquitination of Hras at Lys^{170} (K170) was abrogated in MEFs lacking Lztr1 (Fig. 2F and fig. S6G), indicating that endogenous Ras may serve as a substrate for the LZTR1-CUL3 complex. We also optimized a proximity ligation assay (PLA) with paired antibodies to ubiquitin (Ub) and panRAS. Consistent with the MS results, Hras-K170R (Lys^{170}→Arg) knock-in or depletion of LZTR1 led to a decrease in panRAS-Ub proximity signals (Fig. 2G and fig. S7). MS analyses failed to detect any C-terminal peptides of Nras or Kras, perhaps because these isoforms are not highly expressed in MEFs and their C termini are lysine-rich (fig. S8A). However, LZTR1 interacted with (fig. S5F) and ubiquitinated all three RAS isoforms (fig. S6F), consistent with evolutionary conservation of K170 (fig. S8D). Thus, the LZTR1-CUL3 complex appears to mediate ubiquitination of all RAS isoforms.

Although multiple truncating and missense mutations of *LZTR1* have been reported in Noonan syndrome and schwannomatosis (*1–3, 14*), no recurrent germline *LZTR1* mutations have been identified to date. Additional sequencing analysis of blood samples from schwannomatosis patients revealed several recurrent germline mutations of *LZTR1* within the BTB (broad-complex, tramtrack, and bric-a-brac)–BACK domains predicted to mediate dimerization and CUL3 binding (*11, 15*) (Fig. 3A). Concordantly, the BTB-BACK LZTR1 mutants, except L812P (Leu^{812}→Pro), exhibited reduced binding to CUL3 (Fig. 3B and fig. S9A). Although LZTR1-L812P retained interaction with CUL3, it failed to form dimers (Fig. 3C). Oligomerization of BTB domains determines the subcellular distribution of CUL3 adaptors (*15, 16*). Indeed, both endogenous and ectopically expressed HA-tagged LZTR1 showed punctate endomembrane immunostaining (fig. S9B), whereas the BTB-BACK domain LZTR1 mutants, including LTZR1-L812P, showed diffuse cytoplasmic staining (Fig. 3D and fig. S9C).

Missense mutations within the LZTR1 Kelch domain predicted to mediate substrate binding are also found in human disease. In co-IP assays, Kelch domain LZTR1 mutants showed decreased binding to RAS (Fig. 3E). The Kelch domain mutants, like

wt-LZTR1, displayed punctate immunostaining, but only wt-LZTR1 led to relocalization of RAS to the LZTR1-CUL3–containing puncta, which represent loci of LZTR1-CUL3–mediated ubiquitination (Fig. 3F and fig. S9, D and E). Consistently, the LZTR1-L812P mutant, which does not form puncta, only weakly ubiquitinated RAS, as did the LZTR1-Y726* (Tyr^{726}→Stop) mutant (Fig. 3G). Thus, disease-associated LZTR1 mutations appear to abrogate RAS ubiquitination by disrupting the formation of the RAS-LZTR1-CUL3 complex.

RAS ubiquitination affects RAS–mitogen-activated protein kinase (MAPK) signaling (*17*). Loss of LZTR1 led to increased RAS activity and phosphorylation of MEK1/MEK2 and ERK1/ERK2 in all tested model systems, whereas enhanced phosphorylation of V-Akt murine thymoma viral oncogene homolog (AKT) was cell dependent (Fig. 4A and fig. S10). After serum stimulation, $Lztr1^{-/-}$ MEFs showed higher MEK1/MEK2 activity at all time points, whereas $Lztr1^{+/-}$ MEFs had higher MEK1/MEK2 phosphorylation only at later time points (fig. S11A). Thus, Lztr1 abundance may fine-tune the activation of Ras signaling. Restoration of wt-LZTR1 expression in LZTR1-indel cells decreased MEK1/MEK2 activity (fig. S11B). Finally, LZTR1-mutated schwannomas showed strong
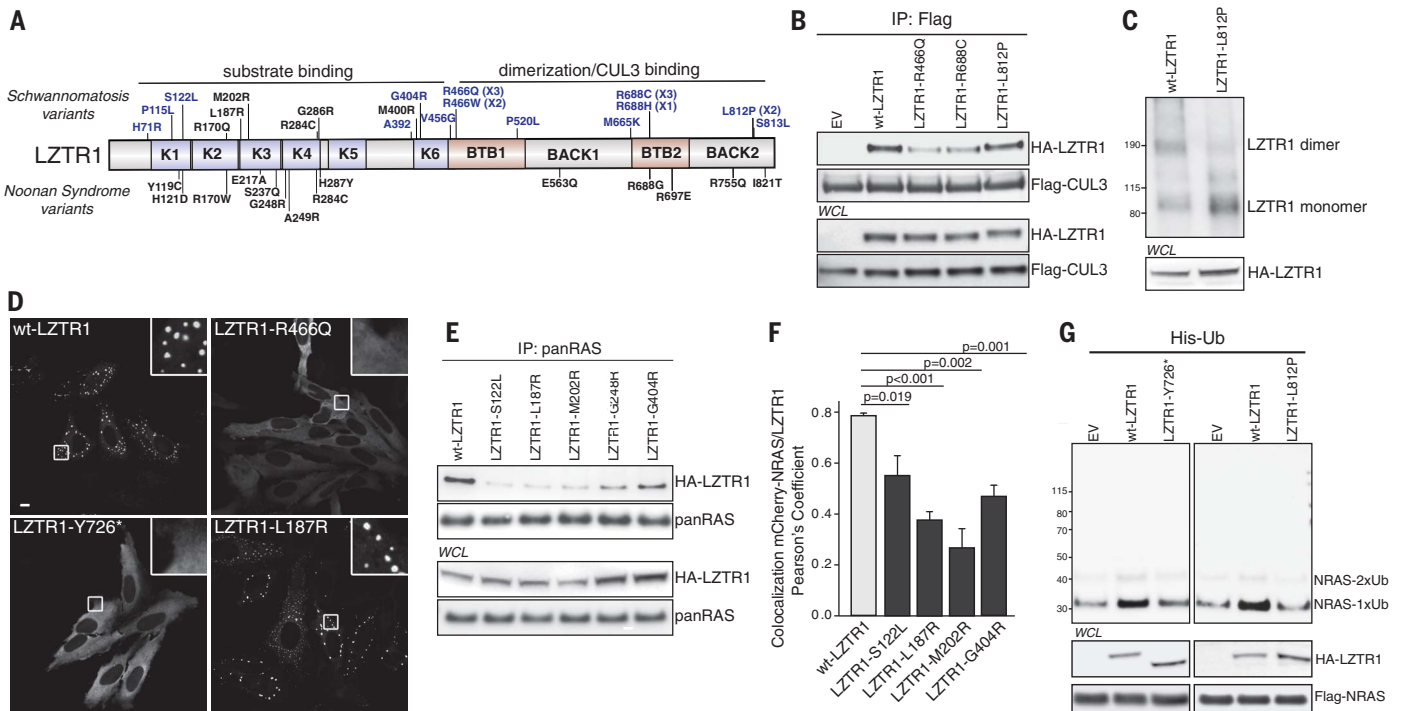
Fig. 3. Disease-associated LZTR1 mutations are loss of function.
(**A**) LZTR1 mutations in schwannomatosis and Noonan syndrome individuals. Missense LZTR1 mutations identified in our cohort of schwannomatosis patients are shown in blue. In the schematic, K indicates Kelch domain. See Fig. 2 legend for amino acid abbreviations. (**B**) Flag-tagged CUL3 purified from HEK293T cells was incubated with HA-tagged LZTR1-overexpressing cell lysates and then immunoprecipitated using anti-Flag resin. LZTR1 was detected by immunoblotting with anti-HA antibody. (**C**) Cross-linking reactions were performed using HA-tagged LZTR1 purified from HEK293T cells. LZTR1 was detected by immunoblotting using

anti-HA antibody. (**D**) Immunostaining of HeLa cells expressing HA-tagged wt-LZTR1 or LZTR1 mutants with anti-HA antibody. Scale bar, 10 μm. (**E**) RAS proteins were immunoprecipitated with antibody against panRAS. LZTR1 was detected by immunoblotting with anti-HA antibody. (**F**) Colocalization of mCherry-NRAS and HA-tagged LZTR1 expressed in HeLa-Cas9/gLZTR1 cells. Values are means ± SEM. *P* values were detected by two-sided Student's *t* test. (**G**) Ubiquitinated NRAS was purified from HEK293T cells expressing the indicated constructs by Co^{2+} metal affinity chromatography and detected by anti-Flag antibody.

staining of phosphorylated ERK1/ERK2 compared to wt-LZTR1 nerve trunk (fig. S11, C and D). The MEK1 inhibitor pimasertib abolished the colony growth difference between wt-LZTR1 and LZTR1-mutant cells (fig. S11E). Pimasertib treatment also rescued the embryonic lethality of $Lztr1^{-/-}$ mice (Fig. 4B). Thus, LZTR1-mediated phenotypes arise, at least in part, from increased RAS signaling.

Although our MS analysis detected Ras ubiquitination at several lysines, loss of Lztr1 abrogated ubiquitination of Ras only at K170 (Fig. 4C). Thus, ubiquitination of Hras at K170 may specifically require Lzrt1. Indeed, though LZTR1 depletion hindered ubiquitination of wt-HRAS, it did not affect ubiquitination of the HRAS-K170R mutant (Fig. 4D). Loss of LZTR1 also abolished the difference in Ras ubiquitination between wt-Hras and Hras-K170R MEFs (Fig. 4E and fig. S12A). Nonetheless, the LZTR1-CUL3 complex did ubiquitinate mutant HRAS-K170R in vitro (fig. S6A). The site specificity in vivo could be directed by anchoring of RAS to the membrane. Moreover, overexpression of the HRAS-K170R mutant led to higher activation of ERK1/ERK2 than did overexpression of wt-HRAS, and LZTR1 depletion did not affect ERK1/ERK2 activity in cells overexpressing HRAS-

K170R (Fig. 4F and fig. S12B). K170R knock-in MEFs also showed increased MAPK signaling and growth rates (fig. S12, C and D). Collectively, these data indicate that LZTR1-mediated ubiquitination of RAS at K170 suppresses RAS-MAPK signaling.

Ubiquitination of RAS can inhibit its activity by triggering its degradation (18). However, quantitative MS analysis did not reveal an increase in RAS protein abundance in $Lztr1^{-/-}$ MEFs (fig. S6G). wt-LZTR1 and LZTR1-indel Schwann cells treated with the protein synthesis inhibitor cycloheximide also showed similar RAS stability (fig. S12E), Thus, LZTR1 regulates RAS by a
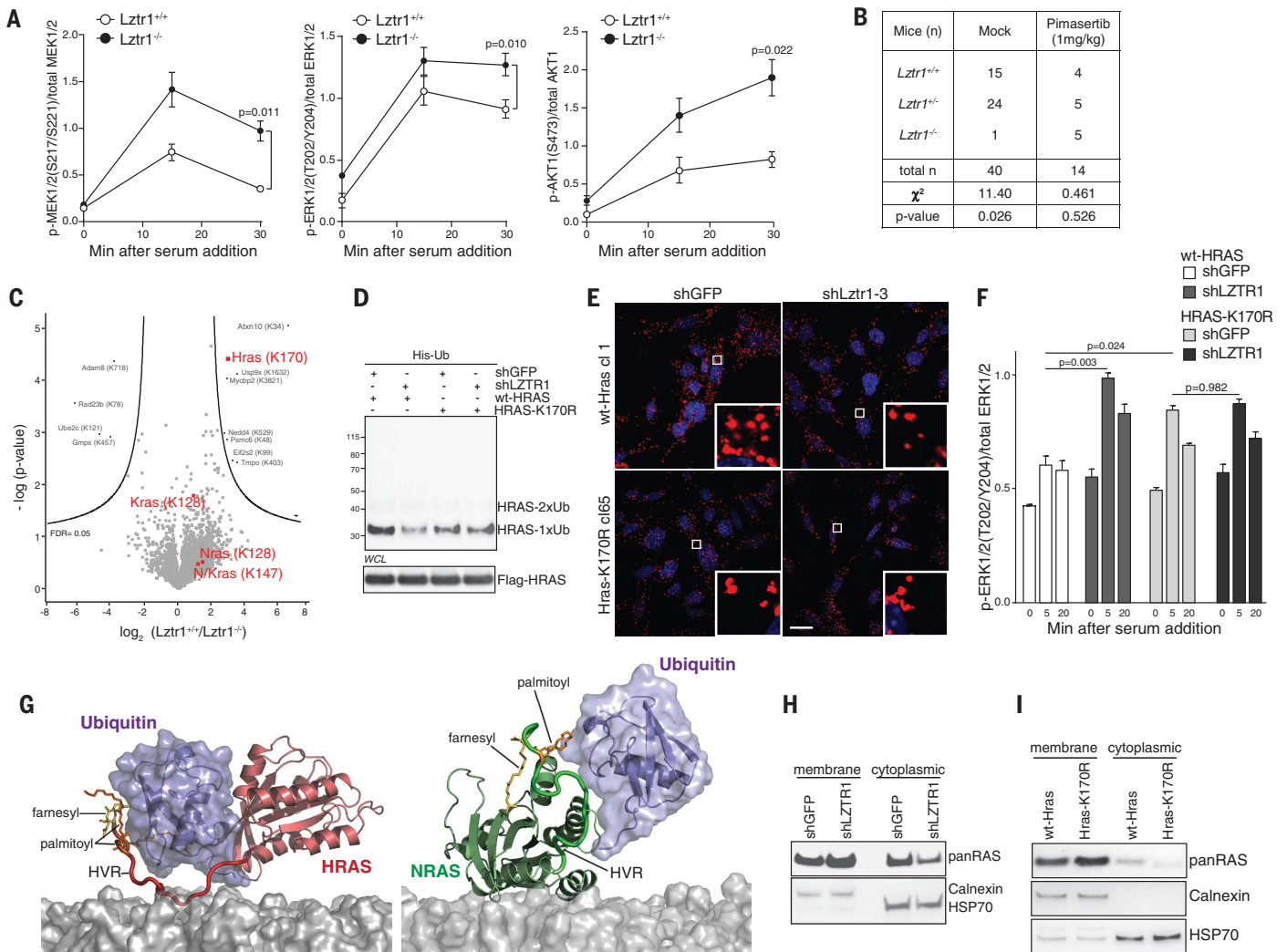
Fig. 4. Ubiquitination at K170 inhibits RAS by impairing its association to the membrane. (**A**) MEFs isolated from three $Lztr1^{+/+}$ and three $Lztr1^{-/-}$ embryos were serum-starved, stimulated with 10% serum, and analyzed by immunoblotting. Values are means of phosphorylated (p) relative to nonphosphorylated protein levels ± SEM. P values are from a two-way ANOVA. (**B**) Progeny from the indicated $Lztr1^{+/-}$ matings. Pregnant mice were treated with pimasertib starting from E7.5. (**C**) Quantitative ubiquitome analysis of $Lztr1^{+/+}$ and $Lztr1^{-/-}$ MEFs. FDR, false discovery rate. (**D**) Ubiquitinated RAS was purified from HEK293T cells expressing the indicated constructs by Co^{2+} metal affinity chromatography and detected by immunoblotting. (**E**) The PLA analysis of wt-Hras and Hras-K170R MEFs

expressing shGFP or shLztr1 using antibodies against panRAS and Ub. Red, PLA signal; blue, 4′,6-diamidino-2-phenylindole; scale bar, 10 μm. (**F**) HEK293T cells expressing the indicated constructs were serum-starved overnight, stimulated with 10% serum, and analyzed by immunoblotting. Values are means of phosphorylated relative to nonphosphorylated protein levels ± SEM; n = 3. P values are from a two-way ANOVA. (**G**) Snapshots of Ub-conjugated RAS at the lipid bilayer composed of 1,2-dioleoyl-sn-glycero-3-phosphocholine (DOPC) and 1,2-dioleoyl-sn-glycero-3-phosphoethanolamine (DOPE) lipids (3:1 molar ratio). (**H** and **I**) Immunoblotting of the membrane and cytoplasmic fractions isolated from HeLa cells expressing shGFP and shLZTR1 (H) or wt-Hras and Hras-K170R MEFs (I). HSP70, heat shock protein 70.

nondegradative mechanism. Ubiquitination of RAS also induces its relocalization to endomembranes (*19*, *20*). However, LZTR1 overexpression increased the endomembrane fraction of both wt-RAS and the HRAS-K170R mutant (fig. S12F). LZTR1 alone also only slightly increased RAS ubiquitination (Fig. 2D) and did not affect the MAPK pathway (fig. S12G), suggesting that LZTR1 overexpression promotes endomembrane localization of RAS independently of its ability to mediate ubiquitination at K170.

To assess how ubiquitination of RAS at K170 controls its activity, we elucidated modes of the interaction between RAS and conjugated Ub. LZTR1 colocalized with NRAS at RAB11–Transferrin receptor–positive recycling endosomes (fig. S13), suggesting that LZTR1 regulates ubiquitination of farnesylated and palmitoylated RAS. Therefore, we performed molecular simulations on lipidated RAS. In the initial structures of Ub conjugated to K170 of RAS, the hypervariable regions (HVRs) of RAS exposed their anchor portions to the solution. The long-lasting simulations showed that Ub secured the anchor portion of the HVR by sequestering the farnesyl and palmitoyl groups (fig. S14). Concordantly to a rapid kinetics of spontaneous insertion of lipidated RAS into the membrane (*21*–*24*), the HVRs of nonubiquitinated RAS straightforwardly associated with membranes. However, Ub conjugation to K170 of RAS prevented the HVRs from binding to and inserting into membranes (Fig. 4G). Thus, ubiquitination at K170 may disrupt the association of RAS to the membrane. Indeed, loss of LZTR1 or Hras-K170R knock-in increased the fraction of membrane-bound RAS (Fig. 4, H and I, and fig. S15). These results are all consistent with RAS ubiquitination at K170 inhibiting RAS activity by impairing its association with the membrane.

Our results indicate that LZTR1-mediated ubiquitination of RAS on K170 modulates RAS activity, dysregulation of which leads to human disease. An accompanying study shows that LZTR1 dysregulation also confers drug resistance (*25*). Understanding this unconventional mechanism of RAS activation may help to identify patients who might benefit from RAS pathway inhibitors and inform new therapeutic approaches for these patients.

REFERENCES AND NOTES

1. I. Paganini *et al.*, *Eur. J. Hum. Genet.* **23**, 963–968 (2015).
2. A. Piotrowski *et al.*, *Nat. Genet.* **46**, 182–187 (2014).
3. M. J. Smith *et al.*, *Neurology* **84**, 141–147 (2015).
4. Cancer Genome Atlas Research Network, *Cell* **169**, 1327–1341. e23 (2017).
5. Z. Ge *et al.*, *Cell Rep.* **23**, 213–226.e3 (2018).
6. A. K. Witkiewicz *et al.*, *Nat. Commun.* **6**, 6744 (2015).
7. P. C. Chen *et al.*, *Proc. Natl. Acad. Sci. U.S.A.* **111**, 11473–11478 (2014).
8. J. J. Johnston *et al.*, *Genet. Med.* **20**, 1175–1185 (2018).
9. G. L. Yamamoto *et al.*, *J. Med. Genet.* **52**, 413–421 (2015).
10. K. R. Jessen, R. Mirsky, *J. Anat.* **200**, 367–376 (2002).
11. P. J. Stogios, G. S. Downs, J. J. S. Jauhal, S. K. Nandra, G. G. Privé, *Genome Biol.* **6**, R82 (2005).
12. S. Eyckerman *et al.*, *Nat. Commun.* **7**, 11416 (2016).
13. M. K. Schwinn *et al.*, *ACS Chem. Biol.* **13**, 467–474 (2018).
14. S. Hutter *et al.*, *Acta Neuropathol.* **128**, 449–452 (2014).
15. P. Genschik, I. Sumara, E. Lechner, *EMBO J.* **32**, 2307–2320 (2013).
16. M. R. Marzahn *et al.*, *EMBO J.* **35**, 1254–1275 (2016).
17. L. K. Nguyen, W. Kolch, B. N. Kholodenko, *Cell Commun. Signal.* **11**, 52 (2013).
18. T. Zeng *et al.*, *Cell Rep.* **7**, 871–882 (2014).
19. L. Xu, V. Lubkov, L. J. Taylor, D. Bar-Sagi, *Curr. Biol.* **20**, 1372–1377 (2010).
20. H. Yan, M. Jahanshahi, E. A. Horvath, H. Y. Liu, C. M. Pfleger, *Curr. Biol.* **20**, 1378–1382 (2010).
21. H. Jang *et al.*, *J. Biol. Chem.* **290**, 9465–9477 (2015).
22. H. Jang, A. Banerjee, T. Chavan, V. Gaponenko, R. Nussinov, *J. Biol. Chem.* **292**, 12544–12559 (2017).
23. H. Jang *et al.*, *FASEB J.* **30**, 1643–1655 (2016).
24. H. Jang, S. Muratcioglu, A. Gursoy, O. Keskin, R. Nussinov, *Biochem. J.* **473**, 1719–1732 (2016).
25. J. W. Bigenzahn *et al.*, **362**, 1171–1177 (2018).

Active site alanine mutations convert deubiquitinases into high-affinity ubiquitin-binding proteins

Marie E Morrow[1], Michael T Morgan[1], Marcello Clerici[2,†], Katerina Growkova[3], Ming Yan[1], David Komander[4] (iD), Titia K Sixma[2], Michal Simicek[3,4] & Cynthia Wolberger[1,*] (iD)

Abstract

A common strategy for exploring the biological roles of deubiquitinating enzymes (DUBs) in different pathways is to study the effects of replacing the wild-type DUB with a catalytically inactive mutant in cells. We report here that a commonly studied DUB mutation, in which the catalytic cysteine is replaced with alanine, can dramatically increase the affinity of some DUBs for ubiquitin. Overexpression of these tight-binding mutants thus has the potential to sequester cellular pools of monoubiquitin and ubiquitin chains. As a result, cells expressing these mutants may display unpredictable dominant negative physiological effects that are not related to loss of DUB activity. The structure of the SAGA DUB module bound to free ubiquitin reveals the structural basis for the 30-fold higher affinity of Ubp8^{C146A} for ubiquitin. We show that an alternative option, substituting the active site cysteine with arginine, can inactivate DUBs while also decreasing the affinity for ubiquitin.

Introduction

Deubiquitinating enzymes (DUBs) play fundamental roles in ubiquitin signaling through their ability to remove ubiquitin from target proteins and disassemble polyubiquitin chains [1]. These enzymes cleave the isopeptide linkage between the C-terminus of ubiquitin and the substrate lysine or, in some cases, the peptide bond between ubiquitin and a substrate protein N-terminus. The human genome encodes more than 90 DUBs [2,3], which can be grouped into

families based on their fold: ubiquitin-specific protease (USP), ubiquitin carboxyl-terminal hydrolase (UCH), ovarian tumor family (OTU), Machado–Joseph domain (MJD) family, and JAMM/MPN domain (JAMM), as well as the recently discovered MINDY and ZUFSP families [4–6]. Studies of deletions as well as disease-causing mutations have revealed specific functions for individual DUBs in biological processes including proteasomal degradation, protein trafficking, transcription, DNA repair, infection, and inflammation [7]. The involvement of DUBs in a variety of oncogenic [8], inflammation, and neurodegenerative pathways [9] has made these enzymes attractive targets for drug discovery [10].

A common approach to determining the role of a particular DUB in cellular pathways is to knock down expression of the endogenous DUB and express a catalytically inactive version of the enzyme [11–13]. With the exception of the JAMM domain family, which are metalloproteases, all other DUBs are cysteine proteases with a papain-like active site in which the catalytic cysteine is activated by an adjacent histidine [14]. Cysteine protease DUBs are typically inactivated by substituting the active site cysteine with another residue. Resulting changes in substrate ubiquitination or downstream signaling pathways in cells expressing the mutant DUB are generally assumed to be due to the absence of deubiquitinating activity, with the notable exceptions of OTUB1, which inhibits E2 enzymes by a mechanism independent of catalytic activity [15–17] and OTUD4, which serves as a scaffold for USP enzymes [18]. Whereas serine is the most conservative substitution for the active site cysteine, alanine substitutions are often used to avoid the possibility that mutants containing a serine substitution may retain some hydrolase activity.

We report here that some active site cysteine-to-alanine substitutions can dramatically increase the affinity of DUBs for either free ubiquitin or polyubiquitin chains. This increase in affinity can confound the interpretation of cell-based experiments, since the mutant DUB is not only incapable of cleaving ubiquitin from substrates but has gained the ability to sequester free ubiquitin and

1   Department of Biophysics and Biophysical Chemistry, Johns Hopkins University School of Medicine, Baltimore, MD, USA
2   Division of Biochemistry and Oncode Institute, Netherlands Cancer Institute, Amsterdam, The Netherlands
3   Faculty of Medicine, University of Ostrava, Ostrava, Czech Republic
4   Medical Research Council Laboratory of Molecular Biology, Cambridge, UK
   *Corresponding author. Tel: +1 410 955 0728; E-mail: cwolberg@jhmi.edu
   †Present address: Department of Biochemistry, University of Zurich, Zurich, Switzerland

polyubiquitin chains. Altering levels of free ubiquitin has been shown to give rise to off-target effects [19]. In addition, these mutant DUBs may stably associate with (poly)ubiquitinated substrates and thereby protect ubiquitin chains from cleavage by other DUBs or prevent interaction with ubiquitin receptors. The effects of such tight-binding DUB mutants thus have the potential to confuse interpretation because of the gain of tight ubiquitin-binding function.

We show here that mutating the active site cysteine of human USP4 and yeast Ubp8 to alanine increases the affinity of the DUB for mono- or diubiquitin by 10–150-fold. A similar effect of alanine substitution was previously found for the OTU enzymes, Cezanne [20] and OTULIN [21]. The structure of the heterotetrameric SAGA DUB module containing Ubp8^{C146A} bound to free ubiquitin reveals the molecular basis for the increased affinity of monoubiquitin for the mutant enzyme. The alanine substitution alleviates steric hindrance by the active site cysteine sulfhydryl, allowing the C-terminal carboxylate of ubiquitin to form additional hydrogen bonds in the enzyme active site and thus accounting for the high affinity of the mutant enzyme for free ubiquitin. We show that substituting the active site cysteine with arginine in representative USP and OTU DUBs inactivates the enzymes while also disrupting binding to ubiquitin, generating an inert DUB. Based on these findings, we strongly recommend that cell-based and *in vivo* studies of DUBs avoid the use of active site alanine substitutions and to instead utilize substitutions such as arginine that ablate both enzymatic activity and ubiquitin binding.

Results and Discussion

Mutation of active site cysteine to alanine increases affinity of the SAGA DUB module for ubiquitin

The yeast SAGA complex is a transcriptional coactivator that is involved in transcription of all RNA polymerase II genes [22,23]. Among the SAGA activities are the removal of monoubiquitin from histone H2B, which promotes transcription initiation and elongation [24]. The deubiquitinating activity of SAGA resides in a four-protein complex known as the DUB module, which comprises the USP family catalytic subunit, Ubp8, as well as Sgf11, Sus1, and the N-terminal ~100 residues of Sgf73 [25,26]. Structural studies of the DUB module complexed with ubiquitin aldehyde [27] and with ubiquitinated nucleosomes [28] have revealed the overall organization of the DUB module and how it interacts with substrate. In addition to its ability to deubiquitinate histone H2B, the DUB module can also cleave a variety of ubiquitin substrates *in vitro* including ubiquitin-AMC and K48-linked diubiquitin [29]. The affinity of the DUB module for ubiquitinated nucleosome has been estimated at around 2 μM [28] and the K_M for the model substrate, ubiquitin-AMC, has been estimated at 24 μM [29]; however, neither the K_M nor binding affinity for other substrates is known.

In order to measure the affinity of the DUB module for other substrates using binding assays, we expressed and purified catalytically inactive versions of the DUB module containing Ubp8 with its active site cysteine, C146, substituted with either serine (C146S) or alanine (C146A). The absence of catalytic activity for both mutants was first verified in a ubiquitin-AMC cleavage assay (Fig EV1). We

measured the affinity of both mutant complexes for K48-linked diubiquitin using isothermal titration calorimetry (ITC; Fig 1E and F). Whereas DUB module containing Ubp8^{C146S} bound to K48 diubiquitin with a K_d of 4.6 μM, DUB module containing Ubp8^{C146A} bound to K48-linked diubiquitin with a K_d of 0.47 μM, representing 10-fold tighter binding. We also measured the affinity of the reaction product, monoubiquitin, to DUB module containing either wild-type or mutant Ubp8 (Fig 1A–C). Whereas DUB module containing wild-type Ubp8 or Ubp8^{C146S} bound ubiquitin with a K_d of 13.9 μM and 12.8 μM, respectively, the Ubp8^{C146A} mutant bound ~30-fold more tightly to monoubiquitin with a K_d of 0.43 μM.

A Ubp8 C146A substitution enables hydrogen bonding with the ubiquitin C-terminus

To determine the structural basis for the marked increase in affinity for free ubiquitin when the active site cysteine is substituted with alanine, we solved the crystal structure of the SAGA DUB module containing Ubp8^{C146A} bound to free ubiquitin at a resolution of 2.1 Å (Table 1 and Fig 2A). The overall fold and contacts with ubiquitin are virtually identical to those found in the structure of the wild-type enzyme bound to ubiquitin aldehyde, superimposing all atoms with an RMSD of 0.58 Å [27]. The active site of the C146A mutant is virtually identical to that in the wild-type apoenzyme [29], with no significant reordering of residues (Fig 2B) [29]. In the Ubp8^{C146A} complex with free ubiquitin, the negatively charged carboxylate of the ubiquitin C-terminal Gly76 forms two hydrogen bonds with backbone amides from Ubp8 residues Thr145 and Ala146, as well as with active site residues, Asn141 and His427 (Figs 2B and EV2). Importantly, the observed position of the ubiquitin C-terminus would not be compatible with the presence of the wild-type active site residue, Cys146, since the sulfhydryl group would clash with the C-terminal residue of ubiquitin, Gly76 (Fig 2C). The multiple hydrogen bonding interactions observed between the C-terminal carboxylate of ubiquitin and Ubp8 can therefore only occur when the active Cys146 is replaced with the smaller alanine side chain, thus explaining the higher affinity of DUB module-Ubp8^{C146A} for free ubiquitin as compared to the wild-type enzyme.

Active site cysteine-to-alanine substitution increases the affinity USP4 for ubiquitin

Mutating the active site cysteine to alanine has a dramatic effect on the affinity of the human USP family DUB, USP4, for free ubiquitin. USP4 regulates a broad variety of cellular pathways, including TGF-β and NF-κB signaling as well as splicing [26,30,31]. The affinity of USP4 for free ubiquitin was measured by fluorescence polarization using ubiquitin labeled with an N-terminal fluorophore. As shown in Fig 3, the K_d of ubiquitin for the wild-type enzyme is 92 ± 21 nM, whereas USP4 containing an alanine substituted for the active site cysteine, C311, binds ubiquitin with 0.60 ± 0.17 nM affinity, a ~150-fold difference [32]. The pre-steady-state kinetics of ubiquitin dissociation measured by fluorescence polarization in a stopped-flow device shows that the greater affinity of the USP4^{C311A} mutant is due to a dramatic decrease in off-rate (Fig EV3A). Interestingly, ubiquitin dissociation has been shown to be promoted by USP4 N-terminal DUSP-Ubl domain and to regulate USP4 activity

[32]. The increase in affinity for the mutant enzyme is not unique to ubiquitin with a free C-terminus, as ubiquitin conjugated to either an 18-mer peptide or C-terminal fluorophore also binds with similar affinity to USP4[C311A] (Fig EV3C and D). Since the active sites of USP family DUBs are highly conserved, we speculate that the observed increase in binding affinity is due a relief of steric clash, as is the case for Ubp8.

Substitution of the catalytic cysteine with arginine disrupts ubiquitin binding in USP and OTU class DUBs

We sought to identify alternative active site mutations that would abrogate catalytic activity as well as reduce the affinity of the inactive DUB polyubiquitin chains or ubiquitinated substrates. We reasoned that substituting the active site cysteine with arginine could both inactivate
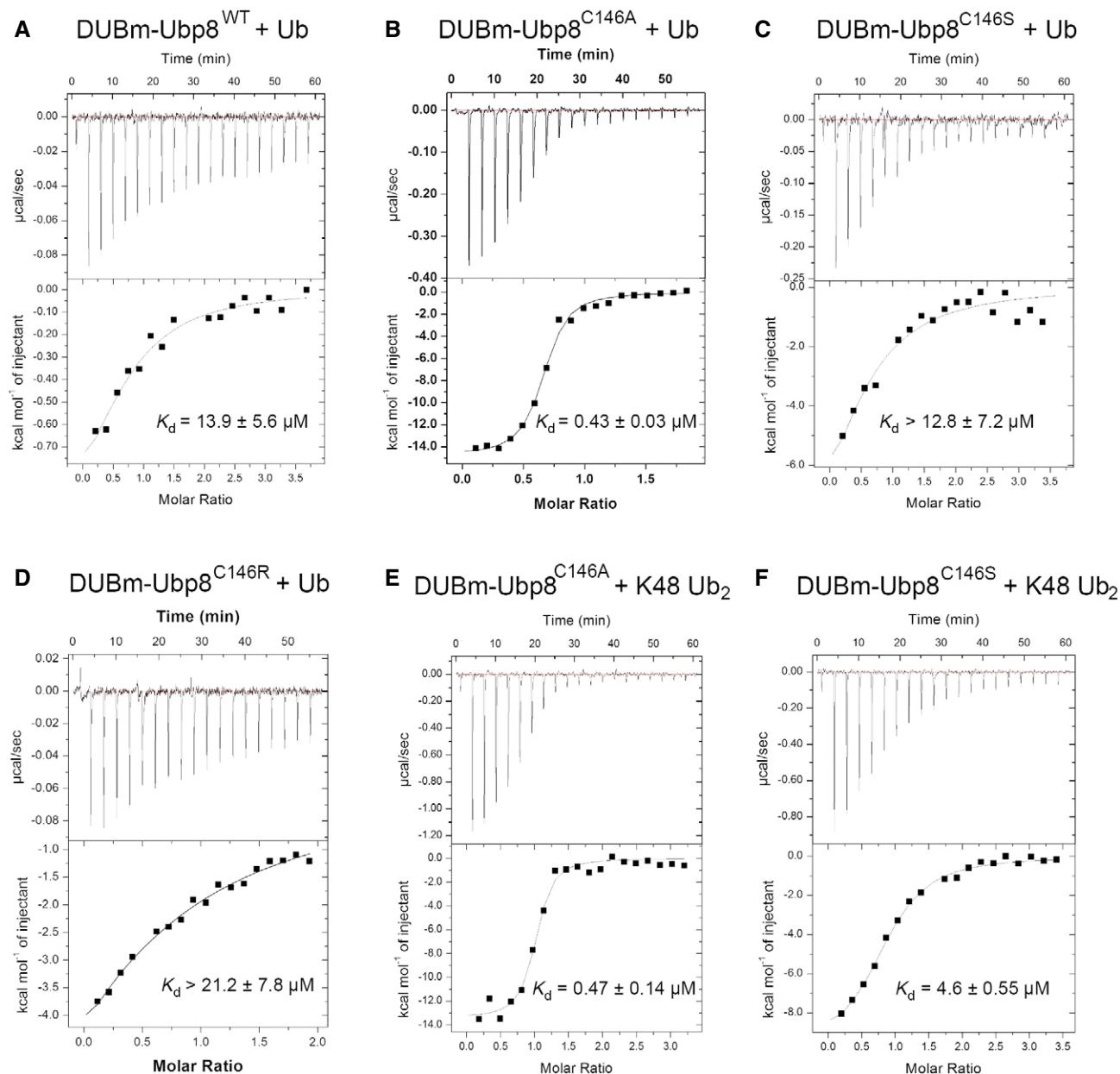

Figure 1. Isothermal titration calorimetry assays of SAGA DUB module binding to K48 diubiquitin or monoubiquitin.

A Binding of wild-type DUBm-Ubp8 to monoubiquitin.
B Binding of DUBmUbp8[C146A] to monoubiquitin.
C Binding of DUBm-Ubp8[C146S] to monoubiquitin.
D Binding of DUBm-Ubp8[C146R] to monoubiquitin.
E Binding of DUBm-Ubp8[C146A] to K48 diubiquitin.
F Binding of DUBm-Ubp8[C146S] to K48 diubiquitin.

Data information: Error ranges for K_d values were determined from nonlinear least squares fitting of the data to a one-site binding model.

**Table 1. X-ray crystallographic data and refinement statistics.**

Wavelength (Å)	0.979
Resolution (Å)	2.10
Unique reflections	54,195
Redundancy	5.7 (5.7)
Completeness (%)	99.2 (99.7)
Average I/σ (I)	13.3 (3.0)
R_{merge}	0.093 (0.572)
R_{meas}	0.103 (0.630)
R_{pim}	0.043 (0.259)
CC1/2	0.998 (0.857)
CC*	0.999 (0.961)
Refinement statistics	
Space group	$P2_12_12_1$
Unit cell (Å)	a = 78.8, b = 103.2, c = 112.8
Molecules per asymmetric unit	1
R_{work} (%)	20.1
R_{free} (%)	24.9
Rmsd bonds (Å)	0.0198
Rmsd angles (°)	1.855
Protein atoms	6,302
Zinc ions	8
Average B (Å²)	40.3

the enzyme and prevent ubiquitin binding because of the bulky nature of the side chain compared to cysteine. To test this hypothesis, we mutated the catalytic cysteine of Ubp8 to arginine and first verified that SAGA DUB module containing the mutant Ubp8[C146R] protein was inactive in a Ub-AMC cleavage assay (Fig EV1). The affinity of the DUB module containing Ubp8[C146R] for monoubiquitin as measured by ITC was comparable to that of the wild-type protein (Fig 1D).

Substitution of the active cysteine with arginine similarly reduces the affinity for polyubiquitin chains by the OTU family member, OTUD1, which is also a cysteine protease. This DUB preferentially cleaves K63-linked polyubiquitin chains [20], has recently been shown to regulate the nuclear localization and transcriptional coactivator activity of the YAP oncoprotein [33], represses metastasis by deubiquitinating SMAD7 during TGF-β signaling [34], and negatively regulates RIG-I-like receptor (RLR) signaling during viral infection by deubiquitinating Smurf1 [35]. We measured the affinity of catalytic mutants of OTUD1 for fluorescently labeled K63-linked diubiquitin using a fluorescence polarization assay (Fig 4A). While OTUD1 with an alanine substituted for the active site cysteine (OTUD1[C320A]) binds K63-linked diubiquitin with a K_d of ~40 μM, an arginine substitution, OTUD1[C320R], not only inactivated the enzyme but also completely abolished detectable binding to K63-linked diubiquitin (Fig 4A).

Active site arginine substitutions can overcome artifacts of alanine substitution in cells

As mentioned above, active site cysteine-to-alanine substitutions that markedly increase DUB affinity for mono- or polyubiquitin may
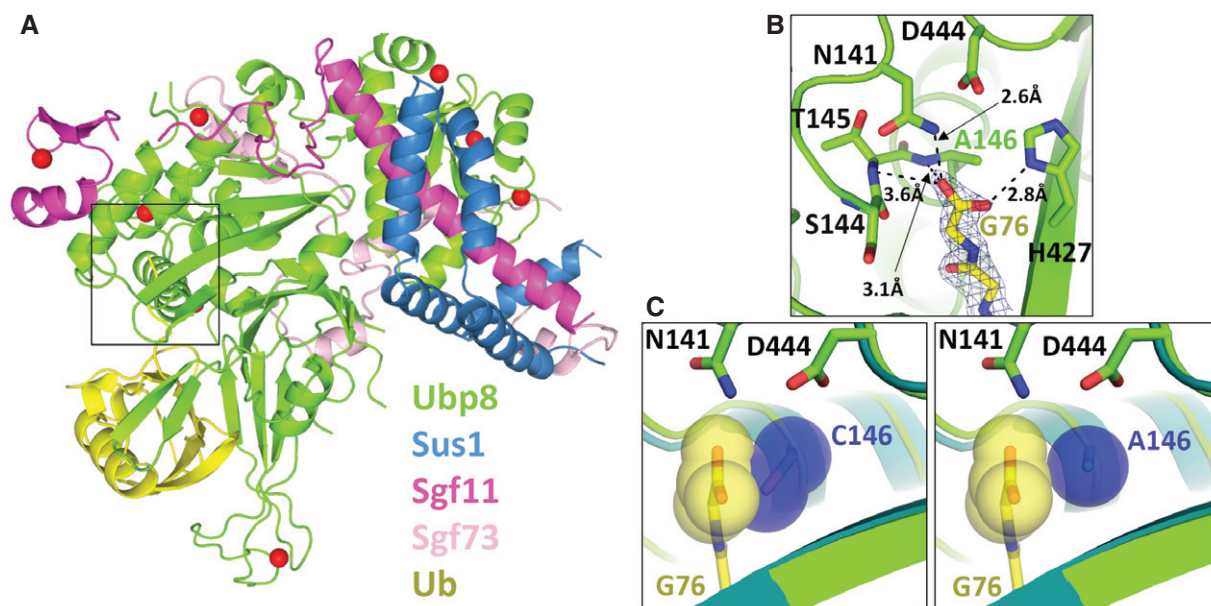
Figure 2. X-ray crystal structure of SAGA DUB module mutant DUBm-Ubp8[C146A] bound to monoubiquitin.

A Overall structure of complex showing Ubp8 (green) with ubiquitin (yellow) bound to the USP domain.
B Hydrogen bonding contacts between the C-terminal carboxylate of ubiquitin and Ubp8.
C In blue spheres, van der Waals radii of C146 and A146 in steric proximity of ubiquitin's C-terminal carboxylate (yellow). DUBm-Ubp8[WT] structure is shown in teal (PDB ID 3MHH) and DUBm-Ubp8[C146A] is shown in green.
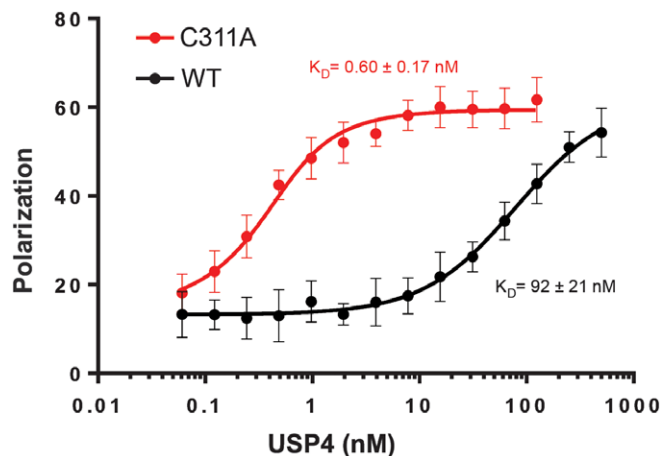
Figure 3. Equilibrium binding of USP4 WT and C311A to TAMRA-labeled monoubiquitin.

Binding was measured by fluorescence polarization using N-terminally TAMRA-labeled monoubiquitin. The dissociation constants for ubiquitin binding to USP4 WT and C311A are 92 ± 21 nM [32] and 0.60 ± 0.17 nM, respectively. Error bars are s.d. calculated on five measurements per point.

render these mutants less suitable for physiological studies. Since such cysteine-to-alanine mutants are essentially high-affinity ubiquitin-binding proteins, these DUB mutants have the potential to stabilize modified substrates and preferred chain types by protecting them from digestion by other DUBs or proteases. For example, when OTULIN C129A is expressed in cells, there is a dramatic accumulation of Met1-linked linear polyubiquitin chains that is not seen when a mutant that abrogates ubiquitin binding, L259E, is expressed [21]. We hypothesized that substituting the active site cysteine with arginine could be a general approach in cell-based studies to inactivating cysteine protease DUBs while also preventing high-affinity binding to polyubiquitin. To test this idea, we expressed

cysteine-to-alanine and cysteine-to-arginine mutants of two DUBs, OTUD1 and USP14, in cells and probed their effects on levels of polyubiquitin. HA-tagged wild-type OTUD1, OTUD1[C320A], or OTUD1[C320R] was expressed in HEK293 cells and whole cell lysates were analyzed by immunoblotting with an antibody specific for K63-polyubiquitin chains. As compared to cells expressing the wild-type protein, cells expressing OTUD1[C320A] had increased levels of K63-linked polyubiquitin (Fig 4B). By contrast, cells expressing OTUD1[C320R] did not show enriched levels of K63-linked chains (Fig 4B).

We also tested the effects of expressing wild-type and mutant USP14, one of the chain-trimming DUBs that bind to the 26S proteasome [36,37]. HA-tagged USP14 containing the wild-type active site cysteine, Cys114, and C114A and C114R mutants were co-expressed in HEK293 cells along with FLAG-PSMD4, a ubiquitin receptor within the proteasome [38]. Proteasome-bound ubiquitinated proteins were co-immunoprecipitated by FLAG-PSMD4 and probed for ubiquitin (Fig 5). Proteasomes with USP14 C114A bind more polyubiquitin chains than USP14 C114R and also retain increased levels of higher molecular weight chains that are unable to be trimmed compared to wild-type USP14 (Fig 5). Both of these results are consistent with the idea that the increase in polyubiquitin chains observed with the cysteine-to-alanine mutants is due to the ability of this mutant to bind to polyubiquitin chains and protect them from cleavage by other DUBs. Our results also validate the benefit of using a Cys to Arg substitution to generate a catalytically inactive DUB that will neither protect nor sequester polyubiquitin chains and ubiquitinated substrates.

Implications for cell-based studies of cysteine protease DUBs

The surprisingly high affinity for ubiquitin exhibited by DUBs containing alanine substituted for the active site cysteine has important implications for cell-based assays in which catalytically inactive DUBs are expressed. We have found that cysteine-to-alanine
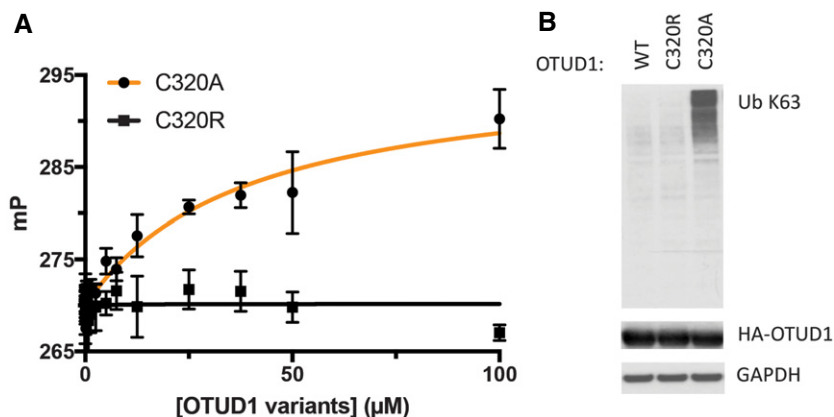

Figure 4. Enhanced binding of OTUD1 C320A to K63 diubiquitin *in vitro* and K63 polyubiquitin chains in cells.

A   Equilibrium binding of OTUD1 C320A and C320R to K63-linked diubiquitin was measured by fluorescence polarization using FlAsH-tagged K63-linked diubiquitin in which the proximal ubiquitin was fluorescently labeled. Error bars indicate s.d. and are based on three measurements per data point. One representative experiment of two is shown.
B   Whole cell lysates of HEK293 cells expressing HA-tagged OTUD1 WT, C320R, and C320A were immunoblotted with indicated antibodies. One representative experiment of three is shown.
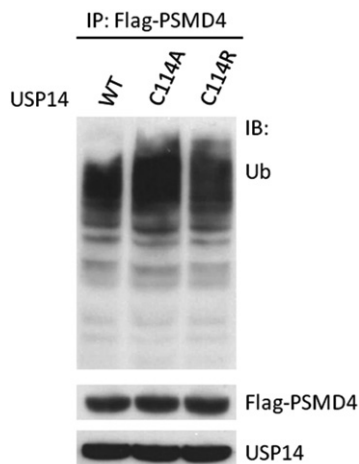
Figure 5. Binding of USP14 C114A to ubiquitin chains in cells.

Polyubiquitin chains were co-immunoprecipitated with FLAG-PSMD4, an ubiquitin receptor for the 26S proteasome, from cells expressing either USP14 wild-type, C114A, or C114R. One representative experiment of two is shown.

substitutions in the USP DUBs, Ubp8 and USP4, dramatically increase their affinity for monoubiquitin (Figs 1 and 3). Similarly, cysteine-to-alanine substitutions in the active sites of Ubp8 and the OTU class DUB, OTUD1, also increase DUB affinity for polyubiquitin (Figs 1 and 4A). The equilibrium dissociation constants of these mutant DUBs are significantly lower than cellular concentrations of their substrates, given the estimated concentration of free ubiquitin in the cell of 4–50 μM [39] and a concentration of polyubiquitin at a fraction of that [40]. The mutant DUBs are therefore expected to bind tightly to free ubiquitin and to polyubiquitin chains when expressed in cells. Particularly in experiments where mutant DUBs are overexpressed, there is the risk that cellular consequences ascribed to a lack of catalytic activity in a particular DUB may instead be due to the ability of the mutant DUB to protect polyubiquitin chains from cleavage or to a difference in free ubiquitin availability to ubiquitin-conjugating enzymes.

The effects of cysteine-to-alanine substitutions shown here for USP and OTU class DUBs are likely to extend to other cysteine protease DUBs. The UCH and MJD classes of cysteine protease DUBs have a conserved active site architecture similar to USP DUBs [14,41] and could thus form similar interactions with ubiquitin if the active site cysteine was substituted with alanine (Fig EV4A and B). Although the MINDY and ZUFSP DUBs share little homology with the other cysteine protease DUBs [4–6], an alanine substitution would similarly relieve steric clash in the active site, thus potentially increasing the DUB's affinity for ubiquitin (Fig EV4C). These observations support the recommendation that alanine substitutions should be avoided in cell-based and *in vivo* studies of cysteine protease DUBs.

We have presented an alternative to alanine substitutions that is equally effective in abrogating DUB activity while having the advantage of preventing ubiquitin binding. In binding assays of Ubp8 and OTUD1, we show that replacing the active site cysteine with arginine inactivates ubiquitin hydrolase activity while also rendering the enzyme incapable of binding ubiquitin detectably (Figs 1D and 4). We speculate that the ability of arginine substitutions to abolish

ubiquitin binding to OTU and USP catalytic domains may be explained by the ability of the arginine side chain to partially occupy the binding site for the C-terminal ubiquitin Gly-Gly in these DUBs. Previous data have indicated that the correct orientation of the ubiquitin C-terminal tail in the DUB S1 site is essential for efficient cleavage [42,43]. An arginine side chain may mimic these interactions in cis, to prevent these important substrate interactions. While we did not test other active site substitutions, it is expected that other amino acids with side chains that are significantly bulkier than cysteine would similarly block ubiquitin binding, in addition to inactivating the enzyme. However, care should be taken to avoid hydrophobic side chains that could cause the protein to aggregate, or side chains that are bulky or beta-branched that could interfere with proper protein folding due to steric clashes with the neighboring protein backbone. Since lysine can be ubiquitinated and is also subject to many other post-translational modifications, this substitution should also be avoided.

We recommend that all cell-based and *in vivo* studies of cysteine protease DUBs avoid alanine substitutions of the active site cysteine and instead utilize arginine substitutions to study effects of inactivating the enzyme. Although the arginine substitution was only tested here on DUBs from the USP and OTU class, it is likely that an arginine would similarly interfere with ubiquitin binding to members of the UCH, MJD, MINDY, and ZUFSP cysteine protease families. Ideally, DUBs with arginine substitutions should first be tested *in vitro* to ensure that this mutation indeed interferes with ubiquitin binding. Adopting this practice can mitigate spurious or dominant negative effects and ensure that any observed phenotypes or changes are due to loss of DUB activity alone rather than an increase in affinity for ubiquitin.

Materials and Methods

Cloning, protein expression, and purification

Rosetta 2(DE3) pLysS cells (EMD Millipore, Merck KGaA, Darmstadt, Germany) were transformed with three plasmids encoding (i) Ubp8[WT], Ubp8[C146A], Ubp8[C146S], or Ubp8[C146R] (pET-32a, EMD Millipore), (ii) Sus1 (pRSF-1, EMD Millipore), and (iii) Sgf73[(1-96)] (pCDFDuet-1 MCSII, EMD Millipore) which was cloned into the same vector as Sgf11 (pCDFDuet-1 MCSI, EMD Millipore). All versions of the DUBm complex were co-expressed and purified using the previously reported protocol for the expression and purification of wild-type DUBm [27]. Untagged ubiquitin (pET3a) was expressed in Rosetta 2 cells and, after lysis, was treated with 1% v/v perchloric acid to precipitate cellular proteins. The supernatant, containing ubiquitin, was dialyzed overnight into 50 mM sodium acetate pH 4.5, then run on a HiTrap SP column, and eluted over a 0–600 mM NaCl gradient in 50 mM sodium acetate pH 4.5. Pure fractions were pooled and buffer exchanged by gel filtration on a HiLoad S75 column into 20 mM HEPES pH 7.5, 50 mM NaCl, and 1 mM DTT.

USP4 (8–925) wild-type and C311A mutant were expressed and purified as in [32].

pOPINK-OTUD1 catalytic domain (residues 287–435) was transformed into *Escherichia coli* Rosetta 2 pLysS (Novagen) and grown to OD 0.6 followed by induction with 0.2 mM IPTG overnight at 20°C. Cells were lysed by sonication in buffer A (50 mM Tris,

50 mM NaCl, 5 mM DTT, pH 8.5), the lysate was cleared by centrifugation (44,000 × *g* for 30 min, 4°C) and subjected to a glutathione resin (GE Healthcare). The resin was washed with cold buffer B (50 mM Tris, 500 mM NaCl, 5 mM DTT, pH 8.5) and subsequently with cold buffer A. The GST-tag was removed by overnight incubation at 4°C with GST-tagged 3C Precision protease in buffer A. Eluted protein was further purified by anion-exchange chromatography and gel filtration in buffer A.

Fluorescence polarization assays

All USP4 pre-steady-state and equilibrium fluorescence polarization assays were performed as described in [32]. Ubiquitin conjugated to lysine-glycine and to a SMAD4-derived peptide [32] was a gift of Huib Ovaa.

Binding assays for OTUD1 interactions with Lys63-linked chains were performed using Lys63-linked diUb that was fluorescently labeled by a FlAsH-tag on the proximal ubiquitin (*21*). For this, diUb chains were diluted to 80 nM in FlAsH buffer (50 mM Tris, 50 mM NaCl, 0.1% β-mercaptoethanol, pH 7.6), and OTUD1^{C320A} and OTUD1^{C320R} were serially diluted in FlAsH buffer to the indicated concentration range. 10 μl of fluorescent diUb was mixed with equal volume of OTUD1^{C320A} and OTUD1^{C320R} at different concentrations and incubated in room temperature for 1 h before measurement. Fluorescence polarization was measured in 384-well format employing a Pherastar FS plate reader, using a fluorescence polarization module with excitation and emission wavelengths at 485 and 520 nm, respectively. A control was used for either linear di- or triUb molecules where 10 μl of FlAsH buffer was added instead. This control was also used for the normalization of anisotropy reading. All binding assays were performed in triplicate.

Ubiquitin-AMC hydrolysis assay

Assays were conducted in 384-well black polystyrene micro-plates at 30°C in a POLARstar Omega plate reader (BMG Labtech, Cary, NC) using an excitation wavelength of 385 nm and emission wavelength of 460 nm. Reactions were performed in DUBm assay buffer containing 50 mM HEPES, pH 7.6, 150 mM NaCl, 5 μM ZnCl$_2$, 5 mM dithiothreitol (DTT), and 7.5% DMSO. The wild-type DUBm and Ubp8 mutant complexes were held at a concentration of 125 nM. Ubiquitin-AMC (Boston Biochem, Cambridge, MA) was diluted into assay buffer and incubated at 30°C for 10 min inside the plate reader. 3 μl of recombinant DUBm was also pre-incubated at 30°C for 10 min before mixing with diluted ubiquitin-AMC buffer to a total volume of 30 μl. The release of AMC was followed at 460 nm, and the first 0–60 s of data was used to fit initial rate.

Isothermal titration calorimetry (ITC)

Isothermal titration calorimetry measurements were performed using a Microcal (Amherst, MA) ITC200 calorimeter at 25°C. DUBm wild-type, Ubp8 mutant complexes, K48-linked diubiquitin and ubiquitin samples were buffered with 20 mM HEPES, pH 7, 150 mM NaCl, 5 nM ZnCl$_2$, and 0.5 mM Tris (2-Carboxyethyl) phosphine hydrochloride (TCEP) and thoroughly degassed before use. The protein concentrations were determined by amino acid analysis. The sample cell (0.22 ml) contained either 30 μM DUBm-Ubp8^{WT} or DUBm Ubp8 mutant. A total of 20 injections of 40 μl of 0.3 mM K48-linked diubiquitin or monoubiquitin were carried out at 180 s intervals. The heat generated due to dilution of the titrants was subtracted for baseline correction. The baseline-corrected data were analyzed with Microcal Origin Ver. 7.0 software. All experiments were duplicated.

Protein crystallization

Protein crystals were grown from a complex of 7 mg/ml DUBm-Ubp8^{C146A} and 1.8 mg/ml ubiquitin that was incubated on ice for 30 min prior to screening. Complex crystals were grown by hanging drop vapor diffusion using a 1:1 ratio of protein to mother liquor. Crystals grew within 2 days at 20°C in 17% PEG3350, 0.1 M HEPES pH 7.0, and 0.1 M ammonium sulfate. Crystals were looped and cryoprotected by stepwise incubation in mother liquor containing increasing concentrations of PEG3350 (17–33%), then flash-frozen in liquid nitrogen.

Data collection, structure determination, and refinement

X-ray diffraction data for the DUBm-Ubp8^{C146A} and ubiquitin complex were collected at Stanford Synchrotron Radiation Lightsource beamline BL12-2. Data were collected on a Pilatus detector using a 10 μm beam at 50% transmission taking 1 s exposures with 0.25° oscillations over 180°. During data collection, the crystal rotated out of the beam, therefore frames 200–300 out of 720 total frames were discarded during data reduction and scaling. Data reduction, scaling, and merging were done in XDS and Aimless [44]). A 2.1 Å structure was determined by molecular replacement in Phaser (Phenix) using the coordinates of the wild-type DUBm bound to ubiquitin aldehyde (PDB ID: 3MHS) as the search model [27,45]. The structure was refined in PHENIX and Coot was used for manual model building [45,46]. Data collection and refinement statistics are shown in Table 1. PyMOL Version 1.5.0.4 (Schrödinger, LLC) was used to generate all structure figures. Coordinates have been deposited in the Protein Data Bank with ID 6AQR.

Immunoblotting and immunoprecipitation

Full-length, N-terminally HA-tagged OTUD1 constructs (WT, C320A, C320R) were cloned into pcDNA3.1 vector and transiently expressed in HEK293 cells. Two days after, transfection cells were washed twice in cold PBS and scraped on ice in lysis buffer (50 mM Tris–HCl pH 7.5, 150 mM NaCl, 1% NP-40) containing protease inhibitor cocktail (Roche) and 20 mM N-ethylmaleimide, and incubated for 30 min on ice. Samples were subsequently cleared by centrifugation for 10 min at 16,000 × *g* at 4°C. For immunoblotting, equivalent amounts of cell lysates were separated on 4–12% Bis-Tris gel, transferred to nitrocellulose membranes, and incubated with the indicated antibodies. The signal was visualized with Pierce ECL Western Blotting Substrate (Thermo Scientific) and exposed on X-ray film.

Full-length USP14 (WT, C114A, C114R) and N-terminally Flag-tagged PSMD4 constructs were cloned into pcDNA3.1 vector and

transiently expressed in HEK293 cells. Two days after, transfection cells were washed twice in cold PBS and scraped on ice in lysis buffer (50 mM Tris–HCl pH 7.5, 150 mM NaCl, 1% NP-40) containing protease inhibitor cocktail (Roche) and 20 mM N-ethylmaleimide, and incubated for 30 min on ice. Samples were subsequently cleared by centrifugation for 10 min at $16,000 \times g$ at 4°C. The cleared lysates were incubated with anti-Flag resin (Sigma-Aldrich) overnight at 4°C, subsequently washed four times with cold lysis buffer and eluted with Flag peptide. Eluted fractions were separated on 4–12% Bis-Tris gel, transferred onto PVDF membranes, and incubated with the indicated antibodies. The signal was visualized with Pierce ECL Western Blotting Substrate (Thermo Scientific) and exposed on X-ray film.

Antibodies

The following antibodies were used in immunoblotting or immunoprecipitation:

Ub K63, rabbit monoclonal Ab, clone Apu3, Millipore (cat # 05-1308); HA, rat monoclonal Ab, clone 3F10, Roche (cat # 11 867 423 001); GAPDH, mouse monoclonal Ab, clone GAPDH-71.1, Sigma-Aldrich (cat # G8795); Ub, mouse monoclonal Ab, clone P4D1, Santa Cruz (cat # sc-8017); Flag, mouse monoclonal Ab, clone M2, Sigma-Aldrich (cat # F1804); USP14, rabbit monoclonal Ab, clone D8Q6S, Cell Signaling Technology (cat # 11931).

Data availability

Coordinates and amplitudes have been deposited in the Protein Data Bank with accession code, 6AQR.

Expanded View for this article is available online.

Author contributions

Binding and structural studies of the SAGA DUB module were carried out by MEM, MTM, and MY, with input and guidance from CW. Studies of USP4 were carried out by MC, with input and guidance from TKS. Biophysical studies on OTUD1 were carried out by MS under guidance of DK. Cell biological studies on OTUD1 and USP14 were designed by MS and carried out by KG and MS.
MEM and CW wrote the initial manuscript, with significant contributions from DK, TKS, and MS. All authors edited the manuscript.

References

1. Clague MJ, Coulson JM, Urbe S (2012) Cellular functions of the DUBs. *J Cell Sci* 125: 277 – 286
2. Reyes-Turcu FE, Ventii KH, Wilkinson KD (2009) Regulation and cellular roles of ubiquitin-specific deubiquitinating enzymes. *Annu Rev Biochem* 78: 363 – 397
3. Clague MJ, Barsukov I, Coulson JM, Liu H, Rigden DJ, Urbe S (2013) Deubiquitylases from genes to organism. *Physiol Rev* 93: 1289 – 1315
4. Abdul Rehman SA, Kristariyanto YA, Choi SY, Nkosi PJ, Weidlich S, Labib K, Hofmann K, Kulathu Y (2016) MINDY-1 is a member of an evolutionarily conserved and structurally distinct new family of deubiquitinating enzymes. *Mol Cell* 63: 146 – 155
5. Haahr P, Borgermann N, Guo X, Typas D, Achuthankutty D, Hoffmann S, Shearer R, Sixma TK, Mailand N (2018) ZUFSP deubiquitylates K63-linked polyubiquitin chains to promote genome stability. *Mol Cell* 70: 165 – 174 e166
6. Kwasna D, Abdul Rehman SA, Natarajan J, Matthews S, Madden R, De Cesare V, Weidlich S, Virdee S, Ahel I, Gibbs-Seymour I *et al* (2018) Discovery and characterization of ZUFSP/ZUP1, a distinct deubiquitinase class important for genome stability. *Mol Cell* 70: 150 – 164 e156
7. Rape M (2018) Ubiquitylation at the crossroads of development and disease. *Nat Rev Mol Cell Biol* 19: 59 – 70
8. Hussain S, Zhang Y, Galardy PJ (2009) DUBs and cancer: the role of deubiquitinating enzymes as oncogenes, non-oncogenes and tumor suppressors. *Cell Cycle* 8: 1688 – 1697
9. Fraile JM, Quesada V, Rodriguez D, Freije JM, Lopez-Otin C (2012) Deubiquitinases in cancer: new functions and therapeutic options. *Oncogene* 31: 2373 – 2388
10. Harrigan JA, Jacq X, Martin NM, Jackson SP (2017) Deubiquitylating enzymes and drug discovery: emerging opportunities. *Nat Rev Drug Discov* 17: 57 – 78
11. Li M, Chen D, Shiloh A, Luo J, Nikolaev AY, Qin J, Gu W (2002) Deubiquitination of p53 by HAUSP is an important pathway for p53 stabilization. *Nature* 416: 648 – 653
12. Brummelkamp TR, Nijman SM, Dirac AM, Bernards R (2003) Loss of the cylindromatosis tumour suppressor inhibits apoptosis by activating NF-kappaB. *Nature* 424: 797 – 801
13. Kovalenko A, Chable-Bessia C, Cantarella G, Israel A, Wallach D, Courtois G (2003) The tumour suppressor CYLD negatively regulates NF-kappaB signalling by deubiquitination. *Nature* 424: 801 – 805
14. Komander D, Clague MJ, Urbe S (2009) Breaking the chains: structure and function of the deubiquitinases. *Nat Rev Mol Cell Biol* 10: 550 – 563
15. Nakada S, Tai I, Panier S, Al-Hakim A, Iemura S, Juang YC, O'Donnell L, Kumakubo A, Munro M, Sicheri F *et al* (2010) Non-canonical inhibition of DNA damage-dependent ubiquitination by OTUB1. *Nature* 466: 941 – 946
16. Juang YC, Landry MC, Sanches M, Vittal V, Leung CC, Ceccarelli DF, Mateo AR, Pruneda JN, Mao DY, Szilard RK *et al* (2012) OTUB1 co-opts Lys48-linked ubiquitin recognition to suppress E2 enzyme function. *Mol Cell* 45: 384 – 397

17. Wiener R, Zhang X, Wang T, Wolberger C (2012) The mechanism of OTUB1-mediated inhibition of ubiquitination. *Nature* 483: 618–622

18. Zhao Y, Majid MC, Soll JM, Brickner JR, Dango S, Mosammaparast N (2015) Noncanonical regulation of alkylation damage resistance by the OTUD4 deubiquitinase. *EMBO J* 34: 1687–1703

19. Dantuma NP, Groothuis TA, Salomons FA, Neefjes J (2006) A dynamic ubiquitin equilibrium couples proteasomal activity to chromatin remodeling. *J Cell Biol* 173: 19–26

20. Mevissen TET, Kulathu Y, Mulder MPC, Geurink PP, Maslen SL, Gersch M, Elliott PR, Burke JE, van Tol BDM, Akutsu M *et al* (2016) Molecular basis of Lys11-polyubiquitin specificity in the deubiquitinase Cezanne. *Nature* 538: 402–405

21. Keusekotten K, Elliott PR, Glockner L, Fiil BK, Damgaard RB, Kulathu Y, Wauer T, Hospenthal MK, Gyrd-Hansen M, Krappmann D *et al* (2013) OTULIN antagonizes LUBAC signaling by specifically hydrolyzing Met1-linked polyubiquitin. *Cell* 153: 1312–1326

22. Baptista T, Grunberg S, Minoungou N, Koster MJE, Timmers HTM, Hahn S, Devys D, Tora L (2017) SAGA is a general cofactor for RNA polymerase II transcription. *Mol Cell* 68: 130–143 e135

23. Warfield L, Ramachandran S, Baptista T, Devys D, Tora L, Hahn S (2017) Transcription of nearly all yeast RNA polymerase II-transcribed genes is dependent on transcription factor TFIID. *Mol Cell* 68: 118–129 e115

24. Henry KW, Wyce A, Lo WS, Duggan LJ, Emre NC, Kao CF, Pillus L, Shilatifard A, Osley MA, Berger SL (2003) Transcriptional activation via sequential histone H2B ubiquitylation and deubiquitylation, mediated by SAGA-associated Ubp8. *Genes Dev* 17: 2648–2663

25. Kohler A, Schneider M, Cabal GG, Nehrbass U, Hurt E (2008) Yeast Ataxin-7 links histone deubiquitination with gene gating and mRNA export. *Nat Cell Biol* 10: 707–715

26. Lee KK, Swanson SK, Florens L, Washburn MP, Workman JL (2009) Yeast Sgf73/Ataxin-7 serves to anchor the deubiquitination module into both SAGA and Slik(SALSA) HAT complexes. *Epigenetics Chromatin* 2: 2

27. Samara NL, Datta AB, Berndsen CE, Zhang X, Yao T, Cohen RE, Wolberger C (2010) Structural insights into the assembly and function of the SAGA deubiquitinating module. *Science* 328: 1025–1029

28. Morgan MT, Haj-Yahya M, Ringel AE, Bandi P, Brik A, Wolberger C (2016) Structural basis for histone H2B deubiquitination by the SAGA DUB module. *Science* 351: 725–728

29. Samara NL, Ringel AE, Wolberger C (2012) A role for intersubunit interactions in maintaining SAGA deubiquitinating module structure and activity. *Structure* 20: 1414–1424

30. Song EJ, Werner SL, Neubauer J, Stegmeier F, Aspden J, Rio D, Harper JW, Elledge SJ, Kirschner MW, Rape M (2010) The Prp19 complex and the Usp4Sart3 deubiquitinating enzyme control reversible ubiquitination at the spliceosome. *Genes Dev* 24: 1434–1447

31. Zhang L, Zhou F, Drabsch Y, Gao R, Snaar-Jagalska BE, Mickanin C, Huang H, Sheppard KA, Porter JA, Lu CX *et al* (2012) USP4 is regulated by AKT phosphorylation and directly deubiquitylates TGF-beta type I receptor. *Nat Cell Biol* 14: 717–726

32. Clerici M, Luna-Vargas MP, Faesen AC, Sixma TK (2014) The DUSP-Ubl domain of USP4 enhances its catalytic efficiency by promoting ubiquitin exchange. *Nat Commun* 5: 5399

33. Yao F, Zhou Z, Kim J, Hang Q, Xiao Z, Ton BN, Chang L, Liu N, Zeng L, Wang W *et al* (2018) SKP2- and OTUD1-regulated non-proteolytic ubiquitination of YAP promotes YAP nuclear localization and activity. *Nat Commun* 9: 2269

34. Zhang Z, Fan Y, Xie F, Zhou H, Jin K, Shao L, Shi W, Fang P, Yang B, van Dam H *et al* (2017) Breast cancer metastasis suppressor OTUD1 deubiquitinates SMAD7. *Nat Commun* 8: 2116

35. Zhang L, Liu J, Qian L, Feng Q, Wang X, Yuan Y, Zuo Y, Cheng Q, Miao Y, Guo T *et al* (2018) Induction of OTUD1 by RNA viruses potently inhibits innate immune responses by promoting degradation of the MAVS/TRAF3/TRAF6 signalosome. *PLoS Pathog* 14: e1007067

36. Borodovsky A, Kessler BM, Casagrande R, Overkleeft HS, Wilkinson KD, Ploegh HL (2001) A novel active site-directed probe specific for deubiquitylating enzymes reveals proteasome association of USP14. *EMBO J* 20: 5187–5196

37. Koulich E, Li X, DeMartino GN (2008) Relative structural and functional roles of multiple deubiquitylating proteins associated with mammalian 26S proteasome. *Mol Biol Cell* 19: 1072–1082

38. Elsasser S, Chandler-Militello D, Muller B, Hanna J, Finley D (2004) Rad23 and Rpn10 serve as alternative ubiquitin receptors for the proteasome. *J Biol Chem* 279: 26817–26822

39. Clague MJ, Heride C, Urbe S (2015) The demographics of the ubiquitin system. *Trends Cell Biol* 25: 417–426

40. Kaiser SE, Riley BE, Shaler TA, Trevino RS, Becker CH, Schulman H, Kopito RR (2011) Protein standard absolute quantification (PSAQ) method for the measurement of cellular ubiquitin pools. *Nat Methods* 8: 691–696

41. Nijman SM, Luna-Vargas MP, Velds A, Brummelkamp TR, Dirac AM, Sixma TK, Bernards R (2005) A genomic and functional inventory of deubiquitinating enzymes. *Cell* 123: 773–786

42. Bekes M, Okamoto K, Crist SB, Jones MJ, Chapman JR, Brasher BB, Melandri FD, Ueberheide BM, Denchi EL, Huang TT (2013) DUB-resistant ubiquitin to survey ubiquitination switches in mammalian cells. *Cell Rep* 5: 826–838

43. Drag M, Mikolajczyk J, Bekes M, Reyes-Turcu FE, Ellman JA, Wilkinson KD, Salvesen GS (2008) Positional-scanning fluorigenic substrate libraries reveal unexpected specificity determinants of DUBs (deubiquitinating enzymes). *Biochem J* 415: 367–375

44. Winn MD, Ballard CC, Cowtan KD, Dodson EJ, Emsley P, Evans PR, Keegan RM, Krissinel EB, Leslie AG, McCoy A *et al* (2011) Overview of the CCP4 suite and current developments. *Acta Crystallogr D Biol Crystallogr* 67: 235–242

45. Adams PD, Afonine PV, Bunkoczi G, Chen VB, Davis IW, Echols N, Headd JJ, Hung LW, Kapral GJ, Grosse-Kunstleve RW *et al* (2010) PHENIX: a comprehensive Python-based system for macromolecular structure solution. *Acta Crystallogr D Biol Crystallogr* 66: 213–221

46. Emsley P, Cowtan K (2004) Coot: model-building tools for molecular graphics. *Acta Crystallogr D Biol Crystallogr* 60: 2126–2132

ARTICLE

Multiple myeloma gammopathies

Transcriptional profiling of circulating tumor cells in multiple myeloma: a new model to understand disease dissemination

Juan-Jose Garcés [1] · Michal Simicek[2,3,4] · Marco Vicari[5] · Lucie Brozova[6] · Leire Burgos[1] · Renata Bezdekova[7] · Diego Alignani[1] · Maria-Jose Calasanz[1] · Katerina Growkova[2,3,4] · Ibai Goicoechea[1] · Xabier Agirre[1] · Ludek Pour[7] · Felipe Prosper [1] · Rafael Rios[8] · Joaquin Martinez-Lopez[9] · Pamela Millacoy[10] · Luis Palomera[11] · Rafael Del Orbe [12] · Albert Perez-Montaña[13] · Sonia Garate[1] · Laura Blanco[1] · Marta Lasa[1] · Patricia Maiso[1] · Juan Flores-Montero[14] · Luzalba Sanoja-Flores[14] · Zuzana Chyra[2,6] · Alexander Vdovin[2,3,4] · Tereza Sevcikova[2,4] · Tomas Jelinek[2,3,4] · Cirino Botta [15] · Halima El Omri[16] · Jonathan Keats [17] · Alberto Orfao[14] · Roman Hajek[2,3] · Jesus F. San-Miguel[1] · Bruno Paiva[1]

Abstract

The reason why a few myeloma cells egress from the bone marrow (BM) into peripheral blood (PB) remains unknown. Here, we investigated molecular hallmarks of circulating tumor cells (CTCs) to identify the events leading to myeloma trafficking into the bloodstream. After using next-generation flow to isolate matched CTCs and BM tumor cells from 32 patients, we found high correlation in gene expression at single-cell and bulk levels ($r \geq 0.94$, $P = 10^{-16}$), with only 55 genes differentially expressed between CTCs and BM tumor cells. CTCs overexpressed genes involved in inflammation, hypoxia, or epithelial–mesenchymal transition, whereas genes related with proliferation were downregulated in CTCs. The cancer stem cell marker *CD44* was overexpressed in CTCs, and its knockdown significantly reduced migration of MM cells towards SDF1-α and their adhesion to fibronectin. Approximately half (29/55) of genes differentially expressed in CTCs were prognostic in patients with newly-diagnosed myeloma ($n = 553$; CoMMpass). In a multivariate analysis including the R-ISS, overexpression of *CENPF* and *LGALS1* was significantly associated with inferior survival. Altogether, these results help understanding the presence of CTCs in PB and suggest that hypoxic BM niches together with a pro-inflammatory microenvironment induce an arrest in proliferation, forcing tumor cells to circulate in PB and seek other BM niches to continue growing.

Introduction

Multiple myeloma (MM) is a hematologic neoplasm characterized by an aberrant expansion of clonal plasma cells (PCs) inside the bone marrow (BM) [1, 2]. Nevertheless, growing evidence demonstrates the presence of circulating tumor cells (CTCs) in peripheral blood (PB) at every stage of the disease, i.e., from monoclonal gammopathy of undetermined significance (MGUS) to smoldering and active newly-diagnosed or relapsed MM [3, 4]. Furthermore, several studies demonstrated that the number of CTCs detected in PB predicts the risk of malignant transformation in MGUS and smoldering MM [4–7], as well as survival in patients with symptomatic MM [4, 8–15]. By contrast, the mechanisms leading to the presence and variable levels of CTCs in the PB of MGUS and MM patients remains largely unknown [3, 4] since only one study attempted to characterize them [16]. Interestingly, CTCs were described as a unique subpopulation of BM clonal PCs with more immature, quiescent and clonogenic features, whose circulation in PB was potentially driven by circadian rhythms.

The complex network of communication between the circadian clock and tumorigenesis is only beginning to be

unraveled [17]. In MM, preliminary data pointed to a marked fluctuation of the daily number of CTCs that overlapped with CD34 hematopoietic stem cells (HSCs) [16]. It has been suggested that a circadian, neurally driven release of HSCs during the resting period may promote the regeneration of the stem cell niche and possibly other tissues [18]. Thus, it could be that in patients with MGUS and MM, CTCs may egress into PB to colonize other sites in the BM or at extramedullary tissues. Such model would fit with the hypothesis that as the disease progresses and the tumor microenvironment becomes hypoxic, clonal PCs constantly invade new regions of the BM through induced systemic recirculation [19]. Although this hypothesis has never been demonstrated, the presence of tumor cells throughout the axial skeleton of most patients suggests continuous dissemination from the primary tumor to different BM niches, leading to the development of active disease at multiple sites.

Due to an increasing interest in liquid biopsies for genetic profiling, prognostication and monitoring of patients with MM, the concordance between the genetic landscape of paired BM clonal PCs and CTCs has been analyzed in three recent studies [20–22]. These have found that CTCs mirror the genetic and transcriptional alterations of clonal PCs in the BM but, due to the low number of patients profiled, the presence of subtle molecular differences that might help explaining the presence of genetically similar tumor clones in different ecosystems (i.e., BM vs. PB) has not been investigated. Although detecting and isolating CTCs for their ulterior characterization is challenging, such information obtained from larger series of patients could help explaining MM trafficking through PB, and may provide a framework to develop specific therapies targeting CTCs.

Here, we investigated the potential mechanisms inducing MM trafficking into the bloodstream, by comparing in 32 patients the transcriptional profile of CTCs with matched BM clonal PCs at the single-cell and bulk levels. Our results unveil specific biologic functions that help understanding why MM cells egress from the BM into PB, identify genes upregulated in CTCs that are associated with more aggressive disease, and how silencing these genes may impact on cellular migration and adhesion.

Patients and methods

Data and materials availability

Raw and normalized (RMA) data from Affymetrix arrays as well as single-cell RNA-seq data (FASTQs, matrix counts and filtered count matrix with all samples) are deposited in the NCBI Gene Expression Omnibus (GEO) database with accession number GSE124438. All other data and processing code are available from the corresponding author upon reasonable request.

Patients and sample collection

A total of 64—PB and BM—paired samples from 32 patients were included in this study: 23 newly-diagnosed MM, eight relapsed MM, and one MGUS. All patients provided written informed consent and the study was conducted in accordance with the Declaration of Helsinki after approved by the University of Navarra (164/2015) and University Hospital Brno (12/3/2014) ethics committees.

Detection and isolation of BM clonal PCs and CTCs

EuroFlow next-generation flow (NGF) cytometry for sensitive detection of PB CTCs was used [4, 23]. Briefly, the EuroFlow lyse-wash-and-stain standard sample preparation protocol (adjusted to 10^6 nucleated cells in BM samples) together with the optimized 2-tube 8-color EuroFlow NGF antibody panel for accurate identification of clonal PCs were used. The two-tube strategy allows detection of clonality with specific confirmation of light-chain restriction on phenotypically aberrant PCs, identified either by antigen underexpression (CD19, CD27, CD38, CD45, and CD81) and/or antigen overexpression (CD56, CD117, and CD138) [4, 23, 24]. Data acquisition was performed in a FACS-Canto II flow cytometer (BD Biosciences, US) using the FACSDiva 6.1.3 software (BD). Data analysis was performed using the Infinicyt software (Cytognos SL, Spain).

Patient-specific aberrant phenotypes identified with NGF were used for sensitive isolation of tumor cells from both PB and BM. Fluorescence activated cell sorting (FACS) of clonal PCs was performed using a FACSAria II flow cytometer (BD) following standard procedures [16] for the isolation of bulk tumor cells, which were cryopreserved in FBS + 10% DMSO. For single-cell RNA sequencing (scRNA-seq), individual CTCs and BM clonal PCs were sorted into cooled 96-well cell capture plates containing 5 µL of BD reagents and molecular-barcoded poly(T) reverse-transcription primers for library preparation, following the instructions of the manufacturer (BD). Four empty wells were kept per plate as controls for data analysis. To record the expression levels of each marker per single cell, the FACS Diva 8.0 "index sorting" function was activated during sorting. BM clonal PCs and CTC percentages for each patient are shown in Supplementary Table 1.

Single-cell RNA sequencing

scRNA-seq libraries were prepared after isolating individual CTCs and BM clonal PCs from three patients, following

BD Precise WTA Single Cell Assay recommendations (BD) [25]. Briefly, immediately after sorting, each plate was sealed, vortexed and spun down to mix cells and the reagent solution, snap frozen on dry ice and stored at $-80\,^{\circ}C$ for ≤6 weeks until libraries preparation. After retrotranscription, pooling and purifying samples, second-strand was synthetized, adapters ligated, and the final entire product were amplified by random primer extension. Final libraries were sequenced in a single Illumina NextSeq 500 run (Illumina, US), with a minimum sequencing depth of 81,000 reads/cell. Of note, PB and BM tumor cells from each patient were processed in parallel.

Demultiplexing, alignment and matrix counts building were performed using the BD Precise Whole Transcriptome Assay Analysis Pipeline. Initial count matrix were merged and normalized trough *SCONE* R package (k_ruv = 3) [26]; downstream analysis for identifying differential expressed genes between clusters was performed with *Seurat* R package (version 2.3.4) [27], using a tSNE resolution of 0.9 and with *SCORPIUS* R package (version 1.0.2) [28] for inferring PC trafficking through pseudotime. Correlation analysis was performed on the average expression for each single-cell using the *Seurat::AverageExpression* function) considering a standard deviation of 0.5 and 1 (dashed and dotted lines in Fig. 1a, respectively), as well as through Pearson correlation on the normalized log-scale reads count for the supervised heatmap with patients distribution. Significance was considered below an adjusted *P* value of 0.01 (Bonferroni correction-based) and a *q*-value (Benjamini–Hochberg correction-based) of 0.1.

Gene expression profiling

RNA was extracted from CTCs and BM clonal PCs isolated from 29 patients using the AllPrep DNA/RNA micro kit (Qiagen, Netherlands) and was hybridized on a GeneChip Human Gene 2.0/1.0 ST array (Affymetrix, US) following manufacturer's instructions. Processing, normalization and differential expression analysis were performed using the Robust Multi-array Average (RMA) procedure from *limma* R package (version 3.34.9) [29]. Significance was considered below an adjusted *P* value of 0.1. Correlation analysis was performed on the median expression for each gene, using the same standard deviations mentioned above (Fig. 1e), as well as through Pearson correlation on the RMA-normalized expression data for the supervised heatmap with patients' distribution. Gene Set Enrichment Analysis (GSEA; version 3.0) [30] was performed using the curated hallmarks and the biological process gene sets (Gene Ontology, GO). The default parameters were used in both analysis, but changing the permutation type to *gene-set*. Significance was established below a false discovery rate (FDR) of 10%.

Cell culture and hypoxic conditions

The MM1.S cell line was purchased from ATCC and the KMS11 cell line was kindly provided by Irene Ghobrial from Dana-Farber Cancer Institute (Boston, USA), both were recently authenticated by STR profiling and tested for mycoplasma contamination. Both cell lines were grown in RPMI-1640 medium supplemented with 10% fetal bovine serum (FBS), 1% L-glutamine, and 1% streptomycin–penicillin, and maintained at $37\,^{\circ}C$ in a humidified 5% CO_2 incubator. To mimic hypoxic conditions, cells were cultured with or without $100\,\mu M$ of $CoCl_2$ for 4, 24, and 48 h as previously described [31], all conditions being tested in triplicate. Afterwards, RNA was extracted using the RNeasy kit (Qiagen, Netherlands) following the manufacturer's indications and total RNA was reversed transcribed with M-MLV (Invitrogen, US). Real-time PCR was performed with SYBR® Green PCR Master Mix (Life Technologies, US) on an Applied Biosystems ViiA™ 7 Real-Time PCR System (Thermofisher, US) using gene-specific primers: *B2M* as gene control (forward primer: TGCTGTCTCCATGTTTGATGTATCT; reverse primer: TCTCTGCTCCCCACCTCTAAGT) and *HIF1A* (F: GCTGCCTTCTCCTTCTGAAA, R: TTCTGCGCTG GTGCTTAGTA), *VEGF* (F: ATCTTCAAGCCATCCTG TGTGC; R: TCGGCTTGTCACATTTTTCTTG), *CD44* (F: TGGCACCCGCTATGTCGAG; R: GTAGCAGGGATTC TGTCTG) and *LGALS1* (F: GTGGCTCCTGACGCTA AGA, R: TAACGGGTGGGCATGAGG). Quantification of selected genes was normalized to *B2M* RNA using the $\Delta\Delta Ct$ method. Statistics was performed in R (version 3.5.1) through *ggpubr* package [32] using an one-way Anova and a two-sided Student's *t*-test for global and paired comparisons, respectively. Significance was established with a *P* value below 0.05.

RNA sequencing

Bulk RNA-seq was performed following the MARS-seq protocol with minor modifications adapted for measuring RNA expression in bulk cells [33, 34]. Briefly, 50,000 MM1. S and KMS11 cells were sorted after 24 h in hypoxia (as described above) in $100\,\mu L$ of Lysis/Binding Buffer (Ambion), vortexed and stored at $-80\,^{\circ}C$ until further processing. Poly-A RNA was reverse-transcribed using poly-dT oligos carrying a 7 bp-index. Pooled samples were subjected to linear amplification by in vitro transcription. Resulting amplified RNA was fragmented and dephosphorylated. Ligation of partial Illumina adaptor sequences [33] was followed by a second RT reaction. Full Illumina adaptor sequences were added during final library amplification. RNA-seq libraries quantification was done with Qubit 3.0 Fluorometer (Life Technologies) and size profiles
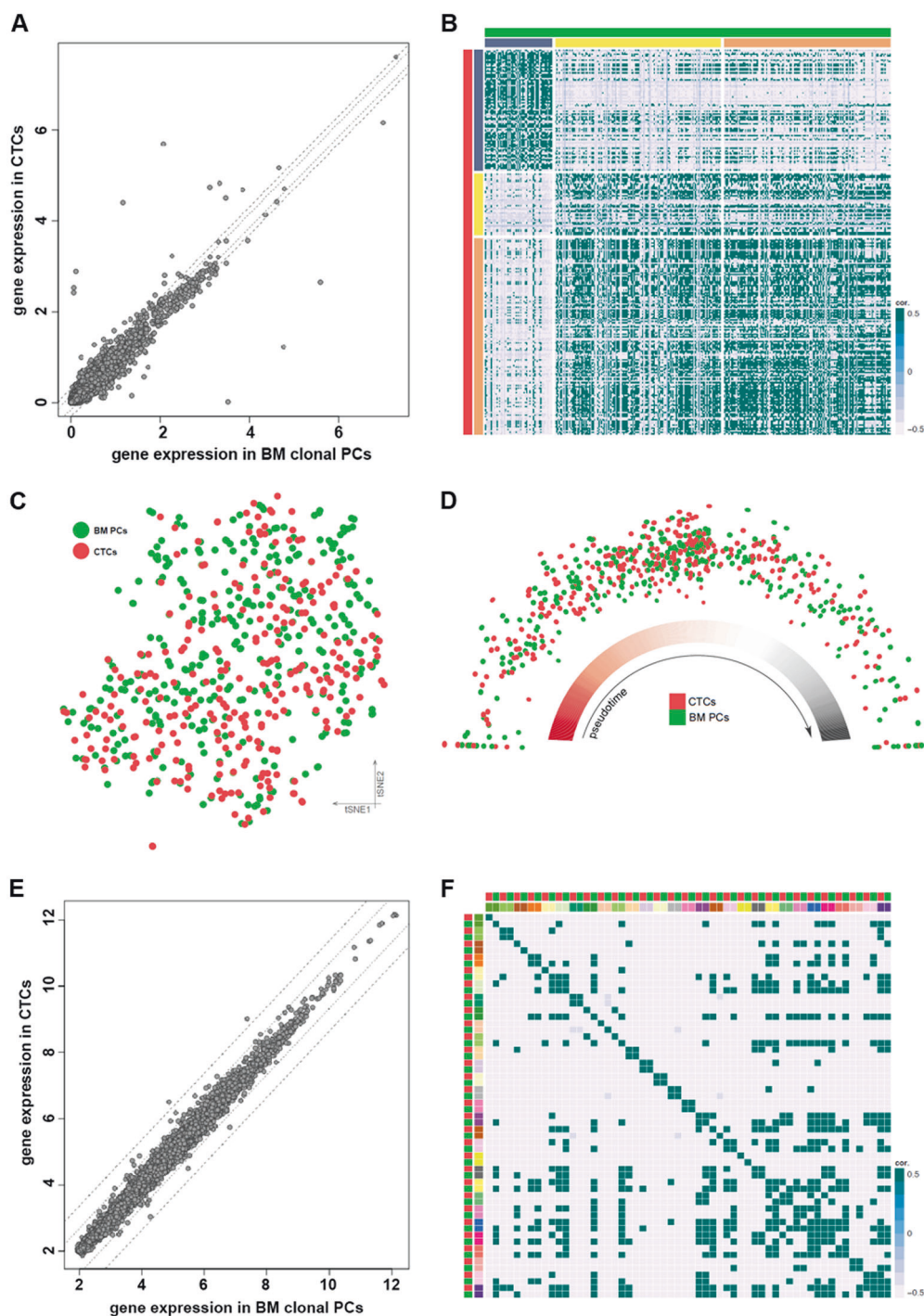
Fig. 1 The transcriptional profile of CTCs mirrors that of BM clonal PCs. a Correlation between gene expression levels observed in individual CTCs and BM clonal PCs from three patients. Every dot corresponds to the average expression of each single cell. **b** Correlation matrix between individual BM clonal PCs (horizontal axis, green) and CTCs (vertical axis, red) from each patient (distinctly colored). **c** tSNE plot and **d** pseudotime analysis based on scRNA-seq of patient-matched CTCs (red) and BM clonal PCs (green). **e** Correlation between gene expression levels observed in bulk CTCs and BM clonal PCs from 29 patients. Every dot corresponds to the median expression of each gene in all samples. For both correlation plots, dashed and dotted lines are showing limits delimited by 0.5 and 1 standard deviation. **f** Correlation matrix between bulk BM clonal PCs and CTCs from 29 patients. Each color corresponds to a different patient and green or red colors indicate BM clonal PCs or CTCs, respectively

examination with Agilent's 4200 TapeStation System. Libraries were sequenced in an Illumina NextSeq 500 at a depth of 10 million reads per sample. Analysis were performed in R (version 3.5.1) trough *DESeq2* [35] considering an adjusted *P* value below 0.01.

Cell culture and lentivirus production

Human MM cell lines U226 and MM1.S were maintained in RPMI-1640 medium containing 100 U/ml penicillin and 100 μg/ml streptomycin, supplemented with 10% (v/v) FBS and 2 mM GlutaMAX (Gibco, ThermoFisher, US), in 5% CO2 at 37 °C. HEK293T cells used for preparation of lentiviral particles were maintained in DMEM medium in the same conditions as MM cell lines. On day 0, HEK293T packaging cells were plated at a density of 3.5×10^6 cells per 10 cm plates. On day 1, cells were transfected with 4.5 μg of control —CD44 or FLNA— pLKO.1 plasmid, 1.5 μg of pMD.2G and 6 μg of psPAX2 for lentivirus packaging (AddGene, US). On day 2, media was replaced and cells cultured for an additional 24 h to obtain viral supernatants. On day 3, media containing virus was harvested, passed through 0.45-μm filters. Overall, 1×10^6 cells/ml were infected with crude viral supernatants in the presence of 8 μg/ml polybrene and spinoculated at 800 g for 60 min at room temperature, subsequently incubated in 5% CO_2 at 37 °C for 16 h and media was then replaced. After 48 h of viral infection, cells expressing shRNAs were selected with puromycin (Sigma-Aldrich, US) at 1 μg/ml for at least 2 days and subjected to each assay (in triplicate). Cell lines were routinely tested to rule out mycoplasma contamination using the MycoAlert Mycoplasma Detection Kit (Lonza, Swiss).

Immunoblot analysis

Cells were harvested, washed with PBS and lysed in RIPA buffer containing a protease inhibitor cocktail (cOmplete, Roche, Swiss). The suspension was incubated for 30 min on ice and centrifuged at 10,000 g for 10 min at 4 °C. Protein concentration in supernatant was measured with the BCA Assay (Thermo Fisher, US). Samples were mixed with 4X LDS loading buffer, boiled at 95 °C for 5 min and subjected to SDS-PAGE. Afterwards, proteins were transferred to a PVDF membrane and blocked in PBS containing 0.1% (v/v) Tween-20 and 5% (w/v) nonfat dry milk for 1 h at RT. Immunoblots were carried out with the following antibodies: anti-CD44 (Clone 156-3C11, Abnova, Taiwan), anti-FLNA (#4762, Cell Signaling Technology, Netherlands) and anti-β-actin (clone c4, Santa Cruz Biotechnology, US), and visualized on X-ray films using the ECL Western Blotting Detection Reagents (GE Healthcare, US).

Migration and adhesion assays

For migration assays, 4×10^5 MM cells labelled with calcein AM (ThermoFisher, US) were suspended in 200 μL of RPMI-1640 medium with 1% FBS and placed in the upper chambers, whereas 500 μL of RPMI-1640 medium with 10% FBS and SDF-1α (20 nM) were placed in the lower chambers of 24-well transwell plates (pore size 8.0 μm, Costar; Sigma-Aldrich, US). After 4 h of incubation at 37 °C, cells migrating to the lower chambers were quantified using a fluorescence plate reader (TECAN, Switzerland), at an excitation wavelength of 485 nm and emission wavelength of 525 nm. The relative percentage of migration was determined by calculating the ratio of fluorescent intensity of migrated cells to that of cells placed in the upper chambers.

To measure adhesion, MM cells were pre-labelled with 1 μM calcein AM (ThermoFisher, US) upon incubation at 37 °C for 30 min. After washing with PBS containing calcium and magnesium, labelled cells were resuspended in PBS (+Ca and Mg), at a concentration of 1×10^6 ml^{-1}. Overall, 1×10^5 cells were then incubated in 96-well plates coated with fibronectin or BSA at 37 °C for 1 h. After measuring the fluorescent intensity of pre-wash samples, wells were washed two to three times with PBS. Fluorescence was quantified using the same TECAN reader and excitation/emission wavelengths. The relative percentage of adhesion was determined by calculating the ratios of the fluorescent intensity of postwash sample to that of prewash sample.

Survival analysis

RNA sequencing data ($n = 553$) from BM clonal PCs of newly-diagnosed MM patients enrolled in the CoMMpass study (version IA11) was provided by the Multiple Myeloma Research Foundation to investigate the prognostic value of genes upregulated in CTCs (adj. $P < 0.1$ and logFC ± 0.5). Expression of these selected genes in each patient was categorized following the tertile-criteria ("low" if expression below the lower tertile; "mid", between the lower and higher tertiles; and "high" above the highest tertile).

We performed a univariate Cox regression (*survival* R package [36]) to determine the prognostic value of individual genes, considering statistically significant differences when $P < 0.05$. Afterwards, a multivariate Cox regression model was performed to identify among all genes differentially expressed in CTCs and the revised International Staging System (R-ISS), those with independent prognostic value. Survival was analyzed through the Kaplan–Meier method (*survminer* R package [37]), and differences between curves were tested for statistical significance with the two-sided log-rank test. In both

analysis, patients were stratified according to sex and age. Progression-free survival (PFS) was defined as the time from diagnosis to disease progression or death from any cause. Overall survival was defined as time from diagnosis to death from any cause. The median follow-up for CoMMpass study was of 27.4 months (range, 1.9–58.4). The UAMS-Total Therapy 2 and 3 (GSE2658, $n = 559$) and HOVON65/GMMG-HD4 (GSE19784, $n = 282$) datasets were used to validate the prognostic value of genes differentially expressed in CTCs.

Results

Gene expression of CTCs reflects the transcriptional state of BM clonal PCs

scRNA-seq was performed in paired CTCs ($n = 266$) and BM clonal PCs ($n = 340$) isolated from three patients. The median number of detected transcripts was 3674 (range, 1592–13782) and 3442 (range, 1554–13253), respectively. We found a significant correlation in gene expression between CTCs and BM clonal PCs ($r = 0.96$, $P < 2.2 \times 10^{-16}$) (Fig. 1a). Thus, dimensionality reduction based on t-Distributed Stochastic Neighbor Embedding (t-SNE) and a "temporal trajectory" placing each individual cell based on pseudotime analysis showed spatial overlap between CTCs and BM clonal PCs (Fig. 1b, c). A correlation matrix confirmed the similarity between the transcriptional states of single PB and BM tumor cells in each individual patient (Fig. 1d). Only 65 genes displayed differential expression (adjusted $P < 0.1$) between CTCs and paired BM clonal PCs (Supplementary Fig. 1). Interestingly, genes previously identified to be induced by hypoxia (e.g., DDIT4) and to be implicated in tumor migration, invasiveness and metastasis (e.g., AGR2, DDX5, MALAT1, TMED2, TPT1) were overexpressed in CTCs.

To confirm the high correlation found in gene expression of paired single CTCs versus BM clonal PCs and to further investigate for subtle transcriptional differences between both, we compared gene expression of bulk CTCs and BM clonal PCs in a larger series of patients. Thus, gene expression profiling was performed in matched PB and BM tumor cells from 29 patients, with median numbers of 5200 (range, 800–193119) CTCs and 53956 (range, 2000–2400000) BM clonal PCs. This approach reproduced previous findings based on scRNA-seq and unveiled once again a significant correlation in gene expression between paired CTCs and BM clonal PCs ($r = 0.94$, $P < 2.2 \times 10^{-16}$) (Fig. 1e). Similarly, there was great resemblance in the transcriptional state of CTCs and BM clonal PCs in each individual patient (Fig. 1f).

Molecular hallmarks of MM trafficking into the bloodstream

The similarity between the transcriptome of paired CTCs and BM clonal PCs gave confidence on the accuracy of gene expression data obtained from low numbers of CTCs. Furthermore, we hypothesized that beneath such similarity there could be subtle but consistent differences between tumor cells egressing from the BM into PB. In such cases, differentially expressed genes would not result from a random process and could represent molecular hallmarks of MM trafficking into the bloodstream. Thus, downstream analysis of bulk CTCs and BM clonal PCs showed 259 differentially expressed genes (adjusted $P < 0.1$), 55 of which with a logarithmic fold-change (logFC) higher than ±0.5 (Fig. 2a; list of all differentially expressed genes in the Supplementary Table 2). Unsupervised clustering with differentially expressed genes resulted in the segregation between most of the PB and BM specimens (Fig. 2b). Even an unsupervised clustering with the top 1000 variable genes segregated CTCs from patient-matched BM clonal PCs in 24 of the 29 (83%) patients (Supplementary Fig. 2). These findings prompted us to investigate the significance of those genes with consistent variable expression.

When compared with BM clonal PCs, CTCs showed overexpression of genes related with cytoskeleton reorganization and actin filament binding (e.g., CFAP54 [38] or EZR [39–41]), migration/invasiveness (e.g., EMP3 [42] or AHNAK [43, 44]), cellular adhesion in MM (e.g., CD44 [45–47], LGALS1 [48, 49] or IQGAP1 [50, 51]) and other neoplasms (e.g., ADGRE5 [52]), inflammation in MM (e.g., BIRC3 [53] or TNFAIP3 [54, 55]) and other cancers (e.g., NFKBIA [56, 57] or GBP2 [58, 59] or LGALS3 [60, 61]), coagulation (e.g., ENPP4 [62]) and cholesterol homeostasis (e.g., INSIG1, LDLR and STARD4), previously associated with MM [63] and other tumors [64, 65]. Conversely, genes responsible for progression through cell cycle (e.g., CENPF [66] or CDC6 [67]) were downregulated in CTCs.

To investigate which molecular pathways were deregulated in CTCs and thereby, potentially related to the egress of tumor cells from the BM into PB, we performed a double GSEA focusing on curated hallmarks and gene ontology. When compared with BM clonal PCs, CTCs displayed an enrichment of various biological functions related to inflammation (e.g., interferon gamma/alpha response, TNFα signaling via NFκB, complement, IL6/JAK/STAT3 and IL2/STAT5 signaling), angiogenesis, hypoxia and apoptosis (e.g., P53 pathway). Interestingly, genes involved in the epithelial–mesenchymal transition (EMT) were also overexpressed in CTCs (Fig. 2c). By contrast, hallmarks of cell cycle (e.g., DNA repair, mitotic spindle formation, G2M checkpoint or targets of E2F factors) were downregulated in CTCs.

Fig. 2 Molecular hallmarks of MM trafficking into the bloodstream. **a** Volcano plot with differentially expressed genes between bulk CTCs and BM clonal PCs. Green-to-red scale indicates the logarithmic fold-change (logFC) of genes with an adjusted P value ≤ 0.1. Genes with a previously ascribed role in MM (orange) or other tumors (blue) are highlighted. **b** Bi-clustering heatmap with differentially expressed genes ($n = 259$). Red and green colors differentiate CTCs and BM clonal PCs, respectively; blue–red gradient shows the expression level for each gene from low to high (scaled). **c** Interaction between hallmark gene sets and differentially expressed genes. Hallmarks enriched in CTCs are colored in red, whereas those enriched in BM clonal PCs are colored in green. The blue to red gradient represents low to high logFC of each gene (low–high). Genes with an ascribed role in MM and other tumors are highlighted in orange and blue, respectively. The barplot in the right panel represents the normalized enrichment score (NES) and the number of genes involved in each significant hallmark gene set. **d** The 50 most significant Gene Ontology (GO) sets. The color of each dot indicates if a GO is enriched in CTCs (red) or BM clonal PCs (green), and its intensity correlates with the false discovery rate (FDR) logarithmic value (the more significant, the darker the color). The size of each dot indicates the number of genes enriching for each GO and the position in the x-axis its NES estimation
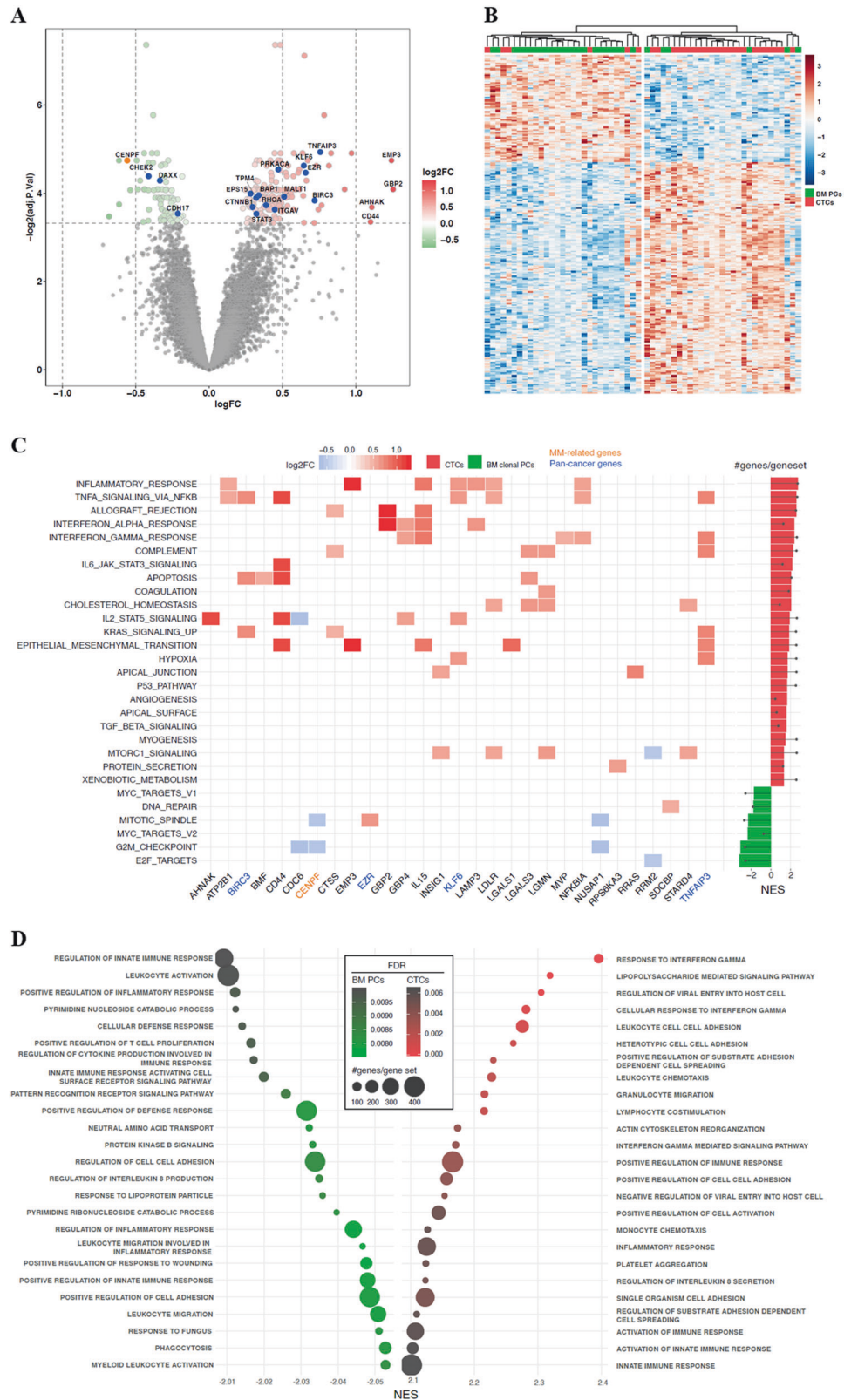
Enrichment analysis based on gene ontology confirmed that biological processes related with inflammation and cell cycle were upregulated in CTCs and BM clonal PCs, respectively (Fig. 2d). In addition, CTCs showed an enrichment in functions such as migration and cellular adhesion. Altogether, these findings suggest that tumor
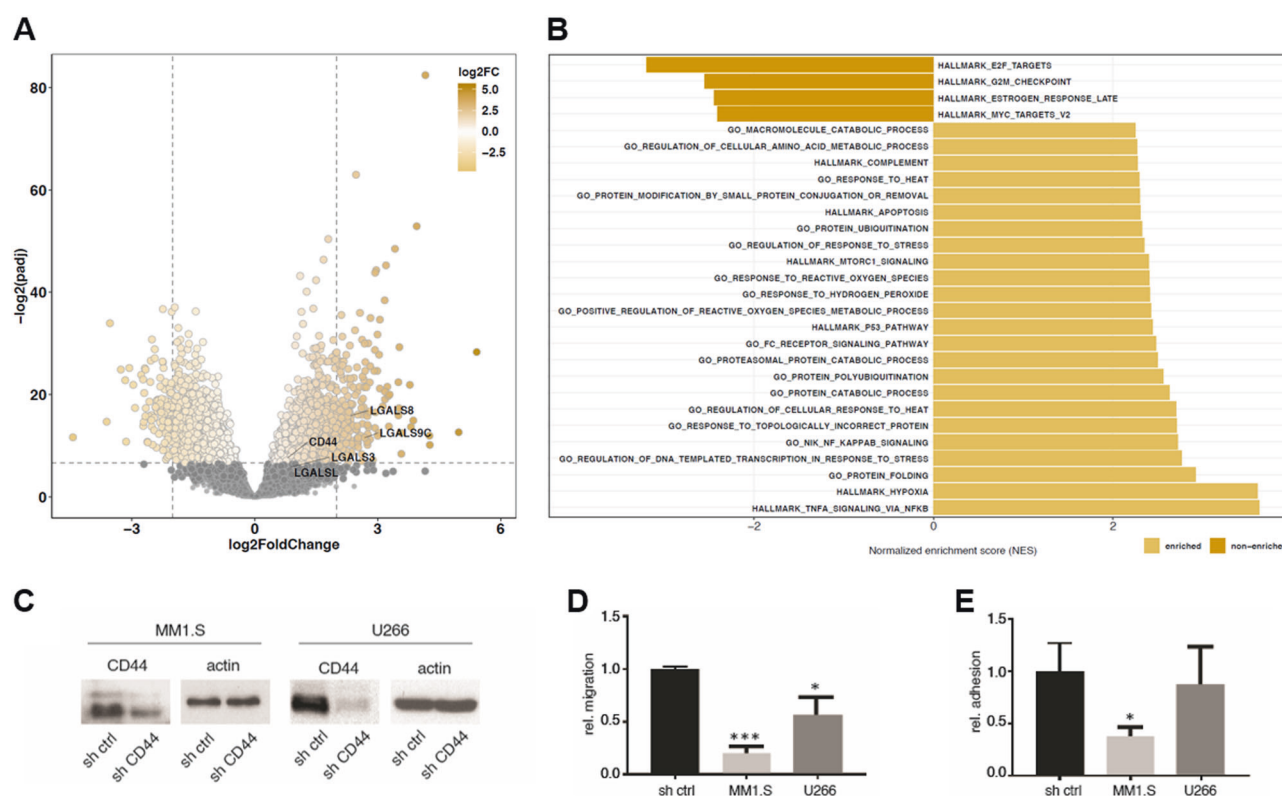
Fig. 3 Knockdown of genes upregulated in hypoxia reduces migration and adhesion of MM cells. **a** Volcano plot and **b** GSEA analysis with differentially expressed genes (FDR ≤ 0.01) in MM1.S cells upon chemically induced-hypoxia with CoCl₂. Enriched and non-enriched functions in hypoxia versus normoxia are colored in light or dark color, respectively. **c** Immunoblot analysis of *CD44* knockdown in MM1.S and U266 cells. **d** MM1.S and U266 cells were placed in the upper chamber of transwell plates with SDF1-α (12.5 nM) in the lower chambers. After 16 h, cells migrating to the lower chambers were quantified. Results are shown as relative migration over the control (mean ± standard deviation of triplicates). **e** MM1.S and U266 cells were incubated in fibronectin-coated plates. After washing, adherent cells were quantified. Results are shown as relative adhesion over the control (mean ± standard deviation of triplicates). All graphics are representative of one experiment (out of three). *$P < 0.05$, **$P < 0.01$, ***$P < 0.001$ compared with control using the Student's t-test

cells in PB may have been forced to egress from hypoxic and inflammatory BM niches no longer supportive to their continuous expansion. In such cases, CTCs may have unique features allowing them to migrate from the PB into other BM niches.

## Knockdown of genes upregulated in hypoxia reduces migration and adhesion of MM cells

To increase the level of evidence supporting our previous results, we determined the transcriptional modulation of MM1.S and KMS11 cells lines under after 24 h in hypoxic conditions. Up to 304 genes became deregulated with a logFC above 2 (Fig. 3a) and, notably, double GSEA unveiled that most hallmarks and gene ontology previously identified as molecular hallmarks of MM trafficking into the bloodstream, emerged in MM cell lines under hypoxic conditions (Fig. 3b). Since we have previously found that CD44 antigen expression was upregulated in the surface membrane of paired CTCs versus BM clonal PCs from patients with MM [16], that CD44 has been described as an essential mediator

of BM adhesion on MM cells [46], and implicated in other processes such as cellular trafficking [68, 69], EMT [70, 71], and stemness [70, 71], we selected *CD44* as a proof-of-concept to investigate the impact on migration and adhesion of silencing a gene that was found to be one of the most overexpressed in CTCs. shRNA knockdown of CD44 (Fig. 3c) resulted in a significant reduction in the potential of MM1.S (5.3-fold; $P < 0.0004$) and U266 (1.8-fold, $P = 0.0157$) MM cells to migrate in the presence of SDF-1α (Fig. 3d). Relative adhesion of MM1.S cells to fibronectin (Fig. 3e) was also impaired by shRNA knockdown of CD44 (2.7-fold; $P < 0.02$). Of note, *CD44* and *LGALS1* (another gene deregulated in CTCs and selected as proof-of-concept) mRNA levels significantly increased under progressive hypoxic conditions (Supplementary Fig. 3).

Genes differentially expressed in CTCs are associated with poor prognosis

If genes differentially expressed in CTCs are the result of a BM microenvironment that induces MM trafficking into

Fig. 4 Genes differentially expressed in CTCs are associated with poor prognosis. **a** Hazard ratio for progression-free survival according to low (green), intermediate (yellow) and high (red) tertile expression of each of the 55 genes differentially expressed in CTCs, measured by RNA-seq in BM clonal PCs from MM patients ($n = 553$) enrolled in the CoMMpass study. "Down" and "up" labels indicate whether genes are infra- or overexpressed in CTCs. Genes highlighted in orange had a significant impact on progression-free survival. Kaplan–Meier curves for progression-free and overall survival according to low (green), intermediate (yellow) and high (red) tertile expression of **b** CENPF and LGALS1 (**c**)
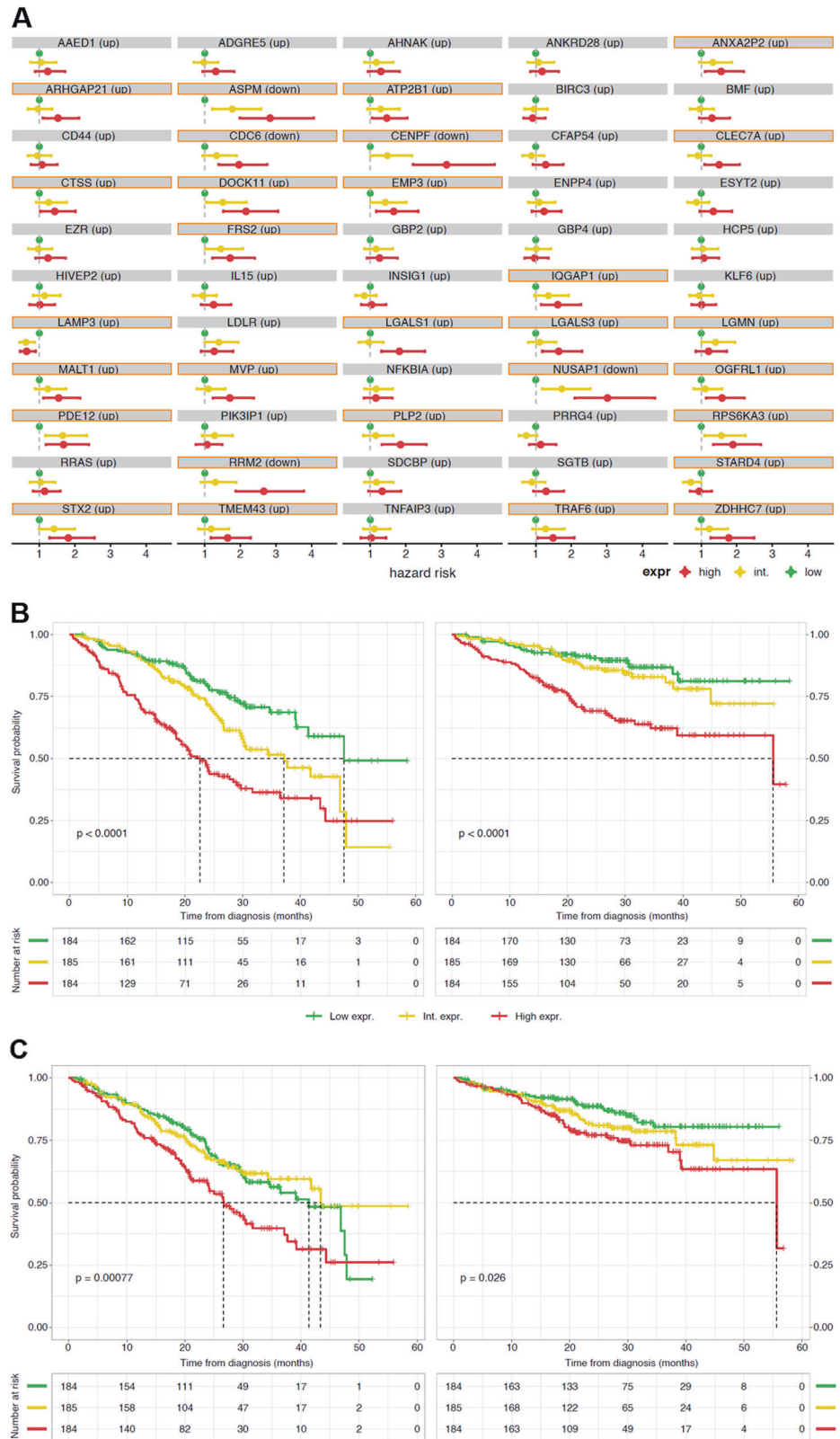
PB, they should have an impact on patients' outcome since the higher the number of CTCs, the worse the prognosis. Thus, we used the RNA-seq dataset from BM clonal PCs of

newly-diagnosed MM patients enrolled in the CoMMpass study, to investigate if the 55 genes previously found to be differentially expressed in CTCs with a logarithmic fold-

Table 1 Multivariate analysis of progression-free and overall survival incorporating the Revised International Staging System (R-ISS) and all 55 genes deregulated in CTCs (only those with significant prognostic value are shown)

Parameter	Group	PFS		OS	
		HR (IC95%)	P	HR (IC95%)	P
CENPF (↓)	Low	(Reference)		(Reference)	
	Int.	1.3 (0.9–2.0)	0.146	1.1 (0.6–2.0)	0.710
	High	2.7 (1.9–3.9)	0.000***	2.7 (1.6–4.6)	0.000***
LGALS1 (↑)	Low	(Reference)		(Reference)	
	Int.	1.0 (0.7–1.4)	0.821	1.5 (0.9–2.6)	0.101
	High	1.5 (1.1–2.1)	0.015*	1.7 (1.0–2.8)	0.048*
R-ISS	1	(Reference)		(Reference)	
	2	1.7 (0.9–3.3)	0.107	4.1 (1.0–17.1)	0.051
	3	2.1 (1.1–4.1)	0.024*	5.7 (1.4–23.6)	0.016

HR hazard ratio, CI confidence interval, ↓ infraexpressed in CTCs, ↑ overexpressed in CTCs

***$P < 0.001$; **$P < 0.01$; *$P < 0.05$

change higher than ±0.5, had prognostic value. Interestingly, univariate analysis showed that 29 of the 55 genes were significantly associated with patients' outcome (Fig. 4a). As expected, elevated expression of genes associated with progression through cell cycle (i.e., *ASPM*, *CDC6*, *CENPF*, *NUSAP* and *RRM2*) was associated with inferior PFS. Furthermore, patients whose BM clonal PCs displayed overexpression of genes related with cell migration (e.g., *ARHGAP21*, *IQGAP1* or *DOCK11*) or inflammation and interferon response (*CLEC7A*, *LGALS1*, *LGALS3* or *MVP*) had significantly inferior PFS. Of note, up to 24 of the 55 genes differentially expressed in CTCs also had significant prognostic value in the UAMS (Total Therapy 2 and 3) and/or in the HOVON65 validation datasets (Supplementary Table 3).

In a multivariate analysis including all 55 genes and the R-ISS [72], *CENPF* and *LGALS1* showed independent prognostic value for progression-free and overall survival (Table 1). Patients with elevated expression of *CENPF* had significantly inferior PFS than cases with intermediate and low expression levels (medians of 22.6, 37.1 and 47.5 months, respectively; $P = .0001$) (Fig. 4b). Patients with elevated expression of *LGALS1* also had significantly inferior PFS than cases with intermediate and low expression levels (medians of 26.7, 43.4 and 41.3 months, respectively; $P = .0008$) (Fig. 4c). Of note, overexpression of *CENPF* and *LGALS1* had a significant impact in patients' overall survival (Fig. 4b, c).

Discussion

MGUS and MM are characterized by the presence of disseminated disease, including frequent multiple tumors (i.e., "plasmacytomas") throughout the axial skeleton, suggesting continuous trafficking and spreading from early to late stages of the disease [19]; in fact, the higher the number of tumor cells in PB, the worse the prognosis [4–6, 13–16]. This level of evidence supports the study of CTCs as a potential model to understand dissemination from "micro-metastatic MGUS to colonized MM" [19], but the genomic characterization of CTCs in large series of patients has not been feasible given the complexity of isolating rare tumor cells from the PB. Thus, the transcriptional state of paired CTCs and BM clonal PCs has been compared in only two studies and, due to the small sample size, it was only possible to infer that CTCs reflected BM disease [20, 21]. Based on the largest series of patient-matched CTCs and BM clonal PCs ever studied, we here confirm previous observations about the accuracy of CTCs for transcriptional liquid biopsies, and provide new insight about the process of MM trafficking into the bloodstream.

Albeit in low numbers, CTCs are readily detectable in patients with MGUS and MM using sensitive next-generation flow cytometry [4], which indicates that cancer cells are constantly entering the circulation. This probably explains similarities between CTCs and BM clonal PCs regarding mutations or copy number alterations [20, 21], and implies that spreading of MM is not driven by tumor cells with specific genetic hits. Accordingly, it was suggested that CTCs represent functional (and not genetic) subclones in the BM with a quiescent phenotype, which, upon reengagement with BM stromal cells, display clonogenic potential [19]. Here, we shed light into those findings by showing that the expression of genes implicated in the progression of cell cycle are downregulated in CTCs versus BM clonal PCs. In addition, we unveiled that transcriptional programs related with inflammation and hypoxia are enriched in CTCs. Albeit we cannot exclude that some genes may be deregulated as a consequence of these cells being in PB, these data suggest a model in which (fully occupied) hypoxic BM niches together with a pro-inflammatory tumor microenvironment induce an arrest in proliferation of cancer, forcing their recirculation into PB to seek for other BM niches to survive and continue growing. Amongst others, CTCs displayed overexpression of *LGALS1* and we reproduced here previous observations showing that its expression becomes upregulated in hypoxic conditions [73]. Furthermore, patients in

whom BM clonal PCs express high levels of *LGALS1* had inferior survival. That notwithstanding, whether CTCs are more aggressive than BM clonal PCs warrants further investigation. Based on the genes and functional pathways differentially expressed in CTCs, our results also suggest that in accordance to recent findings described by Takagi et al. [74], platelets may have a role in promoting hematogenous dissemination of MM cells through angiogenesis and prolonging the survival of CTCs by maintaining an EMT state and secretion of transforming growth factor β in response to CTC activation [75].

EMT is a reversible process that occurs during normal development and cancer progression [76, 77]. Several studies in solid tumors suggest an association between EMT and the invasion-metastasis cascade together with the acquisition of stem cell-like properties leading to chemoresistance [77]. Interestingly, these stem-like cells (usually defined as cancer stem cells, CSCs) have elevated tumor-initiating potential and often express high levels of CD44 compared with their non-CSC counterparts [71, 76, 78]. In addition to its potential role as a CSC marker, CD44 is also known to be involved in homing and maintaining quiescence in solid tumors [70, 71, 79]. More recently, Mueller et al. unveiled that CD44 plays a critical role in the accumulation and survival of clonal mast cells in tissues, and showed that inhibitors of the Ras-MEK pathway and STAT5 lead to downregulation of surface CD44 expression [80]. Here, we confirmed previous observations on phenotypic grounds and showed that MM CTCs upregulate *CD44* [16]. Furthermore, we found an enrichment in *CD44* and other overexpressed genes (e.g., *BIRC3, TNFAIP3, KLF6, AHNAK*) related with the IL2/STAT5 and KRAS signaling pathways. We also demonstrated that amongst others, *CD44* and *LGALS1* were upregulated in hypoxic conditions, and that knockdown of *CD44* impaired MM cells' ability to migrate and adhere, suggesting that targeting molecular hallmarks of CTCs may represent a new therapeutic avenue to find drugs that might prevent the dissemination of MM. Despite previous evidence of a role for CD44 and cell adhesion in mediating resistance to lenalidomide in MM [81], expression of *CD44* in normal cells and immunogenic accumulation of monoclonal antibodies targeting CD44 in non-tumor areas limits the use of this antigen for cancer immunotherapy [82]. Thus, further studies are warranted to identify valid therapeutic targets for the eradication of MM CTCs, such as targeting E-selectin receptor/ligand interactions as proposed by Natoni et al. [83]. Of note, it can be hypothesized that such approaches may have limited value in late stages of the disease while useful in earlier settings, to eliminate CTCs responsible for malignant transformation through the progressive "metastization" of MM.

The conventional paradigm for metastasis postulates that cancer cells within primary tumors undergo EMT and that this is necessary to enter circulation and transit to secondary sites, in which a mesenchymal–epithelial transition occurs before successful metastatic growth [84]. This paradigm bears striking parallels with the CSC model, which postulates that a subpopulation of cells within the tumor has preferential capacity for driving tumor growth and regrowth at a new site and can effectively recreate tumor heterogeneity [84]. Unfortunately, the discovery of therapies targeting CSCs has been unsuccessful probably due to the lack of markers to unequivocally identify and purify CSCs. It should be noted that in MM, Roccaro et al. [85] have reported that CXCR4 regulates the emergence of extramedullary ("metastatic") disease through activation of an EMT-like transcriptional profile, whereas Matsui et al. suggested that CSCs lack CD138 expression and are present in the PB of patients with MM [86, 87]. Based on previous findings demonstrating that CTCs are the only cells in PB harboring the same clonotypic VDJ sequence of BM clonal PCs [88], that CTCs display significantly lower levels [4, 16] or even absence of CD138 (Supplementary Fig. 4) together with data from this study showing activation of EMT and overexpression of *CD44* in CTCs, the notion that this subset of MM cells carries stem cell-like properties (e.g., quiescence, clonogenic potential, activated EMT program, high expression of CSC markers and low CD138) gains further support [19, 89, 90]. Thus, this study should stimulate other groups to confirm if MM CTCs are metastatic stem cells and discover effective therapies for their eradication. Of note, the progressive use of sensitive EuroFlow NGF cytometry to detect minimal residual disease [23] and CTCs [4] creates an opportunity to use a standardized method for isolating these rare clones through cell sorting.

In summary, here we show that the transcriptional state of CTCs resembles that of patient-matched BM clonal PCs, except for a few genes that are involved in interferon and inflammatory response, hypoxia, cell cycle and migration. Although we cannot distinguish amongst BM clonal PCs those that have homed from PB versus those that have never circulated before, we demonstrated that patients harboring BM clonal PCs overexpressing CTC-related genes have more aggressive disease behavior. Thus, deep characterization of CTCs might unveil novel therapeutic targets to overcome disease dissemination and prolong survival of patients with MM.

Compliance with ethical standards

Conflict of interest The authors declare that they have no conflict of interest.

Publisher's note Springer Nature remains neutral with regard to jurisdictional claims in published maps and institutional affiliations.

References

1. Palumbo A, Anderson K. Multiple myeloma. N Engl J Med. 2011;364:1046–60.
2. Rajkumar SV, Dimopoulos MA, Palumbo A, Blade J, Merlini G, Mateos MV, et al. International Myeloma Working Group updated criteria for the diagnosis of multiple myeloma. Lancet Oncol. 2015;15:e538–48.
3. Paiva B, Pérez-Andrés M, Vídriales MB, Almeida J, De Las Heras N, Mateos MV, et al. Competition between clonal plasma cells and normal cells for potentially overlapping bone marrow niches is associated with a progressively altered cellular distribution in MGUS vs myeloma. Leukemia. 2011;25:697–706.
4. Sanoja-Flores L, Flores-Montero J, Garcés JJ, Paiva B, Puig N, García-Mateo A, et al. Next generation flow for minimally-invasive blood characterization of MGUS and multiple myeloma at diagnosis based on circulating tumor plasma cells (CTPC). Blood Cancer J. 2018;8:117.
5. Kumar S, Rajkumar SV, Kyle RA, Lacy MQ, Dispenzieri A, Fonseca R, et al. Prognostic value of circulating plasma cells in monoclonal gammopathy of undetermined significance. J Clin Oncol. 2005;23:5668–74.
6. Bianchi G, Kyle RA, Larson DR, Witzig TE, Kumar S, Dispenzieri A, et al. High levels of peripheral blood circulating plasma cells as a specific risk factor for progression of smoldering multiple myeloma. Leukemia. 2013;27:680–5.
7. Gonsalves WI, Rajkumar SV, Dispenzieri A, Dingli D, Timm MM, Morice WG, et al. Quantification of circulating clonal plasma cells via multiparametric flow cytometry identifies patients with smoldering multiple myeloma at high risk of progression. Leukemia. 2017;31:130–5.
8. Gonsalves WI, Rajkumar SV, Gupta V, Morice WG, Timm MM, Singh PP, et al. Quantification of clonal circulating plasma cells in newly diagnosed multiple myeloma: implications for redefining high-risk myeloma. Leukemia. 2014;28:2060–5.
9. Gonsalves WI, Morice WG, Rajkumar V, Gupta V, Timm MM, Dispenzieri A, et al. Quantification of clonal circulating plasma cells in relapsed multiple myeloma. Br J Haematol. 2014;167:500–5.
10. Chakraborty R, Muchtar E, Kumar SK, Jevremovic D, Buadi FK, Dingli D, et al. Serial measurements of circulating plasma cells before and after induction therapy have an independent prognostic impact in patients with multiple myeloma undergoing upfront autologous transplantation. Haematologica. 2017;102:1439–45.
11. Cowan AJ, Stevenson PA, Libby EN, Becker PS, Coffey DG, Green DJ, et al. Circulating plasma cells at the time of collection of autologous PBSC for transplant in multiple myeloma patients is a negative prognostic factor even in the age of post-transplant maintenance therapy. Biol Blood Marrow Transplant. 2018;24:1386–91.
12. Foulk B, Schaffer M, Gross S, Rao C, Smirnov D, Connelly MC, et al. Enumeration and characterization of circulating multiple myeloma cells in patients with plasma cell disorders. Br J Haematol. 2018;180:71–81.
13. Granell M, Calvo X, Garcia-Guiñón A, Escoda L, Abella E, Martínez CM, et al. Prognostic impact of circulating plasma cells in patients with multiple myeloma: implications for plasma cell leukemia definition. Haematologica. 2017;102:1099–104.
14. Huhn S, Weinhold N, Nickel J, Pritsch M, Hielscher T, Hummel M, et al. Circulating tumor cells as a biomarker for response to therapy in multiple myeloma patients treated within the GMMG-MM5 trial. Bone Marrow Transplant. 2017;52:1194–8.
15. Dingli D, Nowakowski GS, Dispenzieri A, Lacy MQ, Hayman SR, Rajkumar SV, et al. Flow cytometric detection of circulating myeloma cells before transplantation in patients with multiple myeloma: a simple risk stratification system. Blood. 2006;107:3384–8.
16. Paiva B, Paino T, Sayagues JM, Garayoa M, San-Segundo L, Martín M, et al. Detailed characterization of multiple myeloma circulating tumor cells shows unique phenotypic, cytogenetic, functional, and circadian distribution profile. Blood. 2013;122:3591–8.
17. Masri S, Sassone-Corsi P. The emerging link between cancer, metabolism, and circadian rhythms. Nat Med. 2018;24:1795–803.
18. Méndez-Ferrer S, Lucas D, Battista M, Frenette PS. Haematopoietic stem cell release is regulated by circadian oscillations. Nature. 2008;452:442–7.
19. Ghobrial IM. Myeloma as a model for the process of metastasis: implications for therapy. Blood. 2012;120:20–30.
20. Mishima Y, Paiva B, Shi J, Park J, Manier S, Takagi S, et al. The mutational landscape of circulating tumor cells in multiple myeloma. Cell Rep. 2017;19:218–24.
21. Lohr JG, Kim S, Gould J, Knoechel B, Drier Y, Cotton MJ, et al. Genetic interrogation of circulating multiple myeloma cells at single-cell resolution. Sci Transl Med. 2016;8:1–10.
22. Ledergor G, Weiner A, Zada M, Wang S-Y, Cohen YC, Gatt ME, et al. Single cell dissection of plasma cell heterogeneity in symptomatic and asymptomatic myeloma. Nat Med. 2018;24:1867–76.
23. Flores-Montero J, Flores LS, Paiva B, Puig N, García-Sánchez O, Böttcher S, et al. Next generation flow (NGF) for highly sensitive and standardized detection of minimal residual disease in multiple myeloma. Leukemia. 2017;31:2094–103.
24. Puig N, Paiva B, Lasa M, Burgos L, Perez JJ, Merino J, et al. Flow cytometry for fast screening and automated risk assessment in systemic light-chain amyloidosis. Leukemia. 2019;33:1256–67.
25. Fu GK, Wilhelmy J, Stern D, Fan HC, Fodor SPA. Digital encoding of cellular mRNAs enabling precise and absolute gene expression measurement by single-molecule counting. Anal Chem. 2014;86:2867–70.

26. Cole M, Risso D (2019). scone: Single Cell Overview of Normalized Expression data. R package version 1.8.0. https://doi.org/10.18129/B9.bioc.scone.

27. Butler A, Hoffman P, Smibert P, Papalexi E, Satija R. Integrating single-cell transcriptomic data across different conditions, technologies, and species. Nat Biotechnol. 2018;36:411–20.

28. Schlitzer A, Sivakamasundari V, Chen J, Sumatoh HR, Schreuder J, Lum J, et al. Identification of cDC1- and cDC2-committed DC progenitors reveals early lineage priming at the common DC progenitor stage in the bone marrow. Nat Immunol. 2015;16:718–28.

29. Ritchie ME, Phipson B, Wu D, Hu Y, Law CW, Shi W, et al. Limma powers differential expression analyses for RNA-sequencing and microarray studies. Nucleic Acids Res. 2015;43:e47.

30. Subramanian A, Tamayo P, Mootha VK, Mukherjee S, Ebert BL, Gillette MA, et al. Gene set enrichment analysis: a knowledge-based approach for interpreting genome-wide expression profiles. Proc Natl Acad Sci USA. 2005;102:15545–50.

31. Raimondi L, Amodio N, Teresa M, Martino D, Altomare E, Leotta M, et al. Targeting of multiple myeloma-related angiogenesis by miR-199a-5p mimics: in vitro and in vivo anti-tumor activity. Oncotarget. 2014;5:3039–54.

32. Alboukadel Kassambara (2019). ggpubr: 'ggplot2' Based Publication Ready Plots. R package version 0.2.1. https://CRAN.R-project.org/package=ggpubr.

33. Jaitin DA, Kenigsberg E, Keren-Shaul H, Elefant N, Paul F, Zaretsky I, et al. Massively parallel single-cell RNA-seq for marker-free decomposition of tissues into cell types. Science. 2014;343:776–9.

34. Lavin Y, Kobayashi S, Leader A, Amir ED, Elefant N, Bigenwald C, et al. Innate immune landscape in early lung adenocarcinoma by paired single-cell analyses. Cell. 2017;169:750–7. e17

35. Love MI, Huber W, Anders S. Moderated estimation of fold change and dispersion for RNA-seq data with DESeq2. Genome Biol. 2014;15:550.

36. Therneau T (2015). A Package for Survival Analysis in S. R package version 2.38. https://CRAN.R-project.org/package=survival.

37. Alboukadel Kassambara and Marcin Kosinski (2019). survminer: Drawing Survival Curves using 'ggplot2'. R package version 0.4.4. https://CRAN.R-project.org/package=survminer.

38. McKenzie CW, Craige B, Kroeger TV, Finn R, Wyatt TA, Sisson JH, et al. CFAP54 is required for proper ciliary motility and assembly of the central pair apparatus in mice. Mol Biol Cell. 2015;26:3140–9.

39. Martin TA, Harrison G, Mansel RE, Jiang WG. The role of the CD44/ezrin complex in cancer metastasis. Crit Rev Oncol Hematol. 2003;46:165–86.

40. Ivetic A, Ridley AJ. Ezrin/radixin/moesin proteins and Rho GTPase signalling in leucocytes. Immunology. 2004;112:165–76.

41. Zhu Y, Zhu MX, Zhang XD, Xu XE, Wu ZY, Liao LD, et al. SMYD3 stimulates EZR and LOXL2 transcription to enhance proliferation, migration, and invasion in esophageal squamous cell carcinoma. Hum Pathol. 2016;52:153–63.

42. Hsieh Y-H, Chou R-H, Hsieh S-C, Cheng C-W, Lin C-L, Yang S-F, et al. Targeting EMP3 suppresses proliferation and invasion of hepatocellular carcinoma cells through inactivation of PI3K/Akt pathway. Oncotarget. 2015;6:34859–74.

43. Dumitru CA, Bankfalvi A, Gu X, Zeidler R, Brandau S, Lang S. AHNAK and inflammatory markers predict poor survival in laryngeal carcinoma. PLoS ONE. 2013;8:e56420.

44. Davis TA, Loos B, Engelbrecht A-M. AHNAK: the giant jack of all trades. Cell Signal. 2014;26:2683–93.

45. Paiva B, Corchete LA, Vidriales M-B, Puig N, Maiso P, Rodriguez I, et al. Phenotypic and genomic analysis of multiple myeloma minimal residual disease tumor cells: a new model to understand chemoresistance. Blood. 2016;127:1896–906.

46. Waldschmidt JM, Simon A, Wider D, Müller SJ, Follo M, Ihorst G, et al. CXCL12 and CXCR7 are relevant targets to reverse cell adhesion-mediated drug resistance in multiple myeloma. Br J Haematol. 2017;179:36–49.

47. Anreddy N, Hazlehurst LA. Targeting intrinsic and extrinsic vulnerabilities for the treatment of multiple myeloma. J Cell Biochem. 2017;118:15–25.

48. Storti P, Marchica V, Giuliani N. Role of galectins in multiple myeloma. Int J Mol Sci. 2017;18:2740.

49. Glavey SV, Naba A, Manier S, Clauser K, Tahri S, Park J, et al. Proteomic characterization of human multiple myeloma bone marrow extracellular matrix. Leukemia. 2017;31:2426–34.

50. Ma Y, Jin Z, Huang J, Zhou S, Ye H, Jiang S, et al. IQGAP1 plays an important role in the cell proliferation of multiple myeloma via the MAP kinase (ERK) pathway. Oncol Rep. 2013;30:3032–8.

51. Gocke CB, McMillan R, Wang Q, Begum A, Penchev VR, Ali SA, et al. IQGAP1 scaffold-MAP kinase interactions enhance multiple myeloma clonogenic growth and self-renewal. Mol Cancer Ther. 2016;15:2733–9.

52. Aust G, Zhu D, Van Meir EG, Xu L. Adhesion GPCRs in tumorigenesis. Handb Exp Pharmacol. 2016;234:369–96.

53. Demchenko YN, Glebov OK, Zingone A, Keats JJ, Bergsagel PL, Kuehl WMClassical. and/or alternative NF-kB pathway activation in multiple myeloma. Cancer. 2010;115:3541–52.

54. Troppan K, Hofer S, Wenzl K, Lassnig M, Pursche B, Steinbauer E, et al. Frequent down regulation of the tumor suppressor gene A20 in multiple myeloma. PLoS ONE. 2015;10:e0123922.

55. Broyl A, Hose D, Lokhorst H, De Knegt Y, Peeters J, Jauch A, et al. Gene expression profiling for molecular classification of multiple myeloma in newly diagnosed patients. Gene Expr. 2010;116:2543–53.

56. Li D, Wu C, Cai Y, Liu B. Association of NFKB1 and NFKBIA gene polymorphisms with susceptibility of gastric cancer. Tumor Biol. 2017;39:1–6.

57. Zhang M, Huang J, Tan X, Bai J, Wang H, Ge Y, et al. Common polymorphisms in the NFKBIA gene and cancer susceptibility: a meta-analysis. Med Sci Monit. 2015;21:3186–96.

58. Wang Q, Wang X, Liang Q, Wang S, Xiwen L, Pan F, et al. Distinct prognostic value of mRNA expression of guanylate-binding protein genes in skin cutaneous melanoma. Oncol Lett. 2018;15:7914–22.

59. Godoy P, Cadenas C, Hellwig B, Marchan R, Stewart J, Reif R, et al. Interferon-inducible guanylate binding protein (GBP2) is associated with better prognosis in breast cancer and indicates an efficient T cell response. Breast Cancer. 2014;21:491–9.

60. Thijssen VL, Heusschen R, Caers J, Griffioen AW. Galectin expression in cancer diagnosis and prognosis: a systematic review. Biochim Biophys Acta. 2015;1855:235–47.

61. Cheng CL, Hou HA, Lee MC, Liu CY, Jhuang JY, Lai YJ, et al. Higher bone marrow LGALS3 expression is an independent unfavorable prognostic factor for overall survival in patients with acute myeloid leukemia. Blood. 2013;121(Apr):3172–80.

62. Albright RA, Chang WC, Robert D, Ornstein DL, Cao W, Liu L, et al. NPP4 is a procoagulant enzyme on the surface of vascular endothelium. Blood. 2012;120:4432–40.

63. Xu X, Han K, Zhu J, Mao H, Lin X, Zhang Z, et al. An inhibitor of cholesterol absorption displays anti-myeloma activity by targeting the JAK2-STAT3 signaling pathway. Oncotarget. 2016;7:75539–50.

64. Murai T. Cholesterol lowering: role in cancer prevention and treatment. Biol Chem. 2015;396:1–11.

65. Silvente-Poirot S, Poirot M. Cancer. Cholesterol and cancer, in the balance. Science. 2014;343:1445–6.

66. Cohen Y, Gutwein O, Garach-Jehoshua O, Bar-Haim A, Kornberg A. The proliferation arrest of primary tumor cells out-of-niche is associated with widespread downregulation of mitotic and transcriptional genes. Hematology. 2014;19:286–92.

67. Deng Y, Jiang L, Wang Y, Xi Q, Zhong J, Liu J, et al. High expression of CDC6 is associated with accelerated cell proliferation and poor prognosis of epithelial ovarian cancer. Pathol Res Pract. 2016;212:239–46.

68. Avigdor A, Goichberg P, Shivtiel S, Dar A, Peled A, Samira S, et al. CD44 and hyaluronic acid cooperate with SDF-1 in the trafficking of human CD34+ stem/progenitor cells to bone marrow. Blood. 2004;103:2981–9.

69. Dimitroff CJ, Lee JY, Rafii S, Fuhlbrigge RC, Sackstein R. CD44 is a major E-selectin ligand on human hematopoietic progenitor cells. J Cell Biol. 2001;153:1277–86.

70. Kodama H, Murata S, Ishida M, Yamamoto H, Yamaguchi T, Kaida S, et al. Prognostic impact of CD44-positive cancer stem-like cells at the invasive front of gastric cancer. Br J Cancer. 2017;116:186–94.

71. Chanmee T, Ontong P, Kimata K, Itano N. Key roles of hyaluronan and its CD44 receptor in the stemness and survival of cancer stem cells. Front Oncol. 2015;5:180.

72. Palumbo A, Avet-Loiseau H, Oliva S, Lokhorst HM, Goldschmidt H, Rosinol L, et al. Revised International Staging System for Multiple Myeloma: A Report From International Myeloma Working Group. J Clin Oncol. 2015;33:2863–9.

73. Storti P, Marchica V, Airoldi I, Donofrio G, Fiorini E, Ferri V, et al. Galectin-1 suppression delineates a new strategy to inhibit myeloma-induced angiogenesis and tumoral growth in vivo. Leukemia. 2016;30:2351–63.

74. Takagi S, Tsukamoto S, Park J, Johnson KE, Kawano Y, Moschetta M, et al. Platelets enhance multiple myeloma progression via il-1b upregulation. Clin Cancer Res. 2018;24:2430–9.

75. Leblanc R, Peyruchaud O. Metastasis: new functional implications of platelets and megakaryocytes. Blood. 2016;128:24–31.

76. Dongre A, Weinberg RA. New insights into the mechanisms of epithelial–mesenchymal transition and implications for cancer. Nat Rev Mol Cell Biol. 2019;20:69–84.

77. Batlle E, Clevers H. Cancer stem cells revisited. Nat Med. 2017;23:1124–34.

78. Zhang H, Brown RL, Wei Y, Zhao P, Liu S, Liu X, et al. CD44 splice isoform switching determines breast cancer stem cell state. Genes Dev. 2019;33:1–14.

79. Misra S, Heldin P, Hascall VC, Karamanos NK, Skandalis SS, Markwald RR, et al. Hyaluronan-CD44 interactions as potential targets for cancer therapy. FEBS J. 2011;278:1429–43.

80. Mueller N, Wicklein D, Eisenwort G, Jawhar M, Berger D, Stefanzl G, et al. CD44 is a RAS/STAT5-regulated invasion receptor that triggers disease expansion in advanced mastocytosis. Blood. 2018;132:1936–50.

81. Bjorklund CC, Baladandayuthapani V, Lin HY, Jones RJ, Kuiatse I, Wang H, et al. Evidence of a role for CD44 and cell adhesion in mediating resistance to lenalidomide in multiple myeloma: therapeutic implications. Leukemia. 2014;28:373–83.

82. Yan Y, Zuo X, Wei D. Concise review: emerging role of CD44 in cancer stem cells: a promising biomarker and therapeutic target. Stem Cells Transl Med. 2015;4:1033–43.

83. Natoni A, Smith TAG, Keane N, McEllistrim C, Connolly C, Jha A, et al. E-selectin ligands recognised by HECA452 induce drug resistance in myeloma, which is overcome by the E-selectin antagonist, GMI-1271. Leukemia. 2017;31:2642–51.

84. Lytle NK, Barber AG, Reya T. Stem cell fate in cancer growth, progression and therapy resistance. Nat Rev Cancer. 2018;18:669–80.

85. Roccaro AM, Mishima Y, Sacco A, Moschetta M, Tai Y-T, Shi J, et al. CXCR4 regulates extra-medullary myeloma through epithelial-mesenchymal-transition-like transcriptional activation. Cell Rep. 2015;12:622–35.

86. Peacock CD, Wang Q, Gesell GS, Corcoran-Schwartz IM, Jones E, Kim J, et al. Hedgehog signaling maintains a tumor stem cell compartment in multiple myeloma. Proc Natl Acad Sci USA 2007;104:4048–53.

87. Matsui W, Huff CA, Wang Q, Malehorn MT, Barber J, Tanhehco Y, et al. Characterization of clonogenic multiple myeloma cells. Blood. 2004;103:2332–6.

88. Thiago LS, Perez-Andres M, Balanzategui A, Sarasquete ME, Paiva B, Jara-Acevedo M, et al. Circulating clonotypic B cells in multiple myeloma and monoclonal gammopathy of undetermined significance. Haematologica. 2014;99:155–62.

89. Li H, Zhong A, Li S, Meng X, Wang X, Xu F, et al. The integrated pathway of TGFβ/Snail with TNFα/NFκB may facilitate the tumor-stroma interaction in the EMT process and colorectal cancer prognosis. Sci Rep. 2017;7:4915.

90. Manzi M, Bacigalupo ML, Carabias P, Elola MT, Wolfenstein-Todel C, Rabinovich GA, et al. Galectin-1 controls the proliferation and migration of liver sinusoidal endothelial cells and their interaction with hepatocarcinoma cells. J Cell Physiol. 2016;231:1522–33.

Affiliations

Juan-Jose Garcés [iD][1] · Michal Simicek[2,3,4] · Marco Vicari[5] · Lucie Brozova[6] · Leire Burgos[1] · Renata Bezdekova[7] · Diego Alignani[1] · Maria-Jose Calasanz[1] · Katerina Growkova[2,3,4] · Ibai Goicoechea[1] · Xabier Agirre[1] · Ludek Pour[7] · Felipe Prosper [iD][1] · Rafael Rios[8] · Joaquin Martinez-Lopez[9] · Pamela Millacoy[10] · Luis Palomera[11] · Rafael Del Orbe [iD][12] · Albert Perez-Montaña[13] · Sonia Garate[1] · Laura Blanco[1] · Marta Lasa[1] · Patricia Maiso[1] · Juan Flores-Montero[14] · Luzalba Sanoja-Flores[14] · Zuzana Chyra[2,6] · Alexander Vdovin[2,3,4] · Tereza Sevcikova[2,4] · Tomas Jelinek[2,3,4] · Cirino Botta [iD][15] · Halima El Omri[16] · Jonathan Keats [iD][17] · Alberto Orfao[14] · Roman Hajek[2,3] · Jesus F. San-Miguel[1] · Bruno Paiva[1]

1   Clinica Universidad de Navarra, Centro de Investigacion Medica Aplicada (CIMA), Instituto de Investigacion Sanitaria de Navarra (IDISNA), CIBER-ONC numbers CB16/12/00369 and CB16/12/00489, Pamplona, Spain

2   Department of Hematooncology, University Hospital of Ostrava, Ostrava, Czech Republic

3   Faculty of Medicine, University of Ostrava, Ostrava, Czech Republic

[4] Faculty of Science, University of Ostrava, Ostrava, Czech Republic

[5] Campus Bio-Medico University of Rome, Rome, Italy

[6] Masaryk University, Brno, Czech Republic

[7] University Hospital Brno, Brno, Czech Republic

[8] Hospital Universitario Virgen de las Nieves, Granada, Spain

[9] Hospital Universitario 12 de Octubre, Madrid, Spain

[10] Complejo Hospitalario de Navarra, Pamplona, Spain

[11] Hospital Clínico Universitario Lozano Blesa, Zaragoza, Spain

[12] Biocruces Health Research Institute, Barakaldo, Spain

[13] Hospital Son Espases, Palma, Spain

[14] Cancer Research Center (IBMCC-CSIC/USAL-IBSAL), Cytometry Service (NUCLEUS) and Department of Medicine, University of Salamanca (USAL), , CIBER-ONC number CB16/12/00400, Salamanca, Spain

[15] Department of Clinical and Experimental Medicine, Magna Graecia University, Catanzaro, Italy

[16] National Center for Cancer Care and Research, Hamad Medical Corporation, Doha, Qatar

[17] Translational Genomics Research Institute, Phoenix, AZ, USA